Méthodes d'analyse et de modélisation pertinentes pour la propagation des ondes à l'échelle méso dans des milieux hétérogènes

Wen Xu

To cite this version:

Wen Xu. Méthodes d'analyse et de modélisation pertinentes pour la propagation des ondes à l'échelle méso dans des milieux hétérogènes. Physique [physics]. Université Paris Saclay (COmUE), 2018. Français. NNT : 2018SACLC044 . tel-01849626

HAL Id: tel-01849626
https://theses.hal.science/tel-01849626

Submitted on 26 Jul 2018

université
PARIS-SACLAY

CentraleSupélec

NNT : 2018SCALC044

Relevant numerical methods for mesoscale wave propagation in heterogeneous media

Thèse de doctorat de l'Université Paris-Saclay
préparée à CentraleSupélec

École doctorale n°579 : sciences mécaniques et énergétiques,
matériaux et géosciences (SMEMAG)
Spécialité de doctorat: mécanique des solides

Thèse présentée et soutenue à Gif-Sur-Yvette, le 17/07/2018, par

Wen XU

Composition du Jury :

Anne-Sophie Bonnet-Ben Dhia Directrice de recherche, Ensta ParisTech	Présidente
Bruno Lombard Directeur de recherche, Centrale Marseille	Rapporteur
Pedro Díez Professeur, UPC–BarcelonaTech	Rapporteur
Eric Savin Chercheur, ONERA	Examinateur
Xavier Claeys Maître de conférences, Université Pierre et Marie Curie	Examinateur
Régis Cottereau Chargé de recherche, CentraleSupélec	Directeur de thèse
Bing Tie Chargée de recherche, CentraleSupélec	Co-directrice de thèse (invitée)

Thèse de doctorat

Acknowledgements

First and foremost, I would like to express my sincere gratitude to my supervisors Bing Tie and Régis Cottereau, and also Denis Aubry who gave me excellent guidance during the first year of my thesis, for their vast knowledge as well as their constant guidance, encouragement and support for my research. They are behind me all the way, answering my questions patiently and promptly, giving insightful advices and enriching comments. It has been really a great pleasure to work with all of them and I feel so lucky to have them as my supervisors.

Then I would like to thank my thesis reporters, Bruno Lombard and Pedro Díez for their detailed comments that helped me a lot in the improvement of this thesis. Besides, I would like to thank the rest of my dissertation committee members, Anne-sophie Bonnet-Ben Dhia, Xavier Claeys and Eric Savin, for all of their discussion and feedback throughout my defense that have been absolutely invaluable for me.

My sincere gratitude also goes to all teachers and staff members in laboratory MSSMat, especially to Anne-sophie Mouronval for her kindly help and professional support for providing calculation devices, to Ibrahim Baydoun for his help in understanding some important articles that I referred to, to Guillaume Puel for his guidance in the 3rd year of Engineering & Master studies and also to Hachmi Ben Dhia for his help in applying for this PhD thesis.

I thank my fellow labmates, Yu Liu, Benhui Fan, Ahmed Sridi, Angkeara Svay, Khalil Abene, Luciano de Carvalho Paludo, Lucio De Abreu Correa, Fillipo Gatti, Maroua Hammani, Alfonso Panunzio, Hélène Moustacas, Matthieu Bonneric, Delong He, Thiago Milanetto Schlittler, Romain Ruyssen, Sara Touhami, far from being exhausted, for sharing their experience and knowledge, and for all the good times we have had during my four years life here.

Thanks are also due to the Chinese Scholarship Council (CSC) for its financial support that I otherwise would not have been able to develop my scientific discoveries.

Last but not least, I would like to thank my husband Shuimiao DU for always being there with me and for his never-ending support, and also to my parents and to my brother and sister for supporting me spiritually throughout finishing this thesis.

Table of contents

List of notations and definitions

The next list describes several notations and definitions for some spaces, products and norms that are used within the thesis.

$E_{H_0^1(\Omega),(T)}$	Space of functions $\mathbf{w}$ in space $H_0^1(\Omega)$ for $\forall t \in [0,T]$ such that $t \to \mathbf{w}(\cdot,\mathbf{x})$ is in $L^2(0,T)$
$E_{H(\text{div},\Omega),(T)}$	Space of functions $\mathbf{w}$ in space $H(\text{div},\Omega)$ for $\forall t \in [0,T]$ such that $t \to \mathbf{w}(\cdot,\mathbf{x})$ is in $L^2(0,T)$
$(\mathbf{w}_1,\mathbf{w}_2)_{(\Omega)} := (\mathbf{w}_1,\mathbf{w}_2)_{L^2(\Omega)} = \int_\Omega \mathbf{w}_1 \cdot \mathbf{w}_2 d\mathbf{x}$	Inner product in space $L^2(\Omega)$
$(\mathbf{w}_1,\mathbf{w}_2)_{1(\Omega)} := (\mathbf{w}_1,\mathbf{w}_2)_{H_0^1(\Omega)} = \int_\Omega \nabla_\mathbf{x}\mathbf{w}_1 \cdot \nabla_\mathbf{x}\mathbf{w}_2 d\mathbf{x}$	Inner product in space $H_0^1(\Omega)$
$(\mathbf{w}_1,\mathbf{w}_2)_{K(\Omega)} := \int_\Omega \boldsymbol{\sigma}(\mathbf{w}_1) : \boldsymbol{\varepsilon}(\mathbf{w}_2) d\mathbf{x}$	Inner product in space related to the elastic potential energy
$(\mathbf{w}_1,\mathbf{w}_2)_{M(\Omega)} := \int_\Omega \rho \mathbf{w}_1 \cdot \mathbf{w}_2 d\mathbf{x}$	Inner product in space related to the kinetic energy
$\lVert w \rVert_{(T)} := \lVert w \rVert_{L^2(T)}$	L^2-norm in time $[0,T]$
$\lVert w \rVert_{\infty(T)} := \sup_{t\in[0,T]} \lvert w \rvert$	L^∞-norm in time $[0,T]$
$\lVert \mathbf{w} \rVert_{(\Omega)} := \sqrt{(\mathbf{w},\mathbf{w})_{(\Omega)}}$	L^2-norm in space
$\lVert \mathbf{w} \rVert_{1(\Omega)} := \sqrt{(\mathbf{w},\mathbf{w})_{1(\Omega)}}$	H^1-norm in space
$\lVert \mathbf{w} \rVert_{K(\Omega)} := \sqrt{(\mathbf{w},\mathbf{w})_{K(\Omega)}}$	Norm in space related to the elastic potential energy
$\lVert \mathbf{w} \rVert_{M(\Omega)} := \sqrt{(\mathbf{w},\mathbf{w})_{M(\Omega)}}$	Norm in space related to the kinetic energy
$\lVert \mathbf{w} \rVert_{K(\Omega),(T)} := \sqrt{\int_0^T \lVert \mathbf{w} \rVert_{K(\Omega)}^2 dt}$	L^2-norm in time of the elastic potential energy
$\lVert \mathbf{w} \rVert_{K(\Omega),\infty(T)} := \sup_{t\in[0,T]} \lVert \mathbf{w} \rVert_{K(\Omega)}(t)$	L^∞-norm in time of the elastic potential energy
$\lVert \mathbf{w} \rVert_{M(\Omega),(T)} := \sqrt{\int_0^T \lVert \mathbf{w} \rVert_{M(\Omega)}^2 dt}$	L^2-norm in time of the kinetic energy
$\lVert \mathbf{w} \rVert_{M(\Omega),\infty(T)} := \sup_{t\in[0,T]} \lVert \mathbf{w} \rVert_{M(\Omega)}(t)$	L^∞-norm in time of the kinetic energy

Chapter 1

Introduction

Contents

1.1 Context

Wave propagation in homogeneous media and its numerical modelling have been widely developed for many years [1, 27, 85, 108]. However, when waves propagate in heterogeneous media, where the physical properties of media vary continuously or discontinuously, waves interact with heterogeneities and a lot of complicated phenomena arise: reflection, refraction, diffraction, scattering, interference, attenuation, dispersion, etc. [1, 78, 103, 153]. Due to this complex nature, direct numerical simulations on the fine grids become prohibitively expensive and the quantities that are classically considered as relevant for quality control of numerical solutions are always highly oscillating in time-space. It is therefore important and necessary to develop efficient, accurate and even new methods for the quantification of numerical errors.

This work deals with the numerical analysis of wave propagation problems in heterogeneous media and the a posteriori error estimation for its finite element solutions, which allows assessing and controlling their quality.

This project has various applications in different domains, such as the numerical modeling of polycrystalline permeability to ultrasonic waves [15, 16, 69, 145]. Crystalline solids are composed of large quantities of grains (or crystallites). Each grain can belong to a specific class of crystal symmetry exhibiting anisotropic elasticity and possess a unique crystallographic orientation from the neighbouring grains. An elastic wave travelling through a polycrystalline material gets scattered at grain interfaces due to crystallographic misorientations of adjacent grains. This scattering leads to a loss of energy by the coherent wave and results in apparent wave attenuation and noise signals, which depend on ultrasonic frequency, grain size and shape, and the elastic properties of the crystallites. Understanding elastic wave interactions with these media is very important for non-destructive testing [30]. Figure 1.1 illustrates ultrasonic wave propagation in a polycrystalline material.

This project can also be applied in geophysics [49, 121, 149]. Seismic or elastic wave propagation through the earth plays an important role in understanding damages during earthquakes. It is known that the materials in the earth are highly heterogeneous and their elastic properties vary with the depth from one region to another. Although this variation may be gradual, there exist also discontinuities that separate media with different elastic coefficients. The existence of arbitrary-shaped interfaces, inclusions and fractures requires an efficient treatment [4, 99, 100]. Considering that the earth has strong heterogeneities and complex geometries, its numerical modelling is quite a challenging problem. Figure 1.2b gives P-wave velocity of the Marmousi2 model. The geometry of this model is based on a profile through the North Quenguela trough in the Cuanza basin [36, 107]. Figure 1.2c shows a simulation of P-wave propagation in soil.

Furthermore, in geophysics, the length scale is of the order of the kilometre and the physical properties vary continuously or discontinuousely, while in the polycrystalline application, the length scale is of the order of the micrometre and the anisotropic material properties are discontinuous from one grain to another. Even if the involved scales and the frequency of waves are very different in the two cases and the polycrystalline materials reveal much more discontinuities at the interfaces, they present similar issues when efficient numerical simulations are sought for.

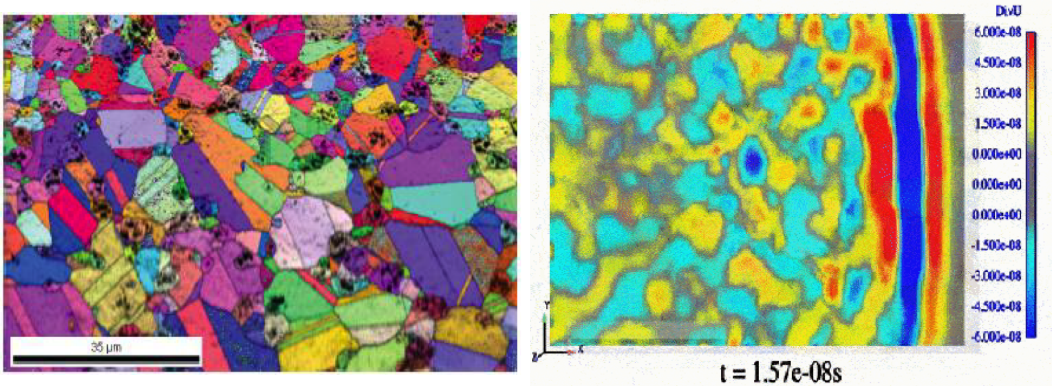

(a) (b)

Fig. 1.1 (a) polycrystalline microstructure, (b) simulation of quasi-P wave propagation in polycristals (by MSSMat, CentraleSupélec)

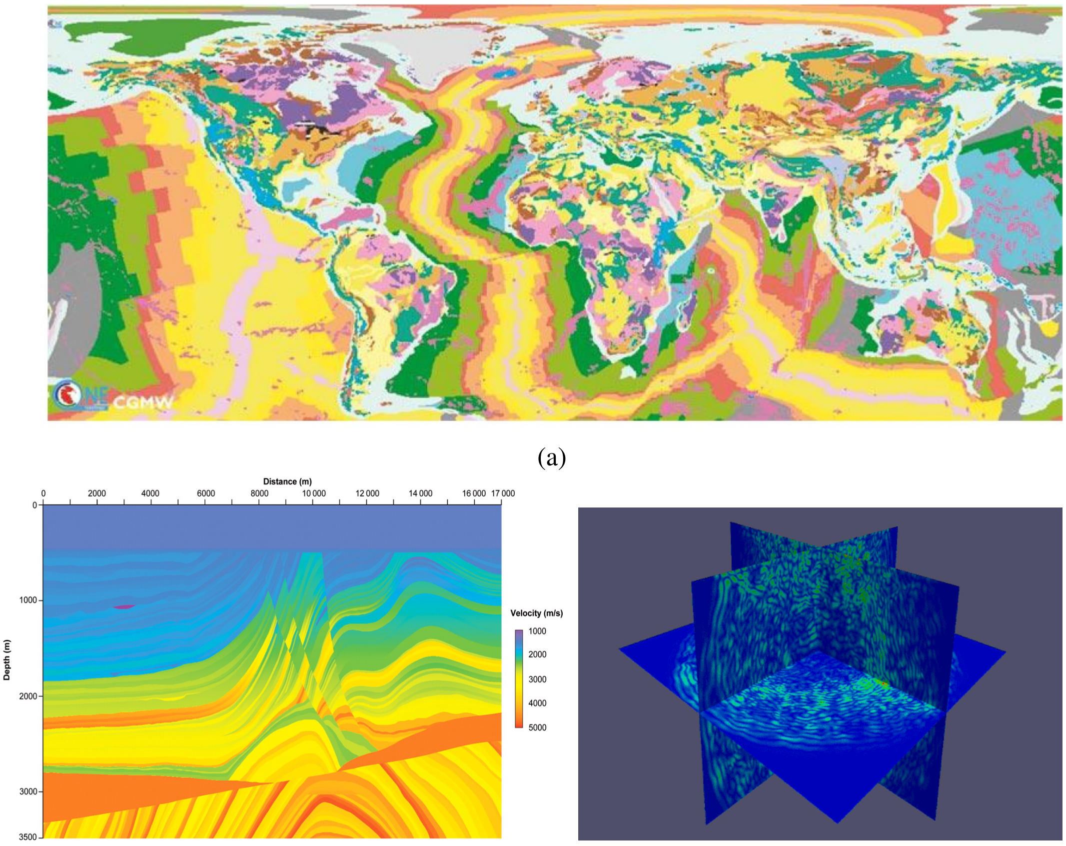

(a)

(b) (c)

Fig. 1.2 (a) example of horizontal heterogeneity at the global scale: geology map of the surface of the Earth [39], (b) Marmousi2 P-wave velocity [107], (c) simulation of P-wave propagation in soil (by MSSMat, CentraleSupélec)

1.2 Modelling of elastic wave propagation in heterogeneous media

In this section, we start with the introduction of the elastodynamic equation in homogeneous media. Then different types of waves and various propagation phenomena in heterogeneous media are presented. Finally, the high frequency (HF) wave propagation in the weak coupling regime studied in this work is introduced in detail.

1.2.1 Wave propagation in homogeneous media

We introduce firstly the elastic wave propagation in homogeneous media in an open domain $\Omega \subseteq \mathbb{R}^3$ and $\mathbb{R}^3$ stands for the general three-dimensional Euclidean space. The density of media is denoted by ρ. The displacement field is denoted by $\mathbf{u}(t,\mathbf{x}) : (0,T)\times\Omega \to \mathbb{R}^3$, where $\mathbf{x}\in\Omega$ is the spatial position vector. The second-order Cauchy stress tensor is denoted by $\boldsymbol{\sigma}(t,\mathbf{x})$ and $\mathbf{f}$ stands for the density of body force.

Then the second-order elastodynamic equation reads:

$$\rho\partial_t^2\mathbf{u}(t,\mathbf{x}) - \nabla_{\mathbf{x}}\cdot\boldsymbol{\sigma}(\mathbf{u}(t,\mathbf{x})) = \mathbf{f} \qquad \forall(t,\mathbf{x})\in(0,T)\times\Omega \tag{1.1}$$

where ρ is independent of $\mathbf{x}$ in the homogeneous case and $\nabla_{\mathbf{x}}$ is the gradient with respect to $\mathbf{x}$. The stress field $\boldsymbol{\sigma}$ is defined by the generalized Hooke's law:

$$\boldsymbol{\sigma}(t,\mathbf{x}) = \mathbf{C} : \boldsymbol{\varepsilon}(t,\mathbf{x}) \tag{1.2}$$

where $\mathbf{C}$ is the fourth-order elasticity tensor, independent of $\mathbf{x}$ in the homogeneous case. For homogeneous isotropic elastic materials [1], eq. (1.2) becomes:

$$\boldsymbol{\sigma} = \lambda\,\mathrm{tr}(\boldsymbol{\varepsilon})\mathbf{I}_3 + 2\mu\boldsymbol{\varepsilon} \tag{1.3}$$

where $\mathrm{tr}(\cdot)$ is the trace operator, $\mathbf{I}_3$ is the 3×3 identity matrix, and λ,μ are two Lamé parameters.The strain tensor $\boldsymbol{\varepsilon}$ is defined by:

$$\boldsymbol{\varepsilon}(t,\mathbf{x}) = \nabla_{\mathbf{x}}\otimes_s\mathbf{u}(t,\mathbf{x}) = \frac{1}{2}\left(\nabla_{\mathbf{x}}\otimes\mathbf{u}(t,\mathbf{x}) + (\nabla_{\mathbf{x}}\otimes\mathbf{u}(t,\mathbf{x}))^T\right) \tag{1.4}$$

where $\otimes_s$ is the symmetrized tensor product of two vectors, $\otimes$ is the tensor product and the superscript T stands for the transpose.

Equation (1.1) is solved subject to the initial conditions and the boundary conditions. At initial instant $t = 0$, the displacement and the velocity are defined as:

$$\mathbf{u}(0,\mathbf{x}) = \mathbf{u}_0(\mathbf{x}), \qquad \partial_t\mathbf{u}(0,\mathbf{x}) = \mathbf{v}_0(\mathbf{x}) \qquad\qquad \forall\mathbf{x}\in\Omega \tag{1.5}$$

The boundary conditions mean that the displacement and/or the stress vectors are specified on $\partial\Omega$, such as Dirichlet or Neumann boundary conditions [152]:

$$\mathbf{u} = \mathbf{0} \quad \text{on} \quad (0,T)\times\Gamma_{\mathbf{u}}, \qquad \boldsymbol{\sigma}(\mathbf{u})\cdot\mathbf{n} = \mathbf{h} \quad \text{on} \quad (0,T)\times\Gamma_{\boldsymbol{\sigma}} \tag{1.6}$$

where $\mathbf{h}$ denote the density of surface force.

In the particular case of harmonic plane waves, the displacement fields have the following form:

$$\mathbf{u}(t,\mathbf{x}) = \mathbf{U}e^{i(\mathbf{x}\cdot\mathbf{k}-t\omega)} \tag{1.7}$$

where $\mathbf{U}$ is the wave mode defining the polarization direction and amplitude, i is the imaginary unit, $\mathbf{k}$ is the wave vector which specifies the direction of propagation and ω is the angular frequency of wave. Now introducing eq. (1.7) to eq. (1.1) and taking $\mathbf{f} = 0$, the so-called Christoffel equation is obtained:

$$\left(\omega^2\mathbf{I}_3 - \boldsymbol{\Gamma}(\mathbf{k})\right)\cdot\mathbf{U} = \mathbf{0} \tag{1.8}$$

where the Christoffel tensor $\boldsymbol{\Gamma}$ is defined as (with Einstein summation convention): $\forall\mathbf{W}$,

$$\boldsymbol{\Gamma}(\mathbf{k})\cdot\mathbf{W} = \rho^{-1}\left(\mathbf{C} : (\mathbf{W}\otimes_s\mathbf{k})\right)\cdot\mathbf{k} \qquad \text{i.e.} \qquad \Gamma_{ik} = \rho^{-1}C_{ijkl}k_jk_l \tag{1.9}$$

From eq. (1.8) it is known that the polarization vector $\mathbf{U}$ and ω^2 are respectively the eigenvector and eigenvalue of $\boldsymbol{\Gamma}(\mathbf{k})$. The wave propagation modes can be obtained by using eigendecomposition. For homogeneous isotropic elastic materials, $\boldsymbol{\Gamma}(\mathbf{k})$ has three eigenvalues:

$$\omega_1^2 = \frac{\lambda+2\mu}{\rho}|\mathbf{k}|^2, \qquad \omega_2^2 = \omega_3^2 = \frac{\mu}{\rho}|\mathbf{k}|^2 \tag{1.10}$$

The corresponding eigenvectors or polarization directions of waves are respectively denoted by three unit vectors $\hat{\mathbf{k}}, \hat{\mathbf{k}}_1^{\perp}$ and $\hat{\mathbf{k}}_2^{\perp}$. $\hat{\mathbf{k}} = \frac{\mathbf{k}}{|\mathbf{k}|}$ is the eigenvector of ω_1^2 and $\left\{\hat{\mathbf{k}}_1^{\perp}, \hat{\mathbf{k}}_2^{\perp}\right\}$ are the eigenvectors of ω_2^2 such as $(\hat{\mathbf{k}}, \hat{\mathbf{k}}_1^{\perp}, \hat{\mathbf{k}}_2^{\perp})$ form an orthonormal triplet. Equation (1.10) are called the dispersion relation for each wave mode. The first eigenvalue corresponds to the P-wave mode and the other one with multiplicity of two to the S-wave mode:

$$\omega_p = c_p|\mathbf{k}| = \sqrt{\frac{\lambda+2\mu}{\rho}}|\mathbf{k}|, \qquad \omega_s = c_s|\mathbf{k}| = \sqrt{\frac{\mu}{\rho}}|\mathbf{k}| \tag{1.11}$$

where c_p and c_s are respectively velocities of P-wave and S-wave. P-waves propagate at a higher velocity than do the S-waves and the two S-waves in an isotropic medium propagate at the same velocity.

We presented above the pure body waves P and S. The mode of propagation of a P-wave is always longitudinal and a S-wave is transverse (fig. 1.3, left). They can travel through the interior of a body such as the Earth's inner layers. When waves meet the boundary or the interface between two homogeneous materials, they can be reflected and transmitted between each other and conversions between P and S-waves exist. Surface waves, in contrast to body waves can only move along the

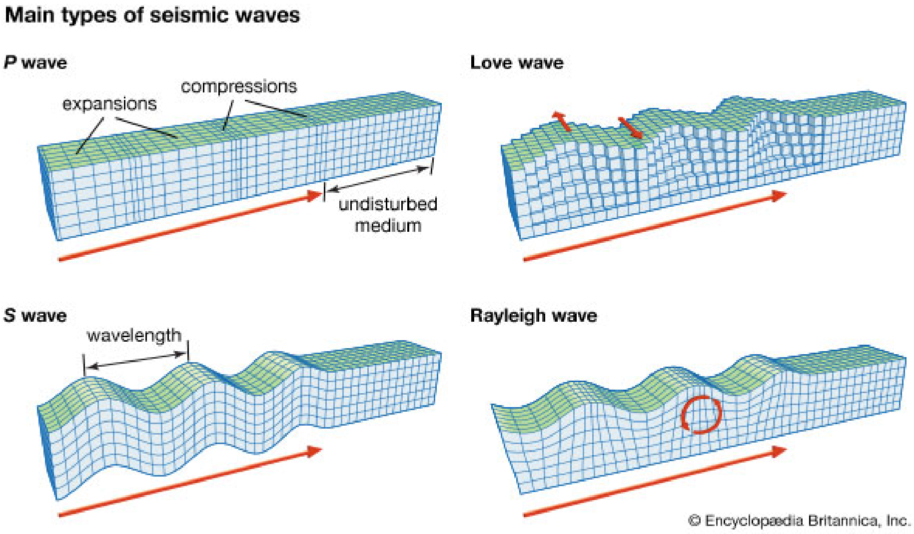

Fig. 1.3 Body waves (left) and surface waves (right) (Encyclopædia Britannica, Inc.)

surface [1, 151]. There are two types of surface waves: Love waves and Rayleigh waves [7]. The Love wave is polarized in the horizontal direction perpendicular to the propagation path, while Rayleigh waves have an ellipsoidal polarization in the vertical plane through the path of propagation (fig. 1.3, right).

1.2.2 Phenomena and scattering regimes for wave propagation in heterogeneous media

Now we focus on heterogeneous media, where physical properties of media $\mathbf{C}$ depend on $\mathbf{x}$ (ρ can also depend on $\mathbf{x}$ but here we assume it constant).

As we mentioned in the section 1.1, various complex phenomena appear when different types of waves propagate in heterogeneous media. More specifically, waves are reflected when they encounter boundaries of material properties through which they are traveling. When waves meet the interface between two media of different material properties, they change directions and this phenomenon is called refraction. Diffraction refers to the ability of waves to bend around corners or slits and to spread whenever they encounter obstacles. Attenuation is the term used to account for loss of wave amplitude due to all mechanisms, including absorption, scattering, and mode conversion. Scattering refers to wave radiation from heterogeneity acting as secondary sources of radiation due to excitation by the incident wave. An example of illustration of some phenomena mentioned above is given in fig. 1.4.

Specifically, scattering can be classified into different regimes according to the characteristic length scales [8, 154]. In fact, it is known that wave propagation in heterogeneous media is a multi-scale problem both mathematically and numerically, and different phenomena can happen for different scales involved. There are at least three fundamental length scales for wave propagation problems: the propagation distance L, the characteristic length of heterogeneity l_c (the scale on

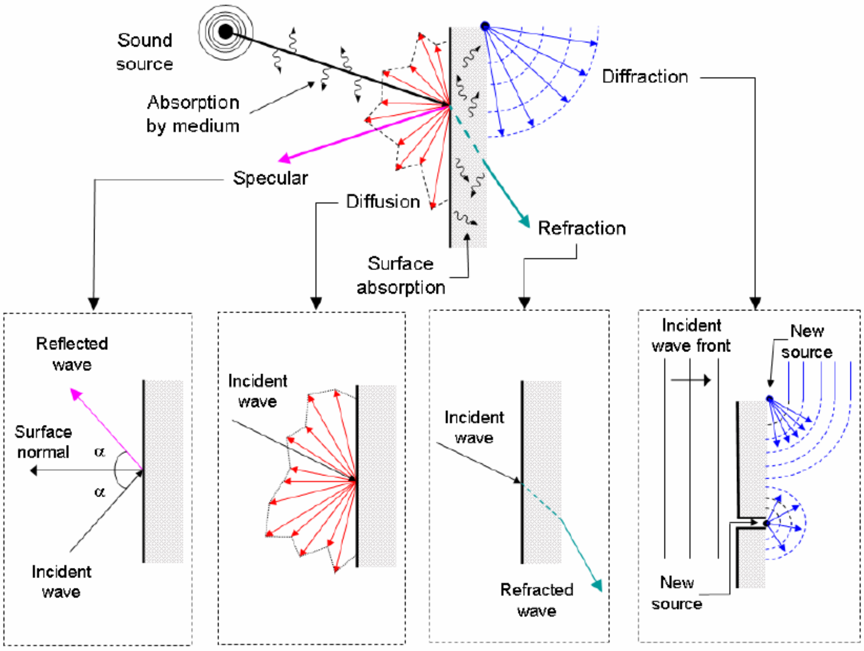

Fig. 1.4 Acoustic wave propagation phenomena: specular reflection, diffuse reflection, refraction and diffraction [84]

which the heterogeneous medium varies) and the dominant wavelength λ. Also, the amplitude of the fluctuations of heterogeneities σ^2 has to be considered. The following scattering regimes and phenomena can be described with different values of dimensionless parameters $\xi := kl_c = 2\pi l_c/\lambda$ and $\varepsilon := \lambda/L$ [155]:

1. quasi-homogeneous or effective medium regime: $\xi < 0.01, \sigma^2 \approx 1$ and $\varepsilon \approx 1$. The medium can be regarded as quasi-homogeneous, because the heterogeneous scale length l_c is very small compared to the typical wavelength λ. The homogenization methods with a deterministic effective wave equation can be applied [38, 56, 98].

2. Rayleigh scattering regime: $0.01 \leq \xi < 0.1$. The amount of scattered energy in 3D is proportional to k^4, leading to apparent attenuation of high frequencies [34, 62]. In the case that the scattering field is much weaker than the incident field, Born approximation is used [69, 133], based on the expansion of elastic constants whose variations are very weak $\sigma^2 \ll 1$.

3. weak coupling regime: $0.1 \leq \xi \leq 10, \sigma^2 \ll 1, \varepsilon \ll 1$. In this regime where the heterogeneity scale length is in the same order with the wavelength and small compared to the propagation distance and the fluctuations of the inhomogeneities are weak, full interactions between wave fields and media can be observed. This regime cannot be treated by usual homogenization and multi-scale techniques. In this case, the transport or the radiative transfer equations are the appropriate models to describe the propagation of the wave energy [17, 119]. In the chapters 3 and 4, our work focuses on applications in this regime.

4. forescattering regime: $\xi \gg 1$. The wavelength is small compared to the length of heterogeneity and the scattered wave energy is mainly concentrated near the forward direction. In this case the parabolic approximation for the full wave equation can be used [43]. It describes a one-way (forward direction) wave propagation, since the back-scattered waves are very weak. The scattering problem becomes a focusing diffraction and interference problem [93, 94].

1.2.3 High frequency setting

The high frequency wave propagation, when we assume the wavelength is small compared to the propagation distance (i.e. $\varepsilon \ll 1$), is specifically introduced here. It should be studied in a different and specific way compared to the low or mid frequency wave propagations. The most relevant observables for modelling wave propagation in HF limit are no longer the wave field $\mathbf{u}_\varepsilon$ or its derivatives, but rather its quadratic quantities like energy or energy density. It can be understood by a simple example discussed in [25, 123].

Considering the following wave field $x \to u_\varepsilon(x)$, which oscillates with an amplitude $a(x)$ and its mean function $u(x)$:

$$u_\varepsilon(x) = u(x) + a(x)\sin\frac{x}{\varepsilon}, \qquad 0 < \varepsilon \ll 1 \tag{1.12}$$

$u_\varepsilon(x)$ has no strong limit when $\varepsilon \to 0$, although $a(x)$ and $u(x)$ vary slowly. However, for any continuous function $\varphi(x)$ having a compact support on $\mathbb{R}$, a weak limit can be obtained:

$$\lim_{\varepsilon\to 0}\int_{\mathbb{R}} \varphi(x)(u_\varepsilon(x))^2 dx = \int_{\mathbb{R}} \varphi(x)\left(u^2(x) + \frac{1}{2}a^2(x)\right) dx \tag{1.13}$$

as a consequence of Riemann-Lebesgue's lemma. The observation function $\varphi(x)$ allows computing a smoothed "energy" of $u_\varepsilon(x)$, locally at a selected point of interest x, given by $u^2(x) + \frac{1}{2}a^2(x)$, and quantifying the influence of oscillations with amplitude a at that point (fig. 1.5). Above all, this weak limit has no longer the oscillating properties of $u_\varepsilon(x)$.

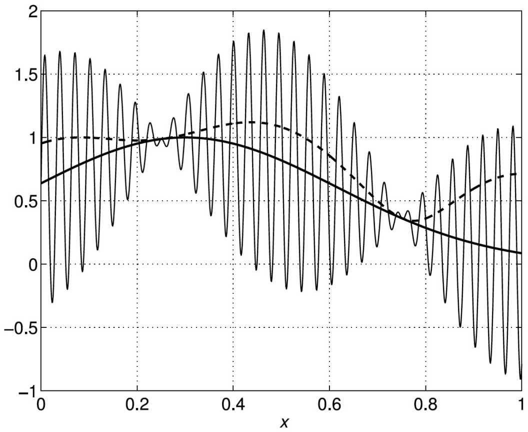

Fig. 1.5 The function $u_\varepsilon(x)$ (thin solid line), its mean $u(x)$ (thick solid line) and its square root weak limit $(u^2(x) + \frac{1}{2}a^2(x))^{\frac{1}{2}}$ (thick dashed line) [25]

Similarly, for wave propagation problems, the highly oscillatory features of quantities such as the velocity and pressure fields (for acoustic waves) or the displacement and stress fields (for elastic waves) are more difficult to understand in a high frequency regime. The energy or the energy density arise as the most relevant observables for the characterization of HF wave propagation. These quadratic quantities are no more highly oscillating. More details can be found in [25, 123, 156]. In this context, we shall thus consider the evolution of the energy density (i.e. Wigner measure, presented in detail in the chapters 3 and 4) associated to high frequency acoustic or elastic waves.

1.2.4 Kinetic model for high frequency wave propagation in the weak coupling limit

When high frequency elastic waves propagate in random media in the weak coupling limit, i.e.

$$\lambda \approx l_c \ll L, \quad \sigma^2 \ll 1 \tag{1.14}$$

and the background physical properties of weakly heterogeneous media can be modelled by a superposition of a homogeneous or slowly varying part, called also slowly background, and a fast fluctuating part, a kinetic model which describes the evolution of wave energy will arise.

Its derivation can be based on the use of the Bethe-Salpeter equation for the propagation of correlations, which satisfies the principle of conservation of total wave energy and the second law of thermodynamics [72, 73]. Or more precisely mathematically, a multi-scale asymptotic analysis by Wigner transforms and their interpretation in terms of semiclassical operators can also be used [17, 123]. For example, Ryzhik et al. [119] derived and analyzed radiative transfer equations for the energy density of acoustic, electromagnetic, and elastic waves in random media with the spatial Wigner transform; Baydoun et al. [25] assessed the influence of material anisotropy on the radiative transfer regime of elastic waves in randomly heterogeneous media. All these methods allow deriving a transport equation (for homogeneous media) or a radiative transfer equation (for heterogeneous media) from the wave equation in terms of energy densities in phase space. We present the main derivation steps of this equation obtained by Wigner transform for homogeneous and heterogenous media respectively in the sections 3.2.1 and 4.1.2.

In general, analytical solutions do not exist for the radiative transfer equation. However, when considering scalar wave propagation in an isotropic homogeneous background medium, it can be solved analytically [73, 112, 147].

Bal and Pinaud [20] compared particularly the energy densities of wave fields by solving the acoustic wave equation with those obtained by solving the radiative transfer equation. The wave equation was simulated by a finite difference forward scheme in time and the radiative transfer equation was solved numerically by Monte Carlo method [91, 106]. Finally a good agreement was found between the two energy quantities integrated in a subdivision of the studied 2D random media. It illustrates the equivalence of these two equations in the weak coupling regime and allows validating the weak limit proposed by the theory of radiative transfer in random media.

As we presented above, the energy density is a more relevant observable in the high frequency limit than wave fields and the radiative transfer equation is equivalent to the wave equation in random media in terms of energy. Thus in this work, we aim at studying this new equation and quantifying errors of numerical solutions of the wave equation in terms of energy based on it.

1.3 Error estimation for numerical solutions of wave equation

For wave propagation in heterogeneous media with complex phenomena presented in the section 1.2.2, described by the partial differential equation (PDE) with varying coefficients and initial or boundary conditions, it is typically impossible to find exact analytical solutions. Various numerical methods are used to find an approximate numerical solution. It is important to verify their validity and quality by some tools of error estimation.

1.3.1 Numerical methods for wave equation

In dynamics, the usual discretization of problem combines space discretization and a time-stepping scheme. The most common numerical methods for space discretization in elastodynamics are the finite difference method (FDM) [33, 130, 148] and the finite element method (FEM) [75, 124, 131, 157]. Others include the spectral method [64, 139], the boundary-element method (BEM) [21, 104], the finite-volume method (FVM) [52, 92].

More specifically, the FDM, based directly on the strong formulation of PDE, discretizes the exact solution through approximations of the partial differential operators. It is mainly adapted to simple geometries. The FEM is based on the variational or the weak form of PDE. It is better adapted to complicated geometries, but sometimes requires more memory space for numerical simulations than FDM. The spectral element method (SEM) [59, 87] is a formulation of FEMs with a subdivision of the computational domain into hexahedral elements. The most important property of the SEM is that the mass matrix is diagonal by construction, which saves time and memory. The BEM transforms PDE describing a boundary value problem to an equivalent representation by integral equations with known and unknown boundary states. Hence, it only requires discretization of the boundary surface rather than the volume, i.e., the dimension of problems is reduced by one. However, the BEM matrix is a unsymmetric and full matrix with non-zero coefficients and the FEM matrix is much larger but very sparsely populated. It means that the latter can be stored and solved more efficiently. Besides, the transformation of PDE to boundary integral equations requires the use of Green function, which is difficult and restricts the applications of the BEM, especially for problems in heterogeneous media. Based on the strong formulation of PDE, the FVM divides the domain into elements (called “control volume”). By the divergence formula, an integral formulation of the fluxes over the boundary of the control volume is then obtained. The fluxes on the boundary are discretized with respect to the discrete unknowns. The FVM is usually used in solving fluid flow problems. As the FEM, the advantage of the FVM is that it is easily formulated to allow for unstructured meshes.

The FEM is chosen in this work. It has been widely used for solving wave propagation problems [48, 146]. Here we present in brief the discretization for the wave equation with the FEM and the related notations and definitions.

Firstly, the weak form of the wave equation (1.1) with initial conditions (1.5) and boundary conditions (1.6) is built by introducing a test function $\mathbf{w}$:

$\forall t$, find $\mathbf{u}(t,\cdot) \in \mathrm{V}(\Omega)$ with $\mathbf{u}(0,\mathbf{x}) = \mathbf{u}_0(\mathbf{x})$, $\partial_t \mathbf{u}(0,\mathbf{x}) = \mathbf{v}_0(\mathbf{x})$ such that $\forall \mathbf{w} \in \mathrm{V}(\Omega)$,

$$(\partial_t^2 \mathbf{u}, \mathbf{w})_{M(\Omega)} + (\mathbf{u}, \mathbf{w})_{K(\Omega)} = (\mathbf{f}, \mathbf{w})_{(\Omega)} + \langle \mathbf{h}, \mathbf{w} \rangle_{(\Gamma_{\boldsymbol{\sigma}})} \tag{1.15}$$

where $\mathrm{V}(\Omega)$ is the space of kinematically admissible displacements. The products in eq. (1.15) are defined as:

$$\begin{aligned} (\mathbf{u}, \mathbf{w})_{(\Omega)} &= \int_\Omega \mathbf{u} \cdot \mathbf{w} d\mathbf{x}, \qquad & (\mathbf{u}, \mathbf{w})_{K(\Omega)} &= \int_\Omega \boldsymbol{\sigma}(\mathbf{u}) : \boldsymbol{\varepsilon}(\mathbf{w}) d\mathbf{x}, \\ (\mathbf{u}, \mathbf{w})_{M(\Omega)} &= (\rho \mathbf{u}, \mathbf{w})_{(\Omega)}, & \langle \mathbf{u}, \mathbf{w} \rangle_{(\Gamma_{\boldsymbol{\sigma}})} &= \int_{\Gamma_{\boldsymbol{\sigma}}} \mathbf{u} \cdot \mathbf{w} d\mathbf{x} \end{aligned} \tag{1.16}$$

Let $\mathrm{V}_h(\Omega)$ be a subspace of $\mathrm{V}(\Omega)$, the FEM consists in reconstructing solutions expanded on a basis $\{\mathbf{w}_h\}$ of $\mathrm{V}_h(\Omega)$, which is defined using a spatial mesh T_h, a partition of the domain Ω into elements (S). The letter h stands for the maximal diametre of the elements. A semi-discretized weak form of the variational problem (1.15) reads:

$\forall t$, find $\mathbf{u}_h(t,\cdot) \in \mathrm{V}_h(\Omega)$ with $\mathbf{u}_h(0,\mathbf{x}) = \mathbf{u}_{0,h}(\mathbf{x})$, $\partial_t \mathbf{u}_h(0,\mathbf{x}) = \mathbf{v}_{0,h}(\mathbf{x})$ such that $\forall \mathbf{w}_h \in \mathrm{V}_h(\Omega)$,

$$(\partial_t^2 \mathbf{u}_h, \mathbf{w}_h)_{M(\Omega)} + (\mathbf{u}_h, \mathbf{w}_h)_{K(\Omega)} = (\mathbf{f}, \mathbf{w}_h)_{(\Omega)} + \langle \mathbf{h}, \mathbf{w}_h \rangle_{(\Gamma_{\boldsymbol{\sigma}})} \tag{1.17}$$

The approximate displacement field $\mathbf{u}_h$ is defined by:

$$\mathbf{u}_h(t,\cdot) = \sum_{A,k} \mathrm{U}_{Ak}(t) w_A(\mathbf{x}) \mathbf{e}_k \tag{1.18}$$

where A is the node of mesh, k stands for the direction in space, $\mathbf{e}_k$ is the unit vector in direction k, w_A is the shape function at node A, U_{Ak} is the node displacement at node A and in direction k. Equation (1.17) can be expressed in the following matrix form:

$$[\mathrm{M}]\left\{\ddot{\mathrm{U}}(t)\right\} + [\mathrm{K}]\{\mathrm{U}(t)\} = \{\mathrm{F}(t)\} \tag{1.19}$$

where $\{\mathrm{U}(t)\}$ is the node displacement vector for instant t, $[\mathrm{M}]$ is the mass matrix and $[\mathrm{K}]$ is the stiffness matrix defined respectively by:

$$\mathrm{M}_{(Ak)(Bl)} = (w_A \mathbf{e}_k, w_B \mathbf{e}_l)_{M(\Omega)}, \qquad \mathrm{K}_{(Ak)(Bl)} = (w_A \mathbf{e}_k, w_B \mathbf{e}_l)_{K(\Omega)} \tag{1.20}$$

and $\{\mathrm{F}(t)\}$ is the vector of forces:

$$\mathrm{F}_{(Bl)} = (\mathbf{f}, w_B \mathbf{e}_l)_{(\Omega)} + \langle \mathbf{h}, w_B \mathbf{e}_l \rangle_{(\Gamma_{\boldsymbol{\sigma}})} \tag{1.21}$$

For solving the system (1.19), various time-stepping schemes can be chosen for the second-order time derivative, such as the forward finite difference scheme [60], the Newmark scheme [105], etc.

Take the forward finite difference scheme as an example. The interval $(0,T)$ is divided into equal subintervals $I_n = (t_n, t_{n+1})$ ($n \in [0, N-1]$ with $t_0 = 0$ and $t_N = T$) of length Δt. We denote $\mathbf{u}^n_{h\Delta t} = \mathbf{u}_h(t_n)$ ($\mathbf{u}^0_{h\Delta t} = \mathbf{u}_0$), the time-stepping scheme reads:

$$\partial_t^2 \mathbf{u}^n_{h\Delta t} = \begin{cases} \frac{\partial_t \mathbf{u}^n_{h\Delta t} - \partial_t \mathbf{u}^{n-1}_{h\Delta t}}{\Delta t}, & n \in [1,N] \\ \mathbf{a}_0, & n = 0 \end{cases} \quad \text{with} \quad \partial_t \mathbf{u}^n_{h\Delta t} = \begin{cases} \frac{\mathbf{u}^n_{h\Delta t} - \mathbf{u}^{n-1}_{h\Delta t}}{\Delta t}, & n \in [1,N] \\ \mathbf{v}_0, & n = 0 \end{cases} \tag{1.22}$$

Then time discrete solutions $\mathbf{u}^n_{h\Delta t}$ are found for all n with eq. (1.22) and eq. (1.19). The semi-discretization in space and time-stepping scheme presented above can also be based on a first-order equation by introducing $\mathbf{u} = \partial_t \mathbf{v}$.

Space-time finite element methods, with or without the continuity in time, can also be used in elastodynamics. For instance, the time discontinuous space-time Galerkin (DG) method has been developped for solving the wave equation [76, 95, 140]. It is based on the following strong first-order form of eq. (1.1):

$$\begin{cases} \rho \partial_t \mathbf{v}(t,\mathbf{x}) - \nabla_{\mathbf{x}} \cdot \boldsymbol{\sigma}(\mathbf{u}(t,\mathbf{x})) = \mathbf{f} \\ \nabla_{\mathbf{x}} \cdot (\boldsymbol{\sigma}(\partial_t \mathbf{u}(t,\mathbf{x}) - \mathbf{v}(t,\mathbf{x}))) = \mathbf{0} \end{cases} \tag{1.23}$$

The time period is subdivided as in what we presented for the time-stepping scheme above. Let a finite element space $\mathrm{V}_n(M_n)$ is given for each space-time slab $M_n = I_n \times \Omega$. The weak form of DG method is then formulated as follows:

find $(\mathbf{u},\mathbf{v}) \in \prod_{n=0}^{N-1} \mathrm{V}_n(M_n) \times \mathrm{V}_n(M_n)$ such that $\forall \mathbf{w} = (\mathbf{w}_{\mathbf{u}}, \mathbf{w}_{\mathbf{v}}) \in \prod_{n=0}^{N-1} \mathrm{V}_n(M_n) \times \mathrm{V}_n(M_n)$

$$A\left((\mathbf{u},\mathbf{v}),\mathbf{w}\right) = L(\mathbf{w}) \tag{1.24}$$

with

$$\begin{aligned} A\left((\mathbf{u},\mathbf{v}),\mathbf{w}\right) = & \underbrace{\sum_{n=0}^{N-1} \int_{I_n} (\partial_t \mathbf{v}, \mathbf{w}_{\mathbf{v}})_{M(\Omega)}\, dt + \sum_{n=0}^{N-1} \int_{I_n} (\mathbf{u}, \mathbf{w}_{\mathbf{v}})_{K(\Omega)} dt}_{\text{equilibrium}} + \underbrace{\sum_{n=1}^{N-1} \left([\mathbf{v}]^n, \mathbf{w}^n_{\mathbf{v},+}\right)_{M(\Omega)} dt + \left(\mathbf{v}^0_+, \mathbf{w}^0_{\mathbf{v},+}\right)_{M(\Omega)}}_{\text{continuities of } \mathbf{v} \text{ in time}} \\ & + \underbrace{\sum_{n=0}^{N-1} \int_{I_n} (\partial_t \mathbf{u}, \mathbf{w}_{\mathbf{u}})_{K(\Omega)} dt - \sum_{n=0}^{N-1} \int_{I_n} (\mathbf{v}, \mathbf{w}_{\mathbf{u}})_{K(\Omega)} dt}_{\text{equivalence of } \partial_t \mathbf{u} \text{ and } \mathbf{v}} + \underbrace{\sum_{n=1}^{N-1} \int_{I_n} ([\mathbf{u}]^n, \mathbf{w}^n_{\mathbf{u},+})_{K(\Omega)} dt + (\mathbf{u}^0_+, \mathbf{w}^n_{\mathbf{u},+})_{K(\Omega)}}_{\text{continuities of } \mathbf{u} \text{ in time}}, \\ L(\mathbf{w}) = & \underbrace{\left(\mathbf{v}_0, \mathbf{w}^0_{\mathbf{v},+}\right)_{M(\Omega)} + (\mathbf{u}_0, \mathbf{w}^0_{\mathbf{u},+})_{K(\Omega)}}_{\text{initial conditions}} + \underbrace{\sum_{n=0}^{N-1} \int_{I_n} (\mathbf{f}, \mathbf{w}_{\mathbf{v}})_{(\Omega)} dt + \sum_{n=0}^{N-1} \int_{I_n} \langle \mathbf{h}, \mathbf{w}_{\mathbf{v}} \rangle_{(\Gamma_{\boldsymbol{\sigma}})}\, dt}_{\text{boundary conditions}} \end{aligned} \tag{1.25}$$

where $\mathbf{u}^n_{\pm}(\mathbf{x}) = \lim_{\tau \to 0^+} \mathbf{u}(t_n \pm \tau, \mathbf{x}), \quad [\mathbf{u}]^n = \mathbf{u}^n_+ - \mathbf{u}^n_-$.

According to eq. (1.24), the displacement and velocity fields $(\mathbf{u},\mathbf{v})$ are continuous in space and discontinuous in time between two successive space-time slabs and the continuity in time is enforced only weakly. To solve eq. (1.24) numerically, the time-space domain M_n is discretized by a space-time finite element mesh, and $\mathbf{u}^n_{h\Delta t}$ and $\mathbf{v}^n_{h\Delta t}$ are then obtained. In our studies, the choice of $\mathrm{V}_n(M_n) = P^1(I_n) \times \mathrm{V}_n(\Omega)$ is adopted, where $P^1(I_n)$ stands for the linear interpolation in I_n. In this work, only one linear element is used in time within each space-time slab. More details can be found in [82].

We denote always $(\mathbf{u}_{h\Delta t}, \mathbf{v}_{h\Delta t})$ for finite element solutions used in this work (obtained by the time discontinuous space-time Galerkin method with code OOFE, MSSMat, CentraleSupélec): in the chapter 2, they stand for reconstructed time continuous solutions based on the obtained time discrete solutions $\left\{(\mathbf{u}^n_{h\Delta t}, \mathbf{v}^n_{h\Delta t})\right\}$; in the chapters 3 and 4, they stand for time discrete solutions $\left\{(\mathbf{u}^n_{h\Delta t}, \mathbf{v}^n_{h\Delta t})\right\}$.

1.3.2 Error estimation methods

Finite element analysis involves always different sources of errors that can compromise the validity of the finite element solutions. One major source of errors is introduced by the spatial-temporal discretization (other sources of errors, such as modelling error, user error, etc. [111, 143], exist but our introduction here is mainly related to the discretization error). These errors can be lowered by using smaller mesh sizes or higher order polynomial basis functions, etc., according to some criteria that characterize the accuracy of the finite element solutions. Error estimation is an important tool for quantifying and controlling the errors between the exact solutions and the finite element solutions.

There are mainly two types of error estimates that serve very different purposes:

- *a priori* error estimate is derived before computing numerical solutions. It tells us the order of convergence for a given finite element method, i.e. how fast the error decreases as the mesh size decreases or the interpolation order increases [14, 40]. When $\mathbf{u}$ is regular enough and $\mathbf{u}_{h\Delta t}$ has some regularities in time, an *a priori* error estimate usually takes the following form:

  $$\|\mathbf{u} - \mathbf{u}_{h\Delta t}\| \leq C(h^k + (\Delta t)^l) \tag{1.26}$$

  where the constant C depends on exact solutions $\mathbf{u}$, $k > 0, l > 0$, $\|\cdot\|$ is some time-space norm. When spatial and temporal approximations are improved, the approximate solutions approach the exact ones and the error goes to 0. However the exact solutions are usually unknown. This method has been already largely applied for the wave equation: Jenkins et al. [80] derived optimal *a priori* error estimates for mixed finite element displacement formulations of the acoustic wave equation; Deka [46] proposed optimal *a priori* error estimates for both semidiscrete and fully discrete schemes for the wave equation and it is verified with a numerical example; other contributions include [3, 22, 60, 76, 114].

- *a posteriori* error estimates give us a much better idea of the actual errors in a given finite element computation than *a priori* estimates. They can be used to perform adaptive mesh refinement [138, 141]. More specifically, *a posteriori* error estimators are used to indicate where the error is particularly high, then the mesh is refined in those locations. A new finite element solution is computed, and the process is repeated until a satisfactory error tolerance is reached. *A posteriori* error estimates usually take the form:

$$\|\mathbf{u}-\mathbf{u}_{h\Delta t}\| \le \eta = \left\{ \sum_{n=0}^{N-1} \sum_{S\in T_h} (\eta_S^n)^2 \right\}^{\frac{1}{2}} \tag{1.27}$$

for dynamic problem. Here $\eta_S^n(\mathbf{u}_{h\Delta t})$ is a quantity related to $\mathbf{u}_{h\Delta t}$ at t^n and in element $S \in T_h$. It is called element estimator or indicator. In contrast to *a priori* estimates, it is used for a practical *a posteriori* assessment of the accuracy of a computed finite element solution.

One may formulate the following properties describing an optimal *a posteriori* error estimate [6, 150]:

1. guaranteed upper bound: ensure that eq. (1.27) holds;
2. local efficiency: ensure that the local estimator represents a lower bound for the actual errors, up to a multiplicative constant, i.e. there exist a constant $C > 0$ such that :

   $$\left\{ \sum_{S\in T_h} (\eta_S^n)^2 \right\}^{\frac{1}{2}} \le C \|\mathbf{u}-\mathbf{u}_{h\Delta t}\|_{I_n}, \qquad \forall n \in [0, N-1] \tag{1.28}$$

   With these two properties it is known that the error estimator should yield guaranteed and sharp upper and lower bounds of the actual errors.
3. asymptotic accuracy: ensure that the effectivity index:

   $$\mathrm{I}_{\mathrm{eff}} = \frac{\eta}{\|\mathbf{u}-\mathbf{u}_{h\Delta t}\|} \tag{1.29}$$

   i.e. the ratio of the estimated and actual error, goes to one as h and Δt decrease;
4. robustness: guarantee the three preceding properties independently of the parameters of the problem and of their variations;
5. small evaluation cost: ensure that the computational cost needed for the evaluation of the estimators η_S^n should be much smaller than the cost required to obtain the approximate solution itself;

A variety of methods are developed for *a posteriori* error estimates (see [6] for a review of main methods for error estimation): element residual method [13, 47, 50], recovery based methods by Zienkiewicz and Zhu [158], the constitutive relation error method by Ladevèze [88, 89], goal-oriented dual weighted method [51, 110, 117], etc. Most of these methods have been successfully applied for error control of elliptic and parabolic problems [23, 28, 29, 44, 45, 54, 55, 117]. However, there are relatively less studies on the error control of finite element methods for second-order hyperbolic problems [3, 22, 136, 137].

For example, Georgoulis et al. [60] derived *a posteriori* error bounds of residual type in the $L^\infty(L^2)$-norm for for the space-discrete problem and the fully-discrete implicit finite element method of the linear wave equation, using elliptic reconstruction and space-time reconstruction technique. Johnson [82] proved *a priori* and *a posteriori* error estimates for a finite element method for linear second-order hyperbolic equations based on a finite element discretization with discontinuous Galerkin methods. Only the error due to space discretization is considered and the error estimates are derived using elliptic reconstruction. Picasso [114] proposed an anisotropic *a posteriori* error estimate. It was derived for a finite element discretization of the wave equation in two space dimensions and numerical results on adapted meshes indicated that the error estimator slightly underestimates the true error. The works of Aubry et al. [10] were based on a space-time Galerkin formulation for elastodynamics. It provides a variational formulation of the error with respect to the residual. The adjoint state gives an upper bound of the error by the norm of the residuals.

1.4 Objectives

The aim of our work is developing tools of error estimation for numerical solutions of wave equation in heterogeneous media.

Firstly, a residual-type *a posteriori* error representation is proposed for finite element solutions of the elastodynamic equation, based on works of Ibrahima [77] for the error estimation of the elastodynamic and acoustic equations. In fact, Vohralík [150] has derived *a posteriori* error estimates in an energy norm for the first-order (in time) heat equation. Ibrahima attempted to extend his idea to the elastodynamic problem but some difficulties appear when dealing with the second-order time derivative term in time. We continued and prolonged his efforts and developed an explicit error estimation in energy norm for the elastodynamic equation.

Secondly, we plan to quantify HF wave propagation in the weak coupling limit, where strong interactions between wave fronts and the heterogeneous medium generate complex propagation phenomena. This is the primary objective in this work. As discussed in the section 1.2, the energy or more generally quadratic quantities are the most relevant observables in the high frequency limit, and the radiative transfer equation for the energy density arises in the weak coupling regime. We propose that numerical errors can be evaluated with radiative transfer equation in terms of energy quantities of numerical waves. The main objective is defining a new evaluation method of numerical errors of wave fields with this new equation, and determining the distribution of mesh size h related to wave length λ and l_c with a more relevant criterion in terms of energy quantities.

In brief, instead of using the classical error method for highly oscillating fields based on the wave equation for $\mathbf{u}_{h\Delta t}$ (fig. 1.6, dashed line), the new errors in terms of energy quantities of wave fields $\mathrm{W}_\varepsilon[\mathbf{u}_{h\Delta t}]$ (W_ε and W denote respectively the Wigner transform and its weak limit, i.e. the Wigner measure) are used to build *a posteriori* error analysis based on the radiative transfer equation (fig. 1.6, solid line). Difficulties are expected in the aspect of the computation of Wigner transform because of its dependance on four variables $(t, \mathbf{x}; \omega, \mathbf{k})$ and the complexity of radiative transfer equation for high dimensions.

It is worth noticing that errors quantified by these two methods have different sources. The first method is classical, only the modelling by the elastic wave equation is considered, and we study the discretization error arising in the finite element solutions of this model. The second method proposes

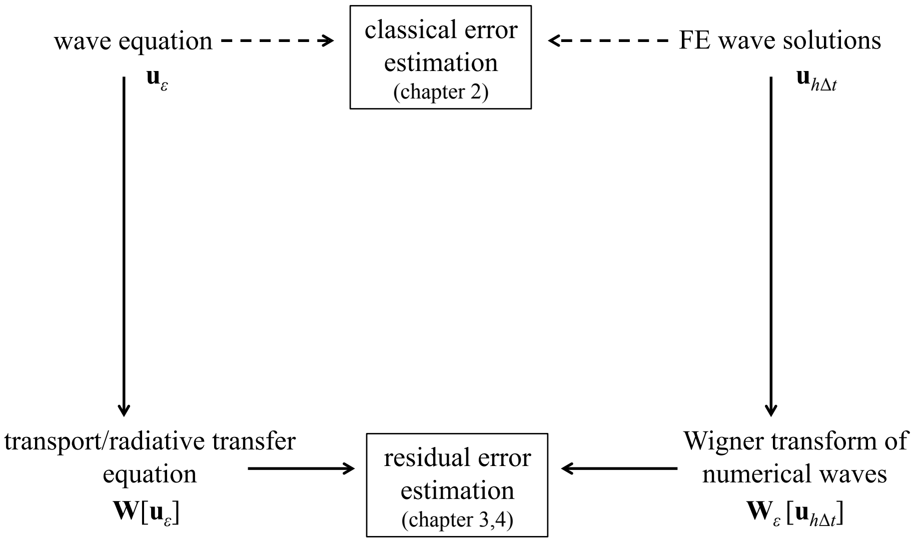

Fig. 1.6 Principle of the two *a posteriori* error estimations considered in this thesis

to use the radiative transfer model for evaluating the errors of numerical finite element solutions of the wave equation. Thus the defined errors can be considered including both the discretization error and “modelling error”, which is the gap between the averaged energy quantities of the exact solutions of the wave equation in a set of "similar" cases and the weak limit defined by the radiative transfer equation for that set.

The manuscript is organized as follows.

In the chapter 2, an explicit *a posteriori* residual based error upper bound is developed theoretically and numerically for the elastodynamic equation. Basically two main ideas are developed: the second-order elastodynamic equation is transformed firstly to a first-order hyperbolic system; and the residual method of *a posteriori* error estimates is exploited with a series of field reconstructions in time and in space. A numerical application with 1D homogeneous and heterogeneous media is given.

Then we develop a residual error estimator for the high frequency wave equation in the weak coupling regime based on radiative transfer modelling in terms of energy quantities. It is realized in homogeneous media in the chapter 3 and heterogeneous media in the chapter 4. This part is the major contribution in this PhD work.

In the chapter 3, we present in detail the Wigner transform and its interest for the analysis of wave equations. We show how it can be used to determine the phase-space energy densities in the high frequency limit and to derive the transport equation in homogeneous media in terms of Wigner measure, the weak limit of the Wigner transform of wave fields. Then a residual type error is based on this equation and it is validated numerically with different mesh sizes in 1D media.

In the chapter 4, following the same idea as the chapter 3, the radiative transfer equation in heterogeneous media is presented. In 1D media, the analytical solutions can be found and the propagation phenomena are introduced and analyzed. A discussion on strong localization is proposed to analyze the numerical results in 1D and to verify the radiative transfer regime. Then the residual errors are defined based on this equation in terms of Wigner transform of approximate solutions of the wave equation. Considering the numerical fluctuations in the calculation of Wigner transform in heterogeneous media, the convolution properties of Wigner transform are used to define a filtered error. Numerical implementation in 1D random media allows to validate these two residual errors. We find that the second one with convolution improves greatly the results of the first one.

Some conclusions and perspectives are finally drawn in the chapter 5.

Chapter 2

Explicit *a posteriori* error estimation for elastodynamic equation

Contents

This chapter introduces a new *a posteriori* error estimation for numerical solutions of a second-order hyperbolic wave equation, based on the work of Ibrahima [77] and Vohralík [150]. A key feature is the use of the residual method and the development of a series of reconstructions in time and in space with respect to different regularities required by corresponding ingredients of the obtained error bound.

At first, different reconstructions in time and in space are introduced and discussed in the section 2.1. Then the section 2.2 gives the detailed proof of the obtained estimator. In the section 2.3, numerical results for wave propagation in 1D media are presented for numerical solutions with uniform mesh. Specifically, the behaviour of exact errors and the effectivity of the error bound are studied numerically.

2.1 Reconstructions in time and in space of finite element wave solutions

Reconstruction methods have been widely used to construct *a posteriori* error estimates for finite element approximations. For instance, Mozolevski and Prudhomme [109] proposed a goal-oriented error estimation in finite element approximations of second-order elliptic problems that combines the dual weighted residual method and equilibrated-flux reconstruction methods for the primal and dual problems. The ZZ-type error estimators due to Zienkiewicz and Zhu [159, 160] are based on reconstruction of an improved stress and define the error as the difference between this stress and the one computed by the standard finite element procedure. The constitutive relation error method proposed by Ladevèze [90] consisted in post-processing the finite element solution in order to construct an admissible displacement-stress pair and then defining error bounds by quantifying the non-verification of the constitutive relations.

In this chapter, we consider the case where approximate solutions $(\mathbf{u}^n_{h\Delta t}, \mathbf{v}^n_{h\Delta t})$ at all instant t^n are calculated by the finite element method. It means that they are discrete in time (fig. 2.1a). Since time integration properties and some regularities in time are required to deduce the error bound, reconstructions in time can be applied to obtain solutions inside each I_n with some regularities. In general, the continuity in space of the exact solution is maintained in the finite element analysis, i.e. $\mathbf{u}^n_{h\Delta t}$ and $\mathbf{v}^n_{h\Delta t}$ are piecewise polynomial and continuous in space. However, the derivative of finite element solutions in space, and consequently the finite element stress vectors are not continuous across element interfaces [150]. Furthermore, the point-wise strong equilibrium is generally not verified (fig. 2.1b), i.e.

$$\boldsymbol{\sigma}(\mathbf{u}^n_{h\Delta t}) \notin H(\mathrm{div},\Omega), \qquad \rho\partial_t \mathbf{v}^n_{h\Delta t} - \nabla_{\mathbf{x}}\cdot\boldsymbol{\sigma}(\mathbf{u}^n_{h\Delta t}) \neq \mathbf{f} \tag{2.1}$$

where $\boldsymbol{\sigma}(\cdot)$ stands for the stress tensor related to a displacement field. Compared to $\mathbf{u}^n_{h\Delta t}$, $\boldsymbol{\sigma}(\mathbf{u}^n_{h\Delta t})$ has the same regularity in time but a reduced regularity in space.

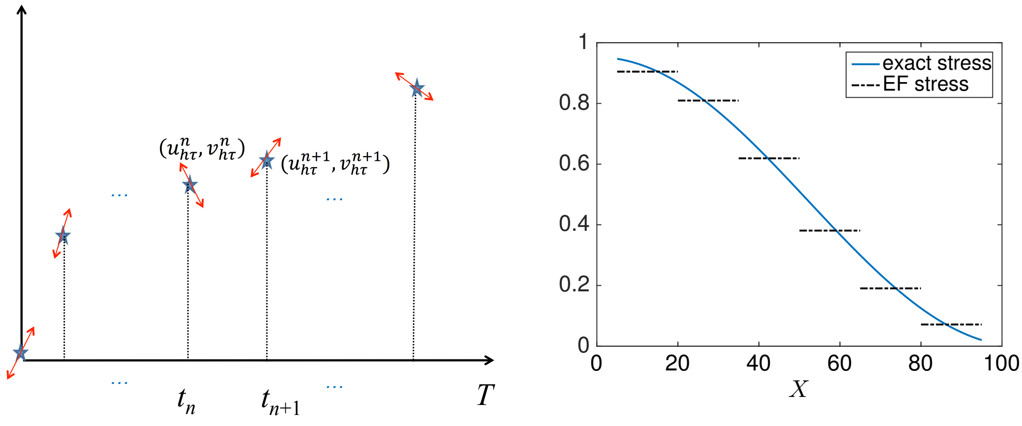

(a)

(b)

Fig. 2.1 (a) finite element solutions $(\mathbf{u}^n_{h\Delta t}, \mathbf{v}^n_{h\Delta t})$ in time, (b) exact and finite element stress in space

Consequently, according to the requirement of regularities by the proposed *a posteriori* error estimator (section 2.2), some reconstructions in time and in space are proposed here:

- two reconstructions in time for displacement and velocity fields, denoted respectively by $\mathbf{u}_{h\Delta t}(t,\mathbf{x})$ and $\mathbf{v}_{h\Delta t}(t,\mathbf{x})$;
- one reconstruction for stress fields in space, denoted by $\boldsymbol{\sigma}_{h\Delta t}(t,\mathbf{x})$.

These reconstructions are also appropriately chosen in order to simplify or eliminate some terms in the proposed error estimator. We give the detailed definitions of reconstructions that are used in the sections 2.2 and 2.3 as follows.

Firstly, $\mathbf{u}_{h\Delta t}$ and $\mathbf{v}_{h\Delta t}$ satisfy always: $\forall n \in [0, N-1]$,

$$\mathbf{u}_{h\Delta t}(t_n,\cdot) = \mathbf{u}^n_{h\Delta t}, \qquad \mathbf{v}_{h\Delta t}(t_n,\cdot) = \mathbf{v}^n_{h\Delta t} \tag{2.2}$$

with initial conditions: $\mathbf{u}_{h\Delta t}(0,\cdot) = \mathbf{u}_0$ and $\mathbf{v}_{h\Delta t}(0,\cdot) = \mathbf{v}_0$. According to the minimum required regularities for our error estimation, $(\mathbf{u}_{h\Delta t}, \mathbf{v}_{h\Delta t})$ should satisfy in time:

$$\mathbf{u}_{h\Delta t} \in C^0((0,T)), \quad \text{i.e.} \quad C^0 \text{ in time} \tag{2.3a}$$

$$\mathbf{v}_{h\Delta t} \in C^1((0,T)) \cap \prod_n C^2(I_n) \quad \text{i.e.} \quad C^1 \text{ in time and } C^2 \text{ in each time interval } I_n \tag{2.3b}$$

Also, it is known that if the values of a time function and its derivatives at two extremities of each time interval I_n are given as $(\mathbf{w}^n, \mathbf{w}^{n+1}, \partial_t \mathbf{w}^n, \partial_t \mathbf{w}^{n+1})$, we can reconstruct a function C^1 in time, cubic in each time interval I_n by the following equation (fig. 2.2):

$$\begin{aligned}\mathbf{w}(t) :=& \frac{(t-t_{n+1})^2(2t+t_{n+1}-3t_n)}{(\Delta t)^3}\mathbf{w}^n + \frac{(t-t_n)^2(-2t-t_n+3t_{n+1})}{(\Delta t)^3}\mathbf{w}^{n+1} \\ &+ \frac{(t-t_{n+1})^2(t-t_n)}{(\Delta t)^2}\partial_t \mathbf{w}^n + \frac{(t-t_n)^2(t-t_{n+1})}{(\Delta t)^2}\partial_t \mathbf{w}^{n+1}\end{aligned} \tag{2.4}$$

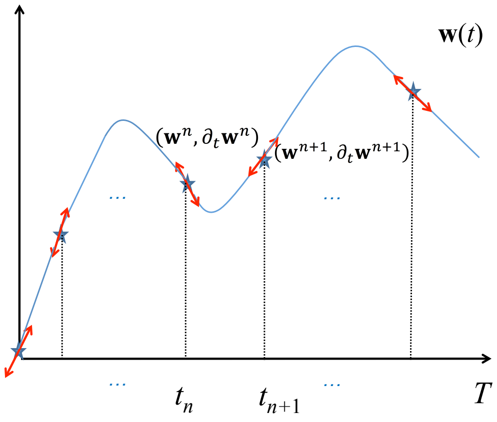

Fig. 2.2 A reconstruction C^1 in time, cubic in each I_n (cubic Hermite interpolation)

The velocity reconstruction $\mathbf{v}_{h\Delta t}$ is introduced firstly. According to eq. (2.3b), $\mathbf{v}_{h\Delta t}$ can be reconstructed by eq. (2.4) with $(\mathbf{v}^n_{h\Delta t}, \mathbf{v}^{n+1}_{h\Delta t}, \mathbf{a}^n_{h\Delta t}, \mathbf{a}^{n+1}_{h\Delta t})$, with $\mathbf{a}^n_{h\Delta t} := \partial_t \mathbf{v}_{h\Delta t}(t_n, \cdot), \forall n$. If the Newmark scheme is used in time, accelerations are already given. For other schemes such as the time discontinuous Galerkin method, $\mathbf{a}^n_{h\Delta t}$ has to be defined. We have the following two definitions of $\mathbf{v}_{h\Delta t}$ for different definitions of $\mathbf{a}^n_{h\Delta t}$.

Definition 2.1 (Basic *v*-reconstruction)**.** We call basic *v*-reconstruction the velocity field obtained with $(\mathbf{v}^n_{h\Delta t}, \mathbf{v}^{n+1}_{h\Delta t}, \mathbf{a}^n_{h\Delta t}, \mathbf{a}^{n+1}_{h\Delta t})$ by eq. (2.4), where $\mathbf{a}^n_{h\Delta t}$ is computed by finite difference:

$$\mathbf{a}^n_{h\Delta t} := \begin{cases} \frac{\mathbf{v}^{n+1}_{h\Delta t} - \mathbf{v}^n_{h\Delta t}}{\Delta t} & \text{for} \quad n = 0 \\ \frac{\mathbf{v}^{n+1}_{h\Delta t} - \mathbf{v}^{n-1}_{h\Delta t}}{2\Delta t} & \text{for} \quad n \in [1, N-1] \\ \frac{\mathbf{v}^{n}_{h\Delta t} - \mathbf{v}^{n-1}_{h\Delta t}}{\Delta t} & \text{for} \quad n = N \end{cases} \tag{2.5}$$

Definition 2.2 (Equilibrated *v*-reconstruction)**.** We call equilibrated *v*-reconstruction the velocity field obtained with $(\mathbf{v}^n_{h\Delta t}, \mathbf{v}^{n+1}_{h\Delta t}, \mathbf{a}^n_{h\Delta t}, \mathbf{a}^{n+1}_{h\Delta t})$ by eq. (2.4), where $\mathbf{a}^n_{h\Delta t}$ is computed by mechanical equilibrium:

$$\forall n, \quad (\rho \mathbf{a}^n_{h\Delta t}, \mathbf{w}_h)_{(\Omega)} + (\boldsymbol{\sigma}(\mathbf{u}^n_{h\Delta t}), \boldsymbol{\varepsilon}(\mathbf{w}_h))_{(\Omega)} = (\mathbf{f}^n, \mathbf{w}_h)_{(\Omega)} \tag{2.6}$$

The computational cost of acceleration in the first v-reconstruction eq. (2.5) is ignorable compared to that in the second one eq. (2.6). Indeed, the computational expense in the latter results mainly from the inverse of the mass matrix. In explicit dynamic analysis, it is at the same cost with the computation of finite element solutions. This is efficient if a diagonalized mass matrix is used. But its influence on reconstructions is not studied here.

Then two definitions are also proposed for the displacement reconstruction $\mathbf{u}_{h\Delta t}$:

Definition 2.3 (Basic *u*-reconstruction)**.** We call basic *u*-reconstruction for the displacement field obtained by eq. (2.4) with $(\mathbf{u}^n_{h\Delta t}, \mathbf{u}^{n+1}_{h\Delta t}, \mathbf{v}^n_{h\Delta t}, \mathbf{v}^{n+1}_{h\Delta t})$ (C^1 in time, cubic in each time interval I_n).

Definition 2.4 (Equilibrated *u*-reconstruction)**.** We call equilibrated *u*-reconstruction the displacement field obtained with $(\mathbf{u}^n_{h\Delta t}, \mathbf{u}^{n+1}_{h\Delta t}, \mathbf{u}^{n+\frac{1}{2}}_{h\Delta t})$ (C^0 in time, quadratic in each time interval I_n), where $\forall n$, $\mathbf{u}^{n+\frac{1}{2}}_{h\Delta t} := \mathbf{u}_{h\Delta t}(t^n + \frac{\Delta t}{2})$, i.e. the value of $\mathbf{u}_{h\Delta t}$ at the centre instant of I_n, obtained by mechanical equilibrium with the following algorithm:

1. reconstruct equilibrated velocity field $\mathbf{v}_{h\Delta t}$ with definition 2.2 and compute

$$\partial_t \mathbf{v}^{n+\frac{1}{2}}_{h\Delta t} = \partial_t \mathbf{v}_{h\Delta t}(t_n + \frac{\Delta t}{2}) \tag{2.7}$$

   for the centre point of I_n;

2. compute $\mathbf{u}^{n+\frac{1}{2}}_{h\Delta t}$ by equilibrium:

$$\left(\rho \partial_t \mathbf{v}^{n+\frac{1}{2}}_{h\Delta t}, \mathbf{w}_h\right)_{(\Omega)} + \left(\boldsymbol{\sigma}(\mathbf{u}^{n+\frac{1}{2}}_{h\Delta t}), \boldsymbol{\varepsilon}(\mathbf{w}_h)\right)_{(\Omega)} = \left(\mathbf{f}^{n+\frac{1}{2}}, \mathbf{w}_h\right)_{(\Omega)}; \tag{2.8}$$

3. reconstruct quadratic $\mathbf{u}_{h\Delta t}$ with the three fields $(\mathbf{u}^n_{h\Delta t}, \mathbf{u}^{n+1}_{h\Delta t}, \mathbf{u}^{n+\frac{1}{2}}_{h\Delta t})$ in each I_n.

It is noted that in eq. (2.8), the computation of $\mathbf{u}^{n+\frac{1}{2}}_{h\Delta t}$ requires to invert the stiffness matrix, which is much more expensive than the inverse of the mass matrix, especially for large models.

Finally, considering the reconstructions in space, since $\nabla_{\mathbf{x}} \cdot \boldsymbol{\sigma}(\mathbf{u}_{h\Delta t})$ is not locally in equilibrium as we introduced before, we propose the following stress reconstruction:

Definition 2.5 (Equilibrated σ-reconstruction)**.** Let $\mathbf{v}_{h\Delta t}$ be the reconstructed velocity field (C^1 in time, cubic in each time interval I_n), we call equilibrated σ-reconstruction any function $\boldsymbol{\sigma}_{h\Delta t}$ constructed from $\mathbf{v}_{h\Delta t}$ which satisfies:

$$\begin{cases} \boldsymbol{\sigma}_{h\Delta t}(t,\mathbf{x}) \in E_{H(\mathrm{div},\Omega),(T)} \\ (\rho\partial_t \mathbf{v}_{h\Delta t} - \nabla_{\mathbf{x}} \cdot \boldsymbol{\sigma}_{h\Delta t}, 1)_{(S)} = (\mathbf{f}, 1)_{(S)} \qquad \forall t \in (0,T), \quad \forall\, S \in \mathrm{T}_h \end{cases} \tag{2.9}$$

where $E_{H(\mathrm{div},\Omega),(T)}$ denotes space of functions $\boldsymbol{\sigma}$ such $\boldsymbol{\sigma}(t,\cdot)$ belongs to $H(\mathrm{div},\Omega)$ in space and $t \to \boldsymbol{\sigma}(\cdot,\mathbf{x})$ is in $L^2(0,T)$. We define also the reconstructed time derivative of stress:

$$\boldsymbol{\delta}_{h\Delta t}(t,\mathbf{x}) := \partial_t \boldsymbol{\sigma}_{h\Delta t}, \qquad \boldsymbol{\delta}_{h\Delta t} \in E_{H(\mathrm{div},\Omega),(T)} \tag{2.10}$$

More precisely, $\boldsymbol{\sigma}_{h\Delta t}$ and $\partial_t \mathbf{v}_{h\Delta t}$ have the same regularities in time, i.e. C^0 in time and quadratic in each time interval. If $\mathbf{f}$ is not locally quadratic in time intervals, we can take its quadratic interpolation as approximation. Note that eq. (2.9) is only a weak form of the equilibrium equation because it holds only for mean values on each mesh element. Thus $\boldsymbol{\sigma}_{h\Delta t}(t,\mathbf{x})$ is not unique with this definition. We propose the following two reconstructions of $\boldsymbol{\sigma}_{h\Delta t}$ that satisfies the definition 2.5:

Definition 2.6 (MRE σ-reconstruction)**.** We call the MRE (Minimum Regularity Ensured) σ-reconstruction any $\boldsymbol{\sigma}_{h\Delta t}$, that is continuous and piecewise linear in space and obtained by the following strategies. As $\nabla_{\mathbf{x}} \cdot \boldsymbol{\sigma}_{h\Delta t}$ is constant in each S, by eq. (2.9), we have:

$$\nabla_{\mathbf{x}} \cdot \boldsymbol{\sigma}_{h\Delta t} = \frac{1}{V(S)} \int_S (\rho\partial_t \mathbf{v}_{h\Delta t} - \mathbf{f})\, d\mathbf{x} \tag{2.11}$$

where $V(S)$ is the volume of element S. Given the constant derivative of $\boldsymbol{\sigma}_{h\Delta t}$ in each element, one more parameter, such as a Neumann-type boundary condition, is needed so as to determine a continuous and piecewise linear reconstructed stress. $\boldsymbol{\sigma}_{h\Delta t}$ is then determined by minimizing the residual errors.

Definition 2.7 (SA σ-reconstruction)**.** We call SA (Statically Admissible) σ-reconstruction the statically admissible stress construction proposed by Ladevèze and Pelle [90], namely it should verify:

$$\forall t,\ \rho\partial_t \mathbf{v}_{h\Delta t} - \nabla_{\mathbf{x}} \cdot \boldsymbol{\sigma}_{h\Delta t} = \mathbf{f}, \quad \text{in } S \tag{2.12}$$

It is known that with the Ladevèze method, at each time step t^n, a SA stress field $\boldsymbol{\sigma}_{h\Delta t}(t^n)$ is reconstructed using the weakly equilibrated finite element stress solutions $\boldsymbol{\sigma}(\mathbf{u}^n_{h\Delta t})$. In our case, in order to obtain a stress field $\boldsymbol{\sigma}_{h\Delta t}(t)$ that is continuous in the whole time and quadratic in each time interval, a SA stress field $\boldsymbol{\sigma}_{h\Delta t}(t^{n+\frac{1}{2}})$ should be reconstructed and for this the equilibrated u-reconstruction at $t^{n+\frac{1}{2}}$ is used. We recall that the latter is based on the equilibrated v-reconstruction according to the definition 2.4. We will see in the section 2.2 that the use of the SA σ-reconstruction allows to cancel one of the indicators and simplify the calculations of the residual error estimators.

The table 2.1 summarizes our propositions of reconstructions presented in this section. They all satisfy the requirement in the obtained error bound and we can make choice according to our demands in numerical applications.

fields	name	description
$\mathbf{u}_{h\Delta t}$	basic u-reconstruction	using $(\mathbf{u}^n_{h\Delta t}, \mathbf{v}^n_{h\Delta t})$, $\forall n$
	equilibrated u-reconstruction	using $\mathbf{u}^n_{h\Delta t}$ and $\mathbf{u}^{n+\frac{1}{2}}_{h\Delta t}$ (equilibrium at $t^{n+\frac{1}{2}}$), $\forall n$
$\mathbf{v}_{h\Delta t}$	basic v-reconstruction	using $(\mathbf{v}^n_{h\Delta t}, \mathbf{a}^n_{h\Delta t})$, $\mathbf{a}^n_{h\Delta t}$ by FD, $\forall n$
	equilibrated v-reconstruction	using $(\mathbf{v}^n_{h\Delta t}, \mathbf{a}^n_{h\Delta t})$, $\mathbf{a}^n_{h\Delta t}$ by equilibrium, $\forall n$
$\boldsymbol{\sigma}_{h\Delta t}$	MRE σ-reconstruction	weak equilibrium verified with mean value
	SA σ-reconstruction	strong equilibrium verified

Table 2.1 Reconstructions in time and in space

2.2 *A posteriori* error estimate for wave equation

In this section, we present the derivation of an *a posteriori* error upper bound in an energy norm between the unknown exact solutions $(\mathbf{u}, \mathbf{v})$ and the reconstructed solutions $(\mathbf{u}_{h\Delta t}, \mathbf{v}_{h\Delta t})$. Only homogeneous Dirichlet boundary conditions are considered here for simplicity.

The main result of the explicit *a posteriori* error upper bound in energy norm is given here:

Theorem 2.8. (Error upper bound for elastodynamic problems) Let $(\mathbf{u}_{h\Delta t}, \mathbf{v}_{h\Delta t}, \boldsymbol{\sigma}_{h\Delta t})$ a group of reconstruction fields chosen in the table 2.1, we have

$$\sqrt{\| \mathbf{v}-\mathbf{v}_{h\Delta t} \|^2_{M(\Omega),\infty(T)} + \| \mathbf{u}-\mathbf{u}_{h\Delta t} \|^2_{K(\Omega),\infty(T)}} \leq 2\|H_{R,DF}\|_{\infty(T)} + 2H_{R,DF}(0) + 2\sqrt{T}\|H_{VN}\|_{(T)} \\ + 2\sqrt{T}\|H_{DE,GV}\|_{(T)} + \sqrt{2}\sqrt{\|H_{R,DF}\|_{(T)}\|H_{VN}\|_{(T)}} \tag{2.13}$$

where $\| \mathbf{v}-\mathbf{v}_{h\Delta t} \|^2_{M(\Omega),\infty(T)} + \| \mathbf{u}-\mathbf{u}_{h\Delta t} \|^2_{K(\Omega),\infty(T)} = \sup_{t\in[0,T]} \| \mathbf{v}-\mathbf{v}_{h\Delta t} \|^2_{M(\Omega)}(t) + \| \mathbf{u}-\mathbf{u}_{h\Delta t} \|^2_{K(\Omega)}(t)$.

The three time dependent residual functions used above are defined below.

The lack of equilibrium function $H_{R,DF}(t)$ is defined as:

$$H_{R,DF}(t) = \left\{ \sum_{S \in T_h} (\eta_{R,S}(t) + \eta_{DF,S}(t))^2 \right\}^{\frac{1}{2}} \tag{2.14}$$

with:

$$\eta_{R,S}(t) = \frac{C_p h_S C_K}{\sqrt{\lambda_{\min}}} \|\mathbf{f}(t,\mathbf{x}) - \rho \partial_t \mathbf{v}_{h\Delta t}(t,\mathbf{x}) + \nabla_{\mathbf{x}} \cdot \boldsymbol{\sigma}_{h\Delta t}(t,\mathbf{x})\|_{(S)} \tag{2.15}$$

$$\eta_{DF,S}(t) = \frac{1}{\sqrt{\lambda_{\min}}} \|\boldsymbol{\sigma}_{h\Delta t}(t,\mathbf{x}) - \boldsymbol{\sigma}(\mathbf{u}_{h\Delta t})(t,\mathbf{x})\|_{(S)} \tag{2.16}$$

The lack of equilibrium rate function $H_{DE,GV}(t)$ is defined as:

$$H_{DE,GV}(t) = \left\{ \sum_{S \in T_h} (\eta_{DE,S}(t) + \eta_{GV,S}(t))^2 \right\}^{\frac{1}{2}} \tag{2.17}$$

with:

$$\eta_{DE,S}(t) = \frac{C_p h_S C_K}{\sqrt{\lambda_{\min}}} \left\|-\partial_t \mathbf{f}(t,\mathbf{x}) + \rho \partial_t^2 \mathbf{v}_{h\Delta t}(t,\mathbf{x}) - \nabla_{\mathbf{x}} \cdot \boldsymbol{\delta}_{h\Delta t}(t,\mathbf{x})\right\|_{(S)} \tag{2.18}$$

$$\eta_{GV,S}(t) = \frac{1}{\sqrt{\lambda_{\min}}} \|-\boldsymbol{\delta}_{h\Delta t}(t,\mathbf{x}) + \boldsymbol{\sigma}(\partial_t \mathbf{u}_{h\Delta t}(t,\mathbf{x}))\|_{(S)} \tag{2.19}$$

The velocity residual $H_{VN}(t)$ is defined as:

$$H_{VN}(t) = \|\partial_t \mathbf{u}_{h\Delta t}(t,\mathbf{x}) - \mathbf{v}_{h\Delta t}(t,\mathbf{x})\ \|_{K(\Omega)} \tag{2.20}$$

where h_S is the mesh size of element S, $\lambda_{\min}$ is the smallest eigenvalue of the fourth-order tensor $\mathbf{C}$, C_p is the constant in the Poincaré's inequality (theorem A.5) and C_K is the constant in the Korn inequality (theorem A.6).

In $H_{R,DF}$, $\eta_{R,S}$ represents the errors related to equilibrium equation and $\eta_{DF,S}$ represents the errors between the reconstructed stress and the stress of reconstructed displacement. $\eta_{R,S}$ vanishes in the case of SA σ-reconstruction according to the definition 2.7. $\|H_{R,DF}\|(0)$ allows involving the initial conditions. $H_{DE,GV}$ results from the residual of time derivative of equilibrium. H_{VN} evaluates the nonconformity between time derivative of the reconstructed displacement and the reconstructed velocity, which equals to 0 only at t^n for our choices of reconstructions.

As a preliminary step to the proof of this theorem, we first define a residual operator and prove a lemma related to it.

Definition 2.9 (Residual operator $\mathbf{R}_{h\Delta t}$). We define the following residual operator $\mathbf{R}_{h\Delta t}$ such that $\forall t \in (0,T)$:

$$(\mathbf{R}_{h\Delta t}(t), \mathbf{w})_{(\Omega)} = (\mathbf{f}(t) - \rho \partial_t \mathbf{v}_{h\Delta t}(t), \mathbf{w})_{(\Omega)} - (\boldsymbol{\sigma}(\mathbf{u}_{h\Delta t})(t), \boldsymbol{\varepsilon}(\mathbf{w}))_{(\Omega)} \tag{2.21}$$

where $\mathbf{w}$ is considered as an H_0^1 function in space.

According to the regularities of $\partial_t \mathbf{v}_{h\Delta t}$ and $\mathbf{u}_{h\Delta t}$, $\mathbf{R}_{h\Delta t}$ is C^0 in time and C^1 in each time interval. Its time derivative $\partial_t \mathbf{R}_{h\Delta t}$ (L^2 in time) can be obtained by:

$$(\partial_t \mathbf{R}_{h\Delta t}, \mathbf{w})_{(\Omega)}(t) = (\partial_t \mathbf{f} - \rho \partial_t^2 \mathbf{v}_{h\Delta t}, \mathbf{w})_{(\Omega)}(t) - (\boldsymbol{\sigma}(\partial_t \mathbf{u}_{h\Delta t}), \boldsymbol{\varepsilon}(\mathbf{w}))_{(\Omega)}(t) \tag{2.22}$$

Otherwise, eq. (2.21) can be written as:

$$(\mathbf{R}_{h\Delta t}, \mathbf{w})_{(\Omega)} = (\mathbf{f} - \rho \partial_t \mathbf{v}_{h\Delta t} + \nabla_{\mathbf{x}} \cdot \boldsymbol{\sigma}(\mathbf{u}_{h\Delta t}), \mathbf{w})_{(\Omega)} + \sum_{S \in T_h} \langle \boldsymbol{\sigma}(\mathbf{u}_{h\Delta t}) \cdot \mathbf{n}, \mathbf{w} \rangle_{(\partial S)} \tag{2.23}$$

where the last term gives rise to the stress vector jumps at the interfaces of elements. Thus this operator involves both the volume and surface residuals. Also, by adding and substracting the equilibrated stress reconstruction $\boldsymbol{\sigma}_{h\Delta t}$ into the definition of residual $\mathbf{R}_{h\Delta t}$ in eq. (2.21), we have

$$(\mathbf{R}_{h\Delta t}, \mathbf{w})_{(\Omega)} = (\mathbf{f} - \rho \partial_t \mathbf{v}_{h\Delta t} + \nabla_{\mathbf{x}} \cdot \boldsymbol{\sigma}_{h\Delta t}, \mathbf{w})_{(\Omega)} + (\boldsymbol{\sigma}_{h\Delta t} - \boldsymbol{\sigma}(\mathbf{u}_{h\Delta t}), \boldsymbol{\varepsilon}(\mathbf{w}))_{(\Omega)} \tag{2.24}$$

It can be seen that this operator contains also the residual of different reconstructions in time.

Finally, according to the weak formulation, we have:

$$(\mathbf{R}_{h\Delta t}, \mathbf{w})_{(\Omega)}(t) = (\rho \partial_t (\mathbf{v} - \mathbf{v}_{h\Delta t}), \mathbf{w})_{(\Omega)}(t) - (\boldsymbol{\sigma}(\mathbf{u} - \mathbf{u}_{h\Delta t}), \boldsymbol{\varepsilon}(\mathbf{w}))_{(\Omega)}(t) \tag{2.25}$$

The definition of $\partial_t \mathbf{R}_{h\Delta t}$ in eq. (2.22) and the property in eq. (2.25) will be used in the derivation of the theorem 2.8.

Lemma 2.10 (Upper bound of residual $\mathbf{R}_{h\Delta t}$). $\forall t \in (0,T)$, we have:

$$(\mathbf{R}_{h\Delta t}, \mathbf{w})_{(\Omega)}(t) \leq H_{R,DF}(t) \|\mathbf{w}\|_{K(\Omega)}(t) \tag{2.26}$$

and

$$\int_0^t (\mathbf{R}_{h\Delta t}, \partial_t \mathbf{w})_{(\Omega)} d\tau \leq \|H_{DE,GV}\|_{(t)} \|\mathbf{w}\|_{K(\Omega),(t)} + H_{R,DF}(t) \|\mathbf{w}\|_{K(\Omega)}(t) + H_{R,DF}(0) \|\mathbf{w}\|_{K(\Omega)}(0) \tag{2.27}$$

where $\mathbf{w}$ is H_0^1 in space, C^0 in time and C^1 in each time interval.

Proof. We prove firstly the equation (2.26) based on eq. (2.24). According to the definition 2.5 of $\boldsymbol{\sigma}_{h\Delta t}$ and assuming that $\mathbf{w}_S$ is the average of $\mathbf{w}$ in element S, we have:

$$(\rho \partial_t \mathbf{v}_{h\Delta t} - \nabla_{\mathbf{x}} \cdot \boldsymbol{\sigma}_{h\Delta t}, \mathbf{w}_S)_{(S)} = (\mathbf{f}, \mathbf{w}_S)_{(S)}, \quad \forall S \tag{2.28}$$

Decomposing eq. (2.24) in space into each element S and introducing eq. (2.28) into eq. (2.24), we can deduce that:

$$(\mathbf{R}_{h\Delta t},\mathbf{w})_{(\Omega)} = \sum_{S\in T_h}(\mathbf{f}-\rho\partial_t\mathbf{v}_{h\Delta t}+\nabla_{\mathbf{x}}\cdot\boldsymbol{\sigma}_{h\Delta t},\mathbf{w}-\mathbf{w}_S)_{(S)} + \sum_{S\in T_h}(\boldsymbol{\sigma}_{h\Delta t}-\boldsymbol{\sigma}(\mathbf{u}_{h\Delta t}),\boldsymbol{\varepsilon}(\mathbf{w}))_{(S)} \tag{2.29}$$

For the first term in eq. (2.29), using respectively Cauchy-Schwarz inequality (theorem A.7), Poincaré's inequality, Korn's inequality and that $\lambda_{\min}$ is the smallest eigenvalue of the fourth-order tensor $\mathbf{C}$:

$$\begin{aligned}(\mathbf{f}-\rho\partial_t\mathbf{v}_{h\Delta t}+\nabla_{\mathbf{x}}\cdot\boldsymbol{\sigma}_{h\Delta t},\mathbf{w}-\mathbf{w}_S)_{(S)} &\le \|\mathbf{f}-\rho\partial_t\mathbf{v}_{h\Delta t}+\nabla_{\mathbf{x}}\cdot\boldsymbol{\sigma}_{h\Delta t}\|_{(S)}\,\|\mathbf{w}-\mathbf{w}_S\|_{(S)}\\ &\le C_p h_S\,\|\mathbf{f}-\rho\partial_t\mathbf{v}_{h\Delta t}+\nabla_{\mathbf{x}}\cdot\boldsymbol{\sigma}_{h\Delta t}\|_{(S)}\,\|\mathbf{w}\|_{1(S)}\\ &\le C_p h_S C_K\,\|\mathbf{f}-\rho\partial_t\mathbf{v}_{h\Delta t}+\nabla_{\mathbf{x}}\cdot\boldsymbol{\sigma}_{h\Delta t}\|_{(S)}\,\|\boldsymbol{\varepsilon}(\mathbf{w})\|_{(S)}\\ &\le \frac{C_p h_S C_K}{\sqrt{\lambda_{min}}}\,\|\mathbf{f}-\rho\partial_t\mathbf{v}_{h\Delta t}+\nabla_{\mathbf{x}}\cdot\boldsymbol{\sigma}_{h\Delta t}\|_{(S)}\,\|\mathbf{w}\|_{K(S)}\\ &= \eta_{R,S}\,\|\mathbf{w}\|_{K(S)}\end{aligned} \tag{2.30}$$

where $\eta_{R,S}$ is defined in eq. (2.15). For the second term in eq. (2.29), using again the Cauchy-Schwarz inequality and the definition of λ_{min} results in:

$$\begin{aligned}(\boldsymbol{\sigma}_{h\Delta t}-\boldsymbol{\sigma}(\mathbf{u}_{h\Delta t}),\boldsymbol{\varepsilon}(\mathbf{w}))_{(S)} &\le \|\boldsymbol{\sigma}_{h\Delta t}-\boldsymbol{\sigma}(\mathbf{u}_{h\Delta t})\|_{(S)}\,\|\boldsymbol{\varepsilon}(\mathbf{w})\|_{(S)}\\ &\le \frac{1}{\sqrt{\lambda_{min}}}\,\|\boldsymbol{\sigma}_{h\Delta t}-\boldsymbol{\sigma}(\mathbf{u}_{h\Delta t})\|_{(S)}\,\|\mathbf{w}\|_{K(S)}\\ &= \eta_{DF,S}\,\|\mathbf{w}\|_{K(S)}\end{aligned} \tag{2.31}$$

where $\eta_{DF,S}$ is defined in eq. (2.16). Introducing eq. (2.30) and eq. (2.31) into eq. (2.29), then applying again the Cauchy-Schwarz inequality, we obtain eq. (2.26):

$$\begin{aligned}(\mathbf{R}_{h\Delta t},\mathbf{w})_{\Omega}(t) &\le \sum_{S\in T_h}(\eta_{R,S}(t)+\eta_{DF,S}(t))\,\|\mathbf{w}\|_{K(S)}(t)\\ &\le \left\{\sum_{S\in T_h}(\eta_{R,S}(t)+\eta_{DF,S}(t))^2\right\}^{\frac{1}{2}}\|\mathbf{w}\|_{K(\Omega)}(t)\\ &= H_{R,DF}(t)\,\|\mathbf{w}\|_{K(\Omega)}(t)\end{aligned} \tag{2.32}$$

Now the same idea of proof can be applied for the second result eq. (2.27) of lemma 2.10. Replacing $\mathbf{w}$ by $\partial_t\mathbf{w}$, applying integration by parts in time and using eq. (2.22), we have:

$$\int_0^t(\mathbf{R}_{h\Delta t},\partial_t\mathbf{w})_{(\Omega)}d\tau = -\int_0^t(\partial_t\mathbf{R}_{h\Delta t},\mathbf{w})_{(\Omega)}d\tau + (\mathbf{R}_{h\Delta t},\mathbf{w})_{(\Omega)}(t) - (\mathbf{R}_{h\Delta t},\mathbf{w})_{(\Omega)}(0) \tag{2.33}$$

Adding and substracting the reconstructed time derivative of stress (eq. (2.10)) into the first term of eq. (2.33) results in:

$$-\int_0^t (\partial_t \mathbf{R}_{h\Delta t}, \mathbf{w})_{(\Omega)} d\tau = \int_0^t (-\partial_t \mathbf{f} + \rho \partial_t^2 \mathbf{v}_{h\Delta t} - \nabla_{\mathbf{x}} \cdot \boldsymbol{\delta}_{h\Delta t}, \mathbf{w})_{(\Omega)} d\tau - \int_0^t (\boldsymbol{\delta}_{h\Delta t} - \boldsymbol{\sigma}(\partial_t \mathbf{u}_{h\Delta t}), \boldsymbol{\varepsilon}(\mathbf{w}))_{(\Omega)} d\tau \tag{2.34}$$

It can be observed that we can proceed with the same steps of proof with eq. (2.24). We have:

$$-\left(\partial_t \mathbf{R}_{h\Delta t}, \mathbf{w}\right)_{(\Omega)}(t) \leq H_{DE,GV}(t) \left\|\mathbf{w}\right\|_{K(\Omega)}(t) \tag{2.35}$$

where $H_{DE,GV}$ is defined in eq. (2.17). Finally, introducing eq. (2.35) into eq. (2.33), using the Cauchy-Schwartz inequality to obtain time-space norm, then applying eq. (2.26) for the last two terms of eq. (2.33), we deduce:

$$\int_0^t (\mathbf{R}_{h\Delta t}, \partial_t \mathbf{w})_{(\Omega)} d\tau \leq \left\|H_{DE,GV}\right\|_{(t)} \left\|\mathbf{w}\right\|_{K(\Omega),(t)} + H_{R,DF}(t) \left\|\mathbf{w}\right\|_{K(\Omega)}(t) + H_{R,DF}(0) \left\|\mathbf{w}\right\|_{K(\Omega)}(0) \tag{2.36}$$

□

Now we start to prove theorem 2.8:

Proof. (Theorem 2.8)

$\forall t$, we have:

$$\begin{aligned}
&\frac{1}{2} \parallel \mathbf{v} - \mathbf{v}_{h\Delta t} \parallel_{M(\Omega)}^2 (t) + \frac{1}{2} \parallel \mathbf{u} - \mathbf{u}_{h\Delta t} \parallel_{K(\Omega)}^2 (t) \\
=&\frac{1}{2} \int_0^t \left\{ \frac{d}{dt} \left\|\mathbf{v} - \mathbf{v}_{h\Delta t}\right\|_{M(\Omega)}^2 + \frac{d}{dt} \left\|\mathbf{u} - \mathbf{u}_{h\Delta t}\right\|_{K(\Omega)}^2 \right\} d\tau + \frac{1}{2} \left\|\mathbf{v} - \mathbf{v}_{h\Delta t}\right\|_{M(\Omega)}^2 (0) + \frac{1}{2} \left\|\mathbf{u} - \mathbf{u}_{h\Delta t}\right\|_{K(\Omega)}^2 (0) \\
=& \int_0^t (\rho \partial_t (\mathbf{v} - \mathbf{v}_{h\Delta t}), \mathbf{v} - \mathbf{v}_{h\Delta t})_{(\Omega)} d\tau + \int_0^t (\boldsymbol{\sigma}(\mathbf{u} - \mathbf{u}_{h\Delta t}), \boldsymbol{\varepsilon}(\partial_t (\mathbf{u} - \mathbf{u}_{h\Delta t})))_{(\Omega)} d\tau
\end{aligned} \tag{2.37}$$

The last two terms related to the initial conditions vanish according to hypothesis for reconstruction fields at $t = 0$: $\mathbf{u}_{h\Delta t}(0, \cdot) = \mathbf{u}_0$ and $\mathbf{v}_{h\Delta t}(0, \cdot) = \mathbf{v}_0$. Then by adding and subtracting $\partial_t \mathbf{u}_{h\Delta t}$ in the first term of the last line of eq. (2.37) and using the definition 2.9 of $\mathbf{R}_{h\Delta t}$ with $\mathbf{w} = \partial_t (\mathbf{u} - \mathbf{u}_{h\Delta t})$, we get:

$$\begin{aligned}
&\frac{1}{2} \parallel \mathbf{v} - \mathbf{v}_{h\Delta t} \parallel_{M(\Omega)}^2 (t) + \frac{1}{2} \parallel \mathbf{u} - \mathbf{u}_{h\Delta t} \parallel_{K(\Omega)}^2 (t) \\
=& \int_0^t (\rho \partial_t (\mathbf{v} - \mathbf{v}_{h\Delta t}), \partial_t \mathbf{u}_{h\Delta t} - \mathbf{v}_{h\Delta t})_{(\Omega)} d\tau + \int_0^t (\rho \partial_t (\mathbf{v} - \mathbf{v}_{h\Delta t}), \mathbf{v} - \partial_t \mathbf{u}_{h\Delta t})_{(\Omega)} d\tau \\
&\qquad + \int_0^t (\boldsymbol{\sigma}(\mathbf{u} - \mathbf{u}_{h\Delta t}), \boldsymbol{\varepsilon}(\partial_t (\mathbf{u} - \mathbf{u}_{h\Delta t})))_{(\Omega)} d\tau \\
=& \underbrace{\int_0^t (\rho \partial_t (\mathbf{v} - \mathbf{v}_{h\Delta t}), \partial_t \mathbf{u}_{h\Delta t} - \mathbf{v}_{h\Delta t})_{(\Omega)} d\tau}_{:=(a)} + \underbrace{\int_0^t (\mathbf{R}_{h\Delta t}, \partial_t (\mathbf{u} - \mathbf{u}_{h\Delta t}))_{(\Omega)} d\tau}_{:=(b)}
\end{aligned} \tag{2.38}$$

The term (b) is obtained according to eq. (2.25). Then the two terms (a) and (b) are treated separately in the following.

Firstly, for the term (a), using eq. (2.25) by taking $\mathbf{w} = (\partial_t \mathbf{u}_{h\Delta t} - \mathbf{v}_{h\Delta t})$, we have:

$$(a) = \int_0^t (\mathbf{R}_{h\Delta t}, \partial_t \mathbf{u}_{h\Delta t} - \mathbf{v}_{h\Delta t})_{(\Omega)} d\tau + \int_0^t (\boldsymbol{\sigma}(\mathbf{u}_{h\Delta t} - \mathbf{u}), \boldsymbol{\varepsilon}(\partial_t \mathbf{u}_{h\Delta t} - \mathbf{v}_{h\Delta t}))_{(\Omega)}\, d\tau \tag{2.39}$$

Now the first equation (2.26) of lemma 2.10 can be applied for the first term of eq. (2.39):

$$\begin{aligned}\int_0^t (\mathbf{R}_{h\Delta t}, \partial_t \mathbf{u}_{h\Delta t} - \mathbf{v}_{h\Delta t})_{(\Omega)} d\tau &\leq \int_0^t H_{R,DF}(\tau) \left\|\partial_t \mathbf{u}_{h\Delta t} - \mathbf{v}_{h\Delta t}\right\|_{K(\Omega)}(\tau) d\tau \\ &\leq \left\|H_{R,DF}\right\|_{(t)} \left\|\partial_t \mathbf{u}_{h\Delta t} - \mathbf{v}_{h\Delta t}\right\|_{K(\Omega),(t)} \\ &\leq \left\|H_{R,DF}\right\|_{(T)} \left\|H_{VN}\right\|_{(T)}\end{aligned} \tag{2.40}$$

where H_{VN} is defined in eq. (2.20). The second term of eq. (2.39) is treated firstly by Cauchy-Schwartz inequality:

$$\begin{aligned}\int_0^t (\boldsymbol{\sigma}(\mathbf{u}_{h\Delta t} - \mathbf{u}), \boldsymbol{\varepsilon}(\partial_t \mathbf{u}_{h\Delta t} - \mathbf{v}_{h\Delta t}))_{(\Omega)}\, d\tau &\leq \left\|\mathbf{u} - \mathbf{u}_{h\Delta t}\right\|_{K(\Omega),(t)} \left\|\partial_t \mathbf{u}_{h\Delta t} - \mathbf{v}_{h\Delta t}\right\|_{K(\Omega),(t)} \\ &= \left\|\mathbf{u} - \mathbf{u}_{h\Delta t}\right\|_{K(\Omega),(t)} \left\|H_{VN}\right\|_{(t)}\end{aligned} \tag{2.41}$$

Using the definition of L^∞ norm, it can be derived that:

$$\left\|\mathbf{u}\right\|^2_{K(\Omega),(t)} = \int_0^t \left\|\mathbf{u}\right\|^2_{K(\Omega)}(\tau) d\tau \leq \int_0^t \sup_\tau \left\{\left\|\mathbf{u}\right\|^2_{K(\Omega)}(\tau)\right\} d\tau = t \sup_{\tau \in [0,t]} \left\{\left\|\mathbf{u}\right\|^2_{K(\Omega)}(\tau)\right\} = t \left\|\mathbf{u}\right\|^2_{K(\Omega),\infty(t)} \tag{2.42}$$

Apply this result for $\left\|\mathbf{u} - \mathbf{u}_{h\Delta t}\right\|_{K(\Omega),(t)}$ in eq. (2.41):

$$\begin{aligned}\int_0^t (\boldsymbol{\sigma}(\mathbf{u}_{h\Delta t} - \mathbf{u}), \boldsymbol{\varepsilon}(\partial_t \mathbf{u}_{h\Delta t} - \mathbf{v}_{h\Delta t}))_{(\Omega)} &\leq \sqrt{t} \left\|\mathbf{u} - \mathbf{u}_{h\Delta t}\right\|_{K(\Omega),\infty(t)} \left\|H_{VN}\right\|_{(t)} \\ &\leq \sqrt{T} \left\|H_{VN}\right\|_{(T)} \left\|\mathbf{u} - \mathbf{u}_{h\Delta t}\right\|_{K(\Omega),\infty(t)}\end{aligned} \tag{2.43}$$

Combing eq. (2.40) and eq. (2.43), the temporary upper bound is found for (a):

$$(a) \leq \left\|H_{R,DF}\right\|_{(T)} \left\|H_{VN}\right\|_{(T)} + \sqrt{T} \left\|H_{VN}\right\|_{(T)} \left\|\mathbf{u} - \mathbf{u}_{h\Delta t}\right\|_{K(\Omega),\infty(T)} \tag{2.44}$$

Secondly, for the term (b), taking $\mathbf{w} = \mathbf{u} - \mathbf{u}_{h\Delta t}$ in the second equation (2.27) of lemma 2.10, we have:

$$\begin{aligned}(b) &\leq \left\|H_{DE,GV}\right\|_{(t)} \left\|\mathbf{u} - \mathbf{u}_{h\Delta t}\right\|_{K(\Omega),(t)} + H_{R,DF}(t) \left\|\mathbf{u} - \mathbf{u}_{h\Delta t}\right\|_{K(\Omega)}(t) + H_{R,DF}(0) \left\|\mathbf{u} - \mathbf{u}_{h\Delta t}\right\|_{K(\Omega)}(0) \\ &\leq \left(\sqrt{T}\left\|H_{DE,GV}\right\|_{(T)} + \left\|H_{R,DF}\right\|_{\infty(T)} + H_{R,DF}(0)\right) \left\|\mathbf{u} - \mathbf{u}_{h\Delta t}\right\|_{K(\Omega),\infty(T)}\end{aligned} \tag{2.45}$$

We have successfully found an upper bound for (a) and (b) in eq. (2.44) and eq. (2.45), then inserting these two inequalities into eq. (2.38), $\forall t \in (0,T]$, we have:

$$\begin{aligned}\| \mathbf{v}-\mathbf{v}_{h\Delta t} \|^2_{M(\Omega)} (t) + \| \mathbf{u}-\mathbf{u}_{h\Delta t} \|^2_{K(\Omega)} (t) &\leq A \, \|\mathbf{u}-\mathbf{u}_{h\Delta t}\|_{K(\Omega),\infty(t)} + B^2 \\ &\leq A \sqrt{\|\mathbf{v}-\mathbf{v}_{h\Delta t}\|^2_{M,\infty(t)} + \|\mathbf{u}-\mathbf{u}_{h\Delta t}\|^2_{K(\Omega),\infty(t)}} + B^2\end{aligned} \tag{2.46}$$

where:

$$\begin{aligned}A &= 2\|H_{R,DF}\|_{\infty(T)} + 2H_{R,DF}(0) + 2\sqrt{T}(\|H_{DE,GV}\|_{(T)} + \|H_{VN}\|_{(T)}) \\ B^2 &= 2\|H_{R,DF}\|_{(T)}\|H_{VN}\|_{(T)}\end{aligned} \tag{2.47}$$

As $x^2 \leq ax + b^2$ implies $x \leq a + b$ whenever a, b positive [1], we find the *a posteriori* error bound:

$$\sqrt{\|\mathbf{v}-\mathbf{v}_{h\Delta t}\|^2_{M(\Omega),\infty(T)} + \|\mathbf{u}-\mathbf{u}_{h\Delta t}\|^2_{K(\Omega),\infty(T)}} \leq A + B$$

□

2.3 Numerical application in 1D homogeneous and heterogeneous media

In this section, we apply numerically the theorem 2.8. Wave propagation in a one-dimensional elastic bar with homogeneous media and two different heterogeneous media is considered here. In these cases, the analytical solutions or reference solutions of the wave equation can be found. We compare numerically the "exact errors" (i.e. errors between analytical or reference solutions and numerical solutions) and the estimated errors defined in eq. (2.13) for numerical solutions with different mesh sizes. The efficiency of the error upper bound is analyzed.

2.3.1 Definition of numerical model and parameters

We consider here a 1D bar with length $L = 3.2$ m, whose left end is subjected to the Neumann boundary condition with a truncated ricker signal $F(t)$ with a magnitude of 1 kN/m^2 and the duration T_R of 0.22 ms (fig. 2.3). The right end of the bar is subjected to the free boundary condition. The total analysis time period is $[0, T_f]$ with $T_f = 1$ ms which allows the wave front to propagate a round trip in this bar.

---

[1] This result is used for deducing a guaranteed upper bound of x here. In fact, $x^2 \leq ax + b^2 \Rightarrow (x - \frac{a}{2})^2 \leq \frac{a^2}{4} + b^2 \Rightarrow (x - \frac{a}{2})^2 \leq (\frac{a}{2} + b)^2 \Rightarrow x \leqslant a + b$ for a, b positive

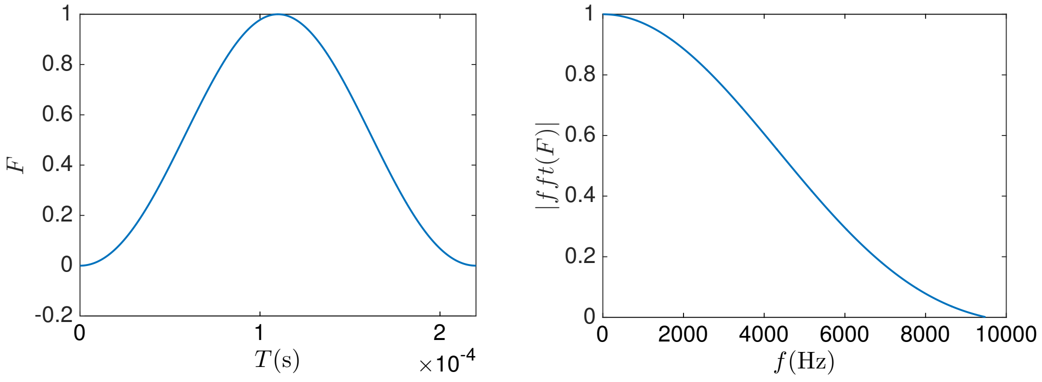

(a) (b)

Fig. 2.3 Truncated ricker signal and its frequency spectrum (amplitude normalized to 1): (a) $F(t)$, (b) $|FFT(F)|$ (fast Fourier transform)

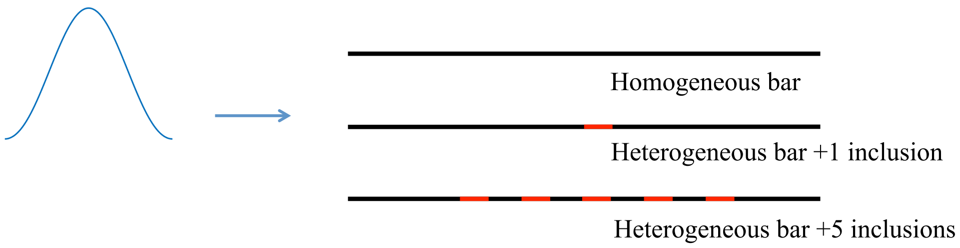

Fig. 2.4 Model for homogeneous or heterogenous bars (black zone: E_1, red zone: E_2)

Figure 2.4 gives three models with different physical properties (the density ρ is constant for all models, only the Young's modulus E can be heterogeneous):

1) a homogeneous bar with $E = E_1$;

2) a heterogeneous bar with one inclusion, with $E = E_2 = E_1/70$ in the inclusion and $E = E_1$ otherwise, where the length of the inclusion is $l = 0.2$ m, and its centre is located at $L/2 = 1.6$ m;

3) a heterogeneous bar with five inclusions, with $E = E_2$ in the inclusions and $E = E_1$ otherwise, where the length of each inclusion is $l = 0.2$ m, and their centres are located respectively at $1, 1.4, 2, 2.4, 2.8$ m. For this bar, the observation period is changed to $3T_f$ to ensure a round trip because the wave velocity in inclusions is smaller.

The numerical parameters are given in the tables 2.2, 2.3 and 2.4. In the table 2.2, f_c is the cutoff frequency of the truncated ricker signal. The table 2.3 presents the different mesh sizes h and time steps Δt used for the homogeneous case and the table 2.4 presents those used for both heterogeneous cases. It can be observed that in heterogeneous cases we have more elements per wavelength in the slow area with E_1 than that with E_2. Thus the obtained numerical solutions describe waves more precisely in these areas.

	media			load (truncated ricker)	
	ρ (kg/m^3)	E (GPa)	c (m/s)	T_R (ms)	f_c (kHz)
homogeneous	2500	$E_1 = 70$	$c_1 = 5300$	0.22	9.5
heterogeneous	2500	$E_1 = 70$ $E_2 = 1$	$c_1 = 5300$ $c_2 = 632$	0.22	9.5

Table 2.2 Numerical parameters of media and load

h (m)	0.55	0.28	0.14	0.07	0.035	0.017	0.008
$\lambda(f_c)/h$	1	2	4	8	16	32	65

Table 2.3 Mesh sizes used in the homogeneous case

h (m)	0.066	0.035	0.017	0.008	0.004	0.002
$(\lambda_1(f_c)/h, \lambda_2(f_c)/h)$	(8,1)	(16,2)	(32,4)	(65,8)	(139,16)	(278,32)

Table 2.4 Mesh sizes used in both heterogeneous cases

2.3.2 Analytical solutions of wave equation

In this section, analytical or reference solutions are given for the homogeneous case and the two heterogeneous cases. It allows computing their differences with numerical solutions.

For the homogeneous case, analytical solutions exist:

$$u(t,x) = \begin{cases} 0 & \text{for} \quad 0 \leq t \leq \frac{x}{c_1} \\ \frac{c_1}{E} \int_0^{t-\frac{x}{c_1}} F(\tau) d\tau & \text{for} \quad \frac{x}{c_1} \leq t \leq \frac{L}{c_1} \\ \frac{c_1}{E} \int_0^{t-\frac{x}{c_1}} F(\tau) d\tau - \frac{c_1}{E} \int_0^{t-\frac{L}{c_1}+\frac{x}{c_1}-\frac{L}{c_1}} F(\tau) d\tau & \text{for} \quad \frac{L}{c_1} \leq t \leq \frac{2L}{c_1} \end{cases} \tag{2.48}$$

For the heterogeneous bar with one inclusion, analytical solutions for the wave equation can be also found. In fig. 2.5, the reflection and transmission of waves at an interface $x = a$ is given. Since the incident stress waves is defined by $\sigma_i = F(t - x/c_1)$, using the continuity of the stress at each interface, the stresses for reflected and transmitted waves can be expressed as [1]:

$$\sigma_r = C_r F(t + (x - 2a)/c_1), \qquad \sigma_t = C_t F(t - a/c_1 - (x - a)/c_2) \tag{2.49}$$

with C_r and C_t are respectively the reflection coefficient and the transmission coefficient given by:

$$C_r = \frac{c_2/c_1 - 1}{c_2/c_1 + 1}, \qquad C_t = \frac{2c_2/c_1}{c_2/c_1 + 1} \tag{2.50}$$

Then total waves can be calculated with the superposition of reflected and transmitted waves.

For the heterogeneous bar with five inclusions, considering the complexity of analytical solutions under a large number of reflections and transmissions, numerical solutions with a relatively small mesh size $h = 1$ mm are used as the reference solution.

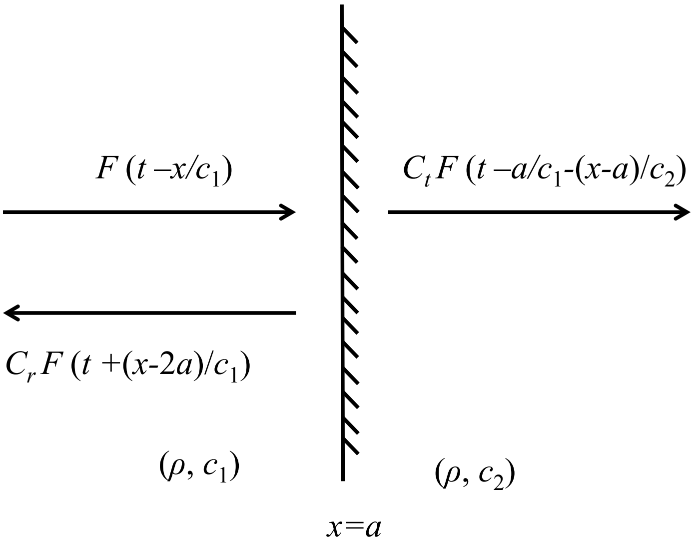

Fig. 2.5 Incident, reflected and transmitted waves

2.3.3 Numerical exact errors for 1D elastic wave propagation

In this section, we observe firstly the errors between analytical solutions found in the section 2.3.2 and numerical finite element solutions in energy norm in 1D media.

Firstly, fig. 2.6 presents an example of numerically calculated velocity fields and local exact errors in energy norm in time-space between approximate solutions and analytical or reference solutions:

$$e_{M+K}(t,x) = \frac{1}{2}\left\{\rho e_v^2 + E(\partial_x e_u)^2\right\}(t,x), \qquad \text{with} \quad e_v = v - v_{h\Delta t},\ e_u = u - u_{h\Delta t} \tag{2.51}$$

It is observed that overall, the errors increase with time and with number of interaction with the interfaces or boundaries.

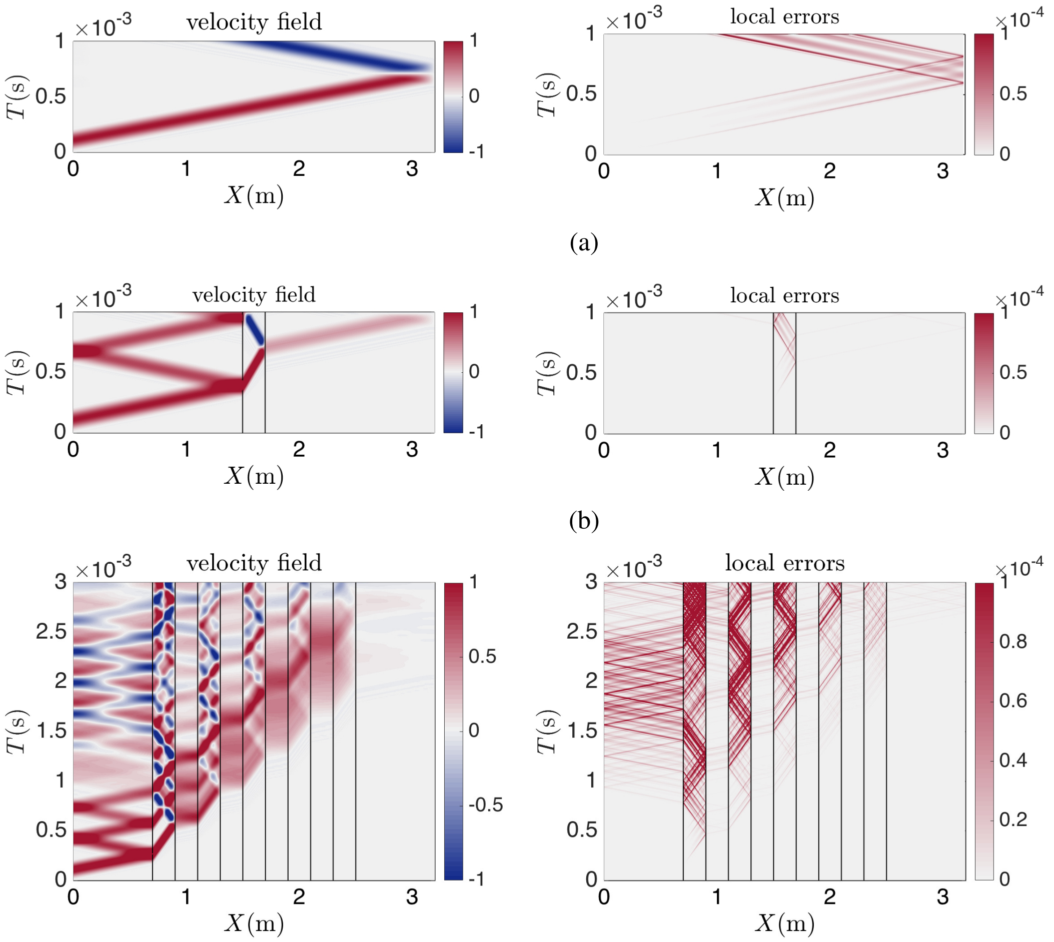

(a)

(b)

(c)

Fig. 2.6 Numerical results of velocity fields $v(t,x)$ and local errors $\frac{1}{2}\left\{\rho e_v^2 + E(\partial_x e_u)^2\right\}(t,x)$ (normalized by total energy $\int_0^L \frac{1}{2}\left\{\rho v^2 + E(\partial_x u)^2\right\} dx = \text{constant}, \forall t$) for: (a) the homogeneous bar ($\lambda/h = 32$), (b) the heterogeneous bar with one inclusion ($\lambda_1/h = 278, \lambda_2/h = 32$), (c) the heterogeneous bar with five inclusions ($\lambda_1/h = 278, \lambda_2/h = 32$)

Then the evolution of errors with time:

$$\|e_v\|_{M(\Omega)}(t) = \left\{\int_0^L \frac{1}{2}\rho e_v^2(t,x)dx\right\}^{\frac{1}{2}}, \qquad \|e_u\|_{K(\Omega)}(t) = \left\{\int_0^L \frac{1}{2}E(\partial_x e_u(t,x))^2 dx\right\}^{\frac{1}{2}} \tag{2.52}$$

is studied so as to observe the error behaviour on the interfaces and the boundary of domain.

In the homogeneous case, $\|e_v\|_{M(\Omega)}(t)$ and $\|e_u\|_{K(\Omega)}(t)$ are presented in fig. 2.7b. Firstly, errors are increasing with time of simulation. A strong oscillation observed in $[t_1, t_2]$ is related to when waves interact with the right boundary (fig. 2.7a). A conversion between errors in two energy norms is obtained, resulting from the conversion of potential energy and kinetic energy.

Now the errors for the first heterogeneous case are shown in fig. 2.8b. We observe always the increase of errors with time and strong oscillations during $[t_1, t_2]$ and $[t_3, T_f]$. From fig. 2.8a it can be known that these two time intervals are corresponding to the period when waves interact either with the two boundaries of bar or the interfaces between two materials. During $[t_2, t_3]$, wave front propagates far from the interfaces or boundaries. Note that during $[0, t_1]$, waves are reflected and refracted by the first interface around $t = 3$ ms but this effect on errors is relative small compared to that in latter times so we neglect here (inset of fig. 2.8b).

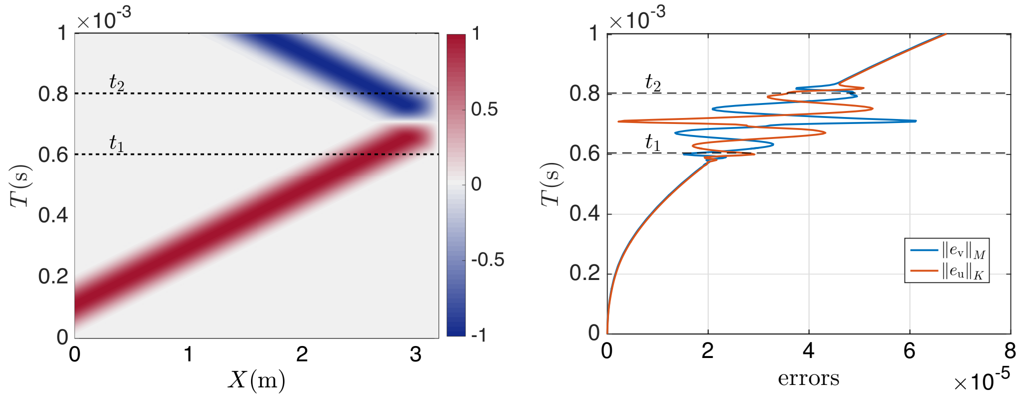

(a) (b)

Fig. 2.7 Homogeneous media ($\lambda/h = 32$): (a) velocity fields $v(t,x)$, (b) $\|e_v\|_M(t)$ and $\|e_u\|_{K(\Omega)}(t)$

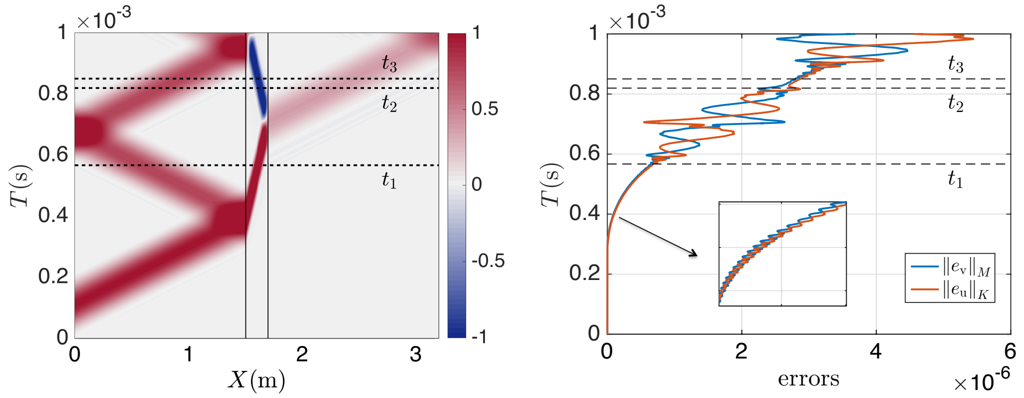

(a) (b)

Fig. 2.8 Heterogeneous media with one inclusion ($\lambda_2/h = 32$): (a) velocity fields $v(t,x)$, (b) $\|e_v\|_M(t)$ and $\|e_u\|_{K(\Omega)}(t)$

Finally, in the highly heterogeneous case with 5 inclusions, it is difficult to identify the instants as what we have done above since waves are largely reflected and refracted here. However, we can still find that oscillation of errors start at t_1 when waves meet the first interface (fig. 2.9).

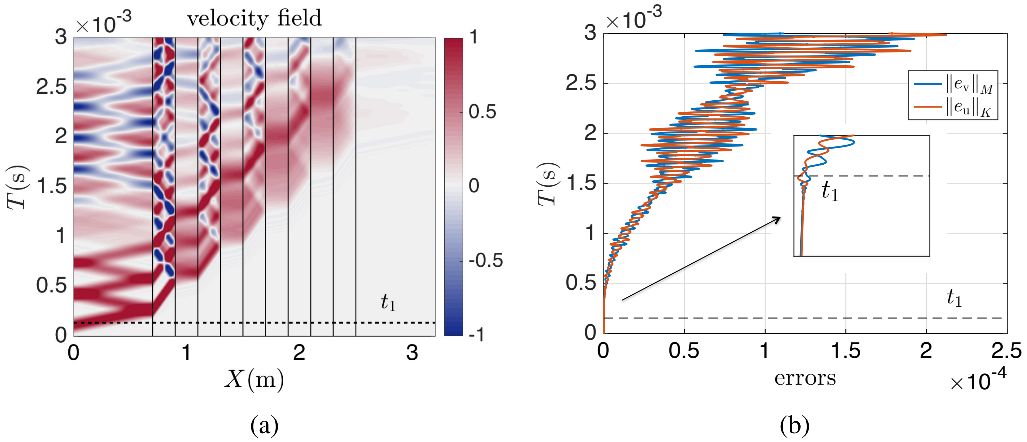

(a) (b)

Fig. 2.9 Heterogeneous media with five inclusions ($\lambda_2/h = 32$): (a) velocity fields $v(t,x)$, (b) $\|e_v\|_M(t)$ and $\|e_u\|_{K(\Omega)}(t)$

Now we focus on our L^∞-time exact errors in energy norm defined in the error bound:

$$\sqrt{\|v - v_{h\Delta t}\|^2_{M(\Omega),\infty(T_f)} + \|u - u_{h\Delta t}\|^2_{K(\Omega),\infty(T_f)}} = \sqrt{\|e_v\|^2_{M(\Omega),\infty(T_f)} + \|e_u\|^2_{K(\Omega),\infty(T_f)}} \tag{2.53}$$

Equation (2.53) is computed for all the mesh sizes in homogeneous and heterogeneous media and we present all the results in terms of degree of freedom in fig. 2.10.

It can be observed in fig. 2.10 that in all cases, exact errors are decreasing with smaller mesh size or larger number of degrees of freedom and more precisely. They are inversely proportional to dof. Errors increase with the number of degrees of heterogeneity for solutions with the same degree of freedom.

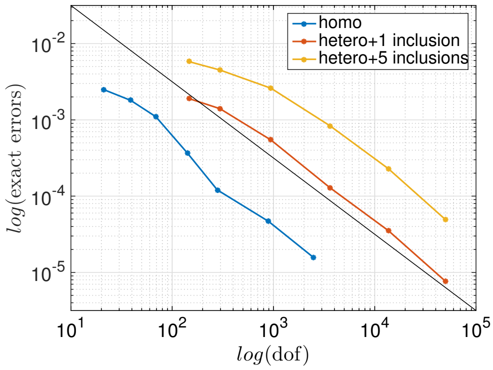

Fig. 2.10 A log-log plot of exact errors $\sqrt{\|e_v\|^2_{M(\Omega),\infty(T_f)} + \|e_u\|^2_{K(\Omega),\infty(T_f)}}$ (black line is used as reference with slope -1)

2.3.4 Numerical estimated errors for 1D elastic wave propagation

Now we compute numerically the error bound in eq. (2.13) and verify its accuracy. Four combinations of the reconstructions in time and in space listed in the table 2.1 of the section 2.1 are studied:

- case1: basic u-reconstruction + basic v-reconstruction + MRE σ-reconstruction;
- case2: basic u-reconstruction + equilibrated v-reconstruction + MRE σ-reconstruction;
- case3: equilibrated u-reconstruction + equilibrated v-reconstruction + MRE σ-reconstruction;
- case4: equilibrated u-reconstruction + equilibrated v-reconstruction + SA σ-reconstruction.

Recall that the SA σ-reconstruction requires both the equilibrated u-reconstruction and the equilibrated v-reconstruction. In the rest of four combinations, we choose three of them here (case1-3).

The error bound is firstly computed in homogeneous media.

In fig. 2.11 we compared numerical exact errors obtained in the section 2.3.3 and estimated errors with the four cases presented above.

Firstly, it is illustrated in fig. 2.11a that estimated errors with four different reconstructions are decreasing with dof, as we expected. They are close to each other. The second case gives the smallest value of errors. Its computational cost is relatively small, especially compared to the last two cases. Secondly, compared to the numerical exact errors, the obtained error bounds are much larger. On the one hand, it can be understood by the existence of a significant constant coefficient before the estimated errors; on the other hand, their rate of convergence is different. In effect, in fig. 2.11b we find that the effectivity index of error bound (i.e. ratio of the estimated and exact errors, see eq. (1.29)) increases with the computational effort. Thus this estimator has a weak asymptotic accuracy.

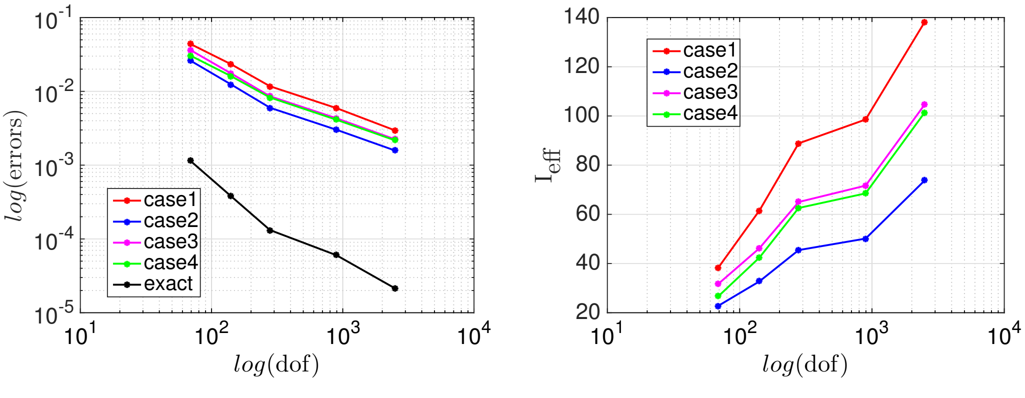

(a) (b)

Fig. 2.11 Error estimation in the homogeneous case: (a) exact errors and estimated errors (log-log graph), (b) effectivity index (semi-log graph)

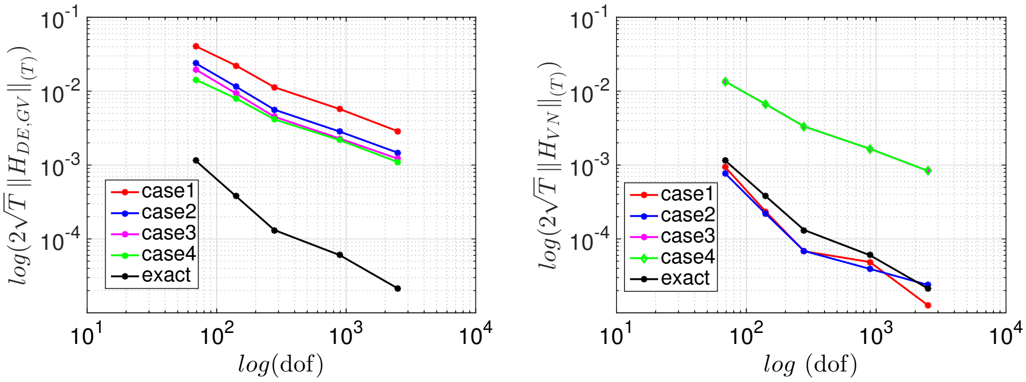

(a) (b)

Fig. 2.12 A log-log plot of two terms of error bound: (a) $2\sqrt{T}\,\|H_{DE,GV}\|_{(T)}$ (b) $2\sqrt{T}\,\|H_{VN}\|_{(T)}$

Now we analyze the major terms that contribute to total estimated errors. In fig. 2.12a, we find $2\sqrt{T}\,\|H_{DE,GV}\|_{(T)}$ is dominant in estimated errors. Recall that:

$$\eta_{DE,S} = \frac{C_p h_S C_K}{\sqrt{\lambda_{\min}}} \left\| -\partial_t f + \rho \partial_t^2 v_{h\Delta t} - \nabla_x \cdot \delta_{h\Delta t} \right\|_{(S)}, \quad \eta_{GV,S} = \frac{1}{\sqrt{\lambda_{\min}}} \left\| -\delta_{h\Delta t} + \sigma(\partial_t u_{h\Delta t}) \right\|_{(S)} \tag{2.54}$$

so it depends on both reconstructions in time and in space. We find that in fact this term contributes most to the total errors due to the nonconformity of the time derivative of equilibrium of reconstruction fields.

In fig. 2.12b, $\|H_{DE,GV}\|_{(T)}$ also contributes a large part of errors in the cases 3 and 4. Recall that $\|H_{DE,GV}\|_{(T)} = \|\partial_t u_{h\Delta t} - v_{h\Delta t}\|_{K(\Omega),(T)}$ so it depends mainly on the reconstructions of u and v in time; it is found in fig. 2.12b that the cases 1 and 2 with basic reconstruction for u, v have a better conformity between $\partial_t u_{h\Delta t}$ and $v_{h\Delta t}$ inside I_n than that in the cases 3 and 4 with equilibrated u-reconstruction and v-reconstruction. Besides, for the cases 3 and 4 same reconstructions $(u_{h\Delta t}, v_{h\Delta t})$ are used so they give the same results.

2.4 Conclusion

In this chapter we derived explicit *a posteriori* error estimates in a non-natural L^∞ norm for elastic wave propagation in heterogeneous media. The numerical results in the homogeneous case indicate that this estimation gives a fully computable upper bound of exact errors. However, its asymptotic exactness remains to be improved. In the work of Vohralík [150], similar reconstructions were also defined and used for an error bound of the first order (in time) heat equation; a nearly constant effectivity index was obtained in its numerical applications. In fact, for the second-order (in time) hyperbolic equation, our error bound includes not only the residual errors related to the equilibrium (as in [150]) but also the residual errors related to the time derivative equilibrium of reconstructed fields. The latter ($H_{DE,GV}$) dominates in the behaviour of the estimated errors. In a future work, more efforts should focus on reconstructions of fields that respect the equilibrium better.

Chapter 3

Energy-based *a posteriori* error estimation for high frequency wave equation in homogeneous media

Contents

As we introduced in the section 1.2.4, the radiative transfer equation arises for high frequency wave propagation in heterogeneous media in the weak coupling limit. It is derived by a two-scale asymptotic expansion of the wave equation in terms of the spatio-temporal Wigner transforms of wave fields. Its particular form in homogeneous media, i.e. the transport equation, is studied in this chapter. It describes the transport of wave energy. Considering the highly oscillating properties of HF wave fields, the classical error estimator that was derived in chapter 2 is no more efficient. The errors based on more relevant quantities, i.e. the energy densities of numerical solutions of wave equation, are studied here with the transport equation.

In the section 3.1, the Wigner transform is introduced in detail. We start with the temporal Wigner transform of a time signal. Its important mathematical properties, especially the interference property and the energy property, are presented and analyzed. Then the scaled spatio-temporal Wigner transform in the high frequency limit is defined and it satisfies also all the properties above. Finally, the discrete Wigner transform is studied and some numerical examples are given.

In the section 3.2, the principal steps for the derivation of the transport equation in terms of Wigner transforms are given. The transition from wave fields to energy densities, from the wave equation model to the energy transport model is presented in detail. Then the theoretical residual errors of finite element solutions of the wave equation based on the transport equation are defined and developed.

In the section 3.3, the numerical application of the defined residual error in a 1D medium is given. Residual errors for finite element solutions with different discretizations in time and in space are compared, that allows validating the obtained error estimator.

3.1 Wigner transform applied to the elastic wave equation

In this section, we give a detailed introduction of the Wigner transform. In the high frequency regime, it is used to derive the transport equation in homogeneous media and the radiative transfer equation in heterogeneous media (chapter 4). Some examples and numerical illustrations are given to clarify its properties and physical meanings.

The Wigner transform is widely used in signal processing [32, 42, 120] as a time-frequency representation since it provides a better simultaneous time-frequency resolution compared to the other representations, such as the Fourier transform (FT) [31, 35], the short-time Fourier transform (STFT) [11, 12], etc.

For time-space dependent functions, the definition of spatio-temporal Wigner transform is given by:

Definition 3.1 (Spatio-temporal Wigner transform)**.** The spatio-temporal Wigner transform of two time-space dependent vector functions $\mathbf{F}(t,\mathbf{x})$ and $\mathbf{G}(t,\mathbf{x})$, $(t,\mathbf{x}) \in \mathbb{R} \times \mathbb{R}^d$, is a second-order tensor defined by:

$$\mathrm{W}[\mathbf{F},\mathbf{G}](t,\mathbf{x};\omega,\mathbf{k}) = \frac{1}{(2\pi)^{1+d}} \int_{\mathbb{R}\times\mathbb{R}^d} \mathbf{F}\left(t-\frac{\tau}{2},\mathbf{x}-\frac{\mathbf{y}}{2}\right) \otimes \mathbf{G}^*\left(t+\frac{\tau}{2},\mathbf{x}+\frac{\mathbf{y}}{2}\right) e^{i(\tau\omega+\mathbf{y}\cdot\mathbf{k})} d\tau d\mathbf{y} \quad (3.1)$$

where d is the spatial dimension and the superscript $*$ denotes the complex conjugation operator.

3.1.1 Temporal Wigner transform in signal processing

The spatio-temporal Wigner transform (3.1) depends on four variables, two in the time-space domain and two in the (ω,k)-phase space. In order to simplify the introduction, we give the definition of temporal Wigner transform for two scalar time signals and introduce its properties in the following. The spatio-temporal Wigner transform satisfies also these properties.

Definition 3.2 (Temporal Wigner transform)**.** The (cross) Wigner transform of two time signals $F(t)$ and $G(t)$ is defined as the Fourier transform of their instantaneous correlation function:

$$\mathrm{W}[F,G](t;\omega) = \frac{1}{2\pi} \int_{\mathbb{R}} F\left(t-\frac{\tau}{2}\right) G^*\left(t+\frac{\tau}{2}\right) e^{i\tau\omega} d\tau \quad (3.2)$$

The (auto-) Wigner transform of $F(t)$ is denoted by: $\mathrm{W}[F](t;\omega) := \mathrm{W}[F,F](t;\omega)$.

Basically, the temporal Wigner transform tells us how the spectral density changes in time. It has several important properties [120]:

Property 1 (Symmetry property)**.** If $F(t)$ is real-valued, $\mathrm{W}[F]$ is an even function of ω.

$$\mathrm{W}[F](t;\omega) = \mathrm{W}[F](t,-\omega) \quad (3.3)$$

Property 2 (Conjugation property)**.**

$$\mathrm{W}[F,G] = (\mathrm{W}[G,F])^* \tag{3.4}$$

Thus $\mathrm{W}[F]$ is real for all $(t;\omega)$. Note that in the case of Wigner transform of two vectorial fields $\mathbf{F}$ and $\mathbf{G}$, $\mathbf{W}[\mathbf{F},\mathbf{G}] = (\mathbf{W}[\mathbf{G},\mathbf{F}])^{*T}$.

Property 3 (Correlation of a sum property)**.** The Wigner transform of a sum of two signals is the square of the correlation in time-frequency of their Wigner transforms.

$$|\mathrm{W}[F_1+F_2](t;\omega)|^2 = \int_{\mathbb{R}\times\mathbb{R}} \mathrm{W}[F_1]\left(t-\frac{\tau}{2};\omega-\frac{\upsilon}{2}\right)\mathrm{W}[F_2]\left(t+\frac{\tau}{2};\omega+\frac{\upsilon}{2}\right)d\tau d\upsilon \tag{3.5}$$

Property 4 (Integration properties)**.** The cross Wigner transform can be seen as a time distribution of the product of spectrums $\hat{F}\hat{G}^*$ or a phase-space description of the product of time signals FG^*.

$$\int_{\mathbb{R}} \mathrm{W}[F,G](t;\omega)dt = \frac{1}{2\pi}\hat{F}(\omega)\hat{G}^*(\omega), \qquad \int_{\mathbb{R}} \mathrm{W}[F,G](t;\omega)d\omega = F(t)G^*(t) \tag{3.6}$$

Property 5 (Energy density properties)**.** The marginal distribution obtained by integrating over time equals the energy spectrum, while the one obtained by integrating over frequency equals the instantaneous energy.

$$\int_{\mathbb{R}} \mathrm{W}[F](t;\omega)dt = \frac{1}{2\pi}\left|\hat{F}(\omega)\right|^2, \qquad \int_{\mathbb{R}} \mathrm{W}[F](t;\omega)d\omega = |F(t)|^2 \tag{3.7}$$

The integration of Wigner transform over the time-frequency domain is equal to the total energy of the signal.

$$\int_{\mathbb{R}\times\mathbb{R}} \mathrm{W}[F](t;\omega)dtd\omega = \int_{\mathbb{R}} |F(t)|^2 dt = \frac{1}{2\pi}\int_{\mathbb{R}} \left|\hat{F}(\omega)\right|^2 d\omega \tag{3.8}$$

The two equations above mean that Wigner transform can be interpreted as a distribution of energy density in time-frequency domain, which is, however, not always positive for all $(t;\omega)$.

Property 6 (Convolution property)**.** The Wigner transform of the product of two signals equals the convolution of the Wigner transform of each signal with respect to frequency. The Wigner transform of the convolution of two signals equals the convolution of the Wigner transform of each signal with respect to time.

$$\mathrm{W}[Fh](t;\omega) = \int_{\mathbb{R}} \mathrm{W}[F](t;\upsilon)\mathrm{W}[h](t;\omega-\upsilon)d\upsilon \tag{3.9a}$$

$$\mathrm{W}[F*h](t;\omega) = \int_{\mathbb{R}} \mathrm{W}[F](\tau;\omega)\mathrm{W}[h](t-\tau;\omega)d\tau \tag{3.9b}$$

where “$*$” denotes the convolution operator of two time functions.

Property 7 (Interference property)**.** The Wigner transform of a sum of two signals has the following form:

$$\mathrm{W}[F_1+F_2](t;\omega) = \mathrm{W}[F_1](t;\omega) + \mathrm{W}[F_2](t;\omega) + 2\mathrm{Re}\left\{\mathrm{W}[F_1,F_2](t;\omega)\right\} \tag{3.10}$$

where “Re” denotes the real part of a complex-valued quantity. This is due to the fact that Wigner transform is bilinear function according to its definition 3.2. $\mathrm{W}[F_1]$ and $\mathrm{W}[F_2]$ are called “auto-terms” and $2\mathrm{Re}\{\mathrm{W}[F_1,F_2](t;\omega)\}$ is called “cross-term” or interference term.

3.1.2 Discussion and analysis of the interference property of Wigner transform

The existence of cross-terms of Wigner transform has a great influence on the time-frequency analysis. In this section we study in detail this property by some theoretical and numerical examples.

The following example is given by [70, 79]. We consider a time signal $F(t) = F_1(t) + F_2(t)$ defined as follows:

$$F_1(t) = A_1 h(t-t_1)e^{i\omega_1 t}, \qquad F_2(t) = A_2 h(t-t_2)e^{i\omega_2 t} \tag{3.11}$$

where A_1 and A_2 are real constant amplitudes, h is thought to be a window function concentrated at 0 in time. Thus F_1 and F_2 are respectively concentrated around $(t_1;\omega_1)$ and $(t_2;\omega_2)$ in the $(t;\omega)$-plane.

Using the interference property eq. (3.10), $\mathrm{W}[F_1+F_2]$ can be computed analytically. The two auto-terms can be obtained by the convolution property eq. (3.9) and by taking into account the fact that $\mathrm{W}[e^{i\omega_1 t}] = \delta(\omega-\omega_1)$:

$$\mathrm{W}[F_1](t;\omega) = A_1^2\mathrm{W}[h](t-t_1;\omega-\omega_1), \qquad \mathrm{W}[F_2](t;\omega) = A_2^2\mathrm{W}[h](t-t_2;\omega-\omega_2) \tag{3.12}$$

Thus as a time-frequency representation of F_1 and F_2, $\mathrm{W}[F_1]$ and $\mathrm{W}[F_2]$ lie respectively in the surroundings of points (t_1,ω_1) and (t_2,ω_2) in the $(t;\omega)$-plane. For the cross term $2\mathrm{Re}\{\mathrm{W}[F_1,F_2](t;\omega)\}$, by the definition of the cross Wigner transform eq. (3.2) and a time shift of h, we obtain:

$$\begin{aligned}2\mathrm{Re}\{\mathrm{W}[F_1,F_2](t;\omega)\} &= 2\mathrm{Re}\left\{A_1A_2\frac{1}{2\pi}\int h\left(t-t_1-\frac{\tau}{2}\right)e^{i\omega_1\left(t-\frac{\tau}{2}\right)}h^*\left(t-t_2+\frac{\tau}{2}\right)e^{-i\omega_2\left(t+\frac{\tau}{2}\right)}e^{i\tau\omega}d\tau\right\}\\ &= 2A_1A_2\cos\left(\omega_d t-(\omega-\omega_m)t_d\right)\mathrm{W}[h](t-t_m;\omega-\omega_m)\end{aligned} \tag{3.13}$$

where the time lag and the frequency lag are denoted by $(t_d;\omega_d) = (t_2-t_1;\omega_2-\omega_1)$, the centre time and the centre frequency are denoted by $(t_m;\omega_m) = (\frac{t_1+t_2}{2};\frac{\omega_1+\omega_2}{2})$. Several properties of cross term are observed with this expression. Firstly, the cross term is a modulated version of the original signal F shifted to the midpoint $(t_m;\omega_m)$ of the segment connecting $(t_1;\omega_1)$ and $(t_2;\omega_2)$ in the $(t;\omega)$-plane. This result can be generalized to a function composed of N time-frequency component signal, which are localized around N different points in the $(t;\omega)$-plane. In this case, there exist $\frac{N(N-1)}{2}$ cross terms between each two components. Secondly, the “cosine” function in cross term can be written as:

$$\cos\left(\omega_d t-(\omega-\omega_m)t_d\right) = \cos\left(\sqrt{\omega_d^2+t_d^2}\left(\frac{\omega_d}{\sqrt{\omega_d^2+t_d^2}}t-\omega\frac{t_d}{\sqrt{\omega_d^2+t_d^2}}\right)+\omega_m t_d\right) \tag{3.14}$$

so it results in oscillations in the direction $(\omega_d;-t_d)$ that is orthogonal to the line that connects the auto-terms in the direction $(t_d;\omega_d)$; the frequency of this oscillation is simply the distance $\sqrt{t_d^2+\omega_d^2}$

in the $(t;\omega)$-plane between the signal components. Then the peak value of the cross term is twice as large as the product of that of the auto-terms. Finally, we will see with the following example that the "cosine" function is in fact the source of negative values of Wigner transform.

Numerical illustration of Wigner transform of a sum of two gaussian complex-valued signals (fig. 3.1a) is given in the following so as to observe the properties of cross terms explained above. We define $h(t)$ and the parameters of the function F in eq. (3.11) by:

$$h(t) = e^{-2t^2}, \quad A_1 = (\frac{4}{\pi})^{\frac{1}{4}},\ (t_1;\omega_1) = (-2;20); \quad A_2 = (\frac{8}{\pi})^{\frac{1}{4}},\ (t_2;\omega_2) = (2;40) \tag{3.15}$$

Figure 3.1b gives the Wigner transform of $F(t)$. It is found that the two auto-terms located at $(t_1;\omega_1)$, $(t_2;\omega_2)$ and the cross term located at their centre $(t_m;\omega_m) = (0;30)$ agree with the theoretical analysis above. We also observe that oscillations of the cross term (along the solid arrowed line) are orthogonal to connecting line of the auto-terms (along the dashed arrowed line). The auto-term $W[F_2]$ and the cross term have the same amplitude and quadruple that of the auto-term $W[F_1]$ in fig. 3.1b.

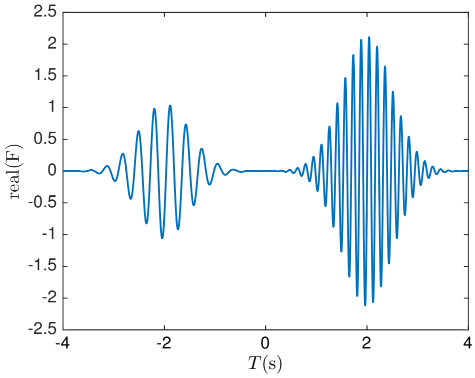

(a)

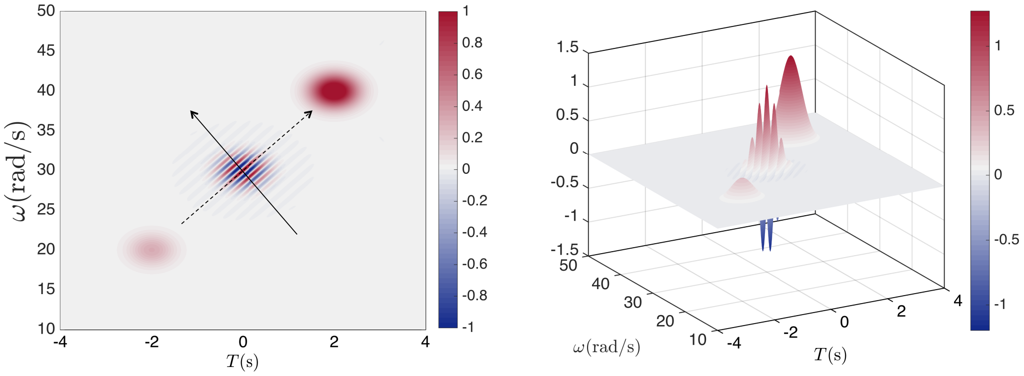

(b)

Fig. 3.1 (a) real part of a complex-valued signal $F(t)$ (eq. (3.11), eq. (3.15)) composed of two gaussian functions localized in both time and frequency domains, (b) Wigner transform in time-frequency domain $\mathrm{W}[F](t;\omega)$: two auto-terms (positive, red round zone); one cross term (positive or negative, oscillating zone)

As expected, it is observed that the cross term contains some negative values, resulting from "cosine" in eq. (3.13). Although the Wigner transform satisfies always energy properties (eq. (3.7) and (3.8)), we cannot interpret it as an exact time-varying energy density estimate. It may be more reasonable to integrate Wigner transform in a period of time or a band of frequency so as to ensure its positivity as a representation of energy (energy density property eq. (3.7)). The integral of auto- or cross terms over frequency is called its energy content. Generally, both auto- and cross terms contribute to signal energy [70, 118]. The oscillations of cross terms suggest that their energy content is small compared to the energy content of auto-terms. In particular, the cross term of disjoint signals (i.e. auto-terms do not overlap) has zero energy content. Figure 3.2 illustrates the energy content of the example above, and no energy exists for the cross term at $t = 0$.

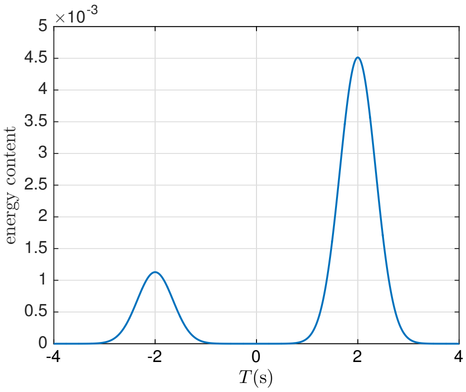

Fig. 3.2 Energy content of $F(t)$ (composed of two disjoint gaussian functions): $\int_{\mathbb{R}} \mathrm{W}[F](t;\omega)d\omega$ normalized to total energy

In this simple case the cross terms are separated spatially from the auto-terms. We can easily identify them and their integration in time has no contribution to total energy. However, for multi-component or continuous frequency signals, cross-terms of their Wigner transform not only appear in the separate area, where the auto-terms are zero or negligible but also spread throughout the domain of the auto-terms, and corrupt them in the complete Wigner transform. Therefore, it is difficult to distinguish between auto-terms and cross terms if more complicated signals are used [71, 116].

What calls for special attention is that a sum of complex-valued signal (3.11) was given above as an example. Solutions of wave propagation problems are always real-valued. It is known that any real-valued signal can be expressed as a sum of two complex-valued signals with positive and negative frequencies. For example, we have: $\cos(\omega t) = \frac{e^{i\omega t}+e^{-i\omega t}}{2}$. Thus the cross terms in the Wigner transform of a sum of two real-valued signals result from not only interactions between intrinsic positive frequencies but also between positive and negative frequencies.

We study now the sum of two real-valued signals $G = G_1 + G_2$ given by:

$$G_1(t) = \frac{F_1(t) + F_1^*(t)}{2} = A_1 h(t-t_1)\cos(\omega_1 t), \quad G_2(t) = \frac{F_2(t) + F_2^*(t)}{2} = A_2 h(t-t_2)\cos(\omega_2 t) \tag{3.16}$$

with F_1 and F_2 already defined in eq. (3.11). So their complex conjugates F_1^* and F_2^* are respectively localized around $(t_1;-\omega_1)$ and $(t_2;-\omega_2)$ in the $(t;\omega)$-plane. Thus $G(t)$ is composed of four frequency components, and there are four auto-terms at $(t_1;\pm\omega_1)$, $(t_2;\pm\omega_2)$ and six cross terms at $(t_1;0)$, $(t_2;0)$, $(t_m;\pm\omega_m)$, $(t_m;\pm\omega_d)$ for its Wigner transform.

Considering the example of a sum of the two real-valued gaussian signals defined by eq. (3.16) with parameters given by eq. (3.15), its Wigner transform is computed and illustrated in fig. 3.3. We get four auto-terms at $(t;\omega) = (-2;\pm 20)$ and $(2;\pm 40)$ and six cross terms at $(t;\omega) = (-2;0), (2;0), (0;\pm 30)$ and $(0;\pm 10)$, which appear between each two auto-terms (fig. 3.3). Every cross term is resulting from the interference of each two auto-terms (marked with solid arrowed lines in fig. 3.3) and its locations, fluctuations and peak value are determined by eq. (3.13).

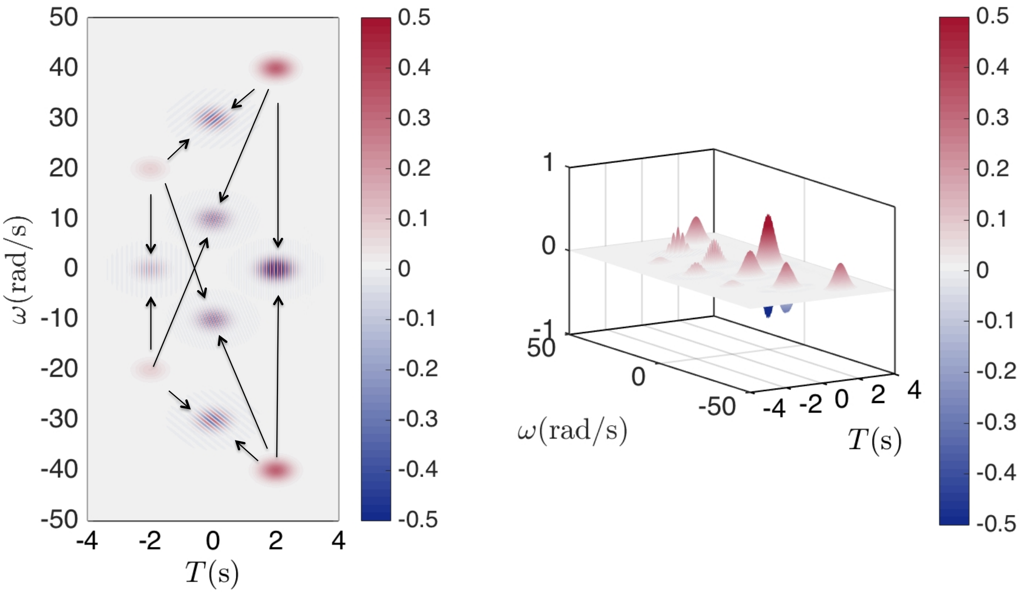

Fig. 3.3 Wigner transform of a signal $G(t)$ (eq. (3.16), eq. (3.15)) composed of two real-valued gaussian functions in time-frequency domain $\mathrm{W}[G](t;\omega)$: four auto-terms (positive, red round zone); six cross terms (positive or negative, oscillating zone)

Until now, we presented the existence and properties of cross terms in Wigner transform. Since the distribution of energy density in terms of frequency may be influenced by these terms, we will try and analyze some methods to remove them. However, the total energy property should not be influenced by that removal since in our work, the Wigner transform of wave fields is studied and the energy transport equation is used for evaluating errors.

For instance, cross terms between positive frequencies and negative frequencies for 1D signal can be suppressed by Hilbert transform. In fact, Hilbert transform of a signal allows eliminating its negative frequency components and we obtain what is called the analytical signal [66, 142]. Thus its Wigner transform contains only cross terms between non negative frequencies. The 1D form of analytical signal using the Hilbert transform has been used extensively in signal processing since their introduction by Gabor [58]. However, their extension to the 2D case and their application to images are limited, due to the non-uniqueness of the multidimensional Hilbert transform. Some usual definitions of 2D Hilbert transform can be found in [101]. However, either negative frequencies are not suppressed totally, or the real part of the constructed analytical signal does not coincide with the original signal. Consequently, since we are concerned with 2D or higher dimension, this method is not practical. Some suppression methods have been already developed to reduce the cross terms between positive frequencies, such as low pass filtering or adding window functions [115, 126], image processing [9, 116], combining the STFT and the Wigner transform [63, 83, 134], etc. Generally, in all cases, cross terms can never be totally removed without affecting the appearance and quality of the resulting time-frequency representation [161]. In detail, a loss of frequency concentration or resolution will appear with these methods and the most important energy properties cannot hold any more. Also, such methods are either computationally expensive or have a very limited applicability. Consequently, we do not use the classical cross term removal methods in our work so as to conserve always the energy properties. However, we should always pay attention to the existence of cross terms and their influence on our numerical computations, especially when explaining phenomena in phase space.

3.1.3 Scaled spatio-temporal Wigner transform in the high frequency limit

As discussed in the introduction of this chapter, we consider high frequency limit where the typical distance of propagation L of waves is much larger that the typical wavelength λ in the system: $\varepsilon = \frac{\lambda}{L} \ll 1$. The spatio-temporal Wigner transform (definition 3.1) should be rescaled and defined as follows:

Definition 3.3 (Scaled spatio-temporal Wigner transform)**.** The scaled spatio-temporal Wigner transform $\mathbf{W}_\varepsilon[\mathbf{u}_\varepsilon, \mathbf{v}_\varepsilon]$ for two vector fields $\mathbf{u}_\varepsilon(t,\mathbf{x})$ and $\mathbf{v}_\varepsilon(t,\mathbf{x})$ is defined as:

$$\begin{aligned}\mathbf{W}_\varepsilon[\mathbf{u}_\varepsilon, \mathbf{v}_\varepsilon](t,\mathbf{x};\omega,\mathbf{k}) &:= \frac{1}{\varepsilon^2}\mathbf{W}[\mathbf{u}_\varepsilon, \mathbf{v}_\varepsilon]\left(t,\mathbf{x};\frac{\omega}{\varepsilon},\frac{\mathbf{k}}{\varepsilon}\right)\\ &= \frac{1}{(2\pi)^{1+d}}\int_{\mathbb{R}\times\mathbb{R}^d}\mathbf{u}_\varepsilon\left(t-\frac{\varepsilon\tau}{2},\mathbf{x}-\frac{\varepsilon\mathbf{y}}{2}\right)\otimes\mathbf{v}_\varepsilon^*\left(t+\frac{\varepsilon\tau}{2},\mathbf{x}+\frac{\varepsilon\mathbf{y}}{2}\right)e^{i(\tau\omega+\mathbf{y}\cdot\mathbf{k})}d\tau d\mathbf{y} \qquad (3.17)\end{aligned}$$

and the (auto-) spatio-temporal Wigner transform $\mathbf{W}_\varepsilon[\mathbf{u}_\varepsilon] := \mathbf{W}_\varepsilon[\mathbf{u}_\varepsilon, \mathbf{u}_\varepsilon]$.

With this definition, the spatio-temporal Wigner transform is properly scaled at ε^{-1} for ω and $\mathbf{k}$ so as to observe all the fast fluctuations of order ε^{-1} and to separate them from slow fluctuations of ε^0. It satisfies always all the properties of the temporal Wigner transform introduced in the section 3.1.1 and section 3.1.2.

Using rules of pseudo-differential calculus presented in Appendix C, we derive the following properties of the scaled Wigner transform:

Lemma 3.4 (Time and space derivative properties of Wigner transform)**.**

$$\partial_t \mathbf{W}_\varepsilon[\mathbf{u}_\varepsilon] = \mathbf{W}_\varepsilon\left[\partial_t \mathbf{u}_\varepsilon, \mathbf{u}_\varepsilon\right] + \left(\mathbf{W}_\varepsilon\left[\partial_t \mathbf{u}_\varepsilon, \mathbf{u}_\varepsilon\right]\right)^{*T} \tag{3.18a}$$

$$\hat{\mathbf{k}} \cdot \nabla_{\mathbf{x}} \mathbf{W}_\varepsilon[\mathbf{u}_\varepsilon] = \mathbf{W}_\varepsilon\left[\hat{\mathbf{k}} \cdot \nabla_{\mathbf{x}} \mathbf{u}_\varepsilon, \mathbf{u}_\varepsilon\right] + \left(\mathbf{W}_\varepsilon\left[\hat{\mathbf{k}} \cdot \nabla_{\mathbf{x}} \mathbf{u}_\varepsilon, \mathbf{u}_\varepsilon\right]\right)^{*T} \tag{3.18b}$$

where $(\hat{\mathbf{k}} \cdot \nabla_{\mathbf{x}} \mathbf{W})_{ij} = k_l \partial_{x_l} \mathrm{W}_{ij}$ (with Einstein summation convention). It is in fact the directional derivative along $\hat{\mathbf{k}}$ of $\mathbf{W}$.

Proof.

Using homogeneous pseudo-differential operator's properties eq. (C.4) and eq. (C.3) with $\varphi(\varepsilon \mathrm{D}_t) = \varepsilon \partial_t$ and $\varphi(\varepsilon \mathbf{D}_{\mathbf{x}}) = \varepsilon \hat{\mathbf{k}} \cdot \nabla_{\mathbf{x}}$, we have

$$\begin{cases} \mathbf{W}_\varepsilon\left[\varepsilon \partial_t \mathbf{u}_\varepsilon, \mathbf{u}_\varepsilon\right] = i\omega \mathbf{W}_\varepsilon[\mathbf{u}_\varepsilon] + \frac{\varepsilon \partial_t}{2} \mathbf{W}_\varepsilon[\mathbf{u}_\varepsilon] \\ \mathbf{W}_\varepsilon\left[\mathbf{u}_\varepsilon, \varepsilon \partial_t \mathbf{u}_\varepsilon\right] = -i\omega \mathbf{W}_\varepsilon[\mathbf{u}_\varepsilon] + \frac{\varepsilon \partial_t}{2} \mathbf{W}_\varepsilon[\mathbf{u}_\varepsilon] \end{cases} \quad \begin{cases} \mathbf{W}_\varepsilon\left[\varepsilon \hat{\mathbf{k}} \cdot \nabla_{\mathbf{x}} \mathbf{u}_\varepsilon, \mathbf{u}_\varepsilon\right] = i\mathbf{k} \mathbf{W}_\varepsilon\left[\mathbf{u}_\varepsilon\right] + \frac{\varepsilon \hat{\mathbf{k}} \cdot \nabla_{\mathbf{x}}}{2} \mathbf{W}_\varepsilon[\mathbf{u}_\varepsilon] \\ \mathbf{W}_\varepsilon\left[\mathbf{u}_\varepsilon, \varepsilon \hat{\mathbf{k}} \cdot \nabla_{\mathbf{x}} \mathbf{u}_\varepsilon\right] = -i\mathbf{k} \mathbf{W}_\varepsilon[\mathbf{u}_\varepsilon] + \frac{\varepsilon \hat{\mathbf{k}} \cdot \nabla_{\mathbf{x}}}{2} \mathbf{W}_\varepsilon[\mathbf{u}_\varepsilon] \end{cases} \tag{3.19}$$

Then taking the sum of each two equations in eq. (3.19), we get:

$$\partial_t \mathbf{W}_\varepsilon[\mathbf{u}_\varepsilon] = \mathbf{W}_\varepsilon[\partial_t \mathbf{u}_\varepsilon, \mathbf{u}_\varepsilon] + \mathbf{W}_\varepsilon[\mathbf{u}_\varepsilon, \partial_t \mathbf{u}_\varepsilon] \tag{3.20a}$$

$$\hat{\mathbf{k}} \cdot \nabla_{\mathbf{x}} \mathbf{W}_\varepsilon[\mathbf{u}_\varepsilon] = \mathbf{W}_\varepsilon[\hat{\mathbf{k}} \cdot \nabla_{\mathbf{x}} \mathbf{u}_\varepsilon, \mathbf{u}_\varepsilon] + \mathbf{W}_\varepsilon[\mathbf{u}_\varepsilon, \hat{\mathbf{k}} \cdot \nabla_{\mathbf{x}} \mathbf{u}_\varepsilon] \tag{3.20b}$$

Recalling the conjugation property (eq. (3.4)) of Wigner transform), thus we obtain eq. (3.18).

□

Now we present the Wigner measure, i.e. the energy density described by the transport equation or the radiative transfer equation.

Definition 3.5 (Wigner measure)**.** The Wigner measure, denoted by $\mathbf{W}$, is the weak limit of the Wigner transform $\mathbf{W}_\varepsilon$ as $\varepsilon \to 0$:

$$\mathbf{W}[\mathbf{u}_\varepsilon] := \lim_{\varepsilon \to 0} \mathbf{W}_\varepsilon[\mathbf{u}_\varepsilon] \tag{3.21}$$

As we observed with the examples in the section 3.1.2, Wigner transform can be positive or negative. However, Wigner measure can be demonstrated to be always positive [97]. Thus Wigner measure can be interpreted as the energy density of waves in phase space. This is exactly the property that makes the Wigner measure a useful tool for the study of wave or quantum interference phenomena.

Furthermore, the potential and kinetic energy of high frequency propagating waves can be estimated by its Wigner measure with the following lemma:

Lemma 3.6 (Energy property of Wigner measure of wave fields)**.**

$$\lim_{\varepsilon\to 0}\frac{1}{2}\int_{\mathbb{R}^d}(\mathbf{C}:\boldsymbol{\varepsilon}(\mathbf{u}_\varepsilon)(t,\mathbf{x})):\boldsymbol{\varepsilon}^*(\mathbf{u}_\varepsilon)(t,\mathbf{x})d\mathbf{x}=\frac{1}{2}\int_{\mathbb{R}\times\mathbb{R}^d\times\mathbb{R}^d}\rho\boldsymbol{\Gamma}(\mathbf{k}):\mathbf{W}[\mathbf{u}_\varepsilon](t,\mathbf{x};\omega,\mathbf{k})d\omega d\mathbf{x}d\mathbf{k} \tag{3.22a}$$

$$\lim_{\varepsilon\to 0}\frac{1}{2}\int_{\mathbb{R}^d}\rho\partial_t\mathbf{u}_\varepsilon(t,\mathbf{x})\cdot\partial_t\mathbf{u}_\varepsilon^*(t,\mathbf{x})d\mathbf{x}=\frac{1}{2}\int_{\mathbb{R}\times\mathbb{R}^d\times\mathbb{R}^d}\rho\mathrm{Tr}\left(\mathbf{W}[\partial_t\mathbf{u}_\varepsilon](t,\mathbf{x};\omega,\mathbf{k})\right)d\omega d\mathbf{k}d\mathbf{x} \tag{3.22b}$$

Proof. For eq. (3.22a), by using the integration property of Wigner transform over (ω,k) (the second equation of eq. (3.6)), we have

$$\begin{aligned}
&\lim_{\varepsilon\to 0}\frac{1}{2}\int_{\mathbb{R}^d}(\mathbf{C}:\boldsymbol{\varepsilon}(\mathbf{u}_\varepsilon)(t,\mathbf{x})):\boldsymbol{\varepsilon}^*(\mathbf{u}_\varepsilon)(t,\mathbf{x})d\mathbf{x}\\
=&\lim_{\varepsilon\to 0}\frac{1}{2}\int_{\mathbb{R}}((\varepsilon\nabla_{\mathbf{x}})^*\cdot(\mathbf{C}:\boldsymbol{\varepsilon}(\mathbf{u}_\varepsilon)(t,\mathbf{x})))\cdot\mathbf{u}_\varepsilon^*(t,\mathbf{x})d\mathbf{x}\\
=&\lim_{\varepsilon\to 0}\frac{1}{2}\int_{\mathbb{R}\times\mathbb{R}^d\times\mathbb{R}^d}\mathrm{Tr}\left(\mathbf{W}_\varepsilon\left[(\varepsilon\nabla_{\mathbf{x}})^*\cdot(\mathbf{C}:\boldsymbol{\varepsilon}(\mathbf{u}_\varepsilon)(t,\mathbf{x})),\mathbf{u}_\varepsilon\right](t,\mathbf{x};\omega,\mathbf{k})\right)d\omega d\mathbf{k}d\mathbf{x}
\end{aligned} \tag{3.23}$$

Then applying the property of pseudo-differential operators eq. (C.3) by taking $\psi(\varepsilon\mathbf{D}_{\mathbf{x}})\mathbf{u}_\varepsilon=(\varepsilon\nabla_{\mathbf{x}})^*\cdot(\mathbf{C}:\boldsymbol{\varepsilon}(\mathbf{u}_\varepsilon)$, we can derive:

$$\begin{aligned}
&\lim_{\varepsilon\to 0}\frac{1}{2}\int_{\mathbb{R}^d}(\mathbf{C}:\boldsymbol{\varepsilon}(\mathbf{u}_\varepsilon)(t,\mathbf{x})):\boldsymbol{\varepsilon}^*(\mathbf{u}_\varepsilon)(t,\mathbf{x})d\mathbf{x}\\
=&\lim_{\varepsilon\to 0}\frac{1}{2}\int_{\mathbb{R}\times\mathbb{R}^d\times\mathbb{R}^d}\rho\left\{\rho^{-1}\mathbf{C}:\left((i\mathbf{k}+\frac{\varepsilon\nabla_{\mathbf{x}}}{2})^*\otimes(i\mathbf{k}+\frac{\varepsilon\nabla_{\mathbf{x}}}{2})\right)\right\}:\mathbf{W}_\varepsilon[\mathbf{u}_\varepsilon](t,\mathbf{x};\omega,\mathbf{k})d\omega d\mathbf{k}d\mathbf{x}\\
=&\frac{1}{2}\int_{\mathbb{R}\times\mathbb{R}^d\times\mathbb{R}^d}\rho\boldsymbol{\Gamma}(\mathbf{k}):\mathbf{W}[\mathbf{u}_\varepsilon](t,\mathbf{x};\omega,\mathbf{k})d\omega d\mathbf{k}d\mathbf{x}
\end{aligned} \tag{3.24}$$

The kinetic energy eq. (3.22b) can be obtained by using directly the energy property of Wigner transform (the second equation of eq. (3.7)).

□

Note that these results in eq. (3.22a) and eq. (3.22b) are valid also in heterogeneous media when the elastic parameters are dependant of **x** [25].

In high frequency limit, highly oscillating quantities such as $\mathbf{u}_\varepsilon^2$, $\boldsymbol{\sigma}_\varepsilon^2$ do not satisfy a closed-form equation in time-space $(t,\mathbf{x})$; however, we will see that the Wigner measure $\mathbf{W}[\mathbf{u}_\varepsilon]$ as $\varepsilon\to 0$ satisfies a closed-form equation that we derive in next section 3.2.

3.1.4 Discrete Wigner transform and analysis of parameters

Before the introduction of the transport equation, numerical computation of Wigner transform is an important aspect in numerical applications. The Wigner transform of numerical solutions of wave equation is quantified in our work and its analytical expression does not exist. Besides, considering the computational cost, Wigner transform should not be computed in an infinite region. Thus we should discuss the numerical computation of Wigner transform.

In this section, the discrete Wigner transform (DWT) is defined and analyzed. DWT for a temporal signal is presented here for simplicity (DWT for a time-space dependent function is realized in the same way). Numerical examples are given for Wigner transform of a ricker signal in time and Wigner transform of wave fields in the time-space domain.

The discretization of the temporal Wigner transform (3.2) is defined in the following:

Definition 3.7 (Discrete Wigner transform)**.** Assuming that a discretized signal is given as $F[N] := F(t = N\Delta t)$, $N \in [1, N_s]$, where N_s is the total number of samples. Δt is the sampling interval. $\zeta_t = N_s \Delta t$ is the sampling length. The summation variable τ in Wigner transform is discretized by $\tau/2 = M\Delta t$, $M \in \mathbb{Z}$. The discretization of frequency is defined as $\omega = 2\pi \frac{L}{N_s \Delta t}, L \in \mathbb{Z}$. Then the discrete Wigner transform $\mathrm{W}[F][N;L]$ is defined as (we use the same notation $\mathrm{W}[F]$ for continuous and discrete Wigner transform):

$$\begin{aligned} \mathrm{W}[F][N;L] &:= \mathrm{W}[F]\left(t = N\Delta t; \omega = 2\pi \frac{L}{N_s \Delta t}\right) \\ &= \frac{1}{\pi} \sum_M F[N-M] F^*[N+M] e^{i4\pi M \frac{L}{N_s}} \end{aligned} \tag{3.25}$$

Compared with the classical discrete Fourier transform (DFT) [35]:

$$\widehat{G}[L] = \sum_M G[M] e^{i2\pi M \frac{L}{N_s}} \tag{3.26}$$

the DWT can be interpreted as a DFT of the correlation function FF^* with twice frequency.

Now we discuss the choice of numerical parameters in DWT: the sampling interval Δt and the sampling length or computation length ζ_t.

According to the Shannon sampling theorem [81], the maximum resolvable frequency must be half the sampling frequency f_s for DFT. Thus for DWT, f_s or Δt satisfies:

$$f_s = \frac{1}{\Delta t} \geq 4 f_F \tag{3.27}$$

where f_F is the frequency of signal $F(t)$. So Δt takes a very small value for high frequency f_F.

Frequency resolution is defined as the distance between two adjacent frequency data points in the DWT so it stands for the precision of the frequency representation of the signal:

$$\Delta f = \frac{1}{2\zeta_t} = \frac{1}{2N_s \Delta t}, \qquad f \in \left[-\frac{1}{4\Delta t}, \frac{1}{4\Delta t}\right] \tag{3.28}$$

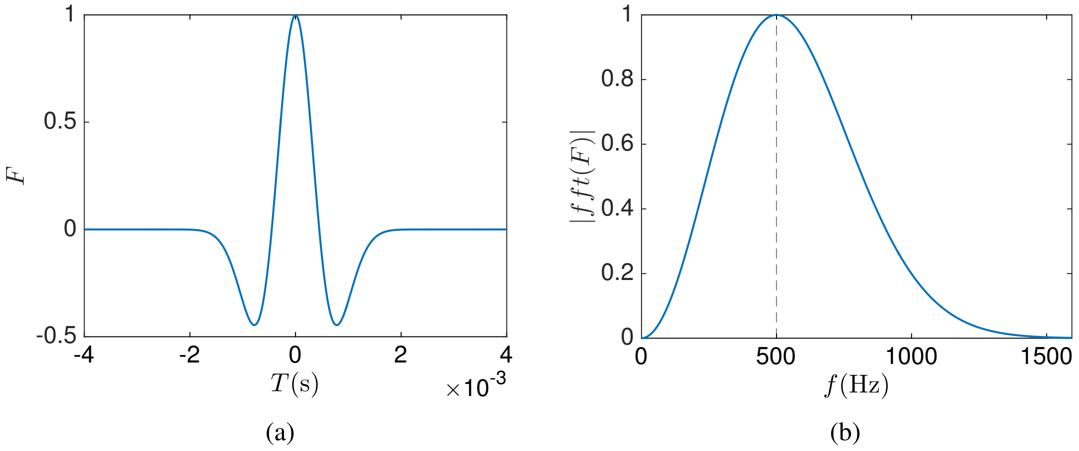

(a) (b)

Fig. 3.4 Ricker signal and its frequency spectrum: (a) $F(t)$, (b) $|FFT(F)|$

Smaller Δf means a better frequency resolution. However, since Δt is very small, increasing ζ_t means increasing a large total number of sampling N_s, that may cause a high computational cost especially for high dimension input. We have to choose an appropriate ζ_t.

We consider firstly identifying the value of ζ_t for two adjacent frequencies of a signal. If we want to separate two peaks with frequencies ω_1 and ω_2 of DWT ($\omega_2 > \omega_1$), we need to have at least one node between these two points in ω axis, i.e.:

$$\frac{\omega_2-\omega_1}{2\pi} \geq 2\Delta f = \frac{1}{\zeta_t}, \qquad \text{i.e.} \quad \zeta_t \geq \frac{2\pi}{\omega_2-\omega_1} \tag{3.29}$$

Now considering a continuous frequency band with a maximum frequency ω_0, it is known that it has a cross term $\frac{\omega_0}{2}$ between ω_0 and low frequency near to zero in Wigner transform. For separating components ω_0 and $\frac{\omega_0}{2}$, we need

$$\zeta_t \geq \frac{4\pi}{\omega_0} \tag{3.30}$$

In conclusion, discrete Wigner transform in time is realized within a chosen computation length ζ_t that satisfies eq. (3.30). Now same analysis of parameters can be extended to the discrete Wigner transform of a time-space dependant signal, denoted by (ζ_t, ζ_x). They should verify:

$$\zeta_t \geq \frac{4\pi}{\omega_0}, \qquad \zeta_x \geq \frac{4\pi}{k_0} \tag{3.31}$$

where k_0 is the frequency related to the space variable, i.e the wave number for wave propagation problems. Since spatio-temporal Wigner transform depends on four parameters $(t,x;\omega,k)$, we fix one time-space point (t_0,x_0) in time-space and represent all the results in phase space (ω,k), computed for the chosen computation region (ζ_t, ζ_x) in time-space. In addition, we know that Wigner transform is real (for $d = 1$) and symmetric about the origin in phase space so we illustrate only positive ω in all the figures.

Now the DWT of a ricker signal is given so as to observe the influence of different computation lengths ζ_t. It can be seen as the Wigner transform of the product of the ricker signal and a rectangular window function with different window lengths ζ_t. Figure 3.4 illustrates a ricker signal centred at $t = 0$ s with period $T_R = 4$ ms. The maximum frequency $f_{max} = 500$ Hz (frequency for maximum amplitude). According to eq. (3.30), $\zeta_t \geq 2/f_{max} = 2T_{max} = 4$ ms for the identification of f_{max}. Note also that $2T_{max} = T_R$ so this choice is reasonable in the sense that this lower bound allows including the whole signal $F(t)$.

Figure 3.5a - 3.5d give the numerical results of $\mathrm{W}[F]$ in terms of time-frequency for four different values of ζ_t. We find also that the maximum value of Wigner transform lies at zero frequency, as a result of superposition of cross terms between all ω_0 and $-\omega_0$ ($\omega_0 \in [0, 2\pi f_{max}]$) since ricker is a real-valued signal in time. The second maximum value of Wigner transform is located around the maximum frequency.

In fig. 3.5e, we compare the four plots fig. 3.5a - 3.5d for a fixed frequency $f = f_{max}$. According to the convolution property of Wigner transform in frequency (eq. (3.9a)), the change of computation region, i.e. the size of rectangular window function has almost no influence on time resolution. The last three lines almost coincide, but $\zeta_t = T_{max} = T_R/2$ differs most from others because it contains only the half signal in time and has a low-resolution in time. It changes principally the frequency resolution. Figure 3.5f shows their values for a fixed time instant $t = 0$: we observe that $\zeta_t = 2T_{max}$ already allows identifying a maximum frequency around $f_{max} = 500$ Hz as expected. With increasing ζ_t, a spectrum with higher resolution is obtained.

Note also that since this ricker signal has a spectrum of frequency over a continuous frequency range, cross terms of its Wigner transform spreads out over the same continuous frequency range. Thus the maximum frequency found by its Wigner transform does not coincide with its real value $f_{max} = 500$ Hz. To investigate the influence of the parameter ζ_t on numerical calculations of Wigner transform, we propose to identify the maximum frequency by the middle point determined by the two adjacent frequencies corresponding to the two highest amplitudes (of course, the maximum at $f = 0$ due to cross terms with negative frequencies is neglected). It is respectively 375 Hz, 564 Hz, 530 Hz, 515 Hz, obtained with fig. 3.5f and illustrated in fig. 3.6 with ζ_t increasing. It shows that the identified maximal frequency of the numerically calculated Wigner transform converges to a value that would be slightly larger than the maximal frequency f_{max} defined by the ricker signal.

Now to study the influence of the size of sampling length on the discrete spatio-temporal Wigner transform, we consider the wave propagation in a 1D semi-infinite homogeneous bar (fig. 3.7). Its end is subjected to Neumann boundary condition by a ricker signal $F(t)$ with a magnitude of 1 kN/m^2 ($t \in [0, T_R]$). The related parameters are given in the table 3.1. Here the analytical solution of wave displacements can be computed with eq. (2.48).

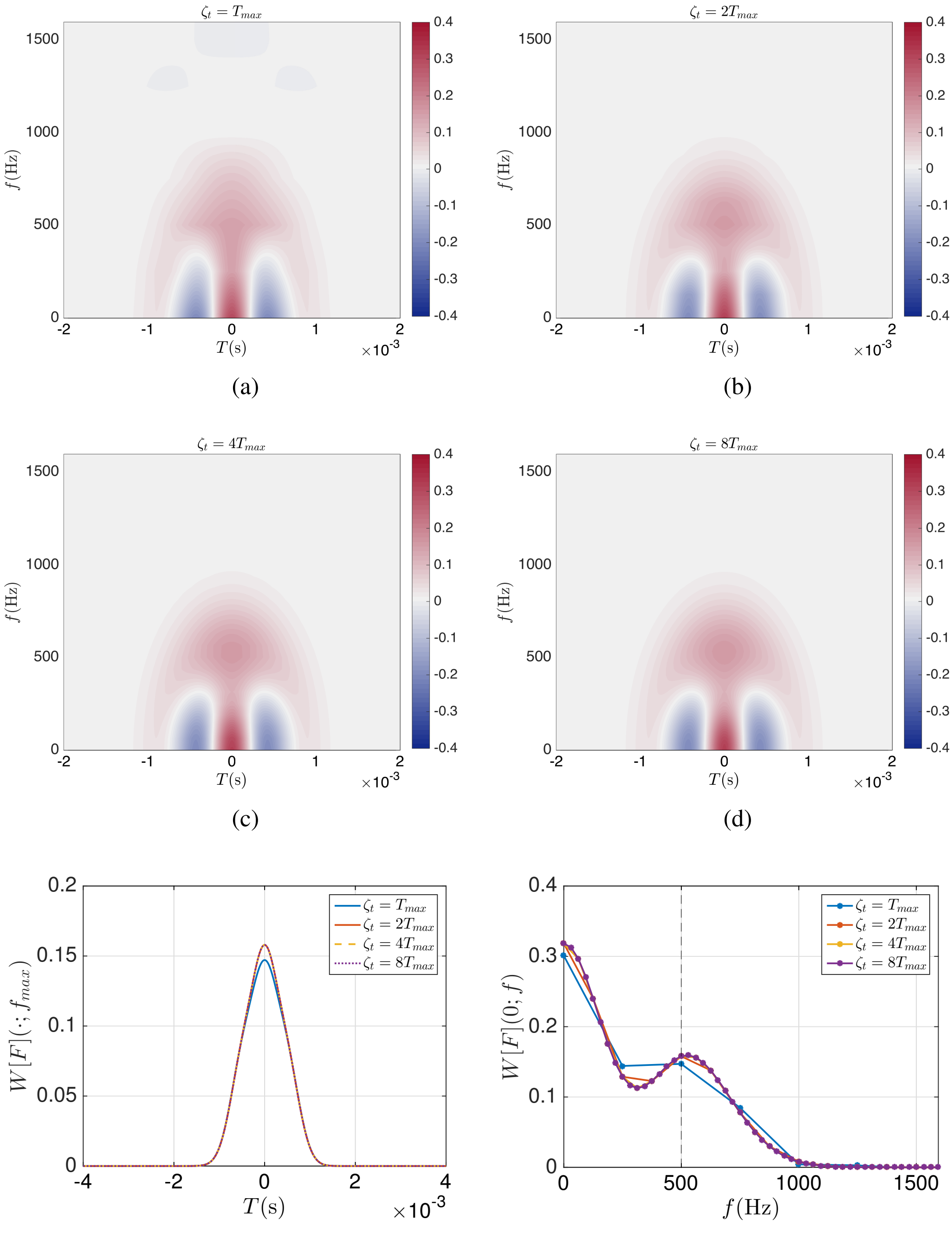

(a) (b) (c) (d) (e) (f)

Fig. 3.5 Wigner transform of ricker signal $\mathrm{W}[F](t;f)$ for (a) $\zeta_t = T_{max}$, (b) $\zeta_t = 2T_{max}$, (c) $\zeta_t = 4T_{max}$, (d) $\zeta_t = 8T_{max}$; comparison of (e) $\mathrm{W}[F](t; f = f_{max})$ and (f) $\mathrm{W}[F](t = 0; f)$ for the four considered values of ζ_t

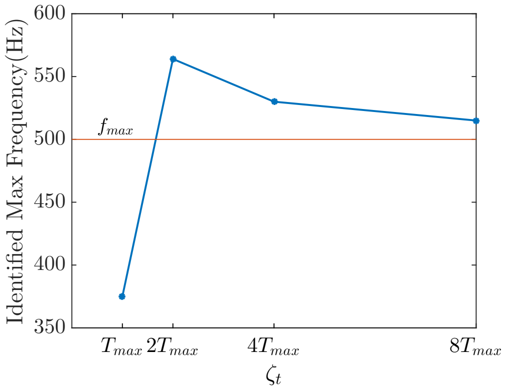

Fig. 3.6 Maximum frequency identified by the numerically calculated Wigner transform depending on the parameter ζ_t increasing

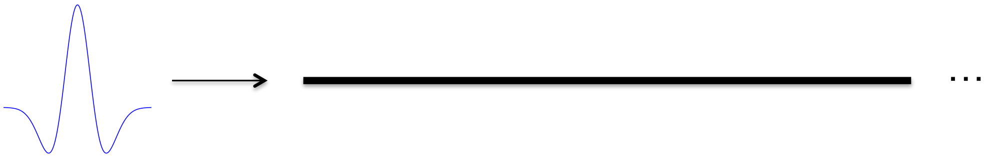

Fig. 3.7 Model in 1D homogeneous media

media		load (ricker)		wave
ρ (kg/m^3)	E_0 (GPa)	T_R (μs)	T_{max} (μs)	λ_{max} (m)
2500	70	15	7.5	0.04

Table 3.1 Numerical parameters of media, load and waves in homogeneous media

In fig. 3.8, Wigner transform of $u(t,x)$ for one point in the vicinity of the wave front ($t_0 = 5.5T_R = 0.083$ ms, $x_0 = 0.4$ m) with three different (ζ_t, ζ_x) is computed numerically. They satisfy $\zeta_t \geq 2T_{max}, \zeta_x \geq 2\lambda_{max}$ according to eq. (3.31). Note that the energy density property eq. (3.7) of Wigner transform:

$$\int_{\left[-\frac{\zeta_t}{2},\frac{\zeta_t}{2}\right]\times\left[-\frac{\zeta_x}{2},\frac{\zeta_x}{2}\right]} \mathrm{W}[u](t_0,x_0;\omega,k)d\omega dk = |u(t_0,x_0)|^2 \tag{3.32}$$

is always verified numerically, independent of the choice of computation region. It can be observed that in phase space, the spatio-temporal Wigner transform gives the energies along the direction of propagation ($\omega = c_0\,|k|$) in all cases.

In 1D homogeneous media, wave displacement is constant along the characteristics $x = \pm c_0 t$. It is known that the Fourier transform of a constant function is a delta dirac function. It means that Wigner transform of wave front should be analytically a dirac function in the direction perpendicular to $\omega = -c_0 k$. However, the numerical computation of Wigner transform along $x = c_0 t$ is realized in a finite region. It can be seen as a Fourier transform for a rectangular function with different widths, so a sinc function is obtained in the direction perpendicular to $\omega = -c_0 k$ in all cases (fig. 3.8d).

Comparing the figures fig. 3.8a to fig. 3.8c, it is shown once again that the parameters $(\zeta_t, \zeta_x) = (8T_{max}, 8\lambda_{max})$ give a higher resolution of Wigner transform. Figure 3.8d gives the value of Wigner transform in the line perpendicular to $\omega = -c_0 k$ across the maximum frequency $k = -k_{max} = -157\text{m}^{-1}$ (black solid line in figs. 3.8a to 3.8c). It can be observed that the main lobe is more and more narrow, i.e. a better concentration, with the increasing of the size of computation region. As the computational cost with this choice is acceptable for our applications, with about 0.08 s for the calculation for one time-space point, thus these parameters are used for all the calculations presented in the section 3.3 and in the chapter 4.

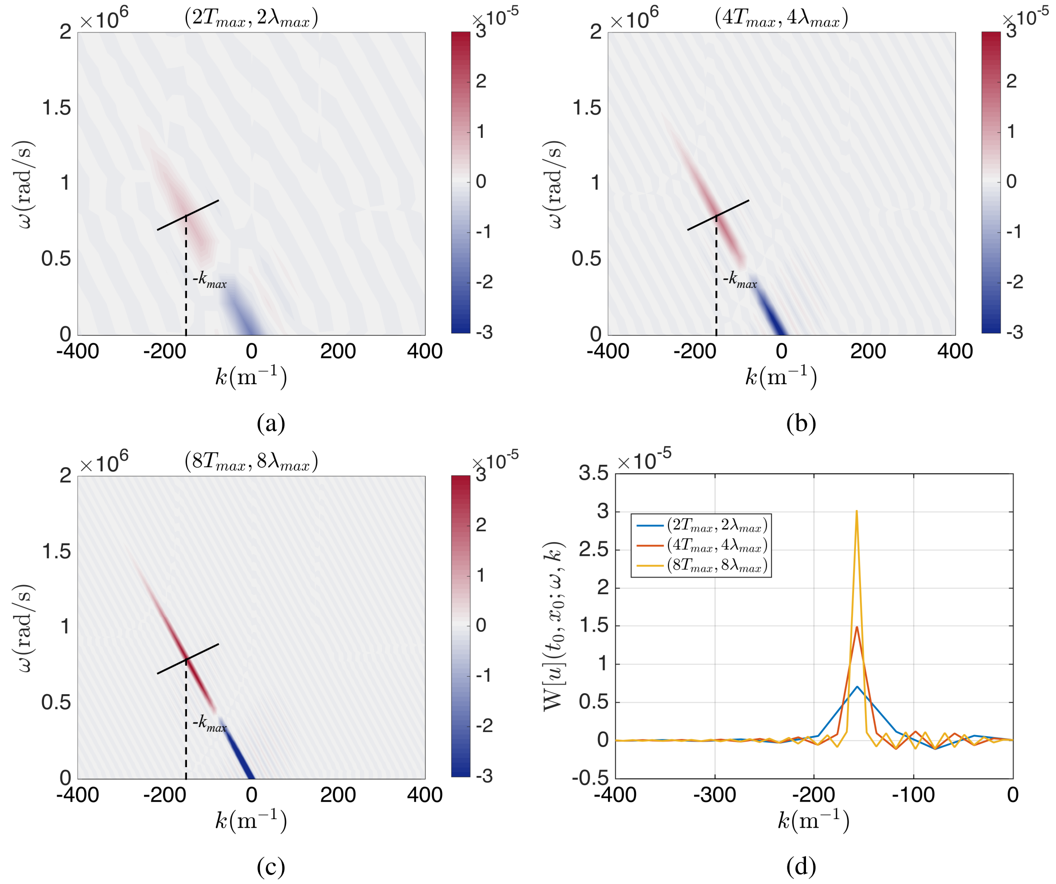

(a) (b)

(c) (d)

Fig. 3.8 $W[u](t,x;\omega,k)$ for (t_0,x_0) at wave front with: (a) $(\zeta_t, \zeta_x) = (2T_{max}, 2\lambda_{max})$, (b) $(\zeta_t, \zeta_x) = (4T_{max}, 4\lambda_{max})$, (c) $(8T_{max}, 8\lambda_{max})$; (d) their value at the line perpendicular to $\omega = -c_0 k$ for the maximum frequency $k = -k_{max}$

3.2 Transport energy-based residual errors of numerical solutions of wave equation

In this section, the transport equation with the scaled Wigner transform is derived in the weak coupling regime, based on the wave equation. It reveals the connection of the wave equation to the energy transport equation in homogeneous media [17, 119]. Then residual-type errors of finite element solutions of the wave equation are defined based on the transport equation in terms of Wigner transform of wave fields.

3.2.1 Transport equation in homogeneous media

The wave equation (1.1) in homogeneous media is considered here with assumption of $\mathbf{f} = \mathbf{0}$. We apply the pseudo-differential calculus for this equation in the following.

$\mathbf{\Gamma}(\varepsilon\nabla_{\mathbf{x}})$ denotes the pseudo-differential operator defined using the same mathematical symbol as the Christoffel operator $\mathbf{\Gamma}(i\varepsilon\mathbf{k})$ (see Appendix C for the definition of the pseudo-differential operator and its symbol). Considering homogeneous and isotropic media, we have:

$$\mathbf{\Gamma}(\hat{\mathbf{k}}) = c_s^2\mathbf{I}_d + (c_p^2 - c_s^2)\hat{\mathbf{k}} \otimes \hat{\mathbf{k}} \tag{3.33}$$

We rescale $t \to t/\varepsilon$ and $x \to x/\varepsilon$ in high frequency limit. Then the wave equation can be expressed as:

$$\big((\varepsilon\partial_t)^2\mathbf{I}_d - \mathbf{\Gamma}(\varepsilon\nabla_{\mathbf{x}})\big) \cdot \mathbf{u}_\varepsilon(t, \mathbf{x}) = \mathbf{0} \tag{3.34}$$

and the cross Wigner transform is applied to this equation and $\mathbf{u}_\varepsilon$:

$$\mathbf{W}_\varepsilon\left[\big((\varepsilon\partial_t)^2\mathbf{I}_d - \mathbf{\Gamma}(\varepsilon\nabla_{\mathbf{x}})\big) \cdot \mathbf{u}_\varepsilon, \mathbf{u}_\varepsilon\right] = \mathbf{0}, \qquad \mathbf{W}_\varepsilon\left[\mathbf{u}_\varepsilon, \big((\varepsilon\partial_t)^2\mathbf{I}_d - \mathbf{\Gamma}(\varepsilon\nabla_{\mathbf{x}})\big) \cdot \mathbf{u}_\varepsilon\right] = \mathbf{0} \tag{3.35}$$

Using the properties of pseudo-differential operators in eq. (C.3), eq. (C.4), and eq. (C.2) by taking $\varphi(\varepsilon\mathrm{D}_t) = (\varepsilon\partial_t)^2$ and $\psi(\varepsilon\mathbf{D}_{\mathbf{x}}) = \mathbf{\Gamma}(\varepsilon\nabla_{\mathbf{x}})$, we obtain:

$$\begin{aligned}
&(i\omega)^2\mathbf{W}_\varepsilon[\mathbf{u}_\varepsilon] + i\varepsilon\omega\partial_t\mathbf{W}_\varepsilon[\mathbf{u}_\varepsilon] = \mathbf{\Gamma}(i\mathbf{k}) \cdot \mathbf{W}_\varepsilon[\mathbf{u}_\varepsilon] - \frac{i\varepsilon}{2}\{\mathbf{\Gamma}(i\mathbf{k}), \mathbf{W}_\varepsilon[\mathbf{u}_\varepsilon]\} + o(\varepsilon^2),\\
&(i\omega)^2\mathbf{W}_\varepsilon[\mathbf{u}_\varepsilon] - i\varepsilon\omega\partial_t\mathbf{W}_\varepsilon[\mathbf{u}_\varepsilon] = \mathbf{W}_\varepsilon[\mathbf{u}_\varepsilon] \cdot \mathbf{\Gamma}((i\mathbf{k}))^{*T} + \frac{i\varepsilon}{2}\left\{\mathbf{W}_\varepsilon[\mathbf{u}_\varepsilon], (\mathbf{\Gamma}(i\mathbf{k}))^{*T}\right\} + o(\varepsilon^2)
\end{aligned} \tag{3.36}$$

where the Poisson bracket is defined by: $\{\mathbf{\Gamma}, \mathbf{W}\} = \nabla_{\mathbf{k}}\mathbf{\Gamma} \cdot \nabla_{\mathbf{x}}\mathbf{W} - \nabla_{\mathbf{x}}\mathbf{\Gamma} \cdot \nabla_{\mathbf{k}}\mathbf{W}$ with the product $\nabla_{\mathbf{k}}\mathbf{\Gamma} \cdot \nabla_{\mathbf{x}}\mathbf{W} := \partial_{k_j}\mathbf{\Gamma} \cdot \partial_{x_j}\mathbf{W}$ (with Einstein summation convention).

The asymptotic expansion of $\mathbf{W}_\varepsilon$ is defined by:

$$\mathbf{W}_\varepsilon := \mathbf{W}^0 + \varepsilon\mathbf{W}^1 + o(\varepsilon^2) \tag{3.37}$$

Note that the 0-order term $\mathbf{W}^0$ is equivalent to the Wigner measure $\mathbf{W}$, as $\mathbf{W}^0 = \lim_{\varepsilon\to 0}\mathbf{W}_\varepsilon$. Introducing eq. (3.37) into eq. (3.36), the leading order $o(\varepsilon^0)$ gives:

$$\left(\omega^2\mathbf{I}_d - \boldsymbol{\Gamma}(\mathbf{k})\right)\mathbf{W}^0 = \mathbf{0} \tag{3.38}$$

Using the eigendecomposition for $\boldsymbol{\Gamma}$ as we did for the Christoffel equation (1.8), it can be found that the non-trivial solutions of eq. (3.38) can be written in the form [17]:

$$\mathbf{W}^0 = \mathrm{W}_p\hat{\mathbf{k}}\otimes\hat{\mathbf{k}} + \mathbf{W}_s = \mathrm{W}_p\hat{\mathbf{k}}\otimes\hat{\mathbf{k}} + \sum_{\alpha,\beta=1,2}\mathrm{W}_{s,\alpha\beta}\hat{\mathbf{k}}_\alpha^\perp\otimes\hat{\mathbf{k}}_\beta^\perp \tag{3.39}$$

and the eigenvalues of the Christoffel tensor:

$$\omega_p^2 = c_p^2\,|\mathbf{k}|^2, \quad \text{or} \quad \omega_s^2 = c_s^2\,|\mathbf{k}|^2 \tag{3.40}$$

In eq. (3.39), $\mathbf{W}^0$ is decomposed into P-mode (associated to the eigenvalue ω_p and the eigenvector $\hat{\mathbf{k}}$) and S-mode (associated to the multiple eigenvalue ω_s and the eigenvectors $\{\hat{\mathbf{k}}_1^\perp,\hat{\mathbf{k}}_2^\perp\}$). W_p is a scalar function and $\mathbf{W}_s$ is a 2×2 matrix (two modes for S-wave) in 3D media. Thus the multiply-scattered wave energy in an elastic medium may be characterized by four parameters, one for the longitudinal wave and three for the transverse wave (according to the symmetry property of Wigner transform, only three coefficients of $\mathbf{W}_s$ are independent).

Now by subtracting the two equations in eq. (3.36) and inserting eq. (3.37), the order $o(\varepsilon)$ of the obtained equation gives:

$$2\omega\partial_t\mathbf{W}^0 = \frac{1}{2}\left(\left\{\boldsymbol{\Gamma}(\mathbf{k}),\mathbf{W}^0\right\} - \left\{\mathbf{W}^0,\boldsymbol{\Gamma}(\mathbf{k})\right\}\right) \tag{3.41}$$

We multiply the above equation on the left and the right by $\hat{\mathbf{k}}$ for mode P and by $\hat{\mathbf{k}}^\perp$ for mode S, and recall that the identity matrix $\mathbf{I}_d = \hat{\mathbf{k}}\otimes\hat{\mathbf{k}} + \mathbf{I}^\perp = \hat{\mathbf{k}}\otimes\hat{\mathbf{k}} + \hat{\mathbf{k}}_1^\perp\otimes\hat{\mathbf{k}}_1^\perp + \hat{\mathbf{k}}_2^\perp\otimes\hat{\mathbf{k}}_2^\perp$. Its right-hand side reads:

$$\begin{cases} \hat{\mathbf{k}}\cdot\left(\left\{\boldsymbol{\Gamma}(\mathbf{k}),\mathbf{W}^0\right\} + \left\{\mathbf{W}^0,\boldsymbol{\Gamma}(\mathbf{k})\right\}\right)\cdot\hat{\mathbf{k}} & = \hat{\mathbf{k}}\cdot\left\{\boldsymbol{\Gamma}(\mathbf{k})\cdot\mathbf{I}_d,\mathbf{W}^0\right\}\cdot\hat{\mathbf{k}} - \hat{\mathbf{k}}\cdot\left\{\mathbf{W}^0,\mathbf{I}_d\cdot\boldsymbol{\Gamma}(\mathbf{k})\right\}\cdot\hat{\mathbf{k}} \\ & = \left\{\omega_p^2,\mathrm{W}_p\right\} - \left\{\mathrm{W}_p,\omega_p^2\right\} \\ & = 2\nabla_{\mathbf{k}}\omega_p^2\cdot\nabla_{\mathbf{x}}\mathrm{W}_p \\ \mathbf{I}^\perp\cdot\left(\left\{\boldsymbol{\Gamma}(\mathbf{k}),\mathbf{W}^0\right\} + \left\{\mathbf{W}^0,\boldsymbol{\Gamma}(\mathbf{k})\right\}\right)\cdot\mathbf{I}^\perp & = \mathbf{I}^\perp\cdot\left\{\boldsymbol{\Gamma}(\mathbf{k})\cdot\mathbf{I}_d,\mathbf{W}^0\right\}\cdot\mathbf{I}^\perp - \mathbf{I}^\perp\cdot\left\{\mathbf{W}^0,\mathbf{I}_d\cdot\boldsymbol{\Gamma}(\mathbf{k})\right\}\cdot\mathbf{I}^\perp \\ & = \left\{\omega_s^2,\mathbf{W}_s\right\} - \left\{\mathbf{W}_s,\omega_s^2\right\} \\ & = 2\nabla_{\mathbf{k}}\omega_s^2\cdot\nabla_{\mathbf{x}}\mathbf{W}_s \end{cases} \tag{3.42}$$

Then introducing eq. (3.42) into eq. (3.41) and using the definition of ω_p and ω_s, the following equations for mode P and S can be found:

$$\begin{cases} \omega\partial_t\mathrm{W}_p[\mathbf{u}_\varepsilon] - c_p^2\mathbf{k}\cdot\nabla_{\mathbf{x}}\mathrm{W}_p[\mathbf{u}_\varepsilon] = 0 \\ \omega\partial_t\mathbf{W}_s[\mathbf{u}_\varepsilon] - c_s^2\mathbf{k}\cdot\nabla_{\mathbf{x}}\mathbf{W}_s[\mathbf{u}_\varepsilon] = \mathbf{0} \end{cases} \tag{3.43}$$

We recall that $\mathbf{k}\cdot\nabla_{\mathbf{x}}$ is the operator of the directional derivative along $\mathbf{k}$. According to eq. (3.40), for example in the case of P-waves, we have $\omega_p = \pm c_p\,|\mathbf{k}|$. Considering that ω is physically always positive and using the symmetry about zero of Wigner transform in phase space, we define $\omega > 0$ and $\pm\mathbf{k}$ that represent the two directions "±". Thus $\mathrm{W}_p[\mathbf{u}_\varepsilon]$ can be projected into these two directions by:

$$\mathrm{W}_p[\mathbf{u}_\varepsilon](t,\mathbf{x};\omega,\mathbf{k}) = \mathrm{W}_p^{+}[\mathbf{u}_\varepsilon](t,\mathbf{x};-\mathbf{k})\delta(\omega - c_p(-\mathbf{k}\cdot\hat{\mathbf{k}})) + \mathrm{W}_p^{-}[\mathbf{u}_\varepsilon](t,\mathbf{x};\mathbf{k})\delta(\omega - c_p(\mathbf{k}\cdot\hat{\mathbf{k}})) \quad (3.44)$$

This shows that the forward wave intensity W_p^{+} propagates in the direction $-\hat{\mathbf{k}}$ and the backward wave intensity W_p^{-} propagates in the direction $\hat{\mathbf{k}}$ in phase space. Note that this definition is consistent with the numerical example in the section 3.1.4. In fig. 3.8, it is noticed that Wigner transform of forward waves $(t, x = c_p t > 0)$ in 1D media takes value with slope of $-c_p$ in phase space (for $k < 0, \omega = -c_p k > 0$). In fact, it is a result of exponential terms $e^{j(\tau\omega + yk)}$ in the definition of Wigner transform, which differs with the common definition of harmonic forward-going plane waves $e^{j(\tau\omega - yk)}$. However, it does not affect the analysis of results. We keep this traditional definition of Wigner transform and use this convention of sign for $(\omega,\mathbf{k})$ in eq. (3.44) in the following. All analysis and definitions above are applied similarly for S-wave.

Introducing eq. (3.44) into eq. (3.43) (note that $\mathbf{k}$ in eq. (3.43) should be changed to $-\mathbf{k}$ for W_p^{+} and $\mathbf{W}_s^{+}$ according to our choice of sign), it can be decomposed into:

$$\begin{cases} \partial_t \mathrm{W}_p^{\pm}[\mathbf{u}_\varepsilon] \pm c_p \hat{\mathbf{k}}\cdot\nabla_{\mathbf{x}} \mathrm{W}_p^{\pm}[\mathbf{u}_\varepsilon] = 0 \\ \partial_t \mathbf{W}_s^{\pm}[\mathbf{u}_\varepsilon] \pm c_s \hat{\mathbf{k}}\cdot\nabla_{\mathbf{x}} \mathbf{W}_s^{\pm}[\mathbf{u}_\varepsilon] = \mathbf{0} \end{cases} \quad (3.45)$$

which are the transport equations for P and S-wave in homogeneous media, subjected to some initial conditions and boundary conditions.

The general solutions of eq. (3.45) for harmonic waves can be expressed as:

$$\begin{cases} \mathrm{W}_p^{\pm}(t,\mathbf{x};\mp\mathbf{k}) = \mathrm{A}_p(\hat{\mathbf{k}}\cdot\mathbf{x} \mp c_p t) \\ \mathbf{W}_s^{\pm}(t,\mathbf{x};\mp\mathbf{k}) = \mathbf{A}_s(\hat{\mathbf{k}}\cdot\mathbf{x} \mp c_s t) \end{cases} \quad (3.46)$$

In the time-space domain $(t,\mathbf{x})$, general solutions of P-wave displacement in homogeneous media $\partial_t^2\mathbf{u} - c_p^2\nabla_{\mathbf{x}}^2\mathbf{u} = 0$ can be expressed as:

$$\mathbf{u}_p(t,\mathbf{x}) = \mathbf{F}(\hat{\mathbf{k}}\cdot\mathbf{x} - c_p t) + \mathbf{G}(\hat{\mathbf{k}}\cdot\mathbf{x} + c_p t) \quad (3.47)$$

where $\mathbf{F}$ and $\mathbf{G}$ are arbitrary functions of their argument. It has two components that represent respectively the propagation of wave fronts in the forward and backward directions. It can be remarked that the energy density W_p (eq. (3.46)) has the same arguments in the time-space domain. Considering the Wigner transform of $\mathbf{u}_p(t,\mathbf{x})$, according to eq. (3.10), it has two auto-terms related to energy density of two directions $\mathrm{W}_p^{\pm}$ in eq. (3.46) and one cross term that vanishes in the weak sense when $\varepsilon \to 0$. The same can be said of the S-wave. In the phase space $(\omega,\mathbf{k})$, Wigner measure presents the relation of dispersion along the characteristics in eq. (3.44), that is verified numerically by the example in fig. 3.8 of section 3.1.4.

3.2.2 Theoretical residual errors based on transport equation

We assume that $\mathbf{u}_{h\Delta t}$ is a finite element solution of the wave equation (1.1) in the high frequency limit. The numerical errors related to $\mathbf{u}_{h\Delta t}$ are evaluated based on transport equations eq. (3.45) in terms of energy quantities of wave fields, i.e. the projections of Wigner transform of $\mathbf{u}_{h\Delta t}$. In the following, its projection on mode P is denoted by $\mathrm{W}_p[\mathbf{u}_{h\Delta t}] = \hat{\mathbf{k}} \cdot \mathrm{W}_\varepsilon[\mathbf{u}_{h\Delta t}] \cdot \hat{\mathbf{k}}$ and on mode S by $\mathbf{W}_s[\mathbf{u}_{h\Delta t}] = \mathbf{I}^\perp \cdot \mathbf{W}_\varepsilon[\mathbf{u}_{h\Delta t}] \cdot \mathbf{I}^\perp$.

Definition 3.8. Residual errors based on transport equations (3.45) are defined as:

$$\begin{cases} \mathrm{R}_p^\pm[\mathbf{u}_{h\Delta t}](t,\mathbf{x};\omega,\mathbf{k}) := \partial_t \mathrm{W}_p^\pm[\mathbf{u}_{h\Delta t}](t,\mathbf{x};\omega,\mathbf{k}) \pm c_p \hat{\mathbf{k}}_p \cdot \nabla_\mathbf{x} \mathrm{W}_p^\pm[\mathbf{u}_{h\Delta t}](t,\mathbf{x};\omega,\mathbf{k}) \\ \mathbf{R}_s^\pm[\mathbf{u}_{h\Delta t}](t,\mathbf{x};\omega,\mathbf{k}) := \partial_t \mathbf{W}_s^\pm[\mathbf{u}_{h\Delta t}](t,\mathbf{x};\omega,\mathbf{k}) \pm c_s \hat{\mathbf{k}}_s \cdot \nabla_\mathbf{x} \mathbf{W}_s^\pm[\mathbf{u}_{h\Delta t}](t,\mathbf{x};\omega,\mathbf{k}) \end{cases} \tag{3.48}$$

Furthermore, it can be demonstrated that eq. (3.48) can be transformed into the following theorem.

Theorem 3.9. The local residual error maps in $(t,\mathbf{x};\omega,\mathbf{k})$ domain can be obtained by:

$$\begin{cases} \mathrm{R}_p^\pm[\mathbf{u}_{h\Delta t}] = \left(\mathrm{W}_p^\pm[\mathbf{v}_{h\Delta t},\mathbf{u}_{h\Delta t}] + \left(\mathrm{W}_p^\pm[\mathbf{v}_{h\Delta t},\mathbf{u}_{h\Delta t}]\right)^{*T}\right) \pm c_p \left(\mathrm{W}_p^\pm[\hat{\mathbf{k}}_p \cdot \nabla_\mathbf{x}\mathbf{u}_{h\Delta t},\mathbf{u}_{h\Delta t}] + \left(\mathrm{W}_p^\pm[\hat{\mathbf{k}}_p \cdot \nabla_\mathbf{x}\mathbf{u}_{h\Delta t},\mathbf{u}_{h\Delta t}]\right)^{*T}\right) \\ \mathbf{R}_s^\pm[\mathbf{u}_{h\Delta t}] = \left(\mathbf{W}_s^\pm[\mathbf{v}_{h\Delta t},\mathbf{u}_{h\Delta t}] + \left(\mathbf{W}_s^\pm[\mathbf{v}_{h\Delta t},\mathbf{u}_{h\Delta t}]\right)^{*T}\right) \pm c_s \left(\mathbf{W}_s^\pm[\hat{\mathbf{k}}_s \cdot \nabla_\mathbf{x}\mathbf{u}_{h\Delta t},\mathbf{u}_{h\Delta t}] + \left(\mathbf{W}_s^\pm[\hat{\mathbf{k}}_s \cdot \nabla_\mathbf{x}\mathbf{u}_{h\Delta t},\mathbf{u}_{h\Delta t}]\right)^{*T}\right) \end{cases} \tag{3.49}$$

Proof. Using lemma 3.4. □

Errors defined with eq. (3.49) is more interesting than eq. (3.48) because it emphasizes the importance of the correlations of the displacement with the velocity and the directional derivative along the wave vector of the displacement. Numerically, it avoids the computation of the time derivatives by finite difference, when numerical velocities are already obtained at each time step.

Considering that the local errors $\mathrm{R}^\pm[\mathbf{u}_{h\Delta t}](t,\mathbf{x};\omega,\mathbf{k})$ depend on four parameters and using the energy properties of Wigner transform (eq. (3.7)), we propose two new error quantities in an energy norm:

$$\bar{\mathrm{R}}[\mathbf{u}_{h\Delta t}](\omega,\mathbf{k}) := \int_{\mathbb{R}\times\mathbb{R}^d} \sum_\alpha \mathrm{tr}\left\{\left|\mathrm{R}_\alpha^+[\mathbf{u}_{h\Delta t}](t,\mathbf{x};\omega,\mathbf{k})\right| + \left|\mathrm{R}_\alpha^-[\mathbf{u}_{h\Delta t}](t,\mathbf{x};\omega,\mathbf{k})\right|\right\} dt d\mathbf{x} \tag{3.50}$$

and

$$\tilde{\mathrm{R}}[\mathbf{u}_{h\Delta t}](t,\mathbf{x}) := \int_{\mathbb{R}\times\mathbb{R}^d} \sum_\alpha \mathrm{tr}\left\{\left|\mathrm{R}_\alpha^+[\mathbf{u}_{h\Delta t}](t,\mathbf{x};\omega,\mathbf{k})\right| + \left|\mathrm{R}_\alpha^-[\mathbf{u}_{h\Delta t}](t,\mathbf{x};\omega,\mathbf{k})\right|\right\} d\omega d\mathbf{k} \tag{3.51}$$

where $\alpha = P,S$ stands for different modes. Taking into account that the existence of cross terms disturbs the distribution of energy in terms of frequency, the second definition $\tilde{\mathrm{R}}(t,\mathbf{x})$ is used and computed in this work.

3.3 Numerical application for wave propagation in a 1D homogeneous medium

In this section, we analyze numerically the defined residual errors eq. (3.54) and eq. (3.55) in a 1D case.

We firstly rewrite the transport equation and the residual errors in 1D media for clarity and simplification of some notations. In this case, only P-wave propagates with constant velocity c_0 and the subscript p can be neglected. The transport equation eq. (3.45) reads:

$$\partial_t \mathrm{W}^{\pm}[u_\varepsilon] \pm c_0 \partial_x \mathrm{W}^{\pm}[u_\varepsilon] = 0 \tag{3.52a}$$

Recall that $\mathrm{W}^{\pm}$ with the convention of sign defined in eq. (3.44) can be written as:

$$\mathrm{W}^{+}[u_\varepsilon] := \mathrm{W}[u_\varepsilon](t,x;\omega = -c_0 k > 0, k < 0), \quad \mathrm{W}^{-}[u_\varepsilon] := \mathrm{W}[u_\varepsilon](t,x;\omega = c_0 k > 0, k > 0) \tag{3.53}$$

The residual error maps in 1D are obtained with eq. (3.49) and eq. (3.51), namely:

$$\mathrm{R}^{\pm}[u_{h\Delta t}](t,x;\omega,k) := 2\mathrm{Re}\left(\mathrm{W}^{\pm}_{\varepsilon}[v_{h\Delta t}, u_{h\Delta t}](t,x;\omega,k)\right) \pm 2c_0 \mathrm{Re}\left(\mathrm{W}^{\pm}_{\varepsilon}[\varepsilon_{h\Delta t}, u_{h\Delta t}](t,x;\omega,k)\right) \tag{3.54}$$

and

$$\tilde{\mathrm{R}}[u_{h\Delta t}](t,x) := \int_{\mathbb{R}\times\mathbb{R}} \left\{ \left|\mathrm{R}^{+}[u_{h\Delta t}](t,x;\omega,k)\right| + \left|\mathrm{R}^{-}[u_{h\Delta t}](t,x;\omega,k)\right| \right\} d\omega dk \tag{3.55}$$

where $v_{h\Delta t}$ and $\varepsilon_{h\Delta t}$ stand for respectively the numerical velocity and strain fields.

Now we consider here the same 1D wave propagation model as the one defined in the section 3.1.4 (fig. 3.7). All the physical parameters are defined already in the table 3.1 except that here we consider a bar with a finite length $L = 1$ m so wave front propagates a round trip in a time period $T_f = 0.4$ ms. The left end is subjected to the Neumann conditions with the ricker signal and the right end to the free boundary condition.

The exact solutions of the wave displacement in the time-space domain are obtained analytically and illustrated in fig. 3.9. Note that the Wigner transform of the exact solutions is calculated numerically.

In order to analyze the evolution of residual errors with refinement, three numerical finite element solutions are computed with different mesh sizes h and time steps Δt shown in the table 3.2. Note that they all satisfy the sampling condition in eq. (3.27): $\frac{1}{\Delta t} \geq 4 f_c$, with f_c the cutoff frequency of the ricker signal, which can be chosen equal to $3 f_{max}$.

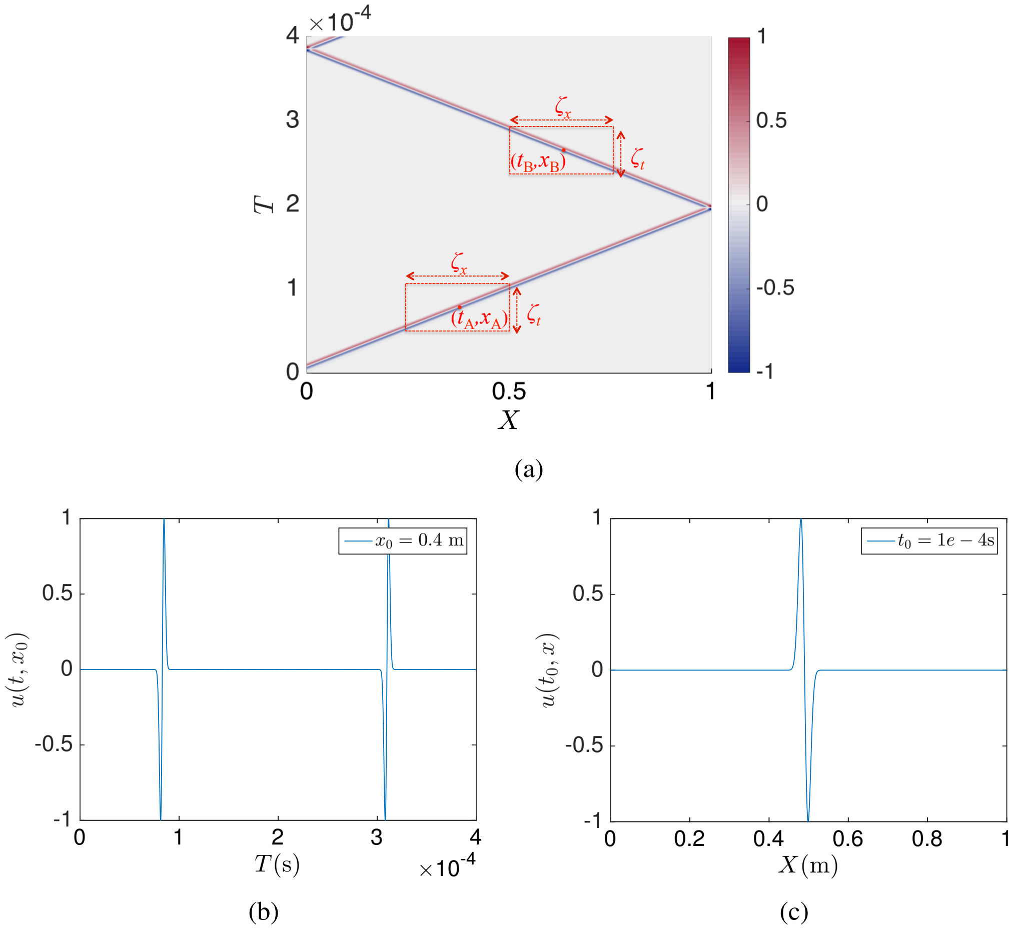

(a)

(b)

(c)

Fig. 3.9 Wave displacement: (a) $u(t,x)$ in the whole computed time-space domain (with two computation regions for Wigner transform at two points A (t_A, x_A) and B (t_B, x_B)), (b) $u(t,x_0)$ for $x_0 = 0.4$ m, (c) $u(t_0,x)$ for $t_0 = 0.1$ ms

	h (mm)	Δt (μs)	$\lambda(f_c = 3f_{max})/h$
1	3.125	0.5	4
2	1.25	0.2	10
3	0.625	0.1	20

Table 3.2 Parameters for finite element solutions of wave equation, h: mesh size, Δt: time step, $\lambda(f_c)/h$: number of elements in the shortest wavelength of interest corresponding to the cutoff frequency

3.3.1 Residual errors in phase space for different refinements of finite element solutions

We choose firstly two representative points: point A ($t = 0.083$ ms, $x = 0.4$ m) at the centre of wave front in the forward path (for W^+) and point B ($t = 0.27$ ms, $x = 0.6$ m) in the return path (for W^-) (fig. 3.9a), and then the residual errors defined in eq. (3.49) in phase space are respectively computed.

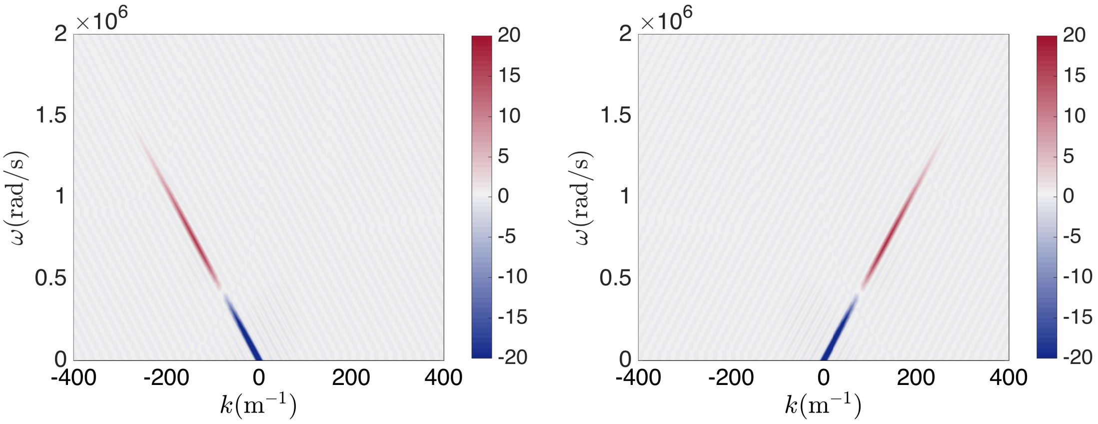

(a)

(b)

Fig. 3.10 Numerical computation of $W_\varepsilon[u_{h\Delta t}](t,x;\omega,k)$ in phase space for a given time-space point: (a) point A, (b) point B

Figure 3.10 gives the results of Wigner transform for the two considered time-space points A and B, numerically calculated with $(\zeta_t, \zeta_x) = (8T_{max}, 8\lambda_{max}) = (0.06\text{ms}, 0.32\text{ m})$ for the FE numerical wave solutions obtained with $h = 0.625$ mm, $\Delta t = 0.1$ μs. It is observed that the Wigner transform takes values along respectively the two characteristic lines of the dispersion relation $\omega = \mp c_0 k$.

Now we compute the residual errors $R^\pm[u_{h\Delta t}](t_0, x_0; \omega, k)$ in phase space in eq. (3.49) for different time-space refinements.

Figure 3.11 give local residual errors distributed in phase space for the points A and B with different numerical solutions. It can be found the tendency of decreasing of errors with increasing refinement. Errors at point B are generally larger that at point A for same size of refinement due to the increase of errors with time.

Generally, the maximum of the estimated errors is located around k_{max} (we ignore the maximum at $k = 0$ where all the cross terms between positive/negative frequencies overlap). In the case $\lambda(f_c)/h = 4$ for point B (the top figure in fig. 3.11b), it is observed that the frequency band is much shorter than other cases and the maximum of errors is approximatively located at $k_{max}/2$. In fact, it can be remarked in fig. 3.12 (more evident in fig. 3.12b) significant errors related to the numerical diffusion of numerical solutions with the time discontinuous Galerkin method used here. It includes the dissipation (associated to the amplitude error) and the dispersion (associated to the phase error).

These effects, depending on mesh size and the size of the time step, increase with time. Consequently, for the coarse refinement ($\lambda(f_c)/h = 4$ here), the quality of estimated errors cannot be ensured. Errors can be underestimated (fig. 3.13b). More studies on diffusion properties of DG or other numerical methods for the wave equation can be found in [5, 74, 136].

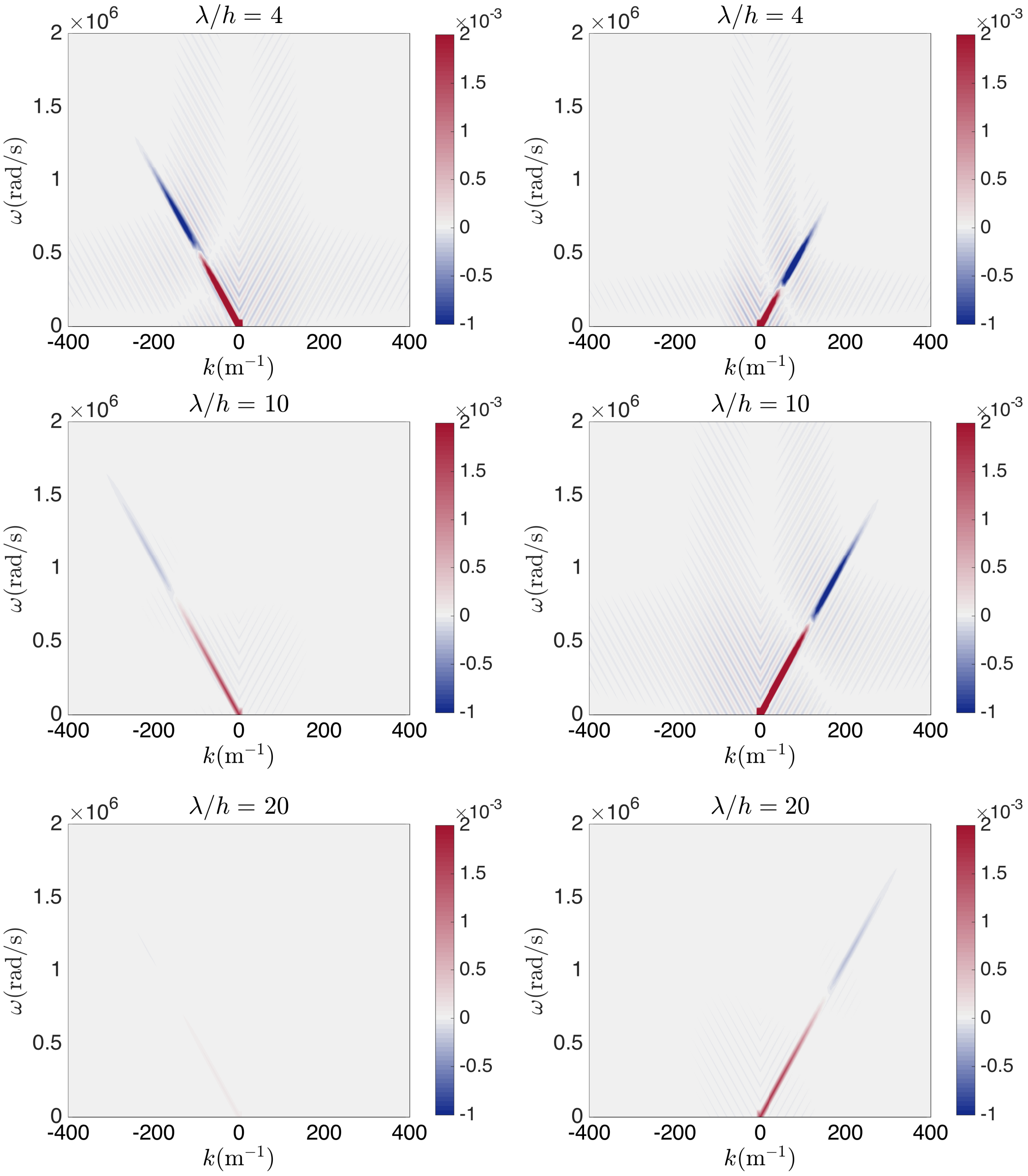

(a)

(b)

Fig. 3.11 (a) $R^{\pm}$ for point A in phase space for different refinements; (b) $R^{\pm}$ for point B in phase space for different refinements

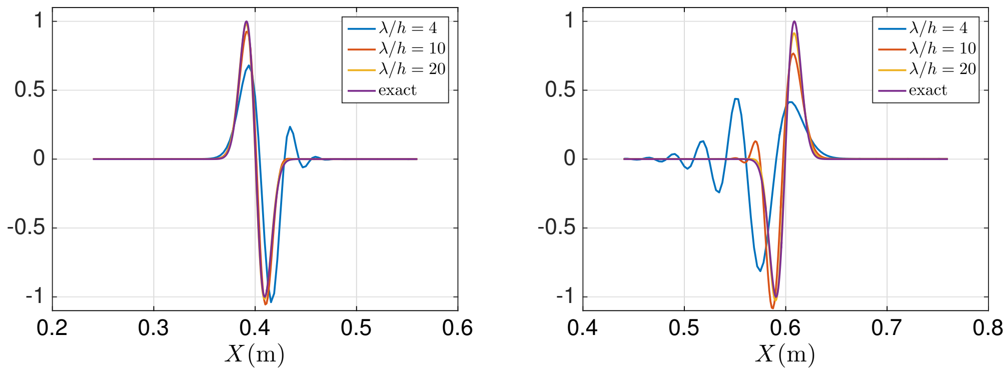

(a) (b)

Fig. 3.12 Wave displacement for different refinements: (a) $u(t_A,:)$, (b) $u(t_B,:)$

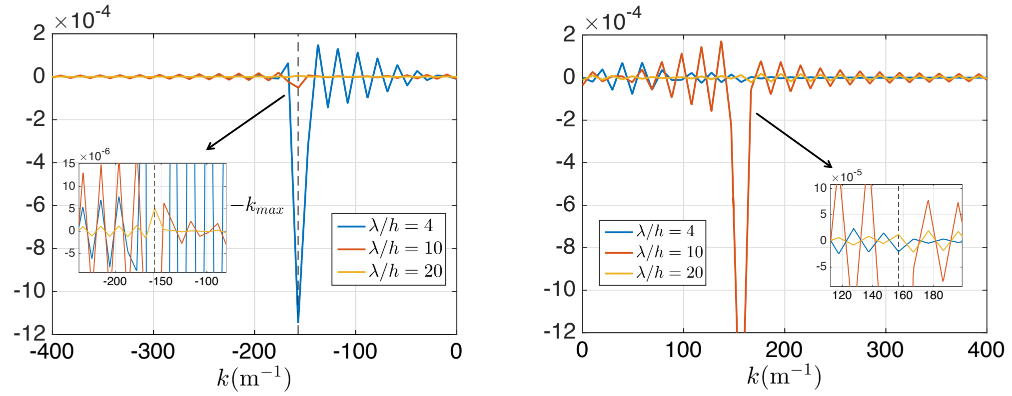

(a) (b)

Fig. 3.13 (a) $\mathrm{R}^{\pm}$ for point A, interpolated on the line perpendicular to $\omega = -c_0 k$ across the $k = -k_{max}$; (b) $\mathrm{R}^{\pm}$ for point B, interpolated on the line perpendicular to $\omega = c_0 k$ across the $k = k_{max}$

Some noticeable fluctuations are also found along $\omega = \mp c_0 k$ (most remarkable for $\lambda(f_c)/h = 4$). At the bottom of fig. 3.13, we give respectively the interpolation of the previous three plots on the line perpendicular to $\omega = \mp c_0 k$ across the $k = \mp k_{max}$ for point A and B. For point A, in the case of $\lambda(f_c)/h = 4$, it is observed that these fluctuations are small compared to the relatively large errors in $\omega = c_0 k$. In the case of $\lambda(f_c)/h = 20$, fluctuations and errors become more comparable. These fluctuations are resulting from "spectral leakage". In simple terms, DFT (so does DWT) for the sampled signal is repeated periodically; if some glitches or discontinuities exist in the boundaries of the chosen computation region, a leakage of frequency will arise. Leakage causes the signal levels to be reduced and redistributed over a broad frequency range. For exact solutions of wave propagation in homogeneous media, if we compute its Wigner transform along the direction of propagation $x = \pm c_0 t$, it can be seen as a constant continuous function. No leakage happens. For numerical solutions, discontinuities always exist and we cannot find a method that allows removing totally these fluctuations. Increasing the size of computation region is one of methods to reduce them. That is also an explanation for choosing a large $(\zeta_t, \zeta_x) = (8T_{max}, 8\lambda_{max})$. A detailed discussion about this phenomenon can be found in appendix B.

3.3.2 Residual errors in time-space for different refinements of finite element solutions

Considering the numerical fluctuations found in last section, $\mathrm{R}(t,x;\omega,k)$ is filtered with a window function and then we compute errors in the time-space domain $\tilde{\mathrm{R}}(t,x)$ defined in eq. (3.55), i.e.

$$\tilde{\mathrm{R}}(t,x) := \int_{\mathbb{R}\times\mathbb{R}} \left|\mathrm{R}^{\pm}(t,x;\omega,k)\right| h_R(\omega,k) d\omega dk \tag{3.56}$$

where $h_R(\omega,k)$ is a window function defined in phase space, which allows the filtering of fluctuations according to our choice. Considering here that the integral area of errors should be only around $\omega = \pm c_0 k$ so we choose naturally a rectangular window defined with the rotational coordinate (it can be also found in Appendix F for a more detailed definition of this new coordinate):

$$\tilde{h}_R(k_\perp, k_\parallel) = h_R(\omega,k) = \mathrm{rect}(k_\perp)\mathrm{rect}(k_\parallel) \qquad \text{with} \quad \begin{cases} k_\perp = \dfrac{\frac{\omega}{c_0} - k}{\sqrt{2}} \\ k_\parallel = \dfrac{\frac{\omega}{c_0} + k}{\sqrt{2}} \end{cases} \tag{3.57}$$

For forward waves (point A, fig. 3.14), the length of $\tilde{h}_R$ along $k_\perp$ is from zero to the cutoff frequency: $k_\perp \in [-3\sqrt{2}k_{max}, 0]$. Its width in $k_\parallel$ direction is carefully chosen as $\zeta_\parallel = 2\sqrt{2}\Delta k$ (recall that Δk is frequency resolution). This width covers at least the main lobe of Wigner transform in this direction. It allows to contain the residual errors along the characteristic line but not too much fluctuations. Indeed, as we discussed in the section 3.1.3, the DWT can be seen as DFT of a rectangular function with period of $\sqrt{(c_0\zeta_t)^2 + \zeta_x^2} = \sqrt{2}\zeta_x$ in the $(c_0 t, x)$-plane along $x = c_0 t$ (t axis is rescaled to $c_0 t$) in homogeneous media, so the width of main lobe is equal to $\frac{2}{\sqrt{2}\zeta_x} = 2\sqrt{2}\Delta k$. For backward waves, errors are distributed in the first quadrant, thus $k_\perp \in [0, 3\sqrt{2}k_{max}]$.

Figure 3.14 illustrates the effect of window function on residual errors for forward waves (for $\lambda/h = 4$ in fig. 3.11a).

Now residual errors are computed for all points (t,x) so we get a time-space maps of errors. Note that the boundaries are neglected since in the present work the chosen calculation domain of Wigner transform and the validity of the transport equation are only considered in the bulk of the medium. In fig. 3.15, the convergence of errors with decreasing mesh size is illustrated. It can be also found in fig. 3.15d that the integral of errors over space is increasing with time (more evident for the coarsest mesh).

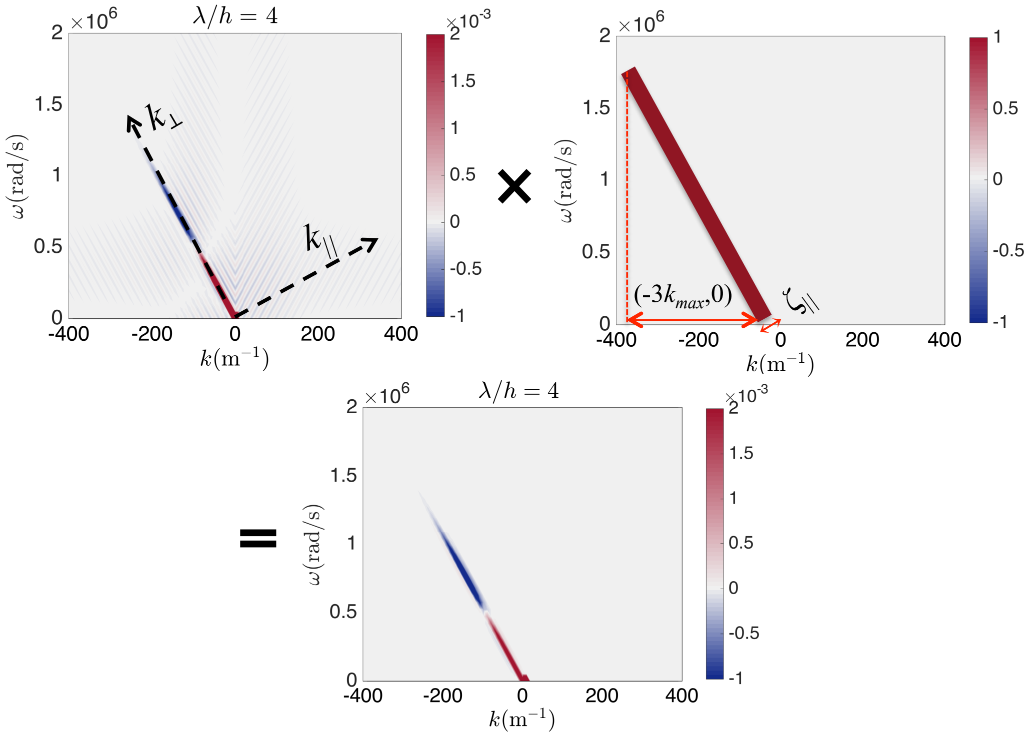

Fig. 3.14 Filtering for residual errors in phase space

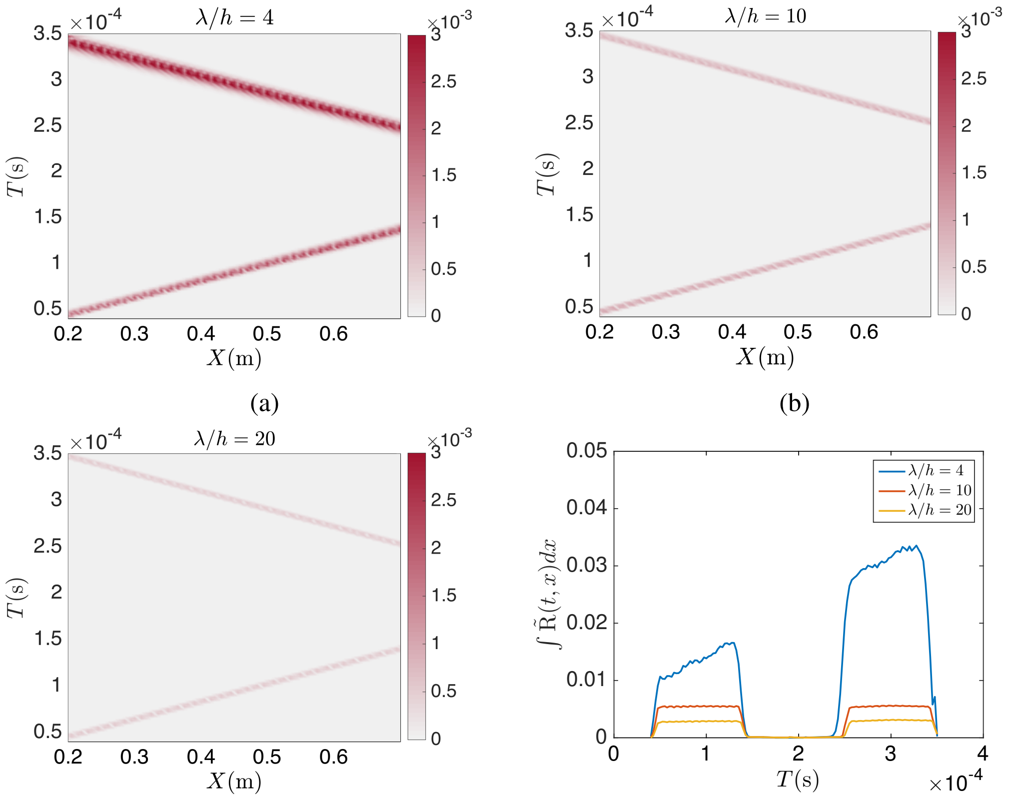

(a) (b)

(c) (d)

Fig. 3.15 $\tilde{\mathrm{R}}(t,x)/\sum\tilde{\mathrm{R}}$ for numerical solutions with different mesh size and time step: (a) $\lambda/h=4$, (b) $\lambda/h=10$, (c) $\lambda/h=20$, (d) $\int_{x\in[0.2,0.7]}\tilde{\mathrm{R}}(t,x)dx$

To understand more clearly, we compare values of all $\tilde{R}(t,x)$ for a certain position x_0 or a certain moment t_0 in one plot. In fig. 3.16, it is observed that the residual errors defined in eq. (3.55) are decreasing with smaller mesh size as we expected. Two errors for exact solutions are given (discretized both with respect to the finest refinement $\lambda/h = 20$): one is computed in coordinates (t,x), another is along the direction of propagation. As we mentioned in last section, Wigner transform of the latter has no leakage. Thus it is noticed in fig. 3.16 that it has much smaller value than the former case and other numerical solutions. It means that the window function h_R allows reducing the fluctuations but it cannot remove totally the effect of frequency leakage. We can conclude that errors resulting from leakage of frequency are very important in numerical computations of Wigner transform but it does not influence the evaluation of errors with refinement here.

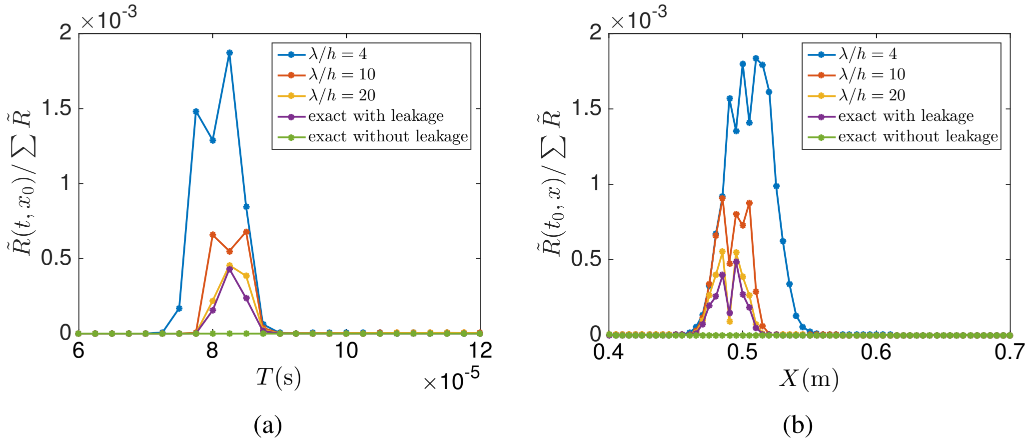

Fig. 3.16 Comparison of residual errors between numerical solutions and exact solutions: (a) $\tilde{R}(t,x_0)$ for $x_0 = 0.4$ m, (b) $\tilde{R}(t_0,x)$ for $t_0 = 0.1$ ms

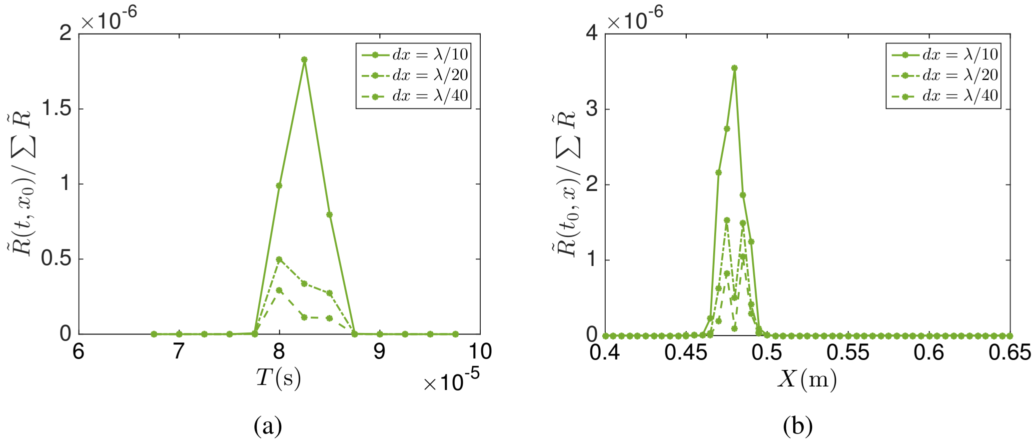

Fig. 3.17 Comparison of residual errors between three exact solutions with different discretizations: (a) $\tilde{\mathrm{R}}(t,x_0)$ for $x_0 = 0.4$ m, (b) $\tilde{\mathrm{R}}(t_0,x)$ for $t_0 = 0.1$ ms

Finally, for only exact solutions without leakage in FFT, sources of residual errors in numerical computations can be considered mainly as the discretization in the time-space domain of analytical equations. Indeed, errors of exact solutions with different sizes of discretization can be also computed and compared in fig. 3.17. We find that they are much smaller than errors in fig. 3.16 so they can be neglected.

3.4 Conclusion

In this chapter, we presented the transport equation which describes the energy transport for HF wave propagation in homogeneous media, derived by the scaled spatio-temporal Wigner transform. The properties of cross terms in Wigner transform were analyzed and discussed in detail. For numerical computations of Wigner transform, an important study of parameters, i.e. the size of computation region in time and in space for discrete Wigner transform was determined in function of signal frequency considering the frequency resolution. Then the energy-based residual errors of the wave equation with the transport equation were proposed analytically. A numerical application of these results is realized in a 1D homogeneous medium. The errors were computed for approximate solutions with different mesh sizes and we compare all these results in the time-space domain. We observed that with increasing number of degrees of freedom, the defined residual errors are decreasing as we expected, which allows validating our tools of error estimator.

Chapter 4

Energy-based *a posteriori* error estimation for high frequency wave equation in heterogeneous media

Contents

This chapter deals with high frequency wave propagation problems in heterogeneous media. Compared to the transport equation in chapter 3, a more general and complicated radiative transfer equation is studied. It is derived from the wave equation in the same way as we did in the section 3.2.1. It describes not only the transport of energy, but also the scattering of energy by heterogeneities, with the effects of coupling between different polarization modes. After a long propagation time, we find the mean amplitude of waves decreases with the distance travelled, since the coherent or mean wave energy is converted to incoherent fluctuations. Considering the difficulties and high computational costs of analyzing errors for highly oscillating wave fields in these media, we propose here to quantify errors of finite element solutions of the wave equation in terms of energy quantities governed by this new equation.

In the section 4.1, we start with the introduction of random media, which is used to model the heterogeneities, and the radiative transfer equation in these media. Then the analytical solutions of the radiative transfer equation in 1D media are obtained. The related propagation phenomena characterized by the scattering mean free length, are discussed. A numerical example of wave propagation in a 1D medium is presented and the localization phenomenon is discussed.

In the section 4.2, the energy-based residual errors of wave fields using the radiative transfer equation are defined analytically and computed numerically for FE wave solutions obtained in 1D heterogeneous media.

In the section 4.3, a filtering of the obtained residual errors with window functions is proposed, which allows smoothing Wigner transform and reducing the influence of cross terms. Its numerical application is presented and analyzed.

Finally, in the section 4.4, the energy-based residual errors of numerical wave solutions obtained with two different refinements are compared.

4.1 Radiative transfer equation in heterogeneous media in the weak coupling limit

In this section, we present the radiative transfer equation in heterogeneous media and the related phenomena. Firstly, the heterogeneities of media are described by a random model of mechanical properties. Then the scaled spatio-temporal Wigner transform defined in the chapter 3 is used for the derivation of the radiative transfer equation in heterogenous media. Some important characteristic lengths and propagation phenomena are discussed in the end.

4.1.1 Statistical description of weak randomly-fluctuating media

As we introduced in the section 1.2.4, we consider the high frequency wave propagation in the weak coupling limit. The physical properties of weakly heterogeneous media are assumed in the form:

$$\mathbf{C}(\mathbf{x}) = \mathbf{C}_0(\mathbf{x}) + \sqrt{\varepsilon}\mathbf{C}_1\left(\frac{\mathbf{x}}{\varepsilon}\right) \tag{4.1}$$

Here $\rho(\mathbf{x})$ is assumed slowly varying so only the elastic tensor is assumed to vary rapidly.

The slowly varying part $\mathbf{C}_0(\mathbf{x})$ satisfies:

$$\mathbf{C}_0(\mathbf{x}) = \mathbb{E}\left[\mathbf{C}(\mathbf{x})\right] \tag{4.2}$$

where $\mathbb{E}[\cdot]$ denotes mathematical expectation or ensemble average.

The fast fluctuating part $\mathbf{C}_1(\mathbf{y})$, with $\mathbf{y} = \frac{\mathbf{x}}{\varepsilon}$, is considered as a statistically homogeneous mean zero random field with unit-variance in the $\mathbf{y}$ variable. The standard deviation of $\mathbf{C}$ is given by the mean square of the fractional fluctuations $\sqrt{\varepsilon}$ before $\mathbf{C}_1$. This size is the unique scaling which allows significantly modifying the energy spreading in the transport regime at a long propagation distance. Indeed, if the random fluctuations are too weak they will not affect significantly energy transport (although strong interactions between waves and media exist in this case with $l_c \approx \lambda$), and too large fluctuations will lead to the localization of wave energy in media where the radiative transfer theory cannot be applied [125]. Note that the period of the fluctuations of the properties is of order ε, as the characteristic length over which the material fluctuates. This model allows an asymptotic analysis of wave propagation problems.

A random medium can be seen as an ensemble of heterogeneous media, called realizations. Each realization differs from another in the detailed spatial structure of fluctuations, but they have some common statistical properties, such as mean value, variance or standard deviation, and covariance function.

Definition 4.1. For any statistically homogeneous random field $\mathbf{U}$, its covariance function $\mathbf{P}(\mathbf{r})$ and power spectral density $\widehat{\mathbf{P}}(\mathbf{k})$ (Fourier transform of covariance function) are respectively defined by:

$$\begin{aligned} \mathbf{P}(\mathbf{r}) &= \mathbf{P}(\mathbf{y}-\mathbf{z}) = \mathbb{E}\left[\mathbf{U}(\mathbf{y}) \otimes \mathbf{U}(\mathbf{z})\right], \\ \widehat{\mathbf{P}}(\mathbf{k}) &= \int_{\mathbb{R}^d} \mathbf{P}(\mathbf{z}) e^{-i\mathbf{z}\cdot\mathbf{k}} d\mathbf{z} \end{aligned} \tag{4.3}$$

With the definition of $\widehat{\mathbf{P}}(\mathbf{k})$, we have:

$$(2\pi)^d \delta(\mathbf{p}+\mathbf{q})\widehat{\mathbf{P}}(\mathbf{p}) = \mathbb{E}\left[\widehat{\mathbf{U}}(\mathbf{p}) \otimes \widehat{\mathbf{U}}(\mathbf{q})\right] \tag{4.4}$$

The covariance function is a statistical measure of the spatial correlation and the magnitude of the fluctuations in the medium. When a medium is isotropic, the covariance function depends only on the lag distance $r = |\mathbf{y}-\mathbf{z}|$. Three covariance functions are given here as examples: the sinc^2, the exponential and the gaussian functions. These three functions and their corresponding power spectral densities are given in the table 4.1 and illustrated in fig. 4.2. Here "sinc" stands for the unnormalized cardinal sine function $\frac{\sin(x)}{x}$ and "tri" stands for the scaled triangular function defined by $\mathrm{tri}(k/a) := \begin{cases} 1-|k|/a & |k| \le a \\ 0 & \text{otherwise} \end{cases}$.

type	covariance function	power spectral density
sinc^2	$P(r) = \sigma^2 \mathrm{sinc}^2(\pi r/l_c)$	$\widehat{P}(k) = \sigma^2 l_c \mathrm{tri}(k l_c/2)$
exp	$P(r) = \sigma^2 e^{-2r/l_c}$	$\widehat{P}(k) = \frac{1}{\pi}\sigma^2 l_c \frac{1}{(1+k^2 l_c^2/4)^2}$
gauss	$P(r) = \sigma^2 e^{-\pi r^2/l_c^2}$	$\widehat{P}(k) = \frac{1}{\pi}\sigma^2 l_c e^{-k^2 l_c^2/(4\pi)}$

Table 4.1 Examples of covariance function and power spectral density ($P(0) = \sigma^2$)

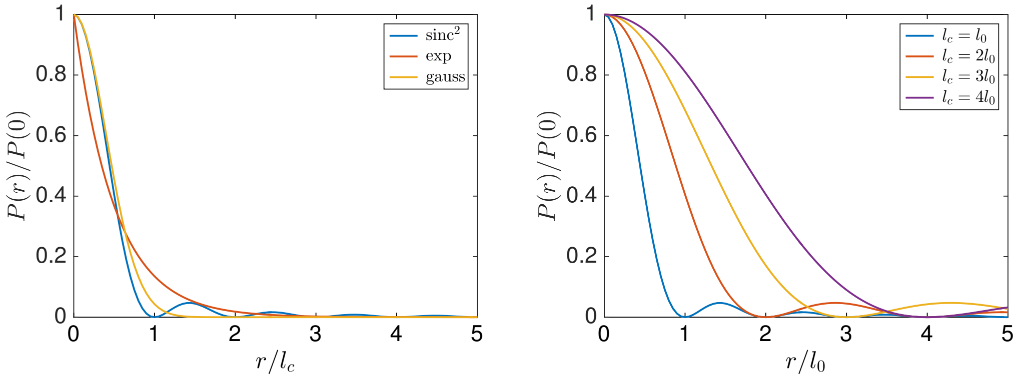

(a) (b)

Fig. 4.1 (a) normalized sinc^2, exponential and gaussian covariance functions, (b) sinc^2 function with different correlation lengths

It can be seen that the covariance function $P(r)$ depends on two parameters: the variance σ^2 and the correlation length l_c. Here l_c is defined so that it satisfies:

$$l_c = 2\int_0^\infty \frac{P(r)}{\sigma^2} dr \tag{4.5}$$

Different definitions for l_c can be found in the literature [41, 127]. Physically, the correlation length l_c refers to an order of magnitude of the distance beyond which the values of the random field are almost uncorrelated.

Briefly, a random medium realization is obtained by the filtering of a white noise. This white noise is filtered with the square root of the power spectral density of the required covariance function in the wave number domain. The inverse Fourier transform provides the fluctuating field which is superposed on the slowly fluctuating background. Figure 4.2 gives one realization of numerical 2D random fields with spectra $\hat{P}(k_x,k_y) = \sigma^2 l_c^2 \mathrm{tri}(k_x l_c/2)\mathrm{tri}(k_y l_c/2)$ by spectral approaches [128, 129]. The influence of the correlation length on media can be observed.

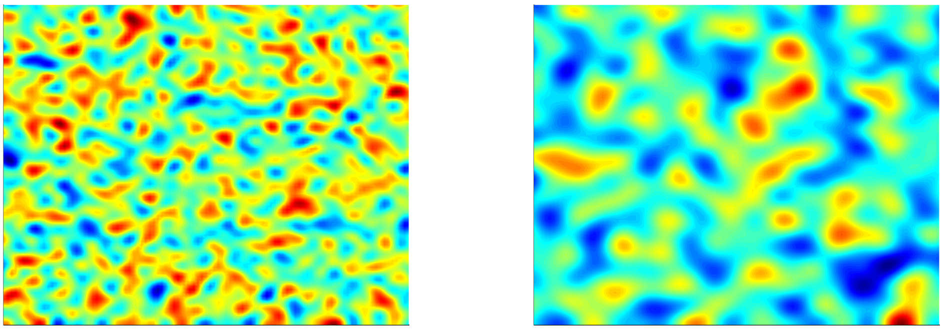

(a) (b)

Fig. 4.2 One realization of 2D random media generated by the covariance function sinc^2 with different correlation lengths: (a) $l_c = l_0$, (b) $l_c = 2l_0$

4.1.2 Radiative transfer equation

In this section, the radiative transfer equation is derived, which describes the high frequency wave propagation in random media in the weak coupling limit. It provides a description of the evolution of wave energy in phase space in terms of the Wigner measure.

We present hereafter only the main steps taken in the derivation of the radiative transfer equation. More details can be found in [17, 25, 119]. The main idea is the same as the derivation of the transport equation presented in the section 3.2.1. However, a special attention should be paid for the new order $\sqrt{\varepsilon}$ in the asymptotic expansion of the Wigner measure, resulting from the magnitude of fast fluctuations of random media defined in eq. (4.1). Besides, the transport equation can be seen as a particular case of the radiative transfer equation by removing the fast fluctuations of media.

First of all, we can also write the rescaled wave equation in the high frequency limit as we did in eq. (3.34):

$$\left((\varepsilon\partial_t)^2\mathbf{I}_d - \mathbf{\Gamma}(\mathbf{x};\varepsilon\nabla_{\mathbf{x}})\right)\cdot\mathbf{u}_\varepsilon(t,\mathbf{x}) = \mathbf{0} \tag{4.6}$$

In the case of heterogeneous media, $\mathbf{\Gamma}$ depends on $\mathbf{x}$. However, we still present the case of isotropy for simplicity. According to the randomly fluctuating elasticity tensor defined by eq. (4.1), the Christoffel tensor $\mathbf{\Gamma}$ is expanded as:

$$\begin{aligned}\boldsymbol{\Gamma}\cdot\mathbf{u}_\varepsilon = &\underbrace{\rho^{-1}(\mathbf{x})\left(\mathbf{C}_0(\mathbf{x}):(\mathbf{k}\otimes_s\mathbf{u}_\varepsilon)\right)\cdot\mathbf{k}}_{\boldsymbol{\Gamma}_0(\mathbf{x};\mathbf{k})}+\underbrace{\sqrt{\varepsilon}\rho^{-1}(\mathbf{x})\left(\mathbf{C}_1(\mathbf{x}/\varepsilon):(\mathbf{k}\otimes_s\mathbf{u}_\varepsilon)\right)\cdot\mathbf{k}}_{\boldsymbol{\Gamma}_1(\mathbf{x},\mathbf{x}/\varepsilon;\mathbf{k})}\\ &+\underbrace{\varepsilon\rho^{-1}(\mathbf{x})\left(\nabla_{\mathbf{x}}\mathbf{C}_0(\mathbf{x}):(\mathbf{k}\otimes_s\mathbf{u}_\varepsilon)\right)\cdot\mathbf{k}}_{\boldsymbol{\Gamma}_2(\mathbf{x};\mathbf{k})}+o(\varepsilon^{\frac{3}{2}})\end{aligned}\tag{4.7}$$

The following equations hold when the spatio-temporal Wigner transform is applied to the wave equation and the wave field:

$$\mathbf{W}_\varepsilon\left[\left((\varepsilon\partial_t)^2\mathbf{I}_d-\boldsymbol{\Gamma}(\mathbf{x};\varepsilon\nabla_{\mathbf{x}})\right)\cdot\mathbf{u}_\varepsilon,\mathbf{u}_\varepsilon\right]=\mathbf{0},\qquad \mathbf{W}_\varepsilon\left[\mathbf{u}_\varepsilon,\left((\varepsilon\partial_t)^2\mathbf{I}_d-\boldsymbol{\Gamma}(\mathbf{x};\varepsilon\nabla_{\mathbf{x}})\right)\cdot\mathbf{u}_\varepsilon\right]=\mathbf{0}\tag{4.8}$$

A two-scale asymptotic expansion of the Wigner transform for these two equations is defined as:

$$\mathbf{W}_\varepsilon(t,\mathbf{x},\mathbf{x}/\varepsilon;\omega,\mathbf{k})=\mathbf{W}^0(t,\mathbf{x};\omega,\mathbf{k})+\sqrt{\varepsilon}\mathbf{W}^1(t,\mathbf{x},\mathbf{x}/\varepsilon;\omega,\mathbf{k})+\varepsilon\mathbf{W}^2(t,\mathbf{x},\mathbf{x}/\varepsilon;\omega,\mathbf{k})+o(\varepsilon^{\frac{3}{2}})\tag{4.9}$$

Introducing eq. (4.7) and eq. (4.8) into eq. (4.6), all the terms inside the Wigner transform and the Christoffel tensor are developed and expanded. Parameter identification is then applied respectively for the first three orders $o(\varepsilon^0), o(\sqrt{\varepsilon})$ and $o(\varepsilon)$.

The order $o(\varepsilon^0)$ gives:

$$\left(\omega^2\mathbf{I}_d-\boldsymbol{\Gamma}_0(\mathbf{x};\mathbf{k})\right)\cdot\mathbf{W}^0=\mathbf{0}\tag{4.10}$$

In the case of $\boldsymbol{\Gamma}_0(\mathbf{x})$ is independent of $\mathbf{x}$, the same equation as that in homogeneous media (eq. (3.38)) is found. In the general case, we also use the same eigendecomposition of $\mathbf{W}^0$ in the P-mode and the S-mode as eq. (3.39), and the dispersion relation eq. (3.40) with $c_p = c_p(\mathbf{x})$ and $c_s = c_s(\mathbf{x})$.

The order $o(\sqrt{\varepsilon})$ allows deriving the Fourier transform of $\mathbf{W}^1$ with respect to $\mathbf{y}$ and the order $o(\varepsilon)$ gives an equation in terms of $\mathbf{W}^0$ and $\mathbf{W}^1$, while $\mathbf{W}^2$ disappears under an assumption of orthogonality. Note that an ensemble average is applied when we deal with the order $o(\varepsilon)$. The projection of $\mathbf{W}^0$ on a mode α, denoted by $\mathbf{W}_\alpha$ ($\alpha = p,s$), obtained in the radiative transfer equation is in fact $\mathbb{E}[\mathbf{W}_\alpha]$. However, we denote it always by $\mathbf{W}_\alpha$ in the rest of document. Besides, a crucial mixing assumption is applied during the derivation: the average of the leading term $\mathbf{W}^0$ is assumed to depend only on slow space variable $\mathbf{x}$ [17, 119]. It allows us to separate the product of the average of $\mathbf{W}^0$ and the average of fast fluctuating variables since they vary on different scales. Finally combing equations in these two orders and using all these assumptions presented above, the 3D radiative transfer equation for the P-mode and the S-mode is obtained and given in the following:

$$\begin{aligned}&\partial_t \mathrm{W}_p^{\pm}(t,\mathbf{x};\mathbf{k})\pm\left\{\omega_p(\mathbf{x};\mathbf{k}),\mathrm{W}_p^{\pm}(t,\mathbf{x};\mathbf{k})\right\}\\ &\quad=\int_{\omega_p(\mathbf{k})=\omega_p(\mathbf{k}')} s_{pp}(\mathbf{x};\mathbf{k},\mathbf{k}')\mathrm{W}_p^{\pm}(t,\mathbf{x};\mathbf{k}')d\mathbf{k}'-S_{pp}(\mathbf{x};\mathbf{k})\mathrm{W}_p^{\pm}(t,\mathbf{x};\mathbf{k})\\ &\quad+\int_{\omega_p(\mathbf{k})=\omega_s(\mathbf{k}')} s_{ps}(\mathbf{x};\mathbf{k},\mathbf{k}')\ \left(\hat{\mathbf{k}}_{\perp'}\otimes\hat{\mathbf{k}}_{\perp'}\right):\mathbf{W}_s^{\pm}(t,\mathbf{x};\mathbf{k}')\ d\mathbf{k}'-S_{ps}(\mathbf{x};\mathbf{k})\mathrm{W}_p^{\pm}(t,\mathbf{x};\mathbf{k})\end{aligned}\tag{4.11a}$$

$$\begin{aligned}
&\partial_t \mathbf{W}_s^{\pm}(t,\mathbf{x};\mathbf{k}) \pm \left\{\omega_s(\mathbf{x};\mathbf{k}), \mathbf{W}_s^{\pm}(t,\mathbf{x};\mathbf{k})\right\} + \left[\mathbf{N}(\mathbf{x};\mathbf{k}), \mathbf{W}_s^{\pm}(t,\mathbf{x};\mathbf{k})\right] \\
&\quad = \int_{\omega_s(\mathbf{k})=\omega_s(\mathbf{k}')} s_{ss}(\mathbf{x};\mathbf{k},\mathbf{k}')\mathbf{G}(\mathbf{k},\mathbf{k}')\cdot \mathbf{W}_s^{\pm}(t,\mathbf{x};\mathbf{k}')\cdot\left(\mathbf{G}(\mathbf{k},\mathbf{k}')\right)^T d\mathbf{k}' - S_{ss}(\mathbf{x};\mathbf{k})\mathbf{W}_s^{\pm}(t,\mathbf{x};\mathbf{k}) \\
&\quad\quad + \int_{\omega_s(\mathbf{k})=\omega_p(\mathbf{k}')} s_{sp}(\mathbf{x};\mathbf{k},\mathbf{k}')\hat{\mathbf{k}}'_{\perp}\otimes\hat{\mathbf{k}}'_{\perp}\mathrm{W}_p^{\pm}(t,\mathbf{x};\mathbf{k}')d\mathbf{k}' - S_{sp}(\mathbf{x};\mathbf{k})\mathbf{W}_s^{\pm}(t,\mathbf{x};\mathbf{k})
\end{aligned} \tag{4.11b}$$

with

$$\mathbf{G}(\mathbf{k},\mathbf{k}') = (\hat{\mathbf{k}}\cdot\hat{\mathbf{k}}')\hat{\mathbf{k}}_i^{\perp}\otimes\hat{\mathbf{k}}_{i,\perp'}^{\perp} + \hat{\mathbf{k}}'_{\perp}\otimes\hat{\mathbf{k}}_{\perp'}, \quad i=1,2 \text{ (with Einstein summation convention)} \tag{4.12}$$

$$S_{\alpha\beta}(\mathbf{x};\mathbf{k}) = \int_{\omega_\alpha(\mathbf{k})=\omega_\beta(\mathbf{k}')} s_{\alpha\beta}(\mathbf{x};\mathbf{k},\mathbf{k}')d\mathbf{k}', \quad \alpha,\beta = p,s \tag{4.13}$$

Recall that $(\hat{\mathbf{k}},\hat{\mathbf{k}}_1^{\perp},\hat{\mathbf{k}}_2^{\perp})$ forms an orthonormal triplet. In the eqs. (4.11) and (4.12), the subscripts $\perp$ and $\perp'$ denote respectively the projection into the plane perpendicular to $\hat{\mathbf{k}}$ and to $\hat{\mathbf{k}}'$. It means:

$$\hat{\mathbf{k}}_{\perp'} = \hat{\mathbf{k}} - (\hat{\mathbf{k}}\cdot\hat{\mathbf{k}}')\hat{\mathbf{k}}', \quad \hat{\mathbf{k}'}_{\perp} = \hat{\mathbf{k}}' - (\hat{\mathbf{k}}'\cdot\hat{\mathbf{k}})\hat{\mathbf{k}}, \quad \hat{\mathbf{k}}_{i,\perp'}^{\perp} = \hat{\mathbf{k}}_i^{\perp} - (\hat{\mathbf{k}}_i^{\perp}\cdot\hat{\mathbf{k}}')\hat{\mathbf{k}}' \tag{4.14}$$

$[\mathbf{A},\mathbf{B}] := \mathbf{AB}-\mathbf{BA}$ stands for the Lie bracket. The matrix $\mathbf{N}(\mathbf{x};\mathbf{k})$ in eq. (4.11b) leads to the coupling of elements of the matrix $\mathbf{W}_s$. It is related to the slow variations of the background $\mathbf{C}_0$ (in proportion to $\frac{\partial c_s}{\partial x_j}$) and vanishes in homogeneous media. $s_{\alpha\beta}(\mathbf{x};\mathbf{k},\mathbf{k}')$ is the differential scattering cross-section for the mode $\alpha-\beta$ scattering, namely the rate of conversion of energy at $\mathbf{x}$ from the mode α with wave number $\mathbf{k}'$ into the mode β with wave number $\mathbf{k}'$. It is associated to the fast fluctuations of media. $S_{\alpha\beta}(\mathbf{x};\mathbf{k})$ is the total scattering cross-section. For simplicity, in order to avoid the multiple S-mode in 3D media, the formula of differential scattering cross-sections in 2D isotropic media are given here. Results for 3D or anisotropic media can be found in [25]. The elasticity tensor $\mathbf{C}(\mathbf{x})$ is determined by two Lamé's coefficients λ and μ in the same form with eq. (4.1):

$$\lambda(\mathbf{x}) = \lambda_0(\mathbf{x}) + \sqrt{\varepsilon}\lambda_1\left(\frac{\mathbf{x}}{\varepsilon}\right), \qquad \mu(\mathbf{x}) = \mu_0(\mathbf{x}) + \sqrt{\varepsilon}\mu_1\left(\frac{\mathbf{x}}{\varepsilon}\right) \tag{4.15}$$

The differential scattering cross-sections are given by :

$$\begin{aligned}
s_{pp}(\mathbf{x};\mathbf{k},\mathbf{k}') = \frac{c_p(\mathbf{x})\,|\mathbf{k}|^2}{4}\Bigg\{ &\frac{(c_p^2(\mathbf{x})-2c_s^2(\mathbf{x}))^2}{c_p^4(\mathbf{x})}\widehat{P}_{\lambda\lambda}(\mathbf{k}-\mathbf{k}') + \frac{4c_s^2(\mathbf{x})(c_p^2(\mathbf{x})-2c_s^2(\mathbf{x}))}{c_p^4(\mathbf{x})}(\hat{\mathbf{k}}\cdot\hat{\mathbf{k}}')^2\widehat{P}_{\lambda\mu}(\mathbf{k}-\mathbf{k}') \\
&+ \frac{4c_s^2(\mathbf{x})}{c_p^4(\mathbf{x})}(\hat{\mathbf{k}}\cdot\hat{\mathbf{k}}')^4\widehat{P}_{\mu\mu}(\mathbf{k}-\mathbf{k}')\Bigg\}
\end{aligned} \tag{4.16}$$

$$s_{ps}(\mathbf{x};\mathbf{k},\mathbf{k}') = \frac{c_s(\mathbf{x})\,|\mathbf{k}|^2}{4}\left\{4(\hat{\mathbf{k}}\cdot\hat{\mathbf{k}}')^2\widehat{P}_{\mu\mu}(\mathbf{k}-\mathbf{k}')\right\} \tag{4.17}$$

$$s_{ss}(\mathbf{x};\mathbf{k},\mathbf{k}') = \frac{c_s(\mathbf{x})\,|\mathbf{k}|^2}{4}\widehat{P}_{\mu\mu}(\mathbf{k}-\mathbf{k}') \tag{4.18}$$

$$s_{sp}(\mathbf{x};\mathbf{k},\mathbf{k}') = \frac{c_s(\mathbf{x})\,|\mathbf{k}'|^2}{4}\left\{4(\hat{\mathbf{k}}\cdot\hat{\mathbf{k}}')^2\widehat{P}_{\mu\mu}(\mathbf{k}-\mathbf{k}')\right\} \tag{4.19}$$

where $\widehat{P}_{\lambda\lambda}, \widehat{P}_{\mu\mu}, \widehat{P}_{\lambda\mu}$ are the power spectral densities of the fast fluctuations of corresponding subscript. For example, $\widehat{P}_{\lambda\mu}$ is defined by (variance $\sigma^2 = \varepsilon$):

$$(2\pi)^2\delta(\mathbf{p}+\mathbf{q})\widehat{P}_{\lambda\mu}(\mathbf{p}) = \varepsilon\mathbb{E}\left[\widehat{\lambda}_1(\mathbf{p})\widehat{\mu}_1(\mathbf{q})\right] \tag{4.20}$$

Equation (4.16) implies that the fast variations $\mathbf{C}_1$ contribute to the right-hand side of the radiative transfer equation only through the power spectral densities of its elasticity parameters.

Compared with the transport equation in homogeneous media (3.45), in the radiative transfer equations eq. (4.11) we have two additional terms on the left-hand side (transport of waves), $\{\omega_\alpha, \mathbf{W}_\alpha^\pm\}$ ($\alpha = p, s$) and $[\mathbf{N}, \mathbf{W}_s^\pm]$, resulting from slow variations $\mathbf{C}_0$, and two additional terms on the right-hand side (scattering of waves), resulting from fast variations $\mathbf{C}_1$.

Now the particular case of 1D heterogenous media with only fast fluctuations, is discussed. We assume that ρ and E_0 are constant, the heterogeneity in eq. (4.1) becomes:

$$E(x) = E_0 + \sqrt{\varepsilon}E_1\left(\frac{x}{\varepsilon}\right) \tag{4.21}$$

The only mode in 1D is a P-mode with velocity $c_0 = \sqrt{\frac{E_0}{\rho}}$, the radiative transfer equation eq. (4.11) becomes (the subscript α for mode P is removed hereafter for simplicity):

$$\partial_t \mathrm{W}^\pm(t,x;k) \pm c_0\partial_x \mathrm{W}^\pm(t,x;k) = \int_{|k|=|k'|} s(k,k')\mathrm{W}^\pm(t,x;k')dk' - S(k)\mathrm{W}^\pm(t,x;k) \tag{4.22}$$

The differential scattering cross-section $s(k,k')$ (4.16) and the total scattering cross-section $S(k)$ (4.13) are:

$$s(k,k') = \frac{c_0k^2}{4}\widehat{P}(k-k'), \qquad S(k) = \int_{|k|=|k'|} s(k,k')dk' \tag{4.23}$$

where $\widehat{P}(k)$ denotes $\widehat{P}_{E_1E_1}(k)$, i.e. the power spectral density for E_1. As a matter of fact, in 1D media only two directions of propagation exist, thus $k' = k$ or $k' = -k$. $s(k,k')$ in eq. (4.23) reads:

$$s(k,k') = \begin{cases} \frac{c_0k^2}{4}\widehat{P}(0), & k' = k \\ \frac{c_0k^2}{4}\widehat{P}(2k), & k' = -k \end{cases}, \quad S(k) = \frac{c_0k^2}{4}\widehat{P}(0) + \frac{c_0k^2}{4}\widehat{P}(2k) \tag{4.24}$$

Thus the scattering part in eq. (4.22) becomes:

$$\begin{aligned} &\int_{|k|=|k'|} s(k,k')\mathrm{W}^\pm(t,x;k')dk' - S(k)\mathrm{W}^\pm(t,x;k) \\ =&\left(\frac{c_0k^2}{4}\widehat{P}(0)\mathrm{W}^\pm(t,x;k) + \frac{c_0k^2}{4}\widehat{P}(2k)\mathrm{W}^\pm(t,x;-k)\right) - \left(\frac{c_0k^2}{4}\widehat{P}(0) + \frac{c_0k^2}{4}\widehat{P}(2k)\right)\mathrm{W}^\pm(t,x;k) \\ =&\frac{c_0k^2}{4}\widehat{P}(2k)\mathrm{W}^\pm(t,x;-k) - \frac{c_0k^2}{4}\widehat{P}(2k)\mathrm{W}^\pm(t,x;k) \end{aligned} \tag{4.25}$$

where the two terms related to $s(k,k)$ cancel each other out. Indeed, waves are scattered only in the direction opposite to their propagation direction.

Substituting eq. (4.25) into eq. (4.22) and using the convention defined by eq. (3.53), we get the 1D radiative transfer equations:

$$\begin{cases} \partial_t \mathrm{W}^+(t,x;-k) + c_0\partial_x \mathrm{W}^+(t,x;-k) = \frac{c_0 k^2}{4}\widehat{P}(2k)\left\{\mathrm{W}^-(t,x;k) - \mathrm{W}^+(t,x;-k)\right\} \\ \partial_t \mathrm{W}^-(t,x;k) - c_0\partial_x \mathrm{W}^-(t,x;k) = \frac{c_0 k^2}{4}\widehat{P}(2k)\left\{\mathrm{W}^+(t,x;-k) - \mathrm{W}^-(t,x;k)\right\} \end{cases} \tag{4.26}$$

Two new quantities emerge from adding and subtracting equations in eq. (4.26):

$$\begin{aligned} \mathrm{W}^{\mathrm{s}}(t,x;k) &= \mathrm{W}^+(t,x;-k) + \mathrm{W}^-(t,x;k), \\ \mathrm{W}^{\mathrm{d}}(t,x;k) &= \mathrm{W}^+(t,x;-k) - \mathrm{W}^-(t,x;k) \end{aligned} \tag{4.27}$$

where W^{s} and W^{d} can be interpreted as the total energy density and the net forward-going density with respect to the propagation direction $\frac{k}{|k|}\mathbf{e}_x$:

$$\begin{cases} \partial_t \mathrm{W}^{\mathrm{s}} + c_0\partial_x \mathrm{W}^{\mathrm{d}} = 0 \\ \partial_t \mathrm{W}^{\mathrm{d}} + c_0\partial_x \mathrm{W}^{\mathrm{s}} = -\frac{c_0 k^2}{2}\widehat{P}(2k)\mathrm{W}^{\mathrm{d}} \end{cases} \tag{4.28}$$

Equation (4.28) is equivalent to eq. (4.26).

Furthermore, by taking respectively the spatial and temporal derivatives of the second equation in eq. (4.28):

$$\begin{cases} \frac{\partial^2 \mathrm{W}^{\mathrm{d}}}{\partial x \partial t} + c_0\partial_x^2 \mathrm{W}^{\mathrm{s}} = -\frac{c_0 k^2}{2}\widehat{P}(2k)\partial_x \mathrm{W}^{\mathrm{d}} \\ \partial_t^2 \mathrm{W}^{\mathrm{d}} + c_0\frac{\partial^2 \mathrm{W}^{\mathrm{s}}}{\partial t \partial x} = -\frac{c_0 k^2}{2}\widehat{P}(2k)\partial_t \mathrm{W}^{\mathrm{d}} \end{cases} \tag{4.29}$$

and introducing the first equation of eq. (4.28) in eq. (4.29), we get:

$$\begin{cases} \partial_t^2 \mathrm{W}^{\mathrm{s}} - c_0^2\partial_x^2 \mathrm{W}^{\mathrm{s}} = -\frac{c_0 k^2}{2}\widehat{P}(2k)\partial_t \mathrm{W}^{\mathrm{s}} \\ \partial_t^2 \mathrm{W}^{\mathrm{d}} - c_0^2\partial_x^2 \mathrm{W}^{\mathrm{d}} = -\frac{c_0 k^2}{2}\widehat{P}(2k)\partial_t \mathrm{W}^{\mathrm{d}} \end{cases} \tag{4.30}$$

Two separate partial differential equations for W^{s} and W^{d} are obtained. If we consider a medium with no scattering, a same form as the traditional 1D wave equation is obtained in terms of W^{s} or W^{d}. For a given frequency k, eq. (4.30) can be seen as "damped" wave equations with a friction coefficient $\frac{c_0^2 k^2}{2}\widehat{P}(2k) > 0$. It is known that the general solutions of the damped wave equation have an exponential decay over time with the coefficient e^{-Ct} ($C > 0$ constant) [37, 67, 96]. The difference between wave energies in two opposite directions decreases quickly with time due to the conversion of energy in these two directions and the sum of energies in two directions decreases at the same rate as they spread out in space with the increase of time.

4.1.3 Scattering mean free path

In this section, an important characteristic length called the scattering mean free path l_s for the radiative transfer regime is presented. The analytical solutions of the radiative transfer equation in 1D media are given firstly. Then we give the definition of l_s and discuss its influence on this regime.

Let us assume two initial conditions for eq. (4.26) defined by

$$\mathrm{W}^+(t=0,x;-k)=\mathrm{W}_0^+(x;-k),\qquad \mathrm{W}^-(t=0,x;k)=\mathrm{W}_0^-(x;k) \tag{4.31}$$

Equation (4.26) can be seen as the telegraph equation for a given wave number k. Thus its analytical solutions for a given k can be found in the following [65, 73, 147]:

$$\begin{cases} \mathrm{W}^+(t,x;-k)=\mathrm{W}_0^+(x-c_0t)e^{-\frac{c_0}{l_s}t}+\int_{x-c_0t}^{x+c_0t}\kappa(t,x,y)\mathrm{W}_0^-(y)dy+\int_{x-c_0t}^{x+c_0t}\kappa_+(t,x,y)\mathrm{W}_0^+(y)dy \\ \mathrm{W}^-(t,x;k)=\mathrm{W}_0^-(x-c_0t)e^{-\frac{c_0}{l_s}t}+\int_{x-c_0t}^{x+c_0t}\kappa(t,x,y)\mathrm{W}_0^+(y)dy+\int_{x-c_0t}^{x+c_0t}\kappa_-(t,x,y)\mathrm{W}_0^-(y)dy \end{cases} \tag{4.32}$$

with:

$$\begin{aligned} l_s(k)&=\frac{4}{k^2\widehat{P}(2k)},\\ \kappa(t,x,y)&=\frac{e^{-\frac{c_0}{l_s}t}}{2l_s}I_0\left(\frac{\sqrt{c_0^2t^2-(y-x)^2)}}{l_s}\right),\\ \kappa_\pm(t,x,y)&=\frac{e^{-\frac{c_0}{l_s}t}}{2l_s}I_1\left(\frac{\sqrt{c_0^2t^2-(y-x)^2)}}{l_s}\right)\frac{c_0t\mp(y-x)}{\sqrt{c_0^2t^2-(y-x)^2}}, \end{aligned} \tag{4.33}$$

where I_0 and I_1 are respectively the zero-order and the first-order modified Bessel functions of the first kind [57].

In fact, the first term of the two solutions in (4.32) represents the original coherent wave supplied by initial conditions, which decays exponentially with c_0t over a characteristic length scale l_s. Thus l_s is the so called mean free path for scattering. It measures the distance of the exponential decrease of the energy density of coherent waves due to scatterings or successive interactions with the underlying medium. Roughly speaking, the second and the third terms in (4.32) with the modified Bessel functions describe the energy of incoherent waves which does not propagate ballistically. The second term results from the scattering of the original coherent waves in the opposite direction. The last term results form the conversion of coherent waves in the same direction when the coherent waves in the first term decrease.

When cumulative scatterings become significant during the propagation, the coherent energy becomes negligibly small. The incoherent energy dominates the field. W^+ and W^- tend to a local equipartition between each other [73]:

$$\mathrm{W}^{+} \approx \mathrm{W}^{-} \approx \frac{e^{-\frac{x^2}{2l_s c_0 t}}}{2\sqrt{2\pi l_s c_0 t}} \tag{4.34}$$

An example of analytical solutions for a single frequency wave is given here so as to illustrate the analysis above, with initial conditions defined by:

$$\mathrm{W}_0^{+}(x;k) = 200\delta(x)\delta(k+k_0)\ \mathrm{m}^3\mathrm{s}, \qquad \mathrm{W}_0^{-}(x;k) = 100\delta(x)\delta(k-k_0)\ \mathrm{m}^3\mathrm{s} \tag{4.35}$$

where parameters are given by: $k_0 = 157\ \mathrm{m}^{-1}$, $c_0 = 4$ km/s. Thus $l_s = 3.46$ m and the sinc^2 function is chosen as the power spectral density.

Figure 4.3a and fig. 4.3b give results of $\mathrm{W}^{\pm}$ in the time-space domain. It can be observed the exponential decay over propagation time-distance along $x = \pm c_0 t$ (red line). More precisely, fig. 4.3c and fig. 4.3d give their natural logarithmic values (denoted by ln) along $x = \pm c_0 t + \Delta x$ in terms of $c_0 t / l_s$ $(0 < \Delta x \ll 1)$. In fact, under the chosen initial conditions, it is known that $\mathrm{W}^{\pm}$ is a dirac function $\delta(0)$ on the characteristics $x = \pm c_0 t$ (eq. (4.32)), so we compute $\ln(\mathrm{W}^{\pm})$ on a adjacent parallel line of the characteristics. The exponential decay of initial energies along the characteristic line (slope = $\pm c_0$) is verified more rigorously. After the propagation over several l_s, the coherent energy in $x = \pm c_0 t$ decreases quickly and it almost totally transforms into the incoherent energy centred around $x = 0$. After a long propagation time, W^{+} and W^{-} become more and more spread out in space. The distribution of total energy satisfies a local equipartition between all possible modes: in fig. 4.3e and fig. 4.3f, W^{+} and W^{-} become equal and symmetric about $x = 0$.

Furthermore, note that l_s depends on wave number k and the formula of power spectral density according to its definition (4.33). The example above is discussed for a given l_s and a given frequency. Now we discuss its dependence on frequency. Choosing the three covariance functions: sinc^2, exponential and gaussian presented in the table 4.1 as examples, their power spectral densities and scattering mean free paths are respectively computed and illustrated in fig. 4.4a and fig. 4.4b. Although their $\widehat{P}(2k)$ and $l_s(k)$ have different supports in frequency, some common properties are found. For the high frequency limit, l_s is approximatively inversely proportional to k^2. For the low frequency limit, l_s is approximatively inversely proportional to k^4 (for all $\widehat{P}(k)$ sufficiently regular at $k = 0$ here). This phenomenon can be noticed in fig. 4.4b for the given parameters $\varepsilon = 0.04$, $l_c = 6$ mm: l_s tends to infinite for these two limits. Hence, no scattering of energy exists in either limit. Physically, this is due to the fact that in the low frequency domain (or the long wavelength limit) the medium becomes effectively homogeneous. In the high frequency limit, geometric optics becomes a good description for the classical wave propagation where the effect of scattering is expected to saturate. More studies of the influence of different correlation models on scattering mean free path can be found in [24, 86, 144].

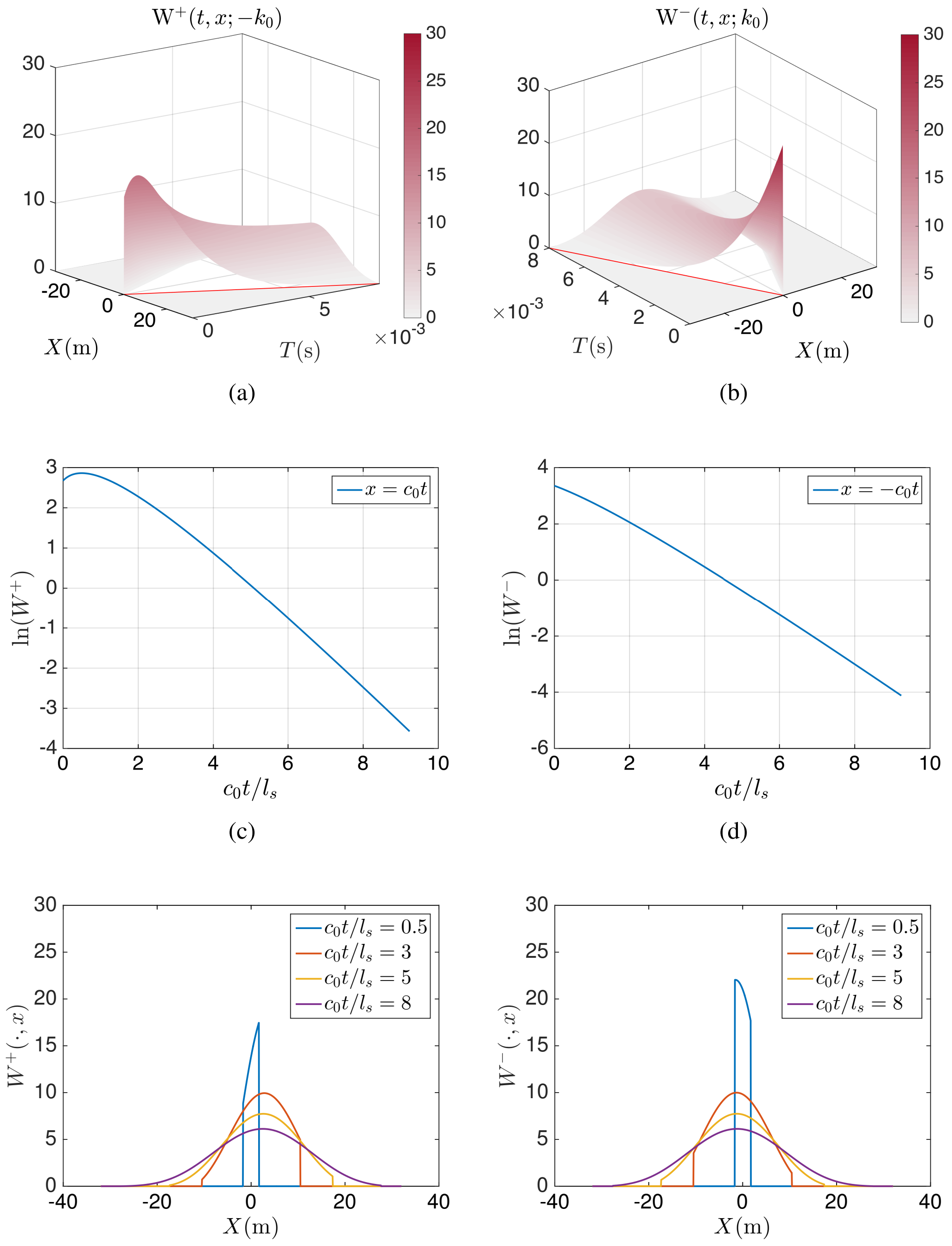

(a) (b)

(c) (d)

(e) (f)

Fig. 4.3 Analytical solutions of $W^{\pm}$ in the time-space domain: (a) $W^+(t,x)$ (red line: $x = c_0t$), (b) $W^-(t,x)$ (red line: $x = -c_0t$), (c) $\ln(W^+)$ on $x = c_0t + \Delta x$, (d) $\ln(W^-)$ on $x = -c_0t + \Delta x$, (e) $W^+(\cdot,x)$ for four time instants, (f) $W^-(\cdot,x)$ for four time instants $t = 0.4$ ms, 2.6 ms, 4.4 ms and 7 ms, which correspond respectively to $c_0t/l_s(k_0) = 0.3$, 3, 5 and 8.

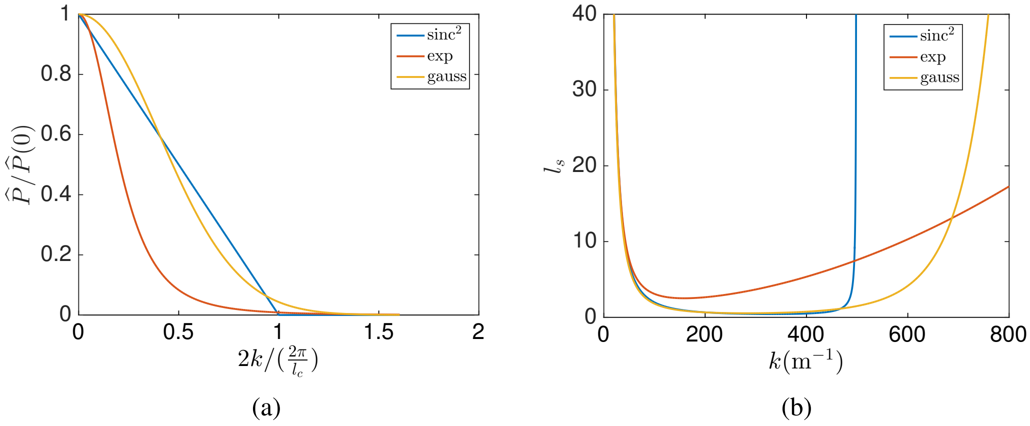

Fig. 4.4 Normalized power spectral density and mean free path for different correlation models: (a) $\widehat{P}(2k)$, (b) $l_s(k)$ (parameters: $\varepsilon = 0.04, l_c = 6$ mm)

Finally, note that what we discussed here remains valid when the waves are scattered by discrete scatterers that are randomly distributed in the medium [119, 147].

4.1.4 Localization phenomenon in 1D heterogeneous media

Localization is a characteristic phenomenon when waves propagate in random media. It means that wave energy remains in a fixed bounded region of space close to the source at all times. It is well known that for (infinite) systems described by one spatial dimension, both quantum mechanical and classical waves are localized even if an infinitesimal amount of randomness is present for sufficiently large propagation distances [144]. When waves are localized and the energy does not propagate, the radiative transfer regime is no more valid to describe the evolution of wave energy. Sheng [125] estimated that in 1D the localization length is approximately four times the mean free path (the factor four is not very accurate and valid especially for low frequency, but they nevertheless tell us that in 1D, the localization length is directly proportional to the mean free path). This offers the possibility of an intermediate range when the radiative transfer might hold.

In this section, we discuss a wave propagation problem in two heterogeneous media with different magnitudes of fluctuations. The localization phenomenon is then observed and analyzed.

Consider here the wave propagation in a heterogeneous bar with a constant density and a weakly fluctuating Young's modulus defined in eq. (4.21). A ricker force $F(t)$ with a magnitude of 1 kN is applied in the centre of bar $x = 0$ so the wave front propagates in two opposite directions (fig. 4.5). Parameters are given in the table 4.2.

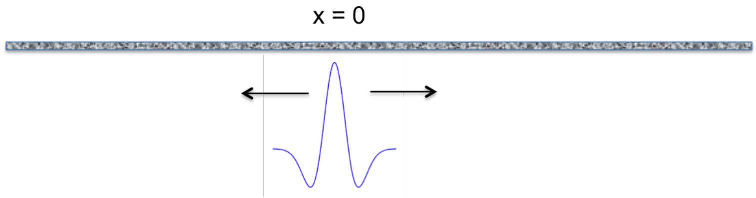

Fig. 4.5 Model in 1D heterogeneous media

media				load (ricker)		wave	mesh
ρ (kg/m^3)	E_0 (GPa)	$\sigma^2(E)=\varepsilon$	l_c (mm)	T_R (ms)	k_{max} (m^{-1})	λ_{max} (m)	h (mm)
2500	40	0.04	6	0.02	157	0.04	5
2500	40	0.008	6	0.02	157	0.04	5

Table 4.2 Numerical parameters of media, load and waves for the numerical examples

The covariance function is chosen as sinc^2 with the parameters defined in the table 4.2. Due to the boundedness of its spectrum (fig. 4.4a), i.e. $2k/(\frac{2\pi}{l_c}) \leq 1$ for nonzero value, we take $2\times 3k_{max} = 2\pi/l_c$ (related to the cutoff frequency $f_c = 3f_{max}$ of ricker). Thus the power spectral density of the main frequency range of ricker does not equal zero, i.e. they have a relatively small and finite scattering mean free path (fig. 4.6). Consequently, $l_c = \frac{\pi}{3k_{max}} = \frac{\lambda_{max}}{6}$ (it satisfies also the condition that λ is of the same order of magnitude as l_c). We choose two values of the variance $\sigma^2 = \varepsilon$ for random media to observe the different phenomena. The mean free paths l_s in these two cases are given in fig. 4.6.

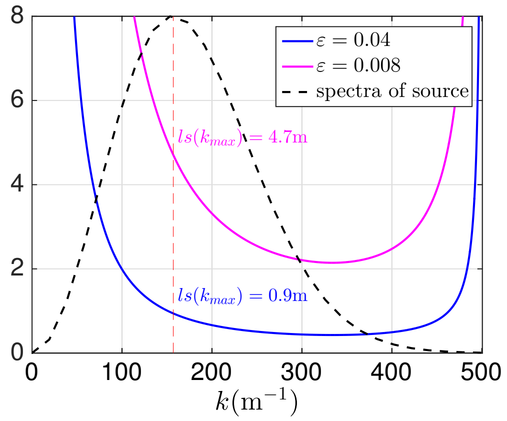

Fig. 4.6 Mean free path $l_s(k)$ (parameters: $\varepsilon = 0.04, 0.008, l_c = 6$ mm)

Consider firstly the case with larger fluctuations $\varepsilon = 0.04$. Numerical solutions of wave equation with mesh size such that $\lambda(3k_{max})/h = 20$ and time step $\Delta t = h/c_0$ are computed for ten realizations of random media. $u_{h\Delta t}$ for one realization is illustrated in fig. 4.7.

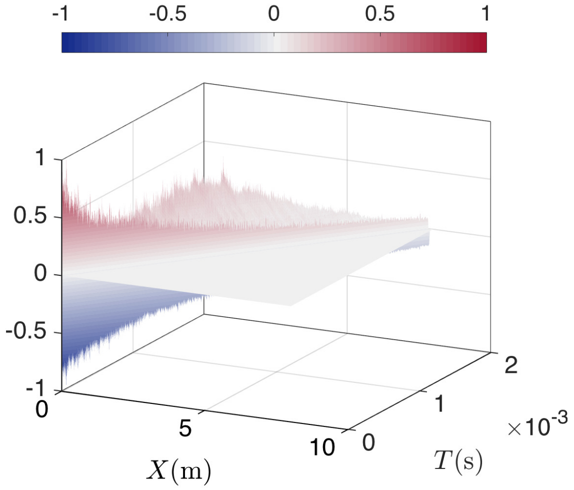

Fig. 4.7 Wave displacement in time- (half) space for one realization ($\varepsilon = 0.04$)

A comparison between the energy obtained by analytical solutions of the radiative transfer equation (denoted by W_a) and by numerical solutions with Wigner transform of wave fields $\mathrm{W}_\varepsilon[u_{h\Delta t}]$ is considered here, as Bal and Pinaud [20] did in 2D random media. On the one hand, the existence of localization phenomena can be verified by observing the evolution of energy. On the other hand, it allows verifying the computation of Wigner transform as we introduced in the section 1.2.4.

Firstly, W_a is obtained analytically with eq. (4.31) subjected to some initial conditions. In this case, it should be noticed that we cannot impose analytically initial conditions for W_a that is equivalent to the energy density of wave fields. However, we can choose an instant t_0 (after the source has vanished) and approximate the initial conditions $\mathrm{W}_a(t = t_0, x; k)$ by Wigner transform of numerical waves:

$$\mathrm{W}_a(t_0, x; k) = \int_{\mathbb{R}} \mathrm{W}_\varepsilon[u_{h\Delta t}](t_0, x; \omega, k) d\omega \tag{4.36}$$

Then the total energy densities (sum of kinetic and potential energies) in the time-space domain computed by analytical Wigner measure and numerical wave solutions in 1D are respectively defined as:

$$\mathrm{E}[\mathrm{W}_a](t,x) := \frac{1}{2}\int_{\mathbb{R}} \left\{\rho\omega^2 \left(\mathrm{W}_a^+(t,x;k) + \mathrm{W}_a^-(t,x;k)\right) + Ek^2 (\mathrm{W}_a^+(t,x;k) + \mathrm{W}_a^-(t,x;k))\right\} dk \tag{4.37a}$$

$$\begin{aligned}\mathrm{E}[u_{h\Delta t}](t,x) &:= \frac{1}{2}\int_{\mathbb{R}^2} \{\rho \mathrm{W}_\varepsilon[\partial_t u_{h\Delta t}](t,x;\omega,k) + E\mathrm{W}_\varepsilon[\partial_x u_{h\Delta t}](t,x;\omega,k)\} d\omega dk \\ &= \frac{1}{2}\left\{\rho(\partial_t u_{h\Delta t}(t,x))^2 + E(\partial_x u_{h\Delta t}(t,x))^2\right\}\end{aligned} \tag{4.37b}$$

Equation (4.37a) is already introduced in the lemma 3.6. Equation (4.37b) can be derived directly by the energy properties of Wigner transform. Considering the results for numerical solutions of one realization are highly oscillating (fig. 4.8), eq. (4.37b) is averaged in ten realizations. The comparison of these two energies is given in fig. 4.9.

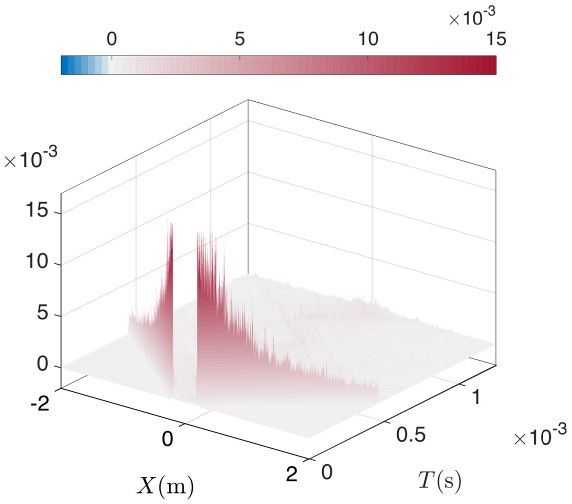

Fig. 4.8 Energy density in the time-space domain ($t \in [0, 2\ \mathrm{ms}], x \in [-2\ \mathrm{m}, 2\ \mathrm{m}]$) obtained by one realization of numerical wave fields $\mathrm{E}[u_{h\Delta t}]$

The two figures fig. 4.9a and fig. 4.9c show that the two energies are quite similar, especially for coherent energy. Some negative values for energy densities $\mathrm{E}[\mathrm{W}_a](t,x)$ are found in fig. 4.9a. In effect, the estimated initial conditions $\mathrm{W}_a(t_0,x;k)$ by eq. (4.36) do not give an exact energy distribution in terms of k (existence of cross terms for Wigner transform) and they contain some negative values for a small part of low frequencies. These values are propagated in latter times and $\mathrm{E}[\mathrm{W}_a](t,x)$ is slightly underestimated. However, these negative energies are relatively small compared to the total energy ($\approx 0.2\%$). As a result, instead of comparing directly the estimated W_a and $\mathrm{W}_\varepsilon[u_{h\Delta t}]$ in phase space, this comparison in terms of time-space energy density is more reasonable. Finally, the two figures fig. 4.9b and fig. 4.9d are plotted with a smaller scale in order to observe and compare the incoherent energy. It seems that a part of energy is localized around $x = 0$.

We can compute the evolution of the total energy with time, defined by:

$$\tilde{\mathrm{E}}[\mathrm{W}_a](t) = \int_{[-2,2]} \mathrm{E}[\mathrm{W}_a](t,x)dx, \qquad \mathbb{E}[\tilde{\mathrm{E}}[u_{h\Delta t}]](t) = \mathbb{E}\left[\int_{[-2,2]} \mathrm{E}[u_{h\Delta t}](t,x)dx\right] \tag{4.38}$$

so as to compare them and also to confirm the existence of localization. In fig. 4.10, it can be observed that the total energy $\tilde{\mathrm{E}}[\mathrm{W}_a](t)$ is underestimated (red line) as we just explained. Thus we propose a "corrected" $\alpha\tilde{\mathrm{E}}[\mathrm{W}_a](t)$ with a correction factor:

$$\alpha = \frac{\mathbb{E}[\tilde{\mathrm{E}}[u_{h\Delta t}]](0)}{\tilde{\mathrm{E}}[\mathrm{W}_a](0)} \approx 1.2 \tag{4.39}$$

that allows roughly eliminating the errors due to the estimated initial conditions. The comparison between the energy of averaged numerical waves (blue line) and the corrected energy of analytical Wigner measure (red dashed line) shows that wave energies are partly localized.

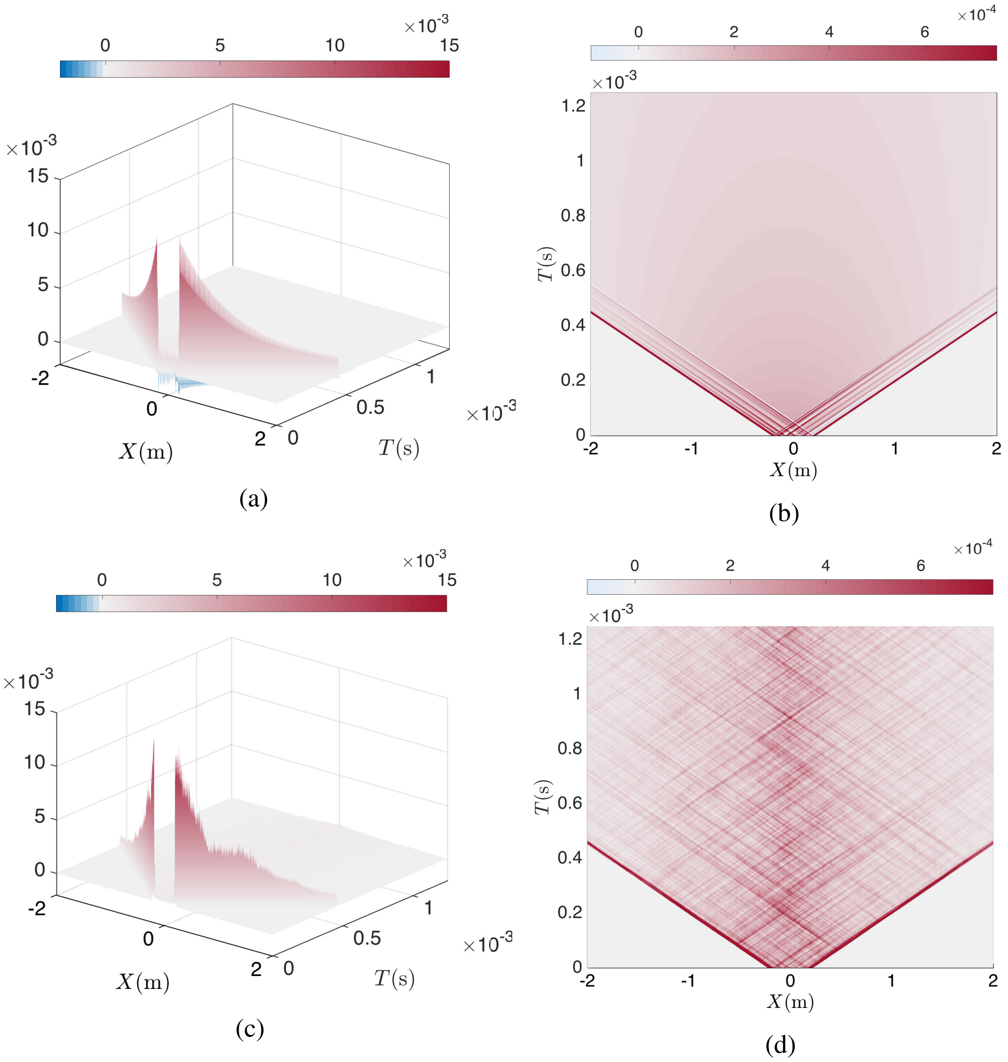

(a) (b) (c) (d)

Fig. 4.9 Energy density in the time-space domain ($t \in [0, 2\text{ ms}], x \in [-2\text{ m}, 2\text{ m}]$) obtained by (a) (b): analytical Wigner measure $\mathrm{E}[\mathrm{W}_a]$, (c) (d): average of 10 numerical wave fields $\mathbb{E}[\mathrm{E}[u_{h\Delta t}]]$

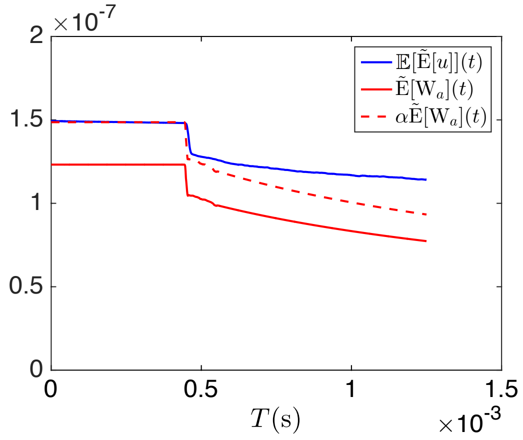

Fig. 4.10 Comparison of the evolution of energy in time obtained by analytical/numerical solutions: $\mathbb{E}[\tilde{\mathrm{E}}[u_{h\Delta t}]]$ (blue solid line), $\tilde{\mathrm{E}}[\mathrm{W}_a]$ (red solid line), $\alpha\tilde{\mathrm{E}}[\mathrm{W}_a]$ (red dashed line)

Furthermore, the evolution in time of the spatial distribution of energies can also be analyzed. Firstly, in fig. 4.11, $\mathrm{E}[\mathrm{W}_a]$ and $\mathbb{E}[\mathrm{E}[u_{h\Delta t}]]$ are compared at $t = 0.5$ ms. Considering that an average of $\mathrm{E}(u_{h\Delta t})$ over ten realizations still gives a largely fluctuating line in space (dashed line), a local average in time-space zone $(5T_{max}, 5\lambda_{max})$ is added for each realization. It allows obtaining a smoother averaged result.

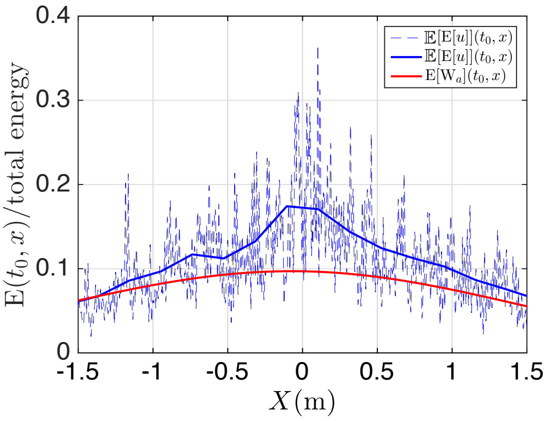

Fig. 4.11 Comparison of energy in time obtained by analytical/numerical solutions at $t_1 = 0.5$ ms: $\mathbb{E}[\mathrm{E}[u_{h\Delta t}]]$ averaged in ten realizations (blue dashed line), $\mathbb{E}[\mathrm{E}[u_{h\Delta t}]]$ averaged in a local time-space domain and in ten realizations (blue solid line), $\mathrm{E}[\mathrm{W}_a]$ (red line)

Now $\mathbb{E}[\mathrm{E}(u_{h\Delta t})]$ and $\mathrm{E}[\mathrm{W}_a]$ are compared in three instants during the period of propagation in fig. 4.12. It is observed that $\mathrm{E}[\mathrm{W}_a]$ decreases in time because energies are more and more overspreading in space. However, $\mathbb{E}[\mathrm{E}[u_{h\Delta t}]]$ remains almost constant with time, which means that wave energies are concentrated around $x = 0$ and they do not propagate.

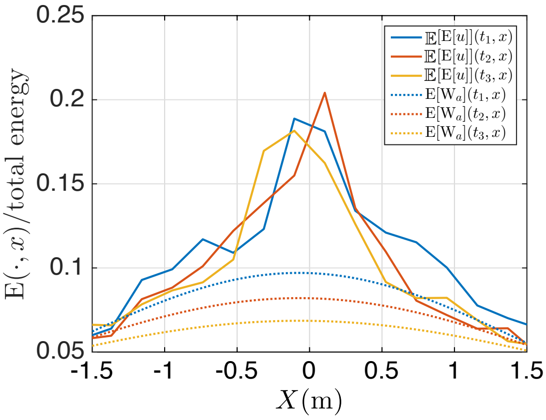

Fig. 4.12 Comparison of variation of energy in time obtained by analytical/numerical solutions for three instants: $t_1 = 0.5$ ms, $t_2 = 0.75$ ms, $t_3 = 1.15$ ms (final time = 2 ms)

According to the discussion above, the medium with the chosen amplitude of fluctuations $\varepsilon = 0.04$ leads to an obvious localization phenomenon during the whole observation period. Now we consider a smaller value $\varepsilon = 0.008$ and other parameters in the table 4.2 remain unchanged, then the same analysis is performed to verify the existence of localization and the validity of radiative transfer regime.

Under this condition, the scattering mean free path is obtained in terms of frequency (fig. 4.6, $l_s(k_{max}) = 4.7$ m). More precisely, l_s is five times larger than that in the case with $\varepsilon = 0.04$. We still choose the same mesh size and time step as the example above for finite element solutions of wave equation. $u_{h\Delta t}$ for one realization is illustrated in fig. 4.13.

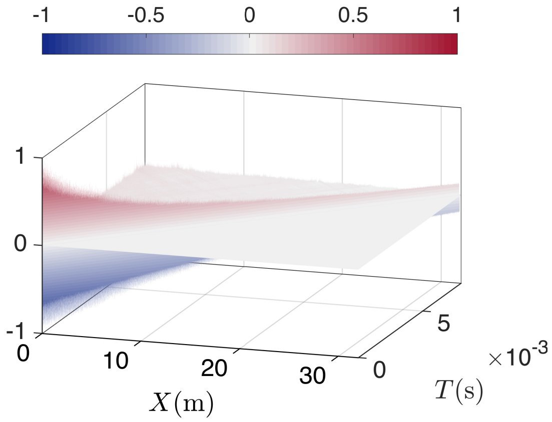

Fig. 4.13 Wave displacement in time- (half) space for one realization ($\varepsilon = 0.008$)

Considering the high cost of computing W_a (numerical integration in a large domain), here we do not compute the two energies for the whole time-space domain as we shown in fig. 4.9. However, the existence of localization can be verified in the same way as we did in fig. 4.12 for three chosen instants and the results are illustrated in fig. 4.14. It is observed that wave energies are less localized with time.

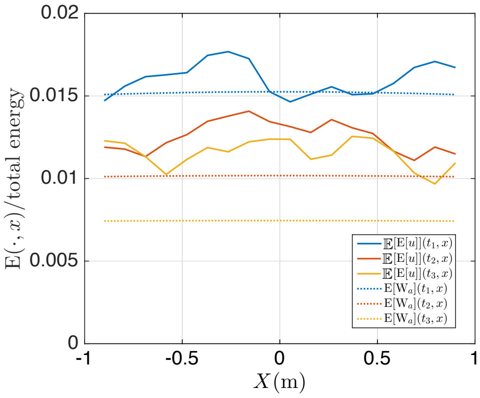

Fig. 4.14 Comparison of variation of energy in time obtained by analytical/numerical solutions for three instants: $t_1 = 1$ ms, $t_2 = 3$ ms, $t_3 = 6$ ms (final time $= 8$ ms)

Finally, we give the comparison of the evolution in time of two energies in time for $x = 0$ in these two cases in fig. 4.15. It is still found that a smaller ε results in less localization.

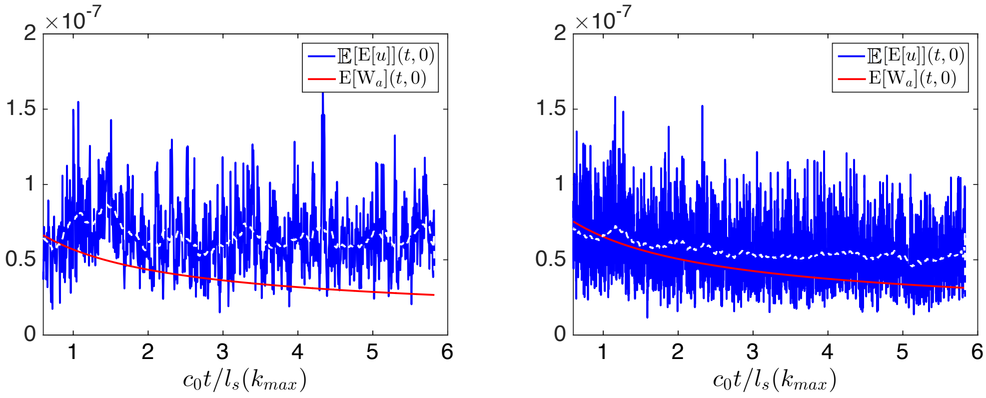

(a) (b)

Fig. 4.15 Comparison of total energy obtained by analytical/averaged numerical solutions in time for $x = 0$ (white dashed line: smoothed value of $\mathbb{E}[\mathrm{E}(u_{h\Delta t})](t,0)$): (a) $\varepsilon = 0.04$, (b) $\varepsilon = 0.008$

With these two examples it is found that the smaller amplitude ε of fluctuations should be chosen to reduce the localization of energy so that the radiative transfer regime remains valid in a larger region. In the next section, the example with $\varepsilon = 0.008$ will be used for the computation of Wigner transform and residual errors.

4.2 Energy-based residual errors of numerical solutions of wave equation

As that defined in eq. (3.49) of residual errors for wave fields based on transport equation, here we can also define it with radiative transfer equations (4.11) in terms of $\mathbf{W}_\varepsilon[\mathbf{u}_{u_{h\Delta t}}]$. In this section, we only introduce this definition for 1D media for simplicity.

4.2.1 Theoretical residual errors based on 1D radiative transfer equation

Based on 1D radiative transfer equation (4.26 and 4.28), residual errors in terms of Wigner transform of wave fields are defined in the following:

Definition 4.2. Residual errors based on 1D radiative transfer equation in terms of $\mathrm{W}^{\pm}$ are defined as:

$$\begin{cases} \mathrm{R}^{+}[u_{h\Delta t}] := \partial_t \mathrm{W}_\varepsilon^{+}[u_{h\Delta t}] + c_0 \partial_x \mathrm{W}_\varepsilon^{+}[u_{h\Delta t}] - \frac{c_0}{l_s}\left(\mathrm{W}_\varepsilon^{-}[u_{h\Delta t}] - \mathrm{W}_\varepsilon^{+}[u_{h\Delta t}]\right) \\ \mathrm{R}^{-}[u_{h\Delta t}] := \partial_t \mathrm{W}_\varepsilon^{-}[u_{h\Delta t}] - c_0 \partial_x \mathrm{W}_\varepsilon^{-}[u_{h\Delta t}] - \frac{c_0}{l_s}\left(\mathrm{W}_\varepsilon^{+}[u_{h\Delta t}] - \mathrm{W}_\varepsilon^{-}[u_{h\Delta t}]\right) \end{cases} \tag{4.40}$$

Definition 4.3. Residual errors based on 1D radiative transfer equation in terms of W^{s} and W^{d} are defined as:

$$\begin{cases} \mathrm{R}^{\mathrm{sd}}_{T}[u_{h\Delta t}] := \partial_t \mathrm{W}^{\mathrm{s}}[u_{h\Delta t}] + c_0 \partial_x \mathrm{W}^{\mathrm{d}}[u_{h\Delta t}] \\ \mathrm{R}^{\mathrm{sd}}_{TS}[u_{h\Delta t}] := \left\{ \partial_t \mathrm{W}^{\mathrm{d}}[u_{h\Delta t}] + \frac{2c_0}{l_s} \mathrm{W}^{\mathrm{d}}[u_{h\Delta t}] \right\} + c_0 \partial_x \mathrm{W}^{\mathrm{s}}[u_{h\Delta t}] \end{cases} \tag{4.41}$$

It can be noticed that $\mathrm{R}^{\mathrm{sd}}_{T}$ contains only transport part of the radiative transfer equation and $\mathrm{R}^{\mathrm{sd}}_{TS}$ contains both transport and scattering parts.

Either of these definitions as a representation of errors can be used since in fact we have $\mathrm{R}^{\mathrm{sd}}_{T} = \mathrm{R}^{+} + \mathrm{R}^{-}$ and $\mathrm{R}^{\mathrm{sd}}_{TS} = \mathrm{R}^{+} - \mathrm{R}^{-}$. In latter numerical applications, $\mathrm{R}^{\mathrm{sd}}_{T}$ and $\mathrm{R}^{\mathrm{sd}}_{TS}$ are chosen to illustrate the results.

4.2.2 Numerical computation of Wigner transform of wave fields in random media

Before calculating numerically the defined errors in last section, the numerical computation of Wigner transform in random media is firstly specifically presented here.

Generally in random media, we evaluate physical quantities by taking the average over the ensemble of realizations of random media (as we did for the comparison of energy in the section 4.1.4). In addition, in the high frequency limit $\varepsilon \to 0$, formal arguments show that the ensemble average of Wigner transform with respect to the randomness converge weakly to the Wigner measure, i.e. the solution of the radiative transfer equation in random media [19, 53, 132].

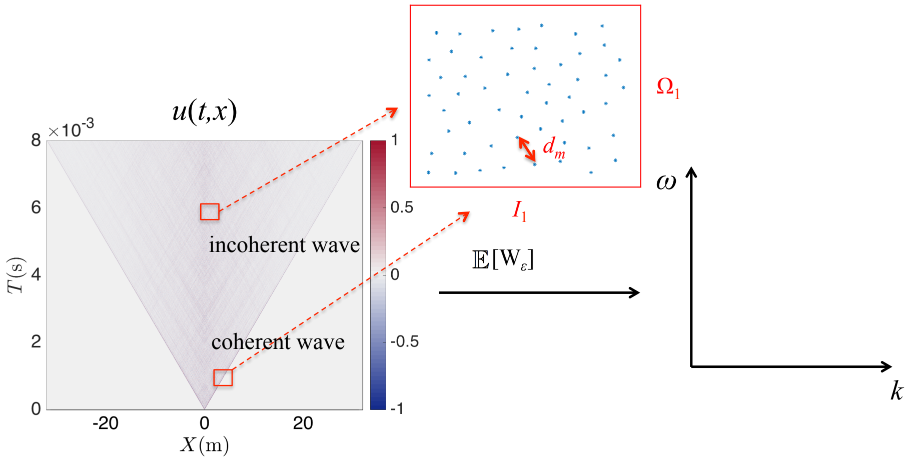

Fig. 4.16 Randomly chosen time-space points for averaging the Wigner transform of numerical waves

Theoretically, W_ε should be averaged over all possible realizations of the heterogeneous medium with given statistics, which causes high computational costs in numerical applications. In practice, we calculate, for example as in the last section, wave solutions in ten realizations of random media. A local average in the time-space domain is added within each realization so as to obtain an equivalent ensemble average, denoted always by $\mathbb{E}[\mathrm{W}_\varepsilon]$, i.e.

$$\mathbb{E}[\mathrm{W}_\varepsilon] = \frac{1}{j_x N_{tx}} \sum_j \sum_{(t_k,x_k)\in I_1\times\Omega_1, k=1,..,N_{tx}} \mathrm{W}_\varepsilon^{(j)}(t_k,x_k) \tag{4.42}$$

Here I_1 and Ω_1 are respectively the time subinterval and subspace. j_x is the total number of realizations and N_{tx} is the total number of time-space points chosen in $I_1 \times \Omega_1$. $\mathrm{W}_\varepsilon^{(j)}$ is the Wigner transform of j-th realization of the random displacement field. $j = 1, ..., 10$ $(j_x = 10)$ in our work. The chosen time-space points should be uncorrelated. In fig. 4.16, a simple illustration of a group of random points with a mean distance $d_m = 6l_c$ between two adjacent points in t-x space. Then we can compute eq. (4.42) over these points and over ten realizations.

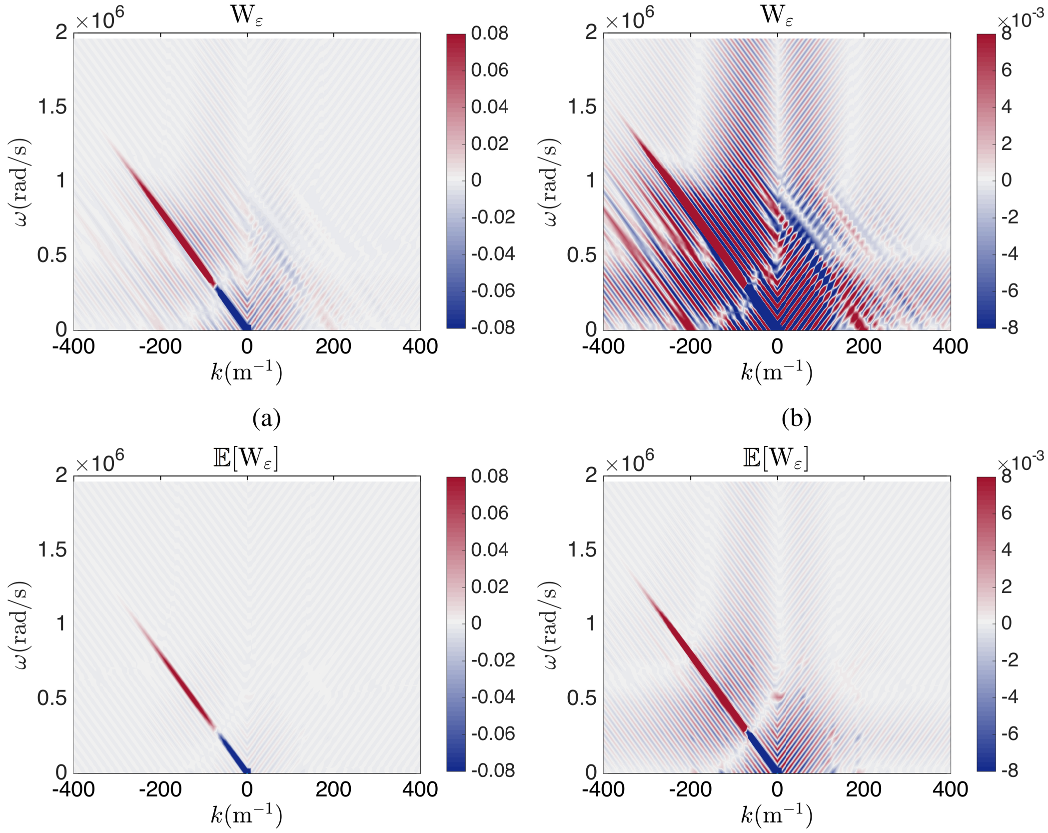

(a) (b)

(c) (d)

Fig. 4.17 Computation of Wigner transform for coherent forward waves in random media: (a) (b) $\mathrm{W}_\varepsilon[u_{h\Delta t}]$ for one point (t_0, x_0) with two different scales, (c) (d) $\mathbb{E}[\mathrm{W}_\varepsilon[u_{h\Delta t}]]$ averaged in time-space and in ten realizations with two different scales

Figure 4.17 gives numerical results of $\mathrm{W}_\varepsilon[u_{h\Delta t}](t,x;\omega,k)$ of coherent forward wave fields. Similar to the homogeneous case in fig. 3.10a, energies are mainly distributed along $\omega = -c_0 k$ since the coherent energy are dominant. However, some fluctuations are also observed here (fig. 4.17b) compared to fig. 3.10a. On the one hand, more discontinuities in the boundary of computation region are found in the heterogeneous case, thus the leakage of frequency will increase here (see Appendix B). On the other hand, coherent wave are reflected by the random heterogeneities, so cross terms between the forward waves and reflected waves arise in phase space. A small amount of energies of reflected waves should be found in $\omega = c_0 k$, but they are polluted by the fluctuations of frequency leakage of coherent waves. For this reason they are not remarkable in fig. 4.17a. In fig. 4.17c, it can be noticed that the average over more points allows reducing largely the numerical fluctuations around $\omega = -c_0 k$. Note that it cannot remove the negative values for low frequencies. In fact, coherent waves are dominant and weakly fluctuating and it is similar to the homogeneous case in fig. 3.10.

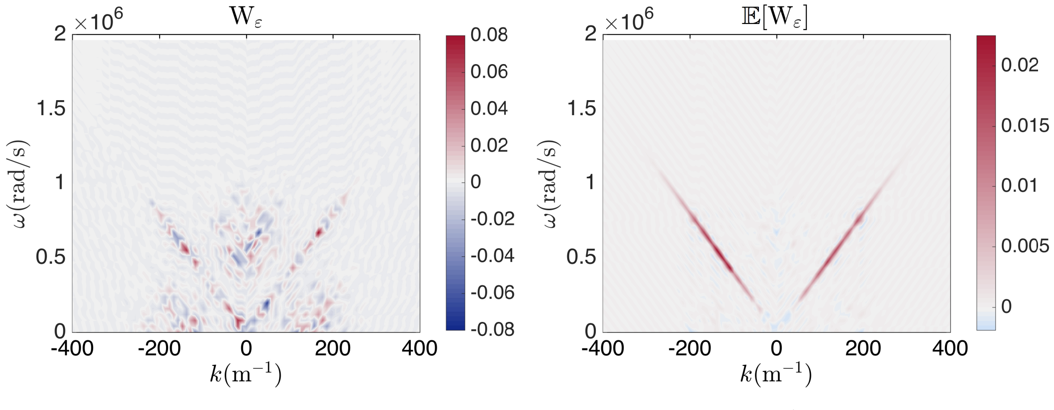

(a) (b)

Fig. 4.18 Computation of Wigner transform for incoherent waves in random media: (a) $\mathrm{W}_\varepsilon[u_{h\Delta t}](t_0, x_0; \omega, k)$, (b) $\mathbb{E}[\mathrm{W}_\varepsilon[u_{h\Delta t}]]$ (averaged in time-space and in 10 realizations)

Figure 4.18 gives numerical results of $\mathrm{W}_\varepsilon[u_{h\Delta t}](t, x; \omega, k)$ of incoherent wave fields. Firstly, it is remarkable in fig. 4.18a that energies are not only distributed in $\omega = \pm c_0 k$ but also between these two characteristic lines. As we explained above, the latter are cross terms due to the interference of waves in two opposite directions. This phenomenon is more obvious than on fig. 4.17a since wave energies in two directions are comparable. Figure 4.18b gives $\mathbb{E}[\mathrm{W}_\varepsilon[u_{h\Delta t}]]$, an average in time-space domain and over 10 realizations. We find that energies are more concentrated along $\omega = \pm c_0 k$. Besides, it takes almost positive values over the entire phase space domain. Indeed, it can be understood by the energy properties of Wigner transform:

$$\int_{\mathbb{R}\times\mathbb{R}} \mathrm{W}_\varepsilon[u](t, x; \omega, k)\, dt\, dx = |\widehat{u}(\omega, k)|^2 > 0 \tag{4.43}$$

It is also observed that $\mathbb{E}[\mathrm{W}_\varepsilon^+[u_{h\Delta t}]]$ and $\mathbb{E}[\mathrm{W}_\varepsilon^-[u_{h\Delta t}]]$ are almost equal. In fact, $\mathbb{E}[\mathrm{W}_\varepsilon^+[u_{h\Delta t}]]$, $\mathbb{E}[\mathrm{W}_\varepsilon^-[u_{h\Delta t}]]$ will always reach an equilibrium after a long time propagation. This result is explained in detail with the analytical solution of radiative transfer equation in the section 4.1.3.

In conclusion, both the ensemble average and the average over a set of uncorrelated space-time points are useful to reduce numerical fluctuations and cross terms in the computation of Wigner transform in random media. From now on, we still denote the average $\mathbb{E}[\mathrm{W}_\varepsilon[u_{h\Delta t}]]$ by $\mathrm{W}_\varepsilon[u_{h\Delta t}]$ for simplicity.

4.2.3 Numerical application of residual errors based on radiative transfer equation

In this section, $u_{h\Delta t}$ with a relatively fine mesh size obtained in the numerical example ($\varepsilon = 0.008$) in the section 4.1.4 is used for calculating errors. Based on the calculations of Wigner transform for coherent waves and incoherent waves in the section 4.2.2, residual errors of $u_{h\Delta t}$ in eq. (4.41) are respectively computed and analyzed. In each case, we present firstly the errors $\left|\mathrm{R}_T^{\mathrm{sd}}\right|$ and $\left|\mathrm{R}_{TS}^{\mathrm{sd}}\right|$ in function of number of realizations N_R. It is expected that errors are close to zero since a relatively fine mesh is used.

Above all, in all figures that represent errors in this chapter, we do not consider the low frequencies since Wigner transform is computed in a bounded region and waves with a large wavelength cannot be totally and exactly captured. More precisely, we choose to observe only waves with:

$$k \geq 2 \times \frac{2\pi}{\zeta_x} = 40\ \mathrm{m}^{-1} \tag{4.44}$$

Recall that ζ_x is the computation region in space defined in the section 3.1.4 (fig. 3.9a) and we chose $\zeta_x = 8\lambda_{max}$ in our work.

Firstly, we compute the residual errors for coherent forward waves in fig. 4.19. As we discussed in the section 4.2.2, a group of random points ($N_{tx} \approx 300$) in the time-space domain is chosen in the region around $x = 0.5$ m. $\mathrm{R}_T^{\mathrm{sd}}$ and $\mathrm{R}_{TS}^{\mathrm{sd}}$ are computed and averaged over these points and over ten random realizations.

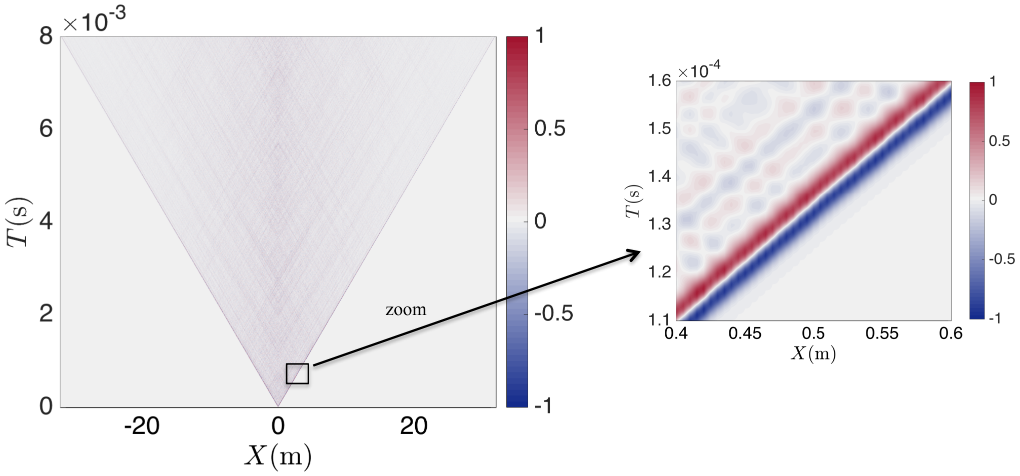

Fig. 4.19 Computation area presented with $u(t,x)$

Figure 4.20 gives absolute values of the residual errors $\left|\mathrm{R}_T^{\mathrm{sd}}\right|$ and $\left|\mathrm{R}_{TS}^{\mathrm{sd}}\right|$ in terms of $|k|$ for three random realizations and the average of ten realizations, normalized by the total energy $\mathbb{E}\left[u_{h\Delta t}^2\right]$. And we find that it is relatively small compared to the total energy. It is observed high varying value of errors for lower frequency with different realizations (blue lines) and a local maximum of errors located at the maximum frequency $k_{max} = 157\ \mathrm{m}^{-1}$ for the averaged errors (red line).

Besides, we give here also $|R^+|$ and $|R^-|$ so as to analyze errrors for waves in two directions. Figure 4.21 gives absolute values of the residual errors in terms of $|k|$, normalized by the total energy. It is found that much smaller errors are obtained for $|R^+|$. As we explained above, waves are mainly transmitted in the forward direction and only a small amount of waves are scattered to the backward direction, so errors for $W_\varepsilon^-[u_{h\Delta t}]$ are polluted by numerical fluctuations of $W_\varepsilon^+[u_{h\Delta t}]$ due to the frequency leakage and cross terms as we explained in fig. 4.17.

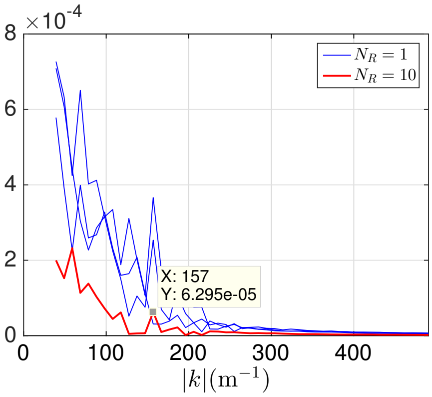

(a) (b)

Fig. 4.20 Residual errors along $\omega = \pm c_0 k$ for coherent wave: (a) $\left|R_T^{\mathrm{sd}}\right|$, (b) $\left|R_{TS}^{\mathrm{sd}}\right|$

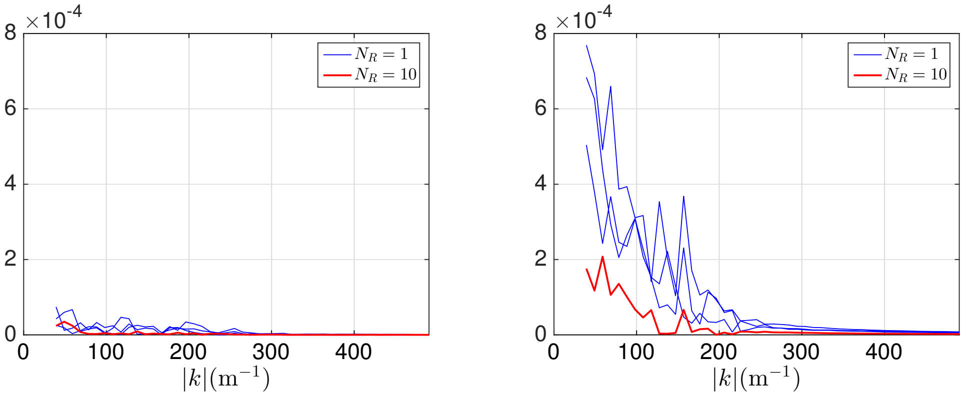

(a) (b)

Fig. 4.21 Residual errors along $\omega = \pm c_0 k$ for coherent wave: (a) $|R^+|$, (b) $|R^-|$

Now the same discussions are focused on the incoherent wave around $x = 0$ (fig. 4.22). In the chosen computation region of time-space domain, it is known that W^+ and W^- tend to a local equipartition between each other after a long time propagation, so $W^s \gg W^d \approx 0$ (fig. 4.23).

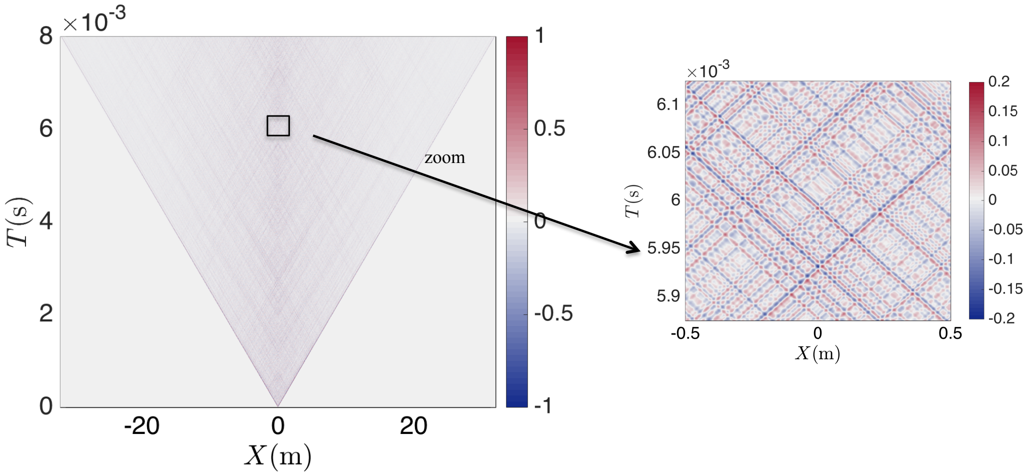

Fig. 4.22 Computation area presented with $u(t,x)$

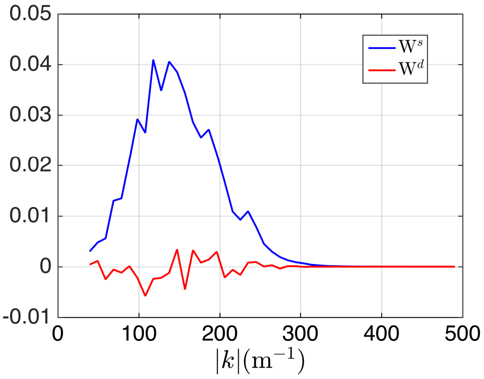

Fig. 4.23 $\mathrm{W^s}$ and $\mathrm{W^d}$ around $x = 0$ and along $\omega = \pm c_0 k$

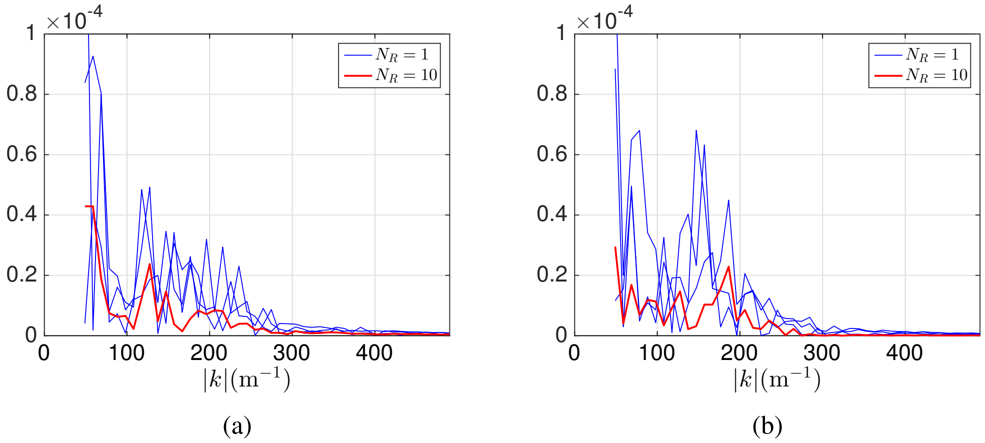

Fig. 4.24 Residual errors along $\omega = \pm c_0 k$ for incoherent wave: (a) $\left|\mathrm{R}_T^{\mathrm{sd}}\right|$, (b) $\left|\mathrm{R}_{TS}^{\mathrm{sd}}\right|$

Figure 4.24 gives residual errors $\left|R_T^{sd}\right|$ and $\left|R_{TS}^{sd}\right|$ in terms of frequency. Errors in each realizations are high oscillating and the average gives a smoother result. It is remarked that although the average of Wigner transform eliminates main cross terms for low frequency in fig. 4.18 and fig. 4.23, the related errors still have a main peak for low frequency. On the one hand, the cross terms cannot totally be suppressed by this average method. On the other hand, the numerical differentiation in eq. (4.41) for small and fluctuating energy density of low frequency will bring some additional errors (average may also reduce a part of such errors but very limited). These additional errors exist also for high frequencies but they are much smaller since we have much less cross terms.

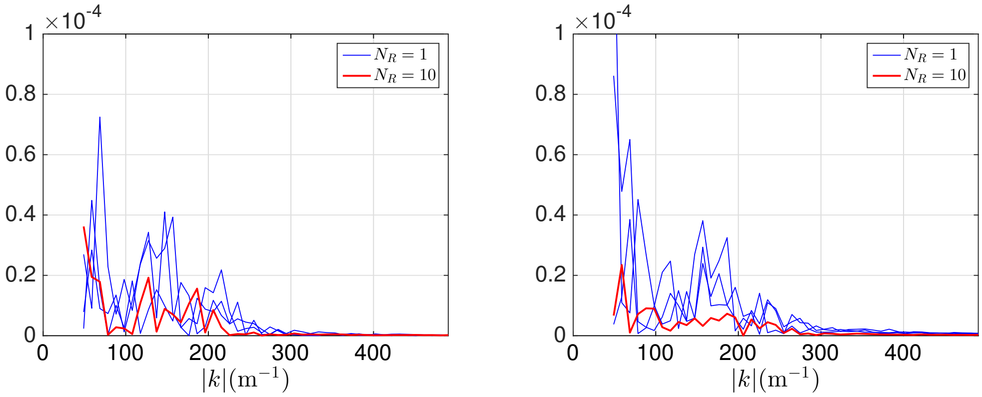

(a) (b)

Fig. 4.25 Residual errors along $\omega = \pm c_0 k$ for incoherent wave: (a) $|R^+|$, (b) $|R^-|$

Figure 4.25 gives residual errors in terms of W^+ and W^-. It can be found that here the contribution to errors of the forward and the backward waves are comparable.

Furthermore, Wigner transform and the related residual errors can also be computed along the direction of propagation $x = \pm c_0 t$. The advantage of this transformation of coordinates is that the edge effects or the discontinuities of boundary for numerical computation of Wigner transform may be smaller in this case. The numerical results can be found in Appendix F. It is found that a similar result is obtained and large errors are still found for low frequencies.

4.3 Filtering of the energy-based residual errors

Considering that the errors found in the last section are highly fluctuating and located largely at lower frequencies due to the superposition of plenty of cross terms in Wigner transform of a multi-frequency signal in random media, a filtering of residual errors is derived analytically in this section. Then we compute the new residual errors of the FE numerical solutions of wave equation in the last section 4.2.3.

We derive firstly the formula of filtered residual errors. In brief, it is based on the convolution of Wigner transform of wave fields with Wigner transform of a window function $h(t,x)$.

We give here the definitions of the double convolution of Wigner transform and the short-time Fourier transform:

Definition 4.4. The double convolution of two spatio-temporal Wigner transforms, denoted by "$**$", is defined with respect to four variables $(t,x;\omega,k)$ by

$$\mathrm{W}_\varepsilon[u_\varepsilon,v_\varepsilon]**\mathrm{W}_\varepsilon[h](t,x;\omega,k):=\int_{\mathbb{R}^4}\mathrm{W}_\varepsilon[u_\varepsilon,v_\varepsilon](t',x';\omega',k')\mathrm{W}_\varepsilon[h](t-t',x-x';\omega-\omega',k-k')dt'dx'd\omega'dk' \tag{4.45}$$

Definition 4.5. The short-time Fourier transform is defined as [11]:

$$|\mathrm{STFT}[u_\varepsilon,h](t,x;\omega,k)|^2:=\left|\frac{\varepsilon}{2\pi}\int_{\mathbb{R}^2}u_\varepsilon(t-\varepsilon\alpha,x-\varepsilon m)\;h^*(\varepsilon\alpha,\varepsilon m)\;e^{i(\alpha\omega+mk)}\;d\alpha dm\right|^2 \tag{4.46}$$

The Wigner transform has the following property:

Property 8. The relation between the double convolution of Wigner transforms and the STFT is the following: $\forall h(t,x)$,

$$\mathrm{W}_\varepsilon[u_\varepsilon,v_\varepsilon]**\mathrm{W}_\varepsilon[h]=\mathrm{STFT}[u_\varepsilon,h]\mathrm{STFT}^*[v_\varepsilon,h] \tag{4.47}$$

Proof. See Appendix D. ☐

It is obvious that we have $\mathrm{W}_\varepsilon[u_\varepsilon]**\mathrm{W}_\varepsilon[h]=|\mathrm{STFT}[u_\varepsilon,h]|^2$. The computation cost of the STFT is in the same order as that of the Wigner transform. Thus the calculation of the right-hand side of eq. (4.47) is more efficient than that of the convolution of two Wigner transforms.

If we choose w as a product of two window functions in time and in space, denoted by $h(t,x)=h_t(t)h_x(x)$, the property 8 illustrates that a filtering in time-space for wave fields will filter also the results of its Wigner transform by the convolution. It means that this filtering results in smoother values in phase space. Besides, a discussion on bilinear properties of STFT can be found in Appendix E. Compared to Wigner transform, STFT suppresses largely cross terms at zero and low frequency and less frequency leakage is observed.

Based on the analysis above and by recalling that $\mathrm{R}^{\mathrm{sd}}_T=\mathrm{R}^++\mathrm{R}^-$ and $\mathrm{R}^{\mathrm{sd}}_{TS}=\mathrm{R}^+-\mathrm{R}^-$, the following results are derived:

Theorem 4.6. Filtered residual errors based on 1D radiative transfer equation are defined as:

$$\begin{aligned}
&\mathrm{R}^\pm[u_{h\Delta t}]**\mathrm{W}_\varepsilon[h_th_x](t,x;\omega=c_0k,\mp k)\\
&=2\mathrm{Re}\left\{\mathrm{STFT}[v_{h\Delta t},h_th_x](t,x;c_0k,\mp k)\mathrm{STFT}^*[u_{h\Delta t},h_th_x](t,x;c_0k,\mp k)\right\}\\
&\pm 2c_0\mathrm{Re}\left\{\mathrm{STFT}[\partial_xu_{h\Delta t},h_th_x](t,x;c_0k,\mp k)\mathrm{STFT}^*[u_{h\Delta t},h_th_x](t,x;c_0k,\mp k)\right\}\\
&+\frac{1}{16}\int_{\mathbb{R}}\mathrm{STFT}[u_{h\Delta t},h_th_x^*](t,x-\varepsilon l;c_0k,\pm k)\mathrm{STFT}^*[u_{h\Delta t},h_th_x^*](t,x+\varepsilon l;c_0k,\pm k)\;P^{(2)}(l)dl\\
&-\frac{1}{16}\int_{\mathbb{R}}\mathrm{STFT}[u_{h\Delta t},h_th_x](t,x-\varepsilon l;c_0k,\mp k)\mathrm{STFT}^*[u_{h\Delta t},h_th_x](t,x+\varepsilon l;c_0k,\mp k)\;P^{(2)}(l)dl
\end{aligned} \tag{4.48}$$

where $P^{(2)}(r)$ is the second-order derivative of the covariance function $P(r)$.

Proof. We can derive the 1D filtered radiative transfer equation by convolutions with eq. (4.26) for each term of the original radiative transfer equation.

For the two transport terms, we can prove the following result by lemma 3.4:

$$\partial_t \mathrm{W}_\varepsilon[u_\varepsilon] ** \mathrm{W}_\varepsilon[h_t h_x] = 2\mathrm{Re}\left\{\mathrm{W}_\varepsilon[\partial_t u_\varepsilon, u_\varepsilon]\right\} ** \mathrm{W}_\varepsilon[h_t h_x] \tag{4.49}$$

As the auto-Wigner transform is always real and by the property 8, we have

$$\begin{aligned}\partial_t \mathrm{W}_\varepsilon[u_\varepsilon] ** \mathrm{W}_\varepsilon[h_t h_x] &= 2\mathrm{Re}\left\{\mathrm{W}_\varepsilon[\partial_t u_\varepsilon, u_\varepsilon] ** \mathrm{W}_\varepsilon[h_t h_x]\right\} \\ &= 2\mathrm{Re}\left\{\mathrm{STFT}[v_\varepsilon, h_t h_x]\mathrm{STFT}^*[u_\varepsilon, h_t h_x]\right\}\end{aligned} \tag{4.50}$$

In the same way, it can be derived that:

$$\partial_x \mathrm{W}_\varepsilon[u_\varepsilon] ** \mathrm{W}_\varepsilon[h_t h_x] = 2\mathrm{Re}\left\{\mathrm{STFT}[\partial_x u_\varepsilon, h_t h_x]\mathrm{STFT}^*[u_\varepsilon, h_t h_x]\right\} \tag{4.51}$$

For the two scattering terms, we have:

$$\begin{aligned}&\frac{k^2}{4}\widehat{P}(2k)\mathrm{W}_\varepsilon[u_\varepsilon] ** \mathrm{W}_\varepsilon[h_t h_x] \\ &= \frac{1}{4}\frac{1}{(2\pi)^4}\int_{\mathbb{R}^6} u_\varepsilon\left(t' - \frac{\varepsilon\tau}{2}, x' - \frac{\varepsilon y}{2}\right) u_\varepsilon^*\left(t' + \frac{\varepsilon\tau}{2}, x' + \frac{\varepsilon y}{2}\right) h_t\left(t - t' - \frac{\varepsilon s}{2}\right) h_x\left(x - x' - \frac{\varepsilon z}{2}\right) \\ &\qquad h_t^*\left(t - t' + \frac{\varepsilon s}{2}\right) h_x^*\left(x - x' + \frac{\varepsilon z}{2}\right) \underbrace{\int_{\mathbb{R}} e^{-i(s-\tau)\omega'} d\omega'}_{:=(a)} \underbrace{\int_{\mathbb{R}} k'^2 \widehat{P}(2k') e^{-i(z-y)k'} dk'}_{:=(b)} \\ &\qquad e^{i(s\omega + yk)}\, dt' dx' d\tau dy ds dz\end{aligned} \tag{4.52}$$

Firstly, the integration (a) can be seen as the Fourier transform of a function in the form $f(x) = e^{iax}$ (a constant). It is known that:

$$(a) = \int_{\mathbb{R}} e^{i\tau\omega'} e^{-is\omega'} d\omega' = 2\pi\delta(s - \tau) \tag{4.53}$$

Secondly, for the integration (b), by using respectively the definition of the inverse Fourier transform and the Fourier transform of function $f(x) = x^n$ [35]:

$$\int_{\mathbb{R}} k^n e^{-jxk} dk = 2\pi i^n \delta^{(n)}(x) \tag{4.54}$$

where n is a natural number and $\delta^{(n)}(x)$ is the n-th distribution derivative of the dirac delta function, we can derive:

$$\begin{aligned}(b) &= \int_{\mathbb{R}} k'^2 \int_{\mathbb{R}} P(x) e^{-i2xk'} dx \, e^{-i(z-y)k'} dk' \\ &= \int_{\mathbb{R}} P(x) \int_{\mathbb{R}} k'^2 e^{-i(2x+z-y)k'} dk' \, dx \\ &= \int_{\mathbb{R}} P(x) \, 2\pi i^2 \delta^{(2)}(2x+z-y) \, dx\end{aligned} \tag{4.55}$$

Then using the derivative property of the dirac delta function [61]:

$$\int f(x)\delta^{(n)}(x)dx = -\int \frac{\partial f}{\partial x}\delta^{(n-1)}(x)dx \tag{4.56}$$

and we get:

$$\begin{aligned}(b) &= -2\pi \int_{\mathbb{R}} P(x)\delta^{(2)}(2x+z-y) \, dx \\ &= -\frac{\pi}{4}P^{(2)}\left(\frac{y-z}{2}\right)\end{aligned} \tag{4.57}$$

Introducing eq. (4.53) and eq. (4.57) to eq. (4.52), we get:

$$\begin{aligned}&\frac{k^2}{4}\widehat{P}(2k)\mathrm{W}_\varepsilon[u_\varepsilon] * * \mathrm{W}_\varepsilon[h_t h_x] \\ &= \frac{1}{4}\frac{1}{(2\pi)^4}\int_{\mathbb{R}^6} u_\varepsilon\left(t' - \frac{\varepsilon\tau}{2}, x' - \frac{\varepsilon y}{2}\right) u_\varepsilon^*\left(t' + \frac{\varepsilon\tau}{2}, x' + \frac{\varepsilon y}{2}\right) h_t\left(t - t' - \frac{\varepsilon s}{2}\right) h_x\left(x - x' - \frac{\varepsilon z}{2}\right) \\ &\qquad h_t^*\left(t - t' + \frac{\varepsilon s}{2}\right) h_x^*\left(x - x' + \frac{\varepsilon z}{2}\right) \; 2\pi\delta(s-\tau) \; (-\frac{\pi}{4})P^{(2)}\left(\frac{y-z}{2}\right) \; e^{i(s\omega + zk)} \; dt'dx'd\tau dy ds dz \\ &= -\frac{\pi}{16}\frac{1}{(2\pi)^3}\int_{\mathbb{R}^5} u_\varepsilon\left(t' - \frac{\varepsilon\tau}{2}, x' - \frac{\varepsilon y}{2}\right) u_\varepsilon^*\left(t' + \frac{\varepsilon\tau}{2}, x' + \frac{\varepsilon y}{2}\right) h_t\left(t - t' - \frac{\varepsilon\tau}{2}\right) h_x\left(x - x' - \frac{\varepsilon z}{2}\right) \\ &\qquad h_t^*\left(t - t' + \frac{\varepsilon\tau}{2}\right) h_x^*\left(x - x' + \frac{\varepsilon z}{2}\right) \; P^{(2)}\left(\frac{y-z}{2}\right) \; e^{i(\tau\omega + zk)} \; dt'dx'd\tau dy dz\end{aligned} \tag{4.58}$$

Then changing the variables in the equation above (t', τ) by (α, β) and (x', y, z) by (m, n, l) with:

$$\begin{cases} t - t' + \frac{\varepsilon\tau}{2} = \varepsilon\alpha \\ t - t' - \frac{\varepsilon\tau}{2} = \varepsilon\beta \end{cases} , \qquad \begin{cases} x - x' + \frac{\varepsilon z}{2} = \varepsilon m \\ x - x' - \frac{\varepsilon z}{2} = \varepsilon n \\ \frac{y-z}{2} = l \end{cases} \tag{4.59}$$

thus $\int_{\mathbb{R}^2} dt'd\tau = \int \varepsilon d\alpha d\beta$ and $\int_{\mathbb{R}^2} dx'dydz = \int 2\varepsilon dm dn dl$. We have:

$$\begin{aligned}&\frac{k^2}{4}\widehat{P}(2k)\mathrm{W}_\varepsilon[u_\varepsilon] * * \mathrm{W}_\varepsilon[h_t h_x] \\ &= -\frac{\varepsilon^2}{16}\frac{1}{(2\pi)^2}\int_{\mathbb{R}}\int_{\mathbb{R}^2} u_\varepsilon(t - \varepsilon\alpha, x - \varepsilon l - \varepsilon m) \; h_t^*(\varepsilon\alpha) h_x^*(\varepsilon m) \; e^{i(\alpha\omega + mk)} \; d\alpha dm \\ &\qquad \int_{\mathbb{R}^2} u_\varepsilon^*(t - \varepsilon\beta, x - \varepsilon l + \varepsilon n) \; h_t(\varepsilon\beta) h_x(\varepsilon n) \; e^{-i(\beta\omega + nk)} \; d\beta dn \; P^{(2)}(l) dl \\ &= -\frac{1}{16}\int_{\mathbb{R}} \mathrm{STFT}[u_\varepsilon, h_t h_x](t, x - \varepsilon l; \omega, k) \mathrm{STFT}^*[u_\varepsilon, h_t h_x](t, x + \varepsilon l; \omega, k) \; P^{(2)}(l) dl\end{aligned} \tag{4.60}$$

Same derivation can be applied for the scattering term in eq. (4.26) with "$-k$" (energy in the opposite direction):

$$\begin{aligned}
&\frac{k^2}{4}\widehat{P}(2k)\mathrm{W}_\varepsilon[u_\varepsilon](-k)**\mathrm{W}_\varepsilon[h_t h_x] \\
&= -\frac{\varepsilon^2}{16}\frac{1}{(2\pi)^2}\int_{\mathbb{R}}\int_{\mathbb{R}^2} u_\varepsilon(t-\varepsilon\alpha, x-\varepsilon l-\varepsilon m)\; h_t^*(\varepsilon\alpha)\; h_x(\varepsilon m)\; e^{i(\alpha\omega-mk)}\; d\alpha dm \\
&\qquad\qquad \int_{\mathbb{R}^2} u_\varepsilon^*(t-\varepsilon\beta, x-\varepsilon l+\varepsilon n)\; h_t(\varepsilon\beta)\; h_x^*(\varepsilon n)\; e^{-i(\beta\omega-nk)}\; d\beta dn\; P^{(2)}(l)dl \\
&= -\frac{1}{16}\int_{\mathbb{R}} \mathrm{STFT}[u_\varepsilon, h_t h_x^*](t, x-\varepsilon l;\omega,-k)\mathrm{STFT}^*[u_\varepsilon, h_t h_x^*](t, x+\varepsilon l;\omega,-k)\; P^{(2)}(l)dl
\end{aligned} \tag{4.61}$$

Combining the two transport terms in equations 4.50, (4.51) and the two scattering terms in eqs. (4.60), (4.61) and projecting in "±", the filtered radiative transfer equation for forward and backward waves is obtained:

$$\begin{aligned}
&2\mathrm{Re}\left\{\mathrm{STFT}[v_{h\Delta t}, h_t h_x](t,x;c_0k,\mp k)\mathrm{STFT}^*[u_{h\Delta t}, h_t h_x](t,x;c_0k,\mp k)\right\} \\
&\pm 2c_0\mathrm{Re}\left\{\mathrm{STFT}[\partial_x u_{h\Delta t}, h_t h_x](t,x;c_0k,\mp k)\mathrm{STFT}^*[u_{h\Delta t}, h_t h_x](t,x;c_0k,\mp k)\right\} \\
=&-\frac{1}{16}\int_{\mathbb{R}} \mathrm{STFT}[u_{h\Delta t}, h_t h_x^*](t,x-\varepsilon l;c_0k,\pm k)\mathrm{STFT}^*[u_{h\Delta t}, h_t h_x^*](t,x+\varepsilon l;c_0k,\pm k)\; P^{(2)}(l)dl \\
&+\frac{1}{16}\int_{\mathbb{R}} \mathrm{STFT}[u_{h\Delta t}, h_t h_x](t,x-\varepsilon l;c_0k,\mp k)\mathrm{STFT}^*[u_{h\Delta t}, h_t h_x](t,x+\varepsilon l;c_0k,\mp k)\; P^{(2)}(l)dl
\end{aligned} \tag{4.62}$$

Then the filtered residual errors are obtained in eq. (4.48) as we did in eq. (4.41).

□

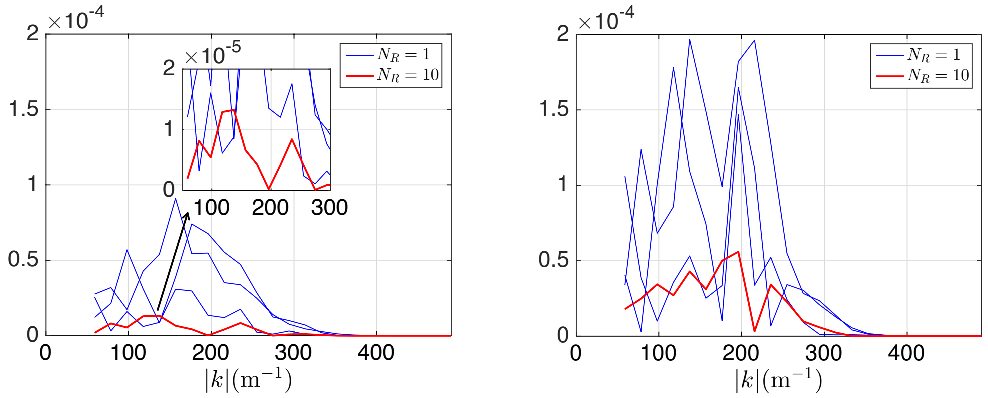

(a) (b)

Fig. 4.26 Filtered residual errors along $\omega = \pm c_0 k$ for coherent wave: (a) $\left|\mathrm{R}_T^{\mathrm{sd}} ** \mathrm{W}[h_t h_x]\right|$, (b) $\left|\mathrm{R}_{TS}^{\mathrm{sd}} ** \mathrm{W}[h_t h_x]\right|$

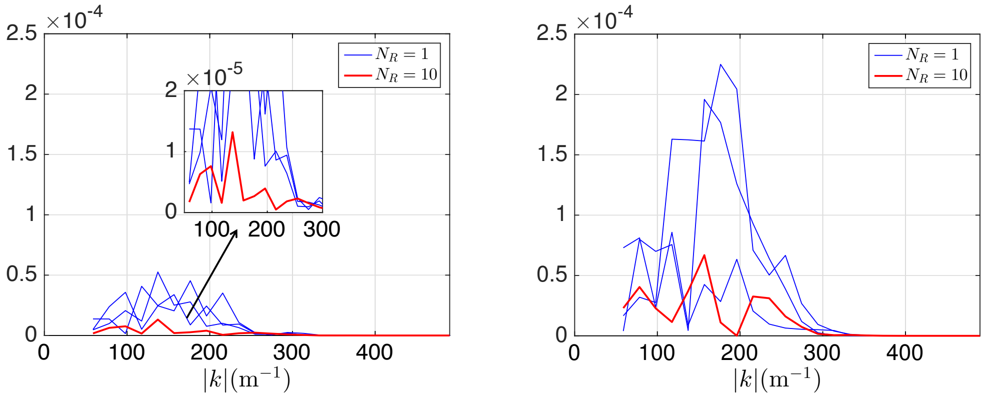

(a) (b)

Fig. 4.27 Filtered residual errors along $\omega = \pm c_0 k$ for incoherent wave: (a) $\left|\mathrm{R}_T^{\mathrm{sd}} * * \mathrm{W}[h_t h_x]\right|$, (b) $\left|\mathrm{R}_{TS}^{\mathrm{sd}} * * \mathrm{W}[h_t h_x]\right|$

We consider the same wave propagation problem in ten realizations of random media as in section 4.2.3. Then we compute the absolute value of the filtered residual errors $\left|\mathrm{R}_T^{\mathrm{sd}}[u_{h\Delta t}] * * \mathrm{W}_\varepsilon[h_t h_x]\right|$ and $\left|\mathrm{R}_{TS}^{\mathrm{sd}}[u_{h\Delta t}] * * \mathrm{W}_\varepsilon[h_t h_x]\right|$ with eq. (4.48) for coherent waves (fig. 4.19) and incoherent waves (fig. 4.22).

Numerical results are illustrated in fig. 4.26 for coherent waves and in fig. 4.27 for incoherent waves. Compared to the residual errors without filtering in fig. 4.20 and fig. 4.24, errors concentrated at low frequencies are largely reduced. It is observed that the errors are mainly concentrated around the main frequency band of wave fields with the effect of the filtering of window functions. It means that we get a more reasonable distribution of errors in terms of frequency.

4.4 Comparison of residual errors for two refinements

In this section, in order to study the behaviour of the proposed residual errors with respect to the discretization size in space and in time, numerical wave solutions obtained by using a space mesh twice coarser and a time step twice larger than those used in the section 4.2.3 are considered, so we have $\lambda(3k_{max})/h = 10, \Delta t = h/c_0$. Otherwise, all the numerical parameters for calculating the energy-based residual errors, such as the computation region of Wigner transform, the random points chosen for average, remain unchanged. The residual errors calculated for both discretization sizes are compared and it is hoped that they would decrease when the discretization in space and in time is refined.

The residual errors defined in eq. (4.41) and the filtered residual errors defined in eq. (4.48) are computed respectively for coherent waves and incoherent waves as we did in the section 4.2.3. The numerical results are illustrated in fig. 4.28 and fig. 4.30, fig. 4.29 and fig. 4.31. It can be observed that for coherent waves (figs. 4.28 and 4.29), as expected both residual errors and filtered residual errors are smaller, especially over the main frequency range defined by the considered ricker signal, for the wave solutions calculated with the finer discretization. Nevertheless, the decrease of residual errors between the two discretizations is largely reduced after the filtering, which is not yet well understood for the moment. As far as the incoherent waves are concerned, both residual errors and filtered residual errors give unsatisfying results, in fact no obvious decrease of errors is observed with the finer discretization (figs. 4.28 and 4.29). There are several reasons that may account for this phenomena. In section 3.3.1, it was observed that numerical dispersion and dissipation may influence the quality of estimated errors. Here after a long propagation time, the dispersion or dissipation of incoherent waves become significant. Thus the decrease of errors are not found as we observed in fig. 3.13b. Besides, when we refine the mesh size and the time step, the elastic parameter E is also refined. It means that the two solutions here are in fact calculated with two numerical models that have slightly different physical properties. That may also disturb the results of errors. There exist also other possible reasons, such as numerical fluctuations resulting from frequency leakage, numerical differentiation and the distribution of cross terms, existence of localization, etc. Further studies are necessary to understand these results and to resolve this problem.

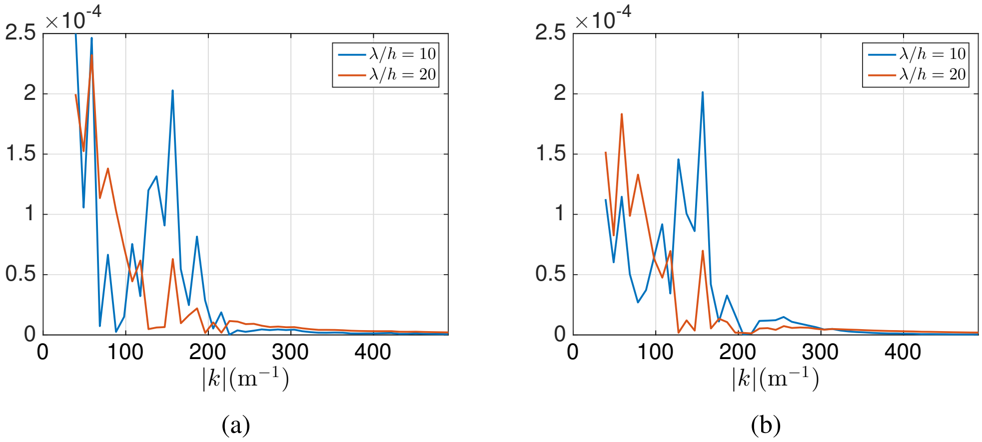

Fig. 4.28 Results for coherent waves: (a) $\left|\mathrm{R}_T^{\mathrm{sd}}\right|$, (b) $\left|\mathrm{R}_{TS}^{\mathrm{sd}}\right|$

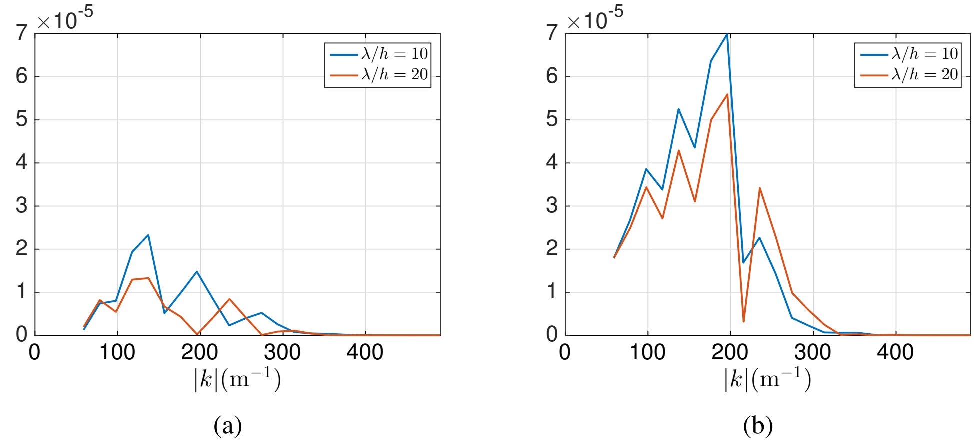

Fig. 4.29 Results for coherent waves: (a) $\left|\mathrm{R}_T^{\mathrm{sd}} * * \mathrm{W}[h_t h_x]\right|$, (b) $\left|\mathrm{R}_{TS}^{\mathrm{sd}} * * \mathrm{W}[h_t h_x]\right|$

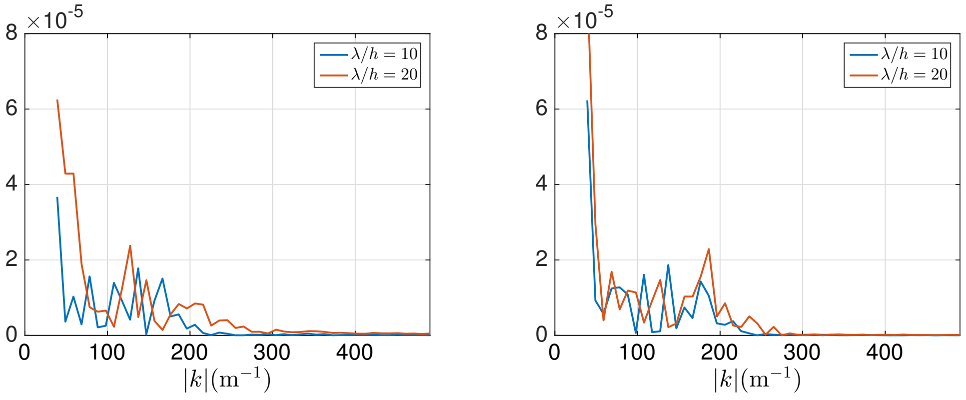

(a) (b)

Fig. 4.30 Results for incoherent waves: (a) $\left|\mathrm{R}_T^{\mathrm{sd}}\right|$, (b) $\left|\mathrm{R}_{TS}^{\mathrm{sd}}\right|$

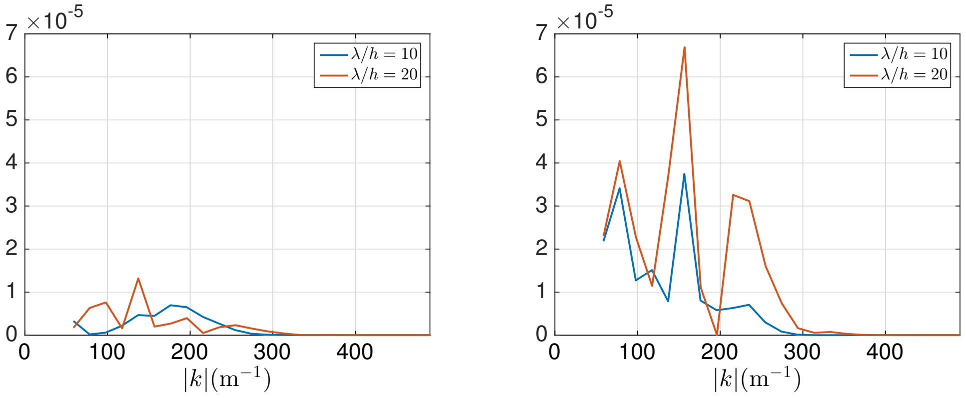

(a) (b)

Fig. 4.31 Results for incoherent waves: (a) $\left|\mathrm{R}_T^{\mathrm{sd}} **\mathrm{W}[h_t h_x]\right|$, (b) $\left|\mathrm{R}_{TS}^{\mathrm{sd}} **\mathrm{W}[h_t h_x]\right|$

4.5 Conclusion

This chapter dealt with energy-based residual error for high frequency wave fields in heterogeneous media. We introduced the heterogeneous media modelled with realizations of random fields of mechanical properties. Radiative transfer equation that describes the transport and the scattering of wave energy is obtained in these media in the weak coupling regime. 1D radiative transfer equations were studied and solved analytically. The characteristic length for wave propagation in random media, i.e. the scattering mean free path was introduced. It was observed that in low frequency and high frequency limits, the scattering mean free path becomes unbounded. The localization phenomenon that always exists in 1D was analyzed by considering the wave propagation problems in two random media with different amplitudes of fluctuations. This analysis allowed finding a region in a random medium where the radiative transfer regime still holds. Then based on the radiative transfer equation, the residual errors of numerical solutions of wave equation were defined and computed numerically. It was found that the obtained errors are very small compared to the total energy. Also, large part of errors are concentrated around low frequencies due to cross terms of Wigner transform of random fields.

In order to eliminate this effect, a filtering of residual errors was derived based on the convolution properties of Wigner transform. It also favours the smoothing of the results. Numerical results showed that this filtering with window function can reduce partly the pollution on errors caused by cross terms, especially for low frequency. Finally, the decrease of errors with refinement was found with coherent waves as we expected. However, the influence of filtering and the unexpected results for incoherent waves remain to be improved.

Chapter 5

Conclusions and perspectives

Wave propagation in heterogeneous media, especially in the high frequency regime is always a challenging and complex problem. Its numerical modelling and simulation require very accurate numerical methods with high computational and memory costs. This work is dedicated to the development of tools of error estimation for finite element solutions of wave equation in heterogeneous media, which will be used to find solutions with a desired precision at a moderate cost.

Firstly, an explicit *a posteriori* upper bound for the errors between the exact solution and the reconstructed approximate solution in an L^∞-norm of energy in time was derived analytically for the elastodynamic equation.

The basic idea of this derivation is based on the residual error method and the use of reconstructions. In consideration of the requirement of regularities for the error bound, we have proposed two reconstructions in time with different quantities or orders for displacement and velocity fields, and two reconstructions in space for stress field: one is a basic reconstruction based on an element-wise weak equilibrium relation, another is the statically admissible reconstruction, inspired by Ladevèze [90]. We studied firstly the behaviour of the exact numerical errors in homogeneous and heterogeneous cases with two different degrees of heterogeneity. The finite element solutions are solved with different mesh sizes and time steps. We found that the errors are decreasing with the refinement in all cases. An exchange between errors in kinetic and potential energy norms has been observed when waves interact with boundaries and interfaces. Finally, by choosing different combinations of reconstructions, the estimated errors were compared with the exact errors in the homogeneous case. A fully computable error upper bound has been found with our error estimator but the ratio of the estimated and exact errors is increasing as the computational effort grows. It means that the asymptotic accuracy of the obtained estimator remains to be improved. Some discussions and analysis on the results showed that the residual errors related to the time derivative of the equilibrium equation are dominant in the contribution of total estimated errors.

Secondly, considering the difficulties encountered in numerical applications of the error bound for the elastodynamic equation, a specific case, the high frequency wave propagation in the weak coupling regime was studied. As the traditional error estimators on the wave equation may not be efficient in this regime, we proposed a quantification of errors with a kinetic model in terms of energy densities, i.e. the transport equation in homogeneous media and the radiative transfer equation in heterogeneous media. This kinetic model allows smoothing out the highly oscillatory features of waves. Based on this new equation, we defined analytically a new residual-type error estimation method. The errors are quantified in terms of energy quantities of numerical waves, which are calculated by the Wigner transform of wave fields.

In 1D homogeneous media, the localization of errors around the characteristics in phase space was observed. Considering the existence of extra fluctuations by frequency leakage, a filtering of errors with window functions in phase space was proposed and a global residual error in time-space domain was defined. The decrease of local and global errors when the discretization size decreases was observed, which allows validating our definition of errors and methods of calculation.

In 1D heterogeneous media, the residual errors in terms of the total energy and the net forward-going energy were proposed analytically. In numerical applications, a 1D medium with a small magnitude of fluctuations was firstly found so that less localization exists and the radiative transfer regime holds. Also an agreement between the radiative transfer energy and the numerical wave energy allowed validating our calculations. Then the defined errors in the chosen medium with a fine mesh were computed with the energy quantities of numerical wave solutions. The results revealed that the defined errors are relatively small compared to the total energy, that allowed validating our definition of errors. In order to reduce the influence of cross terms and other fluctuations on the distribution of errors in terms of frequency and to obtain a smoother result of errors, a filtering of residual errors in terms of the STFT of wave fields was derived. It is based on the convolution of radiative transfer equation with Wigner transform of a window function. This filtering allowed reducing especially the cross terms accumulated in low frequencies. Finally, the comparison of errors in phase space for numerical solutions with two different discretizations sizes was obtained. For coherent waves, residual errors are smaller for the finer discretization size as we expected. However, the decrease of residual errors between the two discretizations was reduced after the filtering. For incoherent waves, no obvious decrease of errors was found with the finer discretization. Some possible reasons were given and a detailed analysis remains to be made in future works.

Some improvements, perspectives and difficulties are discussed here.

In a short term, efforts should be made firstly for resolving the existing problems. For the explicit error bound defined for elastodynamics that has a weak asymptotic accuracy, the reconstructions in time and in space should be reconsidered. They were defined with some desired regularities but they also bring in additional errors since they can be seen as a post-treatment of approximate solutions. Further efforts are needed to propose some new reconstructions so as to achieve a better equilibrium, especially for the time derivative of equilibrium on the entire time interval. For the energy-based residual errors in heterogeneous media, future works should be firstly focused on discussing and analyzing the phenomena in the comparison of errors with two discretization sizes as we discussed above. Besides, at present the identification of energy-based errors in terms of frequency seems difficult to achieve due to the superposition of cross terms between all frequency components. Since the filtering with the STFT allows already reducing largely cross terms in low frequencies, this idea may be applied in future works. It may allow quantifying the effect of numerical dispersion. In the whole work, we merely defined errors to quantify the difference between the exact solutions and the approximate solutions solved by time discontinuous Galerkin method. Other solvers or discretization methods, such as Newmark, should also be tested to observe their influence on the estimator. Note that the proposed reconstructions may be adapted to the choice of solvers.

Furthermore, in the radiative transfer regime, only wave propagation in an infinite region is considered. We ignore the calculation of Wigner transform in the boundaries in the homogeneous case when waves are totally reflected by the boundary. Difficulties arise when the energy densities reach the boundaries of the domain or an interface. Some researchers have studied systematically the boundary or interface conditions for the high frequency waves propagation in media with some specific boundaries or interfaces [18, 122, 135]. But generally it is difficult to construct the Wigner transform of wave fields with respect to boundary conditions in the case with arbitrary geometries of the boundary and interfaces. Future works may be focused on errors based on the initial boundary value problem for the radiative transport equation in some simple cases with specific boundaries and interfaces.

Finally, the energy-based residual errors were analytically defined in 3D, so future works may extend the numerical results of 1D media to a higher dimension. It should be noticed that localization exists always in 1D media so applications on higher dimension are necessary. Note that the computation and storage costs will be very expensive in higher dimensions in the sense that the Wigner transform depends on $(t, \mathbf{x}; \omega, \mathbf{k})$, i.e. six independent variables in 2D, and eight independent variables in 3D. However, considering that the dispersion relation $\omega = c_{p,s} |\mathbf{k}|$ is always obtained and involved in the radiative transfer equation, we can study only the quantities on the hypersurface defined by this relation (2D media), that may allow reducing significantly the storage cost.

References

[1] Achenbach, J. (2012). *Wave propagation in elastic solids*, volume 16. Elsevier.

[2] Adams, R. A. and Fournier, J. J. (2003). *Sobolev spaces*, volume 140. Academic press.

[3] Adjerid, S. (2002). A posteriori finite element error estimation for second-order hyperbolic problems. *Computer methods in applied mechanics and engineering*, 191(41):4699–4719.

[4] Aggelis, D. (2009). Numerical simulation of surface wave propagation in material with inhomogeneity: Inclusion size effect. *Ndt & E International*, 42(6):558–563.

[5] Ainsworth, M., Monk, P., and Muniz, W. (2006). Dispersive and dissipative properties of discontinuous galerkin finite element methods for the second-order wave equation. *Journal of Scientific Computing*, 27(1-3):5–40.

[6] Ainsworth, M. and Oden, J. T. (2011). *A posteriori error estimation in finite element analysis*, volume 37. John Wiley & Sons.

[7] Aki, K. and Richards, P. G. (1980). Quantative seismology: Theory and methods. *New York*, page 801.

[8] Aki, K. and Wu, R.-S. (1988). Scattering and attenuation of seismic waves, part i. *Pure and Applied Geophysics*, 128.

[9] Arce, G. R. and Hasan, S. R. (2000). Elimination of interference terms of the discrete wigner distribution using nonlinear filtering. *IEEE transactions on Signal Processing*, 48(8):2321–2331.

[10] Aubry, D., Lucas, D., and Tie, B. (1999). Adaptive strategy for transient/coupled problems applications to thermoelasticity and elastodynamics. *Computer methods in applied mechanics and engineering*, 176(1-4):41–50.

[11] Auger, F., Flandrin, P., Gonçalvès, P., and Lemoine, O. (1996). Time-frequency toolbox. *CNRS France-Rice University*, 46.

[12] Baba, T. (2012). Time-frequency analysis using short time fourier transform. *The Open Acoustics Journal*, 5(1).

[13] Babuška, I. and Rheinboldt, W. C. (1978). A posteriori error estimates for the finite element method. *International Journal for Numerical Methods in Engineering*, 12(10):1597–1615.

[14] Babuska, I., Whiteman, J., and Strouboulis, T. (2010). *Finite elements: an introduction to the method and error estimation*. Oxford University Press.

[15] Bai, X. (2017). *Finite Element Modeling of Ultrasonic Wave Propagation in Polycrystalline Materials*. PhD thesis, CentraleSupélec. Codirection avec Denis Aubry (MSSMat) et Jean-Hubert Schmitt (MSSMat).

[16] Bai, X., Tie, B., Schmitt, J.-H., and Aubry, D. (Accepted for publication. February 2018.). Finite element modeling of grain size effects on the ultrasonic microstructural noise backscattering in polycrystalline materials. *Ultrasonics*, –(–):23 pages.

[17] Bal, G. (2005). Kinetics of scalar wave fields in random media. *Wave Motion*, 43(2):132–157.

[18] Bal, G., Keller, J. B., Papanicolaou, G., and Ryzhik, L. (1999). Transport theory for acoustic waves with reflection and transmission at interfaces. *Wave Motion*, 30(4):303–327.

[19] Bal, G., Komorowski, T., and Ryzhik, L. (2003). Self-averaging of wigner transforms in random media. *Communications in mathematical physics*, 242(1-2):81–135.

[20] Bal, G. and Pinaud, O. (2006). Accuracy of transport models for waves in random media. *Wave Motion*, 43(7):561–578.

[21] Banerjee, P. K. and Butterfield, R. (1981). *Boundary element methods in engineering science*, volume 17. McGraw-Hill London.

[22] Bangerth, W. and Rannacher, R. (1999). Finite element approximation of the acoustic wave equation: Error control and mesh adaptation. *East West Journal of Numerical Mathematics*, 7(4):263–282.

[23] Bank, R. E. and Weiser, A. (1985). Some a posteriori error estimators for elliptic partial differential equations. *Mathematics of computation*, 44(170):283–301.

[24] Baydoun, I., Baresch, D., Pierrat, R., and Derode, A. (2015). Scattering mean free path in continuous complex media: Beyond the helmholtz equation. *Physical Review E*, 92(3):033201.

[25] Baydoun, I., Savin, É., Cottereau, R., Clouteau, D., and Guilleminot, J. (2014). Kinetic modeling of multiple scattering of elastic waves in heterogeneous anisotropic media. *Wave Motion*, 51(8):1325–1348.

[26] Bebendorf, M. et al. (2003). A note on the poincaré inequality for convex domains.

[27] Bedford, A. and Drumheller, D. (1994). Elastic wave propagation. *John Wileg g Sons*, pages 151–165.

[28] Bergam, A., Bernardi, C., and Mghazli, Z. (2005). A posteriori analysis of the finite element discretization of some parabolic equations. *Mathematics of computation*, 74(251):1117–1138.

[29] Bieterman, M. and Babuška, I. (1982). The finite element method for parabolic equations. *Numerische Mathematik*, 40(3):373–406.

[30] Blitz, J. and Simpson, G. (1995). *Ultrasonic methods of non-destructive testing*, volume 2. Springer Science & Business Media.

[31] Bloomfield, P. (2004). *Fourier analysis of time series: an introduction*. John Wiley & Sons.

[32] Boashash, B. (2015). *Time-frequency signal analysis and processing: a comprehensive reference*. Academic Press.

[33] Boore, D. M. (1972). Finite difference methods for seismic wave propagation in heterogeneous materials. *Methods in computational physics*, 11:1–37.

[34] Boutin, C. (2007). Rayleigh scattering of acoustic waves in rigid porous media. *The Journal of the Acoustical Society of America*, 122(4):1888–1905.

[35] Bracewell, R. N. and Bracewell, R. N. (1986). *The Fourier transform and its applications*, volume 31999. McGraw-Hill New York.

[36] Brougois, A., Bourget, M., Lailly, P., Poulet, M., Ricarte, P., and Versteeg, R. (1990). Marmousi, model and data. In *EAEG Workshop-Practical Aspects of Seismic Data Inversion*.

[37] Burq, N. and Joly, R. (2016). Exponential decay for the damped wave equation in unbounded domains. *Communications in Contemporary Mathematics*, 18(06):1650012.

[38] Capdeville, Y., Guillot, L., and Marigo, J.-J. (2010). 1-d non-periodic homogenization for the seismic wave equation. *Geophysical Journal International*, 181(2):897–910.

[39] Charles, K. (2008). Mother earth gets undressed. *Nature News*.

[40] Ciarlet, P. G. (2002). The finite element method for elliptic problems. *Classics in applied mathematics*, 40:1–511.

[41] Codona, J. L. (1985). *Electromagnetic wave propagation through random media*. Johanan Codona.

[42] Cohen, L. (1989). Time-frequency distributions-a review. *Proceedings of the IEEE*, 77(7):941–981.

[43] Corones, J., Dougherty, R., and McMaken, H. (1984). A new parabolic approximation to the helmholtz equation. In *Review of Progress in Quantitative Nondestructive Evaluation*, pages 123–131. Springer.

[44] Cottereau, R., Chamoin, L., and Diez, P. (2010). Strict error bounds for linear and nonlinear solid mechanics problems using a patch-based flux-free method. *Mechanics & Industry*, 11(3-4):249–254.

[45] Cottereau, R. and Diez, P. (2015). Fast r-adaptivity for multiple queries of heterogeneous stochastic material fields. *Computational mechanics*, 56(4):601–612.

[46] Deka, B. (2017). A priori $L^\infty(L^2)$ error estimates for finite element approximations to the wave equation with interface. *Applied Numerical Mathematics*, 115:142–159.

[47] Demkowicz, L., Oden, J. T., Rachowicz, W., and Hardy, O. (1989). Toward a universal hp adaptive finite element strategy, part 1. constrained approximation and data structure. *Computer Methods in Applied Mechanics and Engineering*, 77(1-2):79–112.

[48] Dhia, A.-S. B.-B., Duclairoir, E.-M., Legendre, G., and Mercier, J.-F. (2007). Time-harmonic acoustic propagation in the presence of a shear flow. *Journal of Computational and Applied Mathematics*, 204(2):428–439.

[49] Dhua, S. and Chattopadhyay, A. (2016). Wave propagation in heterogeneous layers of the earth. *Waves in Random and Complex Media*, 26(4):626–641.

[50] Díez, P., JoséEgozcue, J., and Huerta, A. (1998). A posteriori error estimation for standard finite element analysis. *Computer Methods in Applied Mechanics and Engineering*, 163(1-4):141–157.

[51] Díez, P., Parés, N., and Huerta, A. (2010). Error estimation and quality control. *Encyclopedia of Aerospace Engineering*.

[52] Dormy, E. and Tarantola, A. (1995). Numerical simulation of elastic wave propagation using a finite volume method. *Journal of Geophysical Research: Solid Earth*, 100(B2):2123–2133.

[53] Erdős, L. (1999). Linear boltzmann equation as the weak coupling limit of the random schrödinger equation. In *Mathematical Results in Quantum Mechanics*, pages 233–242. Springer.

[54] Eriksson, K. and Johnson, C. (1991). Adaptive finite element methods for parabolic problems i: A linear model problem. *SIAM Journal on Numerical Analysis*, 28(1):43–77.

[55] Eriksson, K. and Johnson, C. (1995). Adaptive finite element methods for parabolic problems iv: Nonlinear problems. *SIAM Journal on Numerical Analysis*, 32(6):1729–1749.

[56] Fish, J. and Chen, W. (2004). Space–time multiscale model for wave propagation in heterogeneous media. *Computer Methods in applied mechanics and engineering*, 193(45-47):4837–4856.

[57] Furnas, C. (1930). Evaluation of the modified bessel function of the first kind and zeroth order. *The American Mathematical Monthly*, 37(6):282–287.

[58] Gabor, D. (1946). Theory of communication. part 1: The analysis of information. *Journal of the Institution of Electrical Engineers-Part III: Radio and Communication Engineering*, 93(26):429–441.

[59] Gatti, F., Paludo, L. D. C., Svay, A., Cottereau, R., Clouteau, D., et al. (2017). Investigation of the earthquake ground motion coherence in heterogeneous non-linear soil deposits. *Procedia Engineering*, 199:2354–2359.

[60] Georgoulis, E. H., Lakkis, O., and Makridakis, C. (2013). A posteriori $L^{\infty}(L^2)$-error bounds for finite element approximations to the wave equation. *IMA Journal of Numerical Analysis*, 33(4):1245–1264.

[61] Ghatak, A. and Lokanathan, S. (2004). The dirac delta function. In *Quantum Mechanics: Theory and Applications*, pages 3–18. Springer.

[62] Godin, O. A. (2013). Rayleigh scattering of a spherical sound wave. *The Journal of the Acoustical Society of America*, 133(2):709–720.

[63] Gonçalves, P. and Baraniuk, R. G. (1998). Pseudo affine wigner distributions: Definition and kernel formulation. *IEEE Transactions on Signal Processing*, 46(6):1505–1516.

[64] Gottlieb, D. and Orszag, S. A. (1977). *Numerical analysis of spectral methods: theory and applications*, volume 26. Siam.

[65] Hadeler, K. (1996). Reaction telegraph equations and random walk systems. *Stochastic and spatial structures of dynamical systems*, pages 133–161.

[66] Hahn, S. L. (1996). *Hilbert transforms in signal processing*, volume 2. Artech House Boston.

[67] Hancock, M. J. (2006). Solution to problems for the 1-d wave equation.

[68] Harris, F. J. (1978). On the use of windows for harmonic analysis with the discrete fourier transform. *Proceedings of the IEEE*, 66(1):51–83.

[69] Hirsekorn, S. (1982). The scattering of ultrasonic waves by polycrystals. *The Journal of the Acoustical Society of America*, 72(3):1021–1031.

[70] Hlawatsch, F. (1984). Interference terms in the wigner distribution. *Digital signal processing*, 84:363–367.

[71] Hlawatsch, F. and Boudreaux-Bartels, G. F. (1992). Linear and quadratic time-frequency signal representations. *IEEE signal processing magazine*, 9(2):21–67.

[72] Howe, M. (1973). On the kinetic theory of wave propagation in random media. *Philosophical Transactions of the Royal Society of London A: Mathematical, Physical and Engineering Sciences*, 274(1242):523–549.

[73] Howe, M. (1974). A kinetic equation for wave propagation in random media. *The Quarterly Journal of Mechanics and Applied Mathematics*, 27(2):237–253.

[74] Hu, F. Q., Hussaini, M., and Rasetarinera, P. (1999). An analysis of the discontinuous galerkin method for wave propagation problems. *Journal of Computational Physics*, 151(2):921–946.

[75] Hughes, T. J. (2012). *The finite element method: linear static and dynamic finite element analysis*. Courier Corporation.

[76] Hughes, T. J. and Hulbert, G. M. (1988). Space-time finite element methods for elastodynamics: formulations and error estimates. *Computer methods in applied mechanics and engineering*, 66(3):339–363.

[77] Ibrahima, F. (2011). *Estimation d'erreur pour des problèmes de propagation d'ondes en milieux élastiques linéaires hétérogènes*. Internship report, Ecole Centrale Paris.

[78] Ishimaru, A. (1978). *Wave propagation and scattering in random media*, volume 2. Academic press New York.

[79] Janssen, A. (1979). *Application of the Wigner distribution to harmonic analysis of generalized stochastic processes*, volume 114. Mathematisch Centrum Amsterdam.

[80] Jenkins, E. W., Riviaere, B., and Wheeler, M. F. (2002). A priori error estimates for mixed finite element approximations of the acoustic wave equation. *SIAM Journal on Numerical Analysis*, 40(5):1698–1715.

[81] Jerri, A. J. (1977). The shannon sampling theorem—its various extensions and applications: A tutorial review. *Proceedings of the IEEE*, 65(11):1565–1596.

[82] Johnson, C. (1993). Discontinuous galerkin finite element methods for second order hyperbolic problems. *Computer Methods in Applied Mechanics and Engineering*, 107(1-2):117–129.

[83] Kadambe, S. and Boudreaux-Bartels, G. F. (1992). A comparison of the existence of'cross terms' in the wigner distribution and the squared magnitude of the wavelet transform and the short-time fourier transform. *IEEE Transactions on signal processing*, 40(10):2498–2517.

[84] Kapralos, B., Jenkin, M., and Milios, E. (2008). Sonel mapping: a probabilistic acoustical modeling method. *Building Acoustics*, 15(4):289–313.

[85] Karal Jr, F. C. and Keller, J. B. (1959). Elastic wave propagation in homogeneous and inhomogeneous media. *The Journal of the acoustical society of america*, 31(6):694–705.

[86] Khazaie, S. (2015). *Influence of the statistical parameters of a random heterogeneous medium on elastic wave scattering: theoretical and numerical approaches*. PhD thesis, Ecole Centrale Paris.

[87] Komatitsch, D. and Tromp, J. (1999). Introduction to the spectral element method for three-dimensional seismic wave propagation. *Geophysical journal international*, 139(3):806–822.

[88] Ladevèze, P. (2000). Constitutive relation error estimators for time-dependent non-linear fe analysis. *Computer Methods in Applied Mechanics and Engineering*, 188(4):775–788.

[89] Ladeveze, P. and Leguillon, D. (1983). Error estimate procedure in the finite element method and applications. *SIAM Journal on Numerical Analysis*, 20(3):485–509.

[90] Ladevèze, P. and Pelle, J.-P. (2005). *Mastering calculations in linear and nonlinear mechanics*, volume 171. Springer.

[91] Lapeyre, B., Pardoux, E., and Sentis, R. (2003). *Introduction to Monte-Carlo methods for transport and diffusion equations*, volume 6. Oxford University Press on Demand.

[92] LeVeque, R. J. (2002). *Finite volume methods for hyperbolic problems*, volume 31. Cambridge university press.

[93] Li, A., Roberts, R., Margetan, F. J., and Thompson, R. (2002). Influence of forward scattering on ultrasonic attenuation measurement. In *AIP Conference Proceedings*, volume 615, pages 51–58. AIP.

[94] Li, X., Han, X., Li, R., and Jiang, H. (2007). Geometrical-optics approximation of forward scattering by gradient-index spheres. *Applied optics*, 46(22):5241–5247.

[95] Li, X. D. and WIBERG, N.-E. (1996). Structural dynamic analysis by a time-discontinuous galerkin finite element method. *International Journal for Numerical Methods in Engineering*, 39(12):2131–2152.

[96] Lin, W. and Wu, C. (1994). The systems of second order partial differential equations with constant coefficients. In *Partial Differential Equations in China*, pages 173–181. Springer.

[97] Lions, P.-L. and Paul, T. (1993). Sur les mesures de wigner. *Revista matemática iberoamericana*, 9(3):553–618.

[98] Lombard, B., Maurel, A., and Marigo, J.-J. (2017). Numerical modeling of the acoustic wave propagation across a homogenized rigid microstructure in the time domain. *Journal of Computational Physics*, 335:558–577.

[99] Lombard, B. and Piraux, J. (2004). Numerical treatment of two-dimensional interfaces for acoustic and elastic waves. *Journal of Computational Physics*, 195(1):90–116.

[100] Lombard, B. and Piraux, J. (2007). Modeling 1-d elastic p-waves in a fractured rock with hyperbolic jump conditions. *Journal of computational and applied mathematics*, 204(2):292–305.

[101] Lorenzo-Ginori, J. V. (2007). An approach to the 2d hilbert transform for image processing applications. In *International Conference Image Analysis and Recognition*, pages 157–165. Springer.

[102] Lu, W.-k. and Zhang, Q. (2009). Deconvolutive short-time fourier transform spectrogram. *IEEE Signal Processing Letters*, 16(7):576–579.

[103] Manolis, G. D., Dineva, P. S., Rangelov, T. V., and Wuttke, F. (2017). *Seismic Wave Propagation in Non-Homogeneous Elastic Media by Boundary Elements*. Springer.

[104] Mansur, W. and Brebbia, C. (1982). Numerical implementation of the boundary element method for two dimensional transient scalar wave propagation problems. *Applied Mathematical Modelling*, 6(4):299–306.

[105] Marfurt, K. J. (1984). Accuracy of finite-difference and finite-element modeling of the scalar and elastic wave equations. *Geophysics*, 49(5):533–549.

[106] Margerin, L., Campillo, M., and Van Tiggelen, B. (2000). Monte carlo simulation of multiple scattering of elastic waves. *Journal of Geophysical Research: Solid Earth*, 105(B4):7873–7892.

[107] Martin, G. S., Wiley, R., and Marfurt, K. J. (2006). Marmousi2: An elastic upgrade for marmousi. *The Leading Edge*, 25(2):156–166.

[108] McCarthy, F. and Hayes, M. (2013). *Elastic Wave Propagation: Proceedings of the Second IUTAM-IUPAP, Symposium on Elastic Wave Propagation, Galway, Ireland, March 20-25, 1988*, volume 35. Elsevier.

[109] Mozolevski, I. and Prudhomme, S. (2015). Goal-oriented error estimation based on equilibrated-flux reconstruction for finite element approximations of elliptic problems. *Computer Methods in Applied Mechanics and Engineering*, 288:127–145.

[110] Oden, J. T. and Prudhomme, S. (2001). Goal-oriented error estimation and adaptivity for the finite element method. *Computers & mathematics with applications*, 41(5-6):735–756.

[111] Oden, J. T. and Prudhomme, S. (2002). Estimation of modeling error in computational mechanics. *Journal of Computational Physics*, 182(2):496–515.

[112] Paasschens, J. (1997). Solution of the time-dependent boltzmann equation. *Physical Review E*, 56(1):1135.

[113] Payne, L. E. and Weinberger, H. F. (1960). An optimal poincaré inequality for convex domains. *Archive for Rational Mechanics and Analysis*, 5(1):286–292.

[114] Picasso, M. (2010). Numerical study of an anisotropic error estimator in the $L^2(H^1)$ norm for the finite element discretization of the wave equation. *SIAM Journal on Scientific Computing*, 32(4):2213–2234.

[115] Pikula, S. and Beneš, P. (2014). A new method for interference reduction in the smoothed pseudo wigner-ville distribution. In *Proceedings of 8th International Conference on Sensing Technology*, pages 599–603.

[116] Ping, D., Zhao, P., and Deng, B. (2010). Cross-terms suppression in wigner-ville distribution based on image processing. In *Information and Automation (ICIA), 2010 IEEE International Conference on*, pages 2168–2171. IEEE.

[117] Prudhomme, S. and Oden, J. T. (1999). On goal-oriented error estimation for elliptic problems: application to the control of pointwise errors. *Computer Methods in Applied Mechanics and Engineering*, 176(1-4):313–331.

[118] Qian, S. and Morris, J. M. (1992). Wigner distribution decomposition and cross-terms deleted representation. *Signal Processing*, 27(2):125–144.

[119] Ryzhik, L., Papanicolaou, G., and Keller, J. B. (1996). Transport equations for elastic and other waves in random media. *Wave motion*, 24(4):327–370.

[120] Sandsten, M. (2016). Time-frequency analysis of time-varying signals and non-stationary processes. *Lund University Press*.

[121] Sato, H., Fehler, M. C., and Maeda, T. (2012). *Seismic wave propagation and scattering in the heterogeneous earth*, volume 496. Springer.

[122] Savin, É. (2012). Transient vibrational power flows in slender random structures: Theoretical modeling and numerical simulations. *Probabilistic Engineering Mechanics*, 28:194–205.

[123] Savin, É. (2013). Kinetic modeling for transport of elastic waves in anisotropic heterogeneous media. *Procedia IUTAM*, 6:97–107.

[124] Seron, F., Sanz, F., Kindelan, M., and Badal, J. (1990). Finite-element method for elastic wave propagation. *International Journal for Numerical Methods in Biomedical Engineering*, 6(5):359–368.

[125] Sheng, P. (1995). *Introduction to wave scattering, localization and mesoscopic phenomena*, volume 88. Springer Science & Business Media.

[126] Shin, Y. S. and Jeon, J.-J. (1993). Pseudo wigner-ville time-frequency distribution and its application to machinery condition monitoring. *Shock and Vibration*, 1(1):65–76.

[127] Shinozuka, M. and Deodatis, G. (1988). Response variability of stochastic finite element systems. *Journal of Engineering Mechanics*, 114(3):499–519.

[128] Shinozuka, M. and Deodatis, G. (1991). Simulation of stochastic processes by spectral representation. *Applied Mechanics Reviews*, 44(4):191–204.

[129] Shinozuka, M. and Deodatis, G. (1996). Simulation of multi-dimensional gaussian stochastic fields by spectral representation. *Applied Mechanics Reviews*, 49:29–53.

[130] Smith, G. D. (1985). *Numerical solution of partial differential equations: finite difference methods*. Oxford university press.

[131] Smith, W. D. (1975). The application of finite element analysis to body wave propagation problems. *Geophysical Journal International*, 42(2):747–768.

[132] Spohn, H. (1977). Derivation of the transport equation for electrons moving through random impurities. *Journal of Statistical Physics*, 17(6):385–412.

[133] Stanke, F. E. and Kino, G. (1984). A unified theory for elastic wave propagation in polycrystalline materials. *The Journal of the Acoustical Society of America*, 75(3):665–681.

[134] Stanković, L., Alieva, T., and Bastiaans, M. J. (2003). Time–frequency signal analysis based on the windowed fractional fourier transform. *Signal processing*, 83(11):2459–2468.

[135] Staudacher, J. (2013). *Conservative numerical schemes for high-frequency wave propagation in heterogeneous media*. PhD thesis, Ecole Centrale Paris.

[136] Steffens, L. M. and Díez, P. (2009). A simple strategy to assess the error in the numerical wave number of the finite element solution of the helmholtz equation. *Computer methods in applied mechanics and engineering*, 198(15-16):1389–1400.

[137] Süli, E. (1995). *A posteriori error analysis and global error control for adaptive finite element approximations of hyperbolic problems*. Oxford University Computing Laboratory, Numerical Analysis Group.

[138] Süli, E. and Houston, P. (2003). Adaptive finite element approximation of hyperbolic problems. In *Error estimation and adaptive discretization methods in computational fluid dynamics*, pages 269–344. Springer.

[139] Taylor, N. W., Kidder, L. E., and Teukolsky, S. A. (2010). Spectral methods for the wave equation in second-order form. *Physical Review D*, 82(2):024037.

[140] Tie, B. and Aubry, D. (2006). Adaptive time discontinuous galerkin method for numerical modelling of wave propagation in shell and 3d structures. *European Journal of Computational Mechanics/Revue Européenne de Mécanique Numérique*, 15(6):729–757.

[141] Tie, B., Aubry, D., and Boullard, A. (2003). Adaptive computation for elastic wave propagation in plate/shell structures under moving loads. *Revue Europeenne des Elements*, 12(6):717–736.

[142] Turner, C. (2005). Hilbert transforms, analytic functions, and analytic signals. *Retrieved from personal. atl. bellsouth. net/p/h/physics/hilberttransforms. pdf.*

[143] Utku, S. and Melosh, R. J. (1984). Solution errors in finite element analysis. *Computers & structures*, 18(3):379–393.

[144] Van Der Baan, M. (2001). Acoustic wave propagation in one dimensional random media: the wave localization approach. *Geophysical Journal International*, 145(3):631–646.

[145] Van Pamel, A., Brett, C. R., Huthwaite, P., and Lowe, M. J. S. (2015). Finite element modelling of elastic wave scattering within a polycrystalline material in two and three dimensions. *J. Acoust. Soc. Amer.*, 138:2326–2336.

[146] Van Pamel, A., Sha, G., Rokhlin, S., and Lowe, M. (2017). Finite-element modelling of elastic wave propagation and scattering within heterogeneous media. In *Proc. R. Soc. A*, volume 473, page 20160738. The Royal Society.

[147] van Wijk, K., Haney, M., and Scales, J. A. (2004). 1d energy transport in a strongly scattering laboratory model. *Physical Review E*, 69(3):036611.

[148] Virieux, J. (1986). P-sv wave propagation in heterogeneous media: Velocity-stress finite-difference method. *Geophysics*, 51(4):889–901.

[149] Virieux, J., Cruz-Atienza, V., Brossier, R., Chaljub, E., Coutant, O., Garambois, S., Mercerat, D., Prieux, V., Operto, S., Ribodetti, A., et al. (2016). *Modelling seismic wave propagation for geophysical imaging*. Intech.

[150] Vohralík, M. (2013). A posteriori error estimates for efficiency and error control in numerical simulations. *Lecture Notes. Paris: Université Pierre et Marie Curie.*

[151] Wehausen, J. V. and Laitone, E. V. (1960). Surface waves. In *Fluid Dynamics / Strömungsmechanik*, pages 446–778. Springer.

[152] Weisstein, E. W. (2008). Boundary conditions. *From MathWorld–A Wolfram Web Resource. http://mathworld.wolfram.com/BoundaryConditions.html.*

[153] White, J. E. (1965). *Seismic waves: Radiation, transmission, and attenuation.* McGraw-Hill.

[154] Wu, R.-S. and Aki, K. (1988). Introduction: Seismic wave scattering in three-dimensionally heterogeneous earth. *Pure and Applied Geophysics*, 128(1-2):1–6.

[155] Yoon, M.-K. (2005). *Deep seismic imaging in the presence of a heterogeneous overburden.* PhD thesis, Freie Universität Berlin.

[156] Zeng, Y. (2017). Modeling of high-frequency seismic-wave scattering and propagation using radiative transfer theorymodeling of high-frequency seismic-wave scattering and propagation using radiative transfer theory. *Bulletin of the Seismological Society of America*, 107(6):2948–2962.

[157] Zienkiewicz, O. C., Taylor, R. L., Zienkiewicz, O. C., and Taylor, R. L. (1977). *The finite element method*, volume 3. McGraw-hill London.

[158] Zienkiewicz, O. C. and Zhu, J. Z. (1987). A simple error estimator and adaptive procedure for practical engineerng analysis. *International journal for numerical methods in engineering*, 24(2):337–357.

[159] Zienkiewicz, O. C. and Zhu, J. Z. (1992a). The superconvergent patch recovery and a posteriori error estimates. part 1: The recovery technique. *International Journal for Numerical Methods in Engineering*, 33(7):1331–1364.

[160] Zienkiewicz, O. C. and Zhu, J. Z. (1992b). The superconvergent patch recovery and a posteriori error estimates. part 2: Error estimates and adaptivity. *International Journal for Numerical Methods in Engineering*, 33(7):1365–1382.

[161] Zou, H., Lu, X., Dai, Q., and Li, Y. (2002). Nonexistence of cross-term free time-frequency distribution with concentration of wigner-ville distribution. *Science in China Series F: Information Sciences*, 45(3):174–180.

Appendix A

Definition of spaces and useful inequalities

In the following Ω denotes an open set of $\mathbb{R}^d$ equipped with the Lebesgue measure $\mathbf{x}$. We introduce firstly some usual definitions:

Definition A.1 ($L^2(\Omega), L^\infty(\Omega)$)**.** We define:

$$L^2(\Omega) := \left\{ \mathbf{u} : \Omega \to \mathbb{R}^d \mid \mathbf{u} \text{ measurable and } \int_\Omega |\mathbf{u}|^2 d\mathbf{x} < \infty \right\} \tag{A.1}$$

with the L^2-inner product $(\mathbf{u}_1, \mathbf{u}_2)_{(\Omega)} := \int_\Omega \mathbf{u}_1 \cdot \mathbf{u}_2 d\mathbf{x}$ and norm $\|\mathbf{u}\|_{(\Omega)} = \|\mathbf{u}\|_{L^2(\Omega)} := \sqrt{(\mathbf{u}, \mathbf{u})}_{(\Omega)}$.

$$L^\infty(\Omega) := \left\{ \mathbf{u} : \Omega \to \mathbb{R}^d \mid \mathbf{u} \text{ measurable and } \sup_{\mathbf{x} \in \Omega} \mathrm{ess} |\mathbf{u}| < \infty \right\} \tag{A.2}$$

Definition A.2 ($H^1(\Omega), H^1_0(\Omega)$)**.** We define:

$$H^1(\Omega) := \left\{ \mathbf{u} \in L^2(\Omega) \mid D^\alpha \mathbf{u} \in L^2(\Omega), \forall \alpha \text{ such that } |\alpha| \le 1 \right\} \tag{A.3}$$

If Ω is a bound domain $\subset \mathbb{R}^d$ with boundary $\partial\Omega$, we define:

$$H^1_0(\Omega) := \left\{ \mathbf{u} \in H^1(\Omega), \mathbf{u}|_{\partial\Omega} = 0 \right\} \tag{A.4}$$

Definition A.3 (Weak divergence)**.** Let a vector function $\mathbf{v} : \Omega \to \mathbb{R}^d$ be given. $\mathbf{v}$ admits a weak divergence if: 1. $\mathbf{v} \in \left(L^2(\Omega)\right)^d$; 2. there exists a function $w : \Omega \to \mathbb{R}, w \in L^2(\Omega)$ such that

$$(\mathbf{v}, \nabla_\mathbf{x} \varphi)_{(\Omega)} = -(w, \varphi)_{(\Omega)}, \qquad \forall \varphi \in \mathfrak{D}(\Omega) \tag{A.5}$$

where the space $\mathfrak{D}(\Omega)$ is the space of functions from $C^\infty(\bar{\Omega})$ with a compact support in Ω [2]. The function w is called the weak divergence of $\mathbf{v}$ and we note that $\nabla_\mathbf{x} \cdot \mathbf{v} = w$.

Definition A.4 ($H(\mathrm{div},\Omega)$)**.** $H(\mathrm{div},\Omega)$ is the space of all the functions which admit the weak divergence.

Some useful inequalities are also given that are used in our work:

Theorem A.5 (Poincaré's inequality)**.** Suppose that S an element of partition T_h and h_s its size, $\forall \mathbf{u} \in H^1(S)$, there exists a constant C_p such that [26, 113]:

$$\|\mathbf{u}-\mathbf{u}_S\|_{(S)} \leq C_p h_s \|\mathbf{u}-\mathbf{u}_S\|_{1(S)} \tag{A.6}$$

where $\mathbf{u}_S$ is the mean value of $\mathbf{u}$ in S and the norms are defined by $\|\mathbf{u}\|_{(S)} = \|\mathbf{u}\|_{L^2(S)}$ and $\|\mathbf{u}\|_{1(S)} = \|\nabla_{\mathbf{x}} \cdot \mathbf{u}\|_{(S)}$. $\mathbf{u}_s$ is introduced here since the equilibrium of mean value in each element will be used in the derivation of our error upper bound.

Theorem A.6 (Korn's inequality)**.** Assume that Ω is a bound domain and $\Gamma_0 \subset \partial\Omega$ with $|\Gamma_0| > 0$. $\forall \mathbf{u} \in H^1_{\Gamma_0}(\Omega) := \left\{\mathbf{u} \in H^1(\Omega), \mathbf{u}|_{\Gamma_0} = 0\right\}$, there exists a constant $C_k > 0$ such that:

$$\|\mathbf{u}\|_{1(\Omega)} \leq C_k \|\boldsymbol{\varepsilon}(\mathbf{u})\|_{(\Omega)} \tag{A.7}$$

where $\boldsymbol{\varepsilon}(\mathbf{u}) = \frac{1}{2}\left(\nabla_{\mathbf{x}} \otimes \mathbf{u} + (\nabla_{\mathbf{x}} \otimes \mathbf{u})^T\right)$.

Theorem A.7 (Cauchy-Schwarz inequality)**.** For all functions $\mathbf{u}_1$ and $\mathbf{u}_2$ in a vector space F with an inner product $(,)_F$, it is true that:

$$(\mathbf{u}_1,\mathbf{u}_2)_F \leq \sqrt{(\mathbf{u}_1,\mathbf{u}_1)_F(\mathbf{u}_2,\mathbf{u}_2)_F} \tag{A.8}$$

Appendix B

Spectral leakage in FFT

When we calculate Wigner transform in fig. 3.8, some noticeable fluctuations are found around lines that are parallel to the characteristic directions defined by $\omega = \pm c_0 k$. They are in fact the results of a well-known phenomenon called “spectral leakage”, which happens in the discrete Wigner transform calculation.

The spectral leakage is a problem that arises in the digital processing of signals. In fact, for DFT, a signal is truncated firstly in order to obtain a finite set of samples. DFT implicitly assumes that the sampled signal essentially repeats itself after the measured period and hence the signal is continuous (conceptually, juxtapose the measured signal repetitively). This leads to glitches or discontinuities in the boundary of sampling period. Of course, leakage will not occur if a FFT is precisely computed on a periodic signal sampled of an integer number of cycles. However, if the measurement region is purposefully made to be a non-integral multiple of the actual signal rate, these sharp discontinuities will always spread out in the frequency domain leading to spectral leakage. In fig. B.1, when the original periodic signal with one frequency f_0 is sampled in a chosen repeating period with discontinuities in the boundaries, its unique component f_0 in frequency domain has a leakage to other frequencies.

For our wave propagation problems, the Discrete Wigner transform of $u(t,x)$ can be seen as a 2D FT of the auto-correlation functions of displacement $uu^*(\tau,y)$ in a finite area $\zeta_t \times \zeta_x$ (fig. B.2a). The yellow zone can be seen as a time-space period of FFT in 2D.

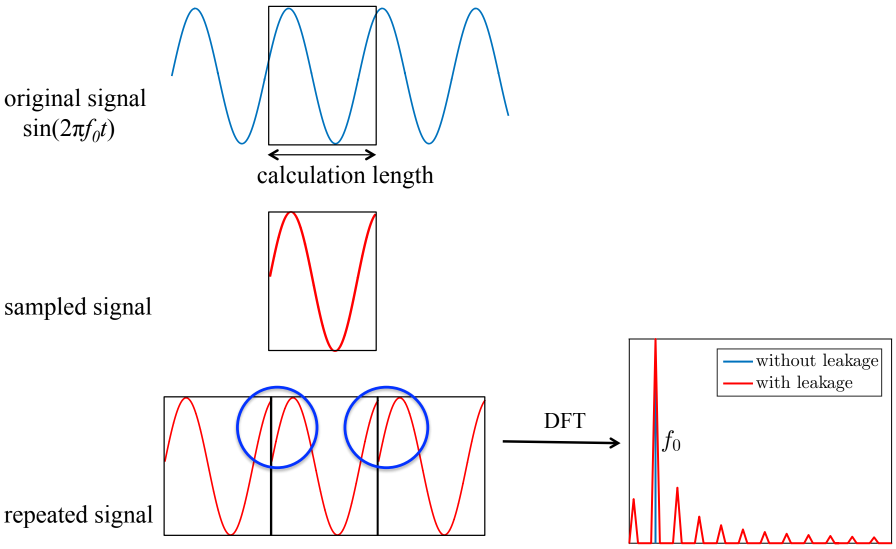

Fig. B.1 Example of the DFT of a periodic signal

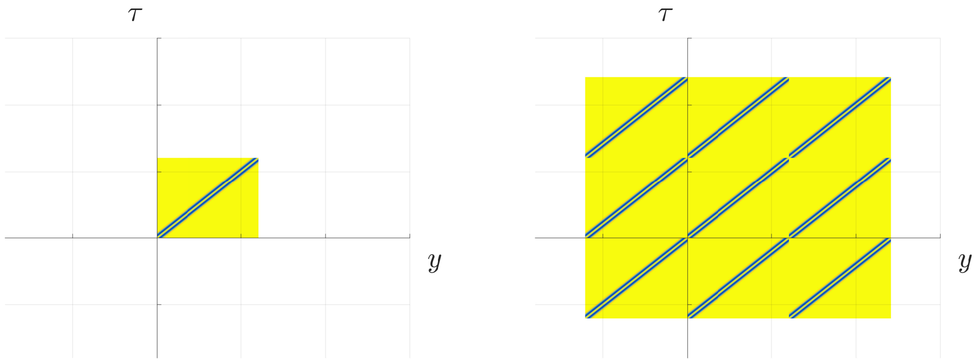

(a) (b)

Fig. B.2 uu^* for point A with discontinuous edges: (a) one period, (b) three periods

Considering the exact solutions of wave propagation in homogeneous media interpolated exactly with respect to $dx = c_0 dt$, uu^* is a rectangular constant function along the characteristic line $x = c_0 t$. Some discontinuities are observed in the two corners of fig. B.2a and more clearly in several periods in fig. B.2b. That is why we obtained the fluctuations around $\omega = -c_0 k$ in phase space in fig. 3.8d. In this case, one method for removing these fluctuations is correcting the discontinuous boundaries by adding points in grid of numerical data such that remains constant (and continuous) along $x = c_0 t$ (fig. B.3a) when it is extended to infinite (fig. B.3b for more periods). Another more simple method is calculating Wigner transform in the rotational coordinates presented in Appendix F. It allows obtaining a constant function in the direction $x = c_0 t$ when the period is repeated. Thus the problem speckage leakage is resolved in this special case (fig. F.2d).

However, for numerical solutions, we can never remove these fluctuations with either of these two methods because of the evolution in time of the numerical dispersions. Also, it cannot be applied in the heterogeneous case since the displacement is no more constant along the propagation direction.

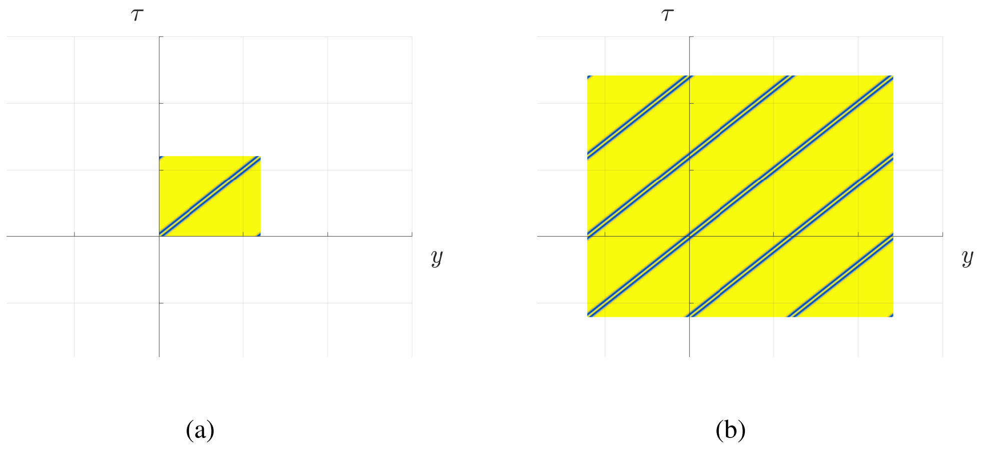

(a)

(b)

Fig. B.3 uu^* for point A with continuous edges: (a) one period, (b) three periods

Several solutions have been proposed by researchers to overcome these edge effects: one popular method for mitigating spectral leakage is called data windowing, which allows to reduce the artificial high frequencies in DFT by finite-length sampling. For example, considering the sampled signal in fig. B.1, it is multiplied by a hann window function. Notice that the sharp discontinuities are eliminated and smoothed out in fig. B.4, even though the repeated signal does not match the original signal. Its DFT has less leakage of frequency for high frequencies and it is more concentrated around f_0. Besides, increasing the sampling length is the best way to decrease spectral leakage regardless of what kind of window you use, which leads to high cost of calculation. In general, we cannot find any method to remove totally the leakage effect.

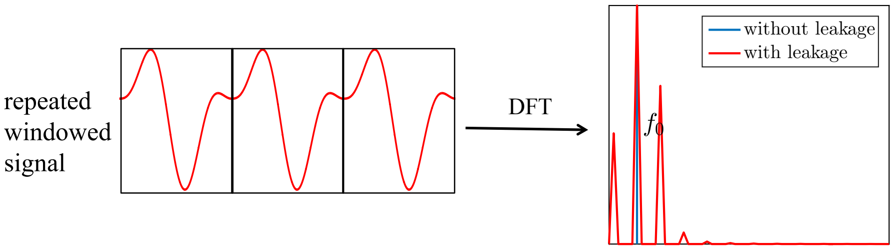

Fig. B.4 Example of the DFT of the periodic signal presented in fig. B.1: sampled signal with a hann window function and its DFT

Appendix C

Pseudo-differential operator

In order to simplify the derivation of the transport equation and the radiative transfer equation with Wigner transform, pseudo-differential calculus are taken into account [25, 97].

Definition C.1 (Pseudo-differential operators)**.** Let $\varphi(t,\varepsilon \mathrm{D}_t)$ and $\psi(x,\varepsilon \mathbf{D}_\mathbf{x})$ be two matrix-valued pseudo-differential operators defined by:

$$\begin{aligned}\varphi(t,\varepsilon \mathrm{D}_t)\mathbf{u}(t,\mathbf{x}) &:= \frac{1}{2\pi}\int_{\mathbb{R}} e^{it\omega}\varphi(t,i\varepsilon\omega)\widehat{\mathbf{u}}(\omega,\mathbf{x})d\omega \\ \psi(\mathbf{x},\varepsilon \mathbf{D}_\mathbf{x})\mathbf{u}(t,\mathbf{x}) &:= \frac{1}{(2\pi)^d}\int_{\mathbb{R}^d} e^{i\mathbf{x}\cdot\mathbf{k}}\psi(\mathbf{x},i\varepsilon\mathbf{k})\widehat{\mathbf{u}}(t,\mathbf{k})d\mathbf{k}\end{aligned} \tag{C.1}$$

We assume that $\varphi(t,i\varepsilon\omega)$ and $\psi(\mathbf{x},i\varepsilon\mathbf{k})$ are smooth functions and use the same mathematical symbols for the operators $\varphi(t,\varepsilon \mathrm{D}_t)$, $\psi(x,\varepsilon \mathbf{D}_\mathbf{x})$ and their symbols $\varphi(t,i\varepsilon\omega)$, $\psi(\mathbf{x},i\varepsilon\mathbf{k})$.

This definition can be seen as a more general expression of time and space differential operators. In effect, by the derivative property of the Fourier transform it is known for example that: $\partial_x f(x) = \frac{1}{2\pi}\int e^{ikx}ik\widehat{f}(k)dk$.

We have the following properties for the pseudo-differential operator [17]:

Lemma C.2. For the heterogeneous operator $\psi(\mathbf{x},\varepsilon \mathbf{D}_\mathbf{x})$, we have:

$$\begin{aligned}\mathbf{W}_\varepsilon[\psi(\mathbf{x},\varepsilon\mathbf{D}_\mathbf{x})\mathbf{u}_\varepsilon,\mathbf{v}_\varepsilon] &= \psi(\mathbf{x},i\mathbf{k})\mathbf{W}_\varepsilon[\mathbf{u}_\varepsilon,\mathbf{v}_\varepsilon] - \frac{i\varepsilon}{2}\{\psi,\mathbf{W}_\varepsilon[\mathbf{u}_\varepsilon,\mathbf{v}_\varepsilon]\} + \frac{i\varepsilon}{2}\nabla_\mathbf{x}\cdot\nabla_\mathbf{k}\psi(\mathbf{x},i\mathbf{k})\mathbf{W}_\varepsilon[\mathbf{u}_\varepsilon,\mathbf{v}_\varepsilon] + o(\varepsilon^2) \\ \mathbf{W}_\varepsilon[\mathbf{u}_\varepsilon,\psi(\mathbf{x},\varepsilon\mathbf{D}_\mathbf{x})\mathbf{v}_\varepsilon] &= \mathbf{W}_\varepsilon[\mathbf{u}_\varepsilon,\mathbf{v}_\varepsilon]^t\psi^*(\mathbf{x},i\mathbf{k}) + \frac{i\varepsilon}{2}\left\{\mathbf{W}_\varepsilon[\mathbf{u}_\varepsilon,\mathbf{v}_\varepsilon],\psi^{*T}\right\} - \frac{i\varepsilon}{2}\mathbf{W}_\varepsilon[\mathbf{u}_\varepsilon,\mathbf{v}_\varepsilon]\nabla_\mathbf{x}\cdot\nabla_\mathbf{k}\psi^{*T}(\mathbf{x},i\mathbf{k}) + o(\varepsilon^2)\end{aligned} \tag{C.2}$$

where the Poisson bracket is defined by: $\{\psi,\mathbf{W}\} = (\nabla_\mathbf{k}\psi\cdot\nabla_\mathbf{x}\mathbf{W} - \nabla_\mathbf{x}\psi\cdot\nabla_\mathbf{k}\mathbf{W})$, and we assume that the differential operator $\mathbf{D}_\mathbf{x}$ within the observable ψ acts on $\mathbf{W}_\varepsilon[\mathbf{u}_\varepsilon,\mathbf{v}_\varepsilon]$ so that $\mathbf{W}_\varepsilon[\mathbf{u}_\varepsilon,\mathbf{v}_\varepsilon](t,\mathbf{x};\omega,\mathbf{k})\psi^{*T}(i\mathbf{k} - \frac{\varepsilon\mathbf{D}_\mathbf{x}}{2})$ should be interpreted as the component-wise inverse Fourier transform (with respect to $\mathbf{k}'$) of the matrix $\widehat{\mathbf{W}}_\varepsilon(t,\mathbf{k}';\omega,\mathbf{k})[\mathbf{u}_\varepsilon,\mathbf{v}_\varepsilon]\psi^{*T}(i\mathbf{k} - \frac{i\varepsilon\mathbf{k}'}{2})$.

If $\psi(\mathbf{x},\varepsilon\mathbf{D_x}) = \psi(\varepsilon\mathbf{D_x})$ is independent of $\mathbf{x}$, the eq. (C.2) becomes:

$$\begin{aligned}\mathbf{W}_\varepsilon[\psi(\varepsilon\mathbf{D_x})\mathbf{u}_\varepsilon,\mathbf{v}_\varepsilon] &= \psi(i\mathbf{k})\mathbf{W}_\varepsilon[\mathbf{u}_\varepsilon,\mathbf{v}_\varepsilon] - \frac{i\varepsilon}{2}\nabla_\mathbf{k}\psi(i\mathbf{k})\cdot\nabla_\mathbf{x}\mathbf{W}_\varepsilon[\mathbf{u}_\varepsilon,\mathbf{v}_\varepsilon]\\ \mathbf{W}_\varepsilon[\mathbf{u}_\varepsilon,\psi(\varepsilon\mathbf{D_x})\mathbf{v}_\varepsilon] &= \mathbf{W}_\varepsilon[\mathbf{u}_\varepsilon,\mathbf{v}_\varepsilon]^t\psi^*(i\mathbf{k}) + \frac{i\varepsilon}{2}\nabla_\mathbf{x}\mathbf{W}_\varepsilon[\mathbf{u}_\varepsilon,\mathbf{v}_\varepsilon]\cdot\nabla_\mathbf{k}\psi^{*T}(i\mathbf{k})\end{aligned} \tag{C.3}$$

In the same way, we can derive for $\varphi(\varepsilon\mathrm{D}_t)$:

$$\begin{aligned}\mathbf{W}_\varepsilon[\varphi(\varepsilon\mathrm{D}_t)\mathbf{u}_\varepsilon,\mathbf{v}_\varepsilon] &= \varphi(i\omega)\mathbf{W}_\varepsilon[\mathbf{u}_\varepsilon,\mathbf{v}_\varepsilon] - \frac{i\varepsilon}{2}\partial_\omega\varphi(i\omega)\cdot\partial_t\mathbf{W}_\varepsilon[\mathbf{u}_\varepsilon,\mathbf{v}_\varepsilon]\\ \mathbf{W}_\varepsilon[\mathbf{u}_\varepsilon,\varphi(\varepsilon\mathrm{D}_t)\mathbf{v}_\varepsilon] &= \mathbf{W}_\varepsilon[\mathbf{u}_\varepsilon,\mathbf{v}_\varepsilon]\varphi^*(i\omega) + \frac{i\varepsilon}{2}\partial_t\mathbf{W}_\varepsilon[\mathbf{u}_\varepsilon,\mathbf{v}_\varepsilon]\cdot\partial_\omega\varphi^*(i\omega)\end{aligned} \tag{C.4}$$

Appendix D

Convolution properties of Wigner transform

In this chapter, we introduce the proof of the property 8 applied in the section 4.3.

Proof. Using the definition of convolution, we have:

$$
\begin{aligned}
&\mathrm{W}_\varepsilon[u_\varepsilon](t,x;\omega,k) **\mathrm{W}_\varepsilon[h_t h_x](t,x;\omega,k)\\
:=&\int_{\mathbb{R}^4} \mathrm{W}_\varepsilon[u_\varepsilon](t',x';\omega',k')\mathrm{W}_\varepsilon[h_t h_x](t-t',x-x';\omega-\omega',k-k')dt'dx'd\omega'dk'\\
=&\int_{\mathbb{R}^4} \frac{1}{(2\pi)^2}\int_{\mathbb{R}^2} u_\varepsilon(t'-\frac{\varepsilon\tau}{2},x'-\frac{\varepsilon y}{2})u_\varepsilon^*(t'+\frac{\varepsilon\tau}{2},x'+\frac{\varepsilon y}{2})e^{i(\tau\omega'+yk')}d\tau dy\\
&\qquad \frac{1}{(2\pi)^2}\int_{\mathbb{R}} h_t(t-t'-\frac{\varepsilon s}{2})h_x(x-x'-\frac{\varepsilon z}{2})h_t^*(t-t'+\frac{\varepsilon s}{2})h_x^*(x-x'+\frac{\varepsilon z}{2})e^{is(\omega-\omega')+iz(k-k')}dsdz\\
&\qquad dt'dx'd\omega'dk'\\
=&\frac{1}{(2\pi)^4}\int_{\mathbb{R}^6} u_\varepsilon(t'-\frac{\varepsilon\tau}{2},x'-\frac{\varepsilon y}{2})u_\varepsilon^*(t'+\frac{\varepsilon\tau}{2},x'+\frac{\varepsilon y}{2})h_t(t-t'-\frac{\varepsilon s}{2})h_x(x-x'-\frac{\varepsilon z}{2})\\
&\qquad\qquad h_t^*(t-t'+\frac{\varepsilon s}{2})h_x^*(x-x'+\frac{\varepsilon z}{2})\int_{\mathbb{R}} e^{-i(s-\tau)\omega'}d\omega'\int_{\mathbb{R}} e^{-i(z-y)k'}dk'\ e^{i(s\omega+yk)}\ dt'dx'd\tau dydsdz
\end{aligned}
\tag{D.1}
$$

By the formula of the Fourier transform of function $f(x)=e^{i\tau x}$:

$$
\widehat{f(s)}=\int_{\mathbb{R}} e^{i\tau x}e^{-isx}dx=\int_{\mathbb{R}} e^{-i(s-\tau)x}dx=2\pi\delta(s-\tau) \tag{D.2}
$$

we find:

$$
\begin{aligned}
&\mathrm{W}_\varepsilon[u_\varepsilon](t,x;\omega,k) **\mathrm{W}_\varepsilon[h_t h_x](t,x;\omega,k)\\
&= \frac{1}{(2\pi)^4}\int_{\mathbb{R}^6} u_\varepsilon(t'-\frac{\varepsilon\tau}{2},x'-\frac{\varepsilon y}{2}) u_\varepsilon^*(t'+\frac{\varepsilon\tau}{2},x'+\frac{\varepsilon y}{2}) h_t(t-t'+\frac{\varepsilon s}{2}) h_x(x-x'+\frac{\varepsilon z}{2})\\
&\qquad\qquad h_t^*(t-t'+\frac{\varepsilon s}{2}) h_x^*(x-x'+\frac{\varepsilon z}{2})\ \ 2\pi\delta(s-\tau)\ \ 2\pi\delta(z-y)\ e^{i(s\omega+yz)}\ dt'dx'd\tau dydsdz\\
&= \frac{1}{(2\pi)^2}\int_{\mathbb{R}^4} u_\varepsilon(t'-\frac{\varepsilon\tau}{2},x'-\frac{\varepsilon y}{2}) h_t^*(t-t'+\frac{\varepsilon\tau}{2}) h_x^*(x-x'+\frac{\varepsilon y}{2})\\
&\qquad\qquad u_\varepsilon^*(t'+\frac{\varepsilon\tau}{2},x'+\frac{\varepsilon y}{2}) h_t(t-t'-\frac{\varepsilon\tau}{2}) h_x(x-x'-\frac{\varepsilon y}{2}) e^{i(\tau\omega+yk)}\ dt'dx'd\tau dy
\end{aligned}
\tag{D.3}
$$

Changing the variables (t',τ) to (α,β) and (x',y) to (m,n) with:

$$
\begin{aligned}
&\begin{cases} t-t'+\frac{\varepsilon\tau}{2}=\varepsilon\alpha\\ t-t'-\frac{\varepsilon\tau}{2}=\varepsilon\beta \end{cases}
&&\begin{cases} x-x'+\frac{\varepsilon y}{2}=\varepsilon m\\ x-x'-\frac{\varepsilon y}{2}=\varepsilon n \end{cases}\\
&\int dt'd\tau=\int \varepsilon d\alpha d\beta, &&\int dx'dy=\int \varepsilon dmdn
\end{aligned}
\tag{D.4}
$$

eq. (D.3) becomes:

$$
\begin{aligned}
&\mathrm{W}_\varepsilon[u_\varepsilon](t,x;\omega,k) **\mathrm{W}_\varepsilon[h_t h_x](t,x;\omega,k)\\
&= \frac{\varepsilon^2}{(2\pi)^2}\int_{\mathbb{R}^4} u_\varepsilon(t-\varepsilon\alpha,x-\varepsilon m)\ h_t^*(\varepsilon\alpha)h_x^*(\varepsilon m)\\
&\qquad\qquad u_\varepsilon^*(t-\varepsilon\beta,x-\varepsilon n)\ h_t(\varepsilon\beta)h_x(\varepsilon n)\ \ e^{i((\alpha-\beta)\omega+(m-n)k)}\ d\alpha d\beta dmdn\\
&= \frac{\varepsilon^2}{(2\pi)^2}\int_{\mathbb{R}^2} u_\varepsilon(t-\varepsilon\alpha,x-\varepsilon m)\ h_t^*(\varepsilon\alpha)h_x^*(\varepsilon m)\ e^{i(\alpha\omega+mk)}\ d\alpha dm\\
&\qquad\qquad \int_{\mathbb{R}^2} u_\varepsilon^*(t-\varepsilon\beta,x-\varepsilon n)\ h_t(\varepsilon\beta)h_x(\varepsilon n)\ e^{-i(\beta\omega+nk)}\ d\beta dn\\
&= \left|\frac{\varepsilon}{2\pi}\int_{\mathbb{R}^2} u_\varepsilon(t-\varepsilon\alpha,x-\varepsilon m)\ h_t^*(\varepsilon\alpha)h_x^*(\varepsilon m)\ e^{i(\alpha\omega+mk)}\ d\alpha dm\right|^2\\
&= |\mathrm{STFT}[u_\varepsilon,h_t h_x](t,x;\omega,k)|^2
\end{aligned}
\tag{D.5}
$$

□

Using the same steps of proof above, we can also derive that:

$$
\begin{aligned}
&\mathrm{W}_\varepsilon[u_\varepsilon](-k) **\mathrm{W}_\varepsilon[h_t h_x] = \left|\frac{\varepsilon}{2\pi}\int_{\mathbb{R}^4} u_\varepsilon(t-\varepsilon\alpha,x-\varepsilon m)\ h_t^*(\varepsilon\alpha)\ h_x(\varepsilon m)\ e^{i(\alpha\omega-mk)}\ d\alpha dm\right|^2\\
&= |\mathrm{STFT}[u_\varepsilon,h_t h_x^*](t,x;\omega,-k)|^2
\end{aligned}
\tag{D.6}
$$

Appendix E

Properties and examples of STFT

The STFT, or the spectrogram (the magnitude squared of the STFT), is a simple extension of the FT. It can be understood as the FT is repeatedly evaluated for a running windowed version of the time-space domain signal. Cross terms exist also for STFT. Consider a general case of the sum of two signals $u_1 + u_2$, its STFT has the following form:

$$\begin{aligned} |\mathrm{STFT}[u_1 + u_2, h_{tx}]|^2 = &|\mathrm{STFT}[u_1, h_{tx}]|^2 + |\mathrm{STFT}[u_2, h_{tx}]|^2 \\ &+ 2\,|\mathrm{STFT}[u_1, h_{tx}]|\,|\mathrm{STFT}^*[u_2, h_{tx}]|\cos\left(\phi_{u_1}(t,x;\omega,k) - \phi_{u_2}(t,x;\omega,k)\right) \end{aligned} \tag{E.1}$$

where $|\mathrm{STFT}[u_i, h_{tx}]|$ and $\phi_{u_i}(t,x;\omega,k), i = 1,2$ are respectively the magnitude and the phase of the STFT of signal u_i. In eq. (E.1), the first two terms are the auto-terms and the last term is the cross term. It can be observed that if two STFTs have no overlapping (t,x)-(ω,k) support, the cross term is zero. Equation (E.1) can also be generalized to sum of N signals.

A summary of the principal properties of cross terms of STFT are given here. More detailed analysis can be found in [83, 102, 120].

1. The STFT cross terms occurs at the intersection of two overlapping transforms and no cross term occurs between two frequency components like Wigner transform in eq. (3.13). Depending upon the amount of overlap of each pair of transforms, the energy distribution of the STFT of an N component signal can have a minimum of zeros and a maximum of $\frac{N(N-1)}{2}$ cross terms, unlike the Wigner transform, which always has $\frac{N(N-1)}{2}$ cross terms in the midway of two Wigner transform auto-terms. However, it also reduces the time-frequency resolution simultaneously.
2. The STFT cross terms can have a maximum magnitude equal to twice the product of the magnitude of the two spectrograms.
3. The STFT cross terms are modulated by a cosine whose argument is a function of the difference of phases of $\mathrm{STFT}[u_i, h_{tx}]$.

Here we study the same example, namely the sum of two complex-valued and separate gaussian signals $F(t)$, as we presented for the Wigner transform in the section 3.1.2 to view the cross term properties of STFT or spectrogram (hann window is used here with length = sample length/6).

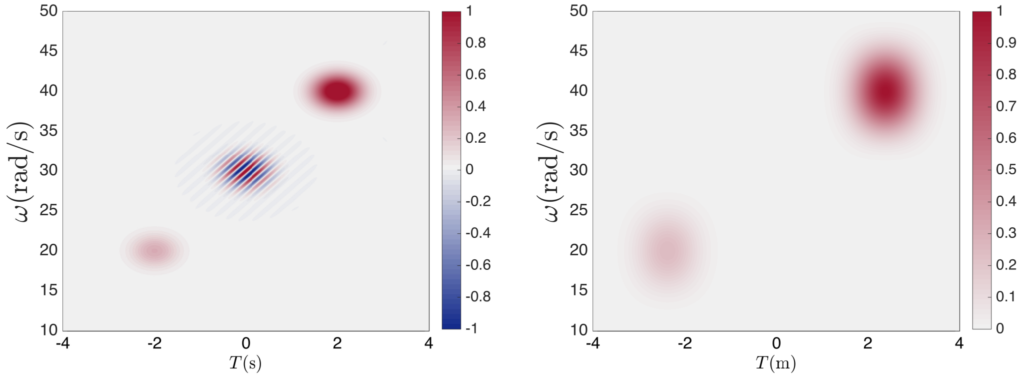

(a) (b)

Fig. E.1 Comparison of Wigner transform and spectrogram of sum of two gaussian signal: (a) Wigner transform, (b) spectrogram$[F](t;\omega)$

In fig. E.1b, it is found that no cross term exists in its spectrogram since the two gaussian signals have no overlapping support as we explained above. Wigner transform has a better concentration. However, if we modify $(t_1,\omega_1)=(1,30)$ so as to have two closely spaced signal in fig. E.2a, the effect of the overlapped components becomes visible and an intersection of two terms is found in fig. E.2b.

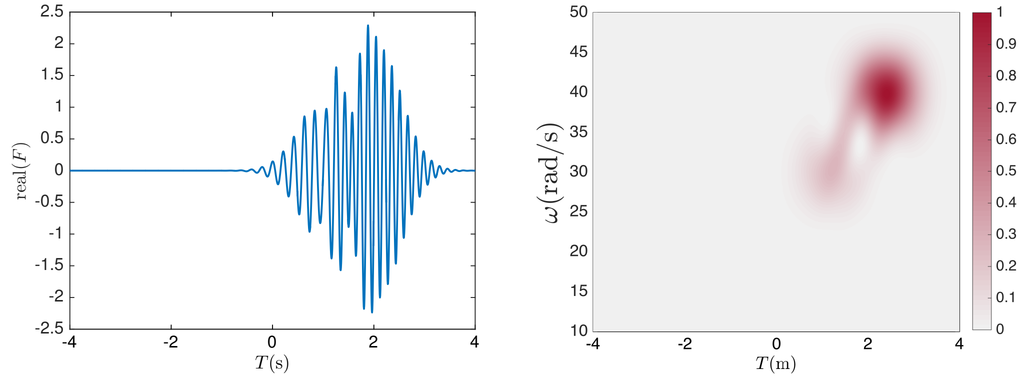

(a) (b)

Fig. E.2 A signal composed of two more closely spaced complex-valued gaussian signals and its spectrogram: (a) $F(t)$(only real-valued part), (b) spectrogram $[F](t,\omega)$

Now we compare of the Wigner transform and the spectrogram for coherent waves as we did in the section 3.1.4 that is used in our application. The Hann window function is used in time and in space for the spectrogram. The same calculation region is chosen for the Wigner transform and the spectrogram so as to have the same sampled signal, see fig. E.3.

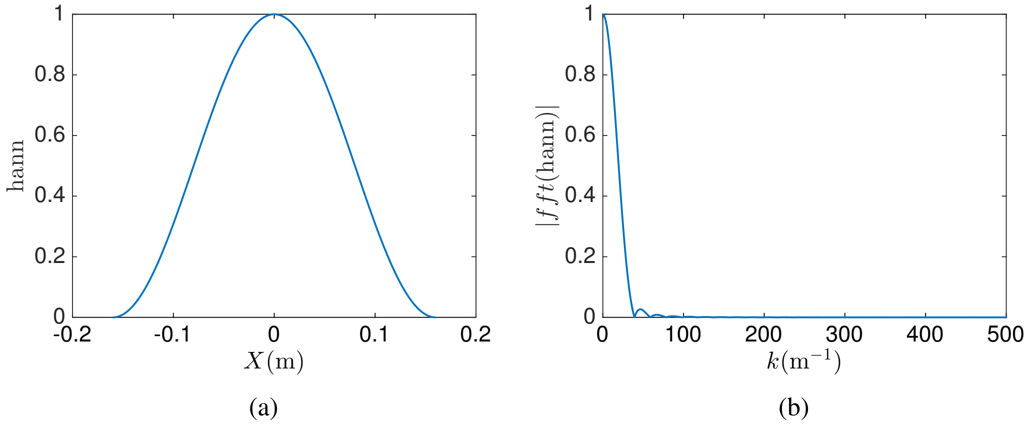

Fig. E.3 Hann window function in space and its frequency spectrum: (a) $h(x)$, (b) $|fft(h)|$

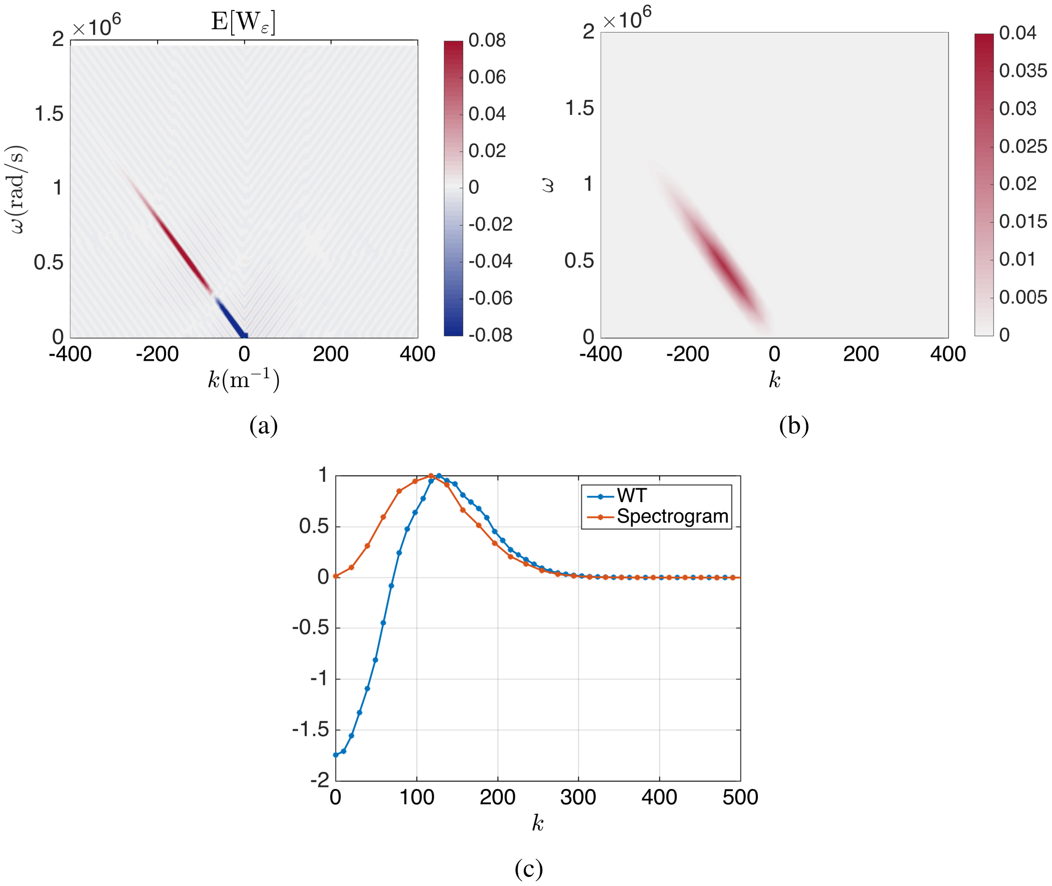

Fig. E.4 Comparison of the Wigner transform and the spectrogram of coherent waves: (a) Wigner transform, (b) spectrogram, (c) values on $\omega = -c_0 k$ with magnitude normalized to 1

With fig. E.4, we have several comments as follows. Firstly, Wigner transform gives a better resolution in phase space. Secondly, spectrogram suppresses almost cross terms at zero and low frequency (we presented in the section 3.1.4 a peak around zero frequency for Wigner transform is due to superposition of cross terms). However, it is known that it cannot suppress all the cross terms between positive frequencies because a continuous frequency range is used here. Finally, less frequency leakage is observed for spectrogram due to the use of window functions. Wigner transform is calculated directly in a limited calculation region and we can treat it as application of a rectangular window, whose frequency spreading is very wide, which may mask important spectrum details at even lower levels. That's why we find small fluctuations everywhere in fig. E.4b. Generally, non-rectangular window functions actually increase the total leakage, but they can also redistribute it to places where it does the least harm. To different degrees they reduce the level of the spreading by increasing the high-level leakage in the near vicinity of the original component [68]. So in fig. E.4c, the use of hann window function increases leakage near main lobe and also allows to reduce frequency leakage at a remote area of the main lobe.

Appendix F

Energy-based residual errors calculated within the local basis defined by the wave propagation characteristics

In this section, we consider the residual errors in 1D heterogeneous media defined in chapter 4 using the local basis defined by the wave propagation characteristics. A transformation of coordinates is firstly performed for the Wigner transform and the radiative transfer equation in 1D case. Then the residual errors are re-calculated respectively for coherent waves and incoherent waves.

We propose a change of variables for $(t,x) \rightarrow (\chi_\perp, \chi_\parallel)$ (fig. F.1):

$$\begin{cases} \chi_\perp = \frac{1}{\sqrt{2}}(c_0 t - x) \\ \chi_\parallel = \frac{1}{\sqrt{2}}(c_0 t + x) \end{cases} \quad \text{i.e.} \quad \begin{cases} t = \frac{1}{\sqrt{2}c_0}(\chi_\perp + \chi_\parallel) \\ x = \frac{1}{\sqrt{2}}(-\chi_\perp + \chi_\parallel) \end{cases} \tag{F.1}$$

and for $(\tau, y) \rightarrow (\phi, \psi)$:

$$\begin{cases} \phi = \frac{1}{\sqrt{2}}(c_0 \tau - y) \\ \psi = \frac{1}{\sqrt{2}}(c_0 \tau + y) \end{cases} \quad \text{i.e.} \quad \begin{cases} \tau = \frac{1}{\sqrt{2}c_0}(\phi + \psi) \\ y = \frac{1}{\sqrt{2}}(-\phi + \psi) \end{cases} \qquad d\tau dy = \frac{1}{c_0} d\phi d\psi \tag{F.2}$$

where the subscripts $\parallel$ and $\perp$ represent respectively the directions along the forward and backward wave propagation characteristics. Recall that τ and y are the shift variables related to t and x in the definition of Wigner transform.

Introducing eq. (F.1) and eq. (F.2) into the definition 3.3 of Wigner transform in 1D:

$$\mathrm{W}_\varepsilon[u_\varepsilon](t,x;\omega,k) = \frac{1}{(2\pi)^2}\int_{\mathbb{R}^2} u_\varepsilon(t - \frac{\varepsilon\tau}{2}, x - \frac{\varepsilon y}{2}) u_\varepsilon^*(t + \frac{\varepsilon\tau}{2}, x + \frac{\varepsilon y}{2}) e^{i(\tau\omega + yk)} d\tau dy \tag{F.3}$$

and we can derive that:

$$\begin{aligned}
\mathrm{W}_{\varepsilon}[u_{\varepsilon}](t,x;\omega,k) &= \frac{1}{(2\pi)^2}\int_{\mathbb{R}^2} u_{\varepsilon}\left(\frac{1}{\sqrt{2}c_0}(\chi_{\perp}+\chi_{\parallel})-\frac{\varepsilon}{2}\frac{1}{\sqrt{2}c_0}(\phi+\psi),\frac{1}{\sqrt{2}}(-\chi_{\perp}+\chi_{\parallel})-\frac{\varepsilon}{2}\frac{1}{\sqrt{2}}(-\phi+\psi)\right)\\
&\qquad u_{\varepsilon}^{*}\left(\frac{1}{\sqrt{2}c_0}(\chi_{\perp}+\chi_{\parallel})+\frac{\varepsilon}{2}\frac{1}{\sqrt{2}c_0}(\phi+\psi),\frac{1}{\sqrt{2}}(-\chi_{\perp}+\chi_{\parallel})+\frac{\varepsilon}{2}\frac{1}{\sqrt{2}}(-\phi+\psi)\right)\\
&\qquad e^{i\left(\frac{1}{\sqrt{2}c_0}(\phi+\psi)\omega+\frac{1}{\sqrt{2}}(-\phi+\psi)k\right)}\frac{1}{c_0}\,d\phi d\psi\\
&= \frac{1}{(2\pi)^2}\int_{\mathbb{R}^2} u_{\varepsilon}\left(\frac{1}{\sqrt{2}c_0}((\chi_{\perp}-\frac{\varepsilon\phi}{2})+(\chi_{\parallel}-\frac{\varepsilon\psi}{2})),\frac{1}{\sqrt{2}}(-(\chi_{\perp}-\frac{\varepsilon\phi}{2})+(\chi_{\parallel}-\frac{\varepsilon\psi}{2}))\right)\\
&\qquad u_{\varepsilon}^{*}\left(\frac{1}{\sqrt{2}c_0}((\chi_{\perp}+\frac{\varepsilon\phi}{2})+(\chi_{\parallel}+\frac{\varepsilon\psi}{2})),\frac{1}{\sqrt{2}}(-(\chi_{\perp}+\frac{\varepsilon\phi}{2})+(\chi_{\parallel}+\frac{\varepsilon\psi}{2}))\right)\\
&\qquad e^{i\left(\phi\frac{\frac{\omega}{c_0}-k}{\sqrt{2}}+\psi\frac{\frac{\omega}{c_0}+k}{\sqrt{2}}\right)}\frac{1}{c_0}\,d\phi d\psi
\end{aligned} \tag{F.4}$$

Defining the displacement field and the Wigner transform in new coordinates by:

$$\begin{aligned}
&\tilde{u}(\chi_{\perp},\chi_{\parallel}) := u\left(\frac{1}{\sqrt{2}c_0}(\chi_{\perp}+\chi_{\parallel}),\frac{1}{\sqrt{2}}(-\chi_{\perp}+\chi_{\parallel})\right);\\
&\tilde{\mathrm{W}}_{\varepsilon}[\tilde{u}_{\varepsilon}](\chi_{\perp},\chi_{\parallel};k_{\perp},k_{\parallel}) := \frac{1}{(2\pi)^2}\int_{\mathbb{R}^2}\tilde{u}_{\varepsilon}(\chi_{\perp}-\frac{\varepsilon\phi}{2},\chi_{\parallel}-\frac{\varepsilon\psi}{2})\tilde{u}_{\varepsilon}^{*}(\chi_{\perp}+\frac{\varepsilon\phi}{2},\chi_{\parallel}+\frac{\varepsilon\psi}{2})e^{i(\phi k_{\chi_{\perp}}+\psi k_{\parallel})}d\phi d\psi
\end{aligned} \tag{F.5}$$

we obtain the following relation:

$$\begin{aligned}
&\tilde{u}(\chi_{\perp},\chi_{\parallel}) = u(t,x);\\
&\mathrm{W}_{\varepsilon}[u_{\varepsilon}](t,x;\omega,k) = \frac{1}{c_0}\tilde{\mathrm{W}}_{\varepsilon}[\tilde{u}_{\varepsilon}](\chi_{\perp},\chi_{\parallel};k_{\perp},k_{\parallel})
\end{aligned} \tag{F.6}$$

with the change of variables in the phase space $\begin{cases} k_{\perp} = \frac{1}{\sqrt{2}}(\frac{\omega}{c_0}-k) \\ k_{\parallel} = \frac{1}{\sqrt{2}}(\frac{\omega}{c_0}+k) \end{cases}$. Then the projections of Wigner transform on the forward and backward directions can be expressed as:

$$\begin{aligned}
\mathrm{W}_{\varepsilon}^{+} &= \mathrm{W}_{\varepsilon}[u_{\varepsilon}](t,x;\omega=c_0k,-k) = \frac{1}{c_0}\tilde{\mathrm{W}}_{\varepsilon}[\tilde{u}_{\varepsilon}](\chi_{\perp},\chi_{\parallel};k_{\perp}=\sqrt{2}k,k_{\parallel}=0) = \frac{1}{c_0}\tilde{\mathrm{W}}_{\varepsilon}^{+}\\
\mathrm{W}_{\varepsilon}^{-} &= \mathrm{W}_{\varepsilon}[u_{\varepsilon}](t,x;\omega=c_0k,k) = \frac{1}{c_0}\tilde{\mathrm{W}}_{\varepsilon}[\tilde{u}_{\varepsilon}](\chi_{\perp},\chi_{\parallel};k_{\perp}=0,k_{\parallel}=\sqrt{2}k) = \frac{1}{c_0}\tilde{\mathrm{W}}_{\varepsilon}^{-}
\end{aligned} \tag{F.7}$$

The local wave-characteristic basis and the associated coordinate system are illustrated in fig. F.1 (with the coherent forward waves, fig. 4.17a) and the calculation region here is $(\zeta_{\perp},\zeta_{\parallel}) = (\sqrt{2}\zeta_x,\sqrt{2}\zeta_x)$. The Wigner transforms within both global and local coordinate systerm are compared fig. F.2. It is found that these two results are very close to each other along the characteristic line (normalized and the coefficient $\frac{1}{c_0}$ considered). Figure F.2d shows that the numerical results calculated using the local coordinate system have less fluctuations (by spectral leakage).

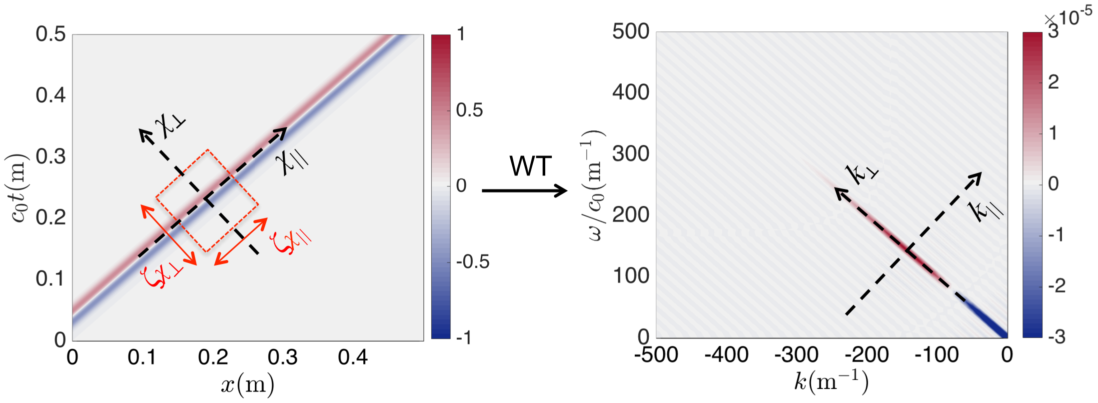

Fig. F.1 The rotational coordinates in the time-space domain (with $u(t,x)$ of a forward wave) and in phase space (with $\mathrm{W}(t_0,x_0;\omega,k)$): $(\chi_\perp,\chi_\parallel) = (\frac{1}{\sqrt{2}}(c_0t-x), \frac{1}{\sqrt{2}}(c_0t+x))$, $(k_\perp,k_\parallel) = (\frac{1}{\sqrt{2}}(\frac{\omega}{c_0}-k), \frac{1}{\sqrt{2}}(\frac{\omega}{c_0}+k))$

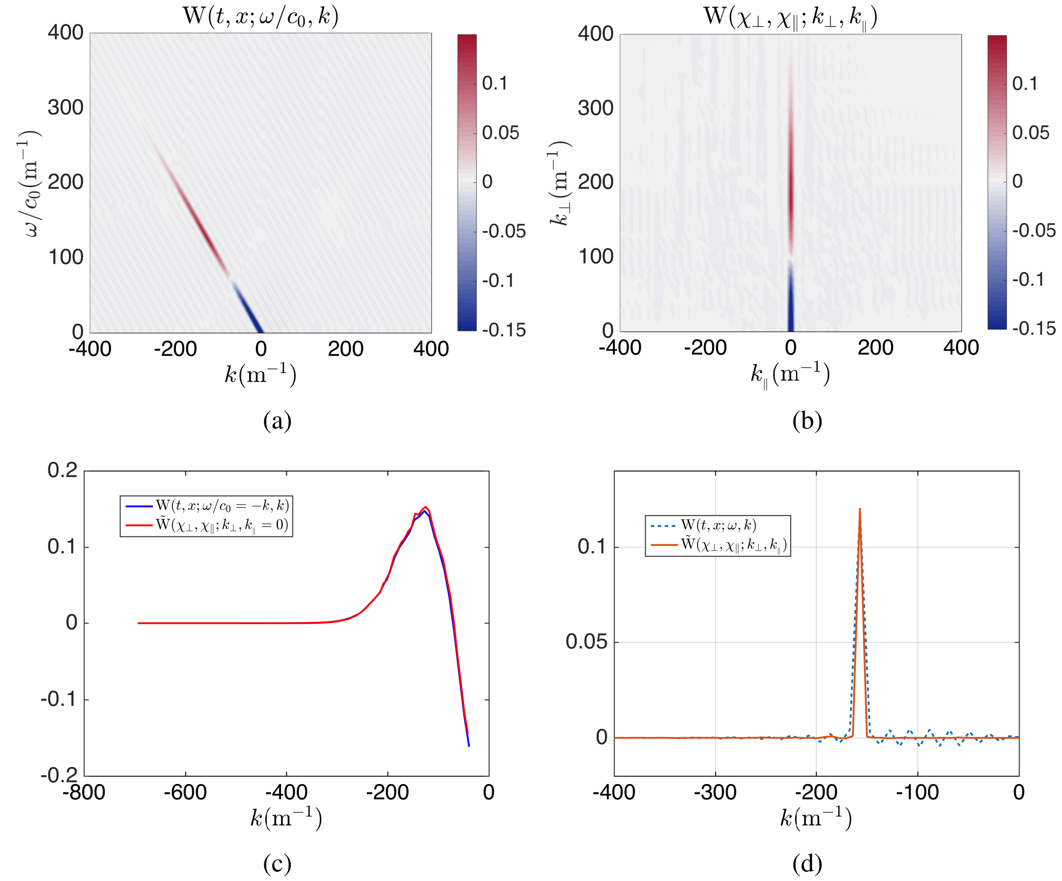

(a) (b)

(c) (d)

Fig. F.2 Wigner transform for coherent forward wave: (a) $\mathrm{W}_\varepsilon[u_\varepsilon](t,x;\omega,k)$ for $(t=t_0,x=x_0)$, (b) $\tilde{\mathrm{W}}_\varepsilon[\tilde{u}_\varepsilon](\chi_\perp,\chi_\parallel;k_\perp,k_\parallel)$ for $(\chi_\perp = \frac{1}{\sqrt{2}}(c_0t_0-x_0), \chi_\parallel = \frac{1}{\sqrt{2}}(c_0t+x_0))$, (c) values along the characteristic line, (d) values in the line perpendicular to the characteristic line for $k = k_{max}$

Now we can derive the radiative transfer equation using the local coordinate system. The two terms of the transport part become:

$$\begin{aligned}\partial_t \mathrm{W}_\varepsilon[u_\varepsilon](t,x;\omega,k) &= \frac{1}{c_0}\partial_{\chi_\perp}\tilde{\mathrm{W}}_\varepsilon[\tilde{u}_\varepsilon](\chi_\perp,\chi_\parallel;k_\perp,k_\parallel)\partial_t\chi_\perp + \frac{1}{c_0}\partial_{\chi_\parallel}\tilde{\mathrm{W}}_\varepsilon[\tilde{u}_\varepsilon](\chi_\perp,\chi_\parallel;k_\perp,k_\parallel)\partial_t\chi_\parallel \\ &= \frac{1}{c_0}\partial_{\chi_\perp}\tilde{\mathrm{W}}_\varepsilon[\tilde{u}_\varepsilon](\chi_\perp,\chi_\parallel;k_\perp,k_\parallel)\frac{c_0}{\sqrt{2}} + \frac{1}{c_0}\partial_{\chi_\parallel}\tilde{\mathrm{W}}_\varepsilon[\tilde{u}_\varepsilon](\chi_\perp,\chi_\parallel;k_\perp,k_\parallel)\frac{c_0}{\sqrt{2}} \\ &= \frac{1}{\sqrt{2}}\partial_{\chi_\perp}\tilde{\mathrm{W}}_\varepsilon[\tilde{u}_\varepsilon](\chi_\perp,\chi_\parallel;k_\perp,k_\parallel) + \frac{1}{\sqrt{2}}\partial_{\chi_\parallel}\tilde{\mathrm{W}}_\varepsilon[\tilde{u}_\varepsilon](\chi_\perp,\chi_\parallel;k_\perp,k_\parallel)\end{aligned} \tag{F.8}$$

and

$$\begin{aligned}\partial_x \mathrm{W}_\varepsilon[u_\varepsilon](t,x;\omega,k) &= \frac{1}{c_0}\partial_{\chi_\perp}\tilde{\mathrm{W}}_\varepsilon[\tilde{u}_\varepsilon](\chi_\perp,\chi_\parallel;k_\perp,k_\parallel)\partial_x\chi_\perp + \frac{1}{c_0}\partial_{\chi_\parallel}\tilde{\mathrm{W}}_\varepsilon[\tilde{u}_\varepsilon](\chi_\perp,\chi_\parallel;k_\perp,k_\parallel)\partial_x\chi_\parallel \\ &= -\frac{1}{c_0}\partial_{\chi_\perp}\tilde{\mathrm{W}}_\varepsilon[\tilde{u}_\varepsilon](\chi_\perp,\chi_\parallel;k_\perp,k_\parallel)\frac{1}{\sqrt{2}} + \frac{1}{c_0}\partial_{\chi_\parallel}\tilde{\mathrm{W}}_\varepsilon[\tilde{u}_\varepsilon](\chi_\perp,\chi_\parallel;k_\perp,k_\parallel)\frac{1}{\sqrt{2}} \\ &= -\frac{1}{\sqrt{2}c_0}\partial_{\chi_\perp}\tilde{\mathrm{W}}_\varepsilon[\tilde{u}_\varepsilon](\chi_\perp,\chi_\parallel;k_\perp,k_\parallel) + \frac{1}{\sqrt{2}c_0}\partial_{\chi_\parallel}\tilde{\mathrm{W}}_\varepsilon[\tilde{u}_\varepsilon](\chi_\perp,\chi_\parallel;k_\perp,k_\parallel)\end{aligned} \tag{F.9}$$

Combing the above two equations and using eq. (F.6) and eq. (F.7), the two radiative transfer equations for $\tilde{\mathrm{W}}^+$ and $\tilde{\mathrm{W}}^-$ in eq. (4.26) become:

$$\begin{cases}\sqrt{2}\partial_{\chi_\parallel}\tilde{\mathrm{W}}^+[\tilde{u}_\varepsilon] = \frac{1}{8}k_\perp^2\hat{P}(\sqrt{2}k_\perp)\left\{\tilde{\mathrm{W}}^-[\tilde{u}_\varepsilon] - \tilde{\mathrm{W}}^+[\tilde{u}_\varepsilon]\right\} \\ \sqrt{2}\partial_{\chi_\perp}\tilde{\mathrm{W}}^-[\tilde{u}_\varepsilon] = \frac{1}{8}k_\parallel^2\hat{P}(\sqrt{2}k_\parallel)\left\{\tilde{\mathrm{W}}^+[\tilde{u}_\varepsilon] - \tilde{\mathrm{W}}^-[\tilde{u}_\varepsilon]\right\}\end{cases} \tag{F.10}$$

Theorem F.1. The residual errors in the local basis associated to the wave propagation characteristics are defined with:

$$\begin{cases}\tilde{\mathrm{R}}^+[\tilde{u}_\varepsilon] = \sqrt{2}\partial_{\chi_\parallel}\tilde{\mathrm{W}}^+[\tilde{u}_\varepsilon] - \frac{1}{8}k_\perp^2\hat{P}(\sqrt{2}k_\perp)\left\{\tilde{\mathrm{W}}^-[\tilde{u}_\varepsilon] - \tilde{\mathrm{W}}^+[\tilde{u}_\varepsilon]\right\} \\ \tilde{\mathrm{R}}^-[\tilde{u}_\varepsilon] = \sqrt{2}\partial_{\chi_\perp}\tilde{\mathrm{W}}^-[\tilde{u}_\varepsilon] - \frac{1}{8}k_\parallel^2\hat{P}(\sqrt{2}k_\parallel)\left\{\tilde{\mathrm{W}}^+[\tilde{u}_\varepsilon] - \tilde{\mathrm{W}}^-[\tilde{u}_\varepsilon]\right\}\end{cases} \tag{F.11}$$

or

$$\begin{cases}\tilde{\mathrm{R}}_T^{\mathrm{sd}} = \tilde{\mathrm{R}}^+ + \tilde{\mathrm{R}}^- \\ \tilde{\mathrm{R}}_{TS}^{\mathrm{sd}} = \tilde{\mathrm{R}}^+ - \tilde{\mathrm{R}}^-\end{cases} \tag{F.12}$$

The filtering of residual errors can also be transformed under $(\chi_\perp,\chi_\parallel;k_\perp,k_\parallel)$ in the same way as we did in theorem 4.6. The detailed derivation is neglected and the results are given here.

Theorem F.2. The filtered residual errors in the local basis associated to the wave propagation characteristics are defined with:

$$\begin{cases}\tilde{\mathrm{R}}_T^{\mathrm{sd}}[\tilde{u}_\varepsilon] * *\tilde{\mathrm{W}}[\tilde{h}_{\chi_\perp}\tilde{h}_{\chi_\parallel}] = \tilde{\mathrm{R}}^+[\tilde{u}_\varepsilon] * *\tilde{\mathrm{W}}[\tilde{h}_{\chi_\perp}\tilde{h}_{\chi_\parallel}] + \tilde{\mathrm{R}}^-[\tilde{u}_\varepsilon] * *\tilde{\mathrm{W}}[\tilde{h}_{\chi_\perp}\tilde{h}_{\chi_\parallel}] \\ \tilde{\mathrm{R}}_{TS}^{\mathrm{sd}}[\tilde{u}_\varepsilon] * *\tilde{\mathrm{W}}[\tilde{h}_{\chi_\perp}\tilde{h}_{\chi_\parallel}] = \tilde{\mathrm{R}}^+[\tilde{u}_\varepsilon] * *\tilde{\mathrm{W}}[\tilde{h}_{\chi_\perp}\tilde{h}_{\chi_\parallel}] - \tilde{\mathrm{R}}^-[\tilde{u}_\varepsilon] * *\tilde{\mathrm{W}}[\tilde{h}_{\chi_\perp}\tilde{h}_{\chi_\parallel}]\end{cases} \tag{F.13}$$

where

$$
\begin{aligned}
&\tilde{\mathrm{R}}^{+}[\tilde{u}_\varepsilon] ** \tilde{\mathrm{W}}[\tilde{h}_{\chi_\perp}\tilde{h}_{\chi_\parallel}](\chi_\perp,\chi_\parallel;k_\perp,k_\parallel)\\
&=2\sqrt{2}\mathrm{Re}\left\{\widetilde{\mathrm{STFT}}[\partial_{\chi_\parallel}\tilde{u}_\varepsilon,\tilde{h}_{\chi_\perp}\tilde{h}_{\chi_\parallel}](\chi_\perp,\chi_\parallel;-\sqrt{2}k,0)\widetilde{\mathrm{STFT}}^{*}[\tilde{u}_\varepsilon,\tilde{h}_{\chi_\perp}\tilde{h}_{\chi_\parallel}](\chi_\perp,\chi_\parallel;-\sqrt{2}k,0)\right\}\\
&+\frac{\sqrt{2}}{16}\int_{\mathbb{R}}\widetilde{\mathrm{STFT}}[\tilde{u}_\varepsilon,\tilde{h}_{\chi_\perp}\tilde{h}^{*}_{\chi_\parallel}](\chi_\perp+\varepsilon l,\chi_\parallel-\varepsilon l;-\sqrt{2}k,0)\widetilde{\mathrm{STFT}}^{*}[\tilde{u}_\varepsilon,\tilde{h}_{\chi_\perp}\tilde{h}^{*}_{\chi_\parallel}](\chi_\perp-\varepsilon l,\chi_\parallel+\varepsilon l;-\sqrt{2}k,0)\,P^{(2)}(\sqrt{2}l)dl\\
&-\frac{\sqrt{2}}{16}\int_{\mathbb{R}}\widetilde{\mathrm{STFT}}[\tilde{u}_\varepsilon,\tilde{h}_{\chi_\perp}\tilde{h}_{\chi_\parallel}](\chi_\perp+\varepsilon l,\chi_\parallel-\varepsilon l;0,-\sqrt{2}k)\widetilde{\mathrm{STFT}}^{*}[\tilde{u}_\varepsilon,\tilde{h}_{\chi_\perp}\tilde{h}_{\chi_\parallel}](\chi_\perp-\varepsilon l,\chi_\parallel+\varepsilon l;0,-\sqrt{2}k)\,P^{(2)}(\sqrt{2}l)dl
\end{aligned}
\tag{F.14}
$$

and

$$
\begin{aligned}
&\tilde{\mathrm{R}}^{-}[\tilde{u}_\varepsilon] ** \tilde{\mathrm{W}}[\tilde{h}_{\chi_\perp}\tilde{h}_{\chi_\parallel}](\chi_\perp,\chi_\parallel;k_\perp,k_\parallel)\\
&=2\sqrt{2}\mathrm{Re}\left\{\widetilde{\mathrm{STFT}}[\partial_{\chi_\perp}\tilde{u}_\varepsilon(\chi_\perp,\chi_\parallel),\tilde{h}_{\chi_\perp}\tilde{h}_{\chi_\parallel}](0,\sqrt{2}k)\widetilde{\mathrm{STFT}}^{*}[\tilde{u}_\varepsilon,\tilde{h}_{\chi_\perp}\tilde{h}_{\chi_\parallel}](\chi_\perp,\chi_\parallel;0,\sqrt{2}k)\right\}\\
&+\frac{\sqrt{2}}{16}\int_{\mathbb{R}}\widetilde{\mathrm{STFT}}[\tilde{u}_\varepsilon,\tilde{h}_{\chi_\perp}\tilde{h}^{*}_{\chi_\parallel}](\chi_\perp+\varepsilon l,\chi_\parallel-\varepsilon l;0,\sqrt{2}k)\widetilde{\mathrm{STFT}}^{*}[\tilde{u}_\varepsilon,\tilde{h}_{\chi_\perp}\tilde{h}^{*}_{\chi_\parallel}](\chi_\perp-\varepsilon l,\chi_\parallel+\varepsilon l;0,\sqrt{2}k)\,P^{(2)}(\sqrt{2}l)dl\\
&-\frac{\sqrt{2}}{16}\int_{\mathbb{R}}\widetilde{\mathrm{STFT}}[\tilde{u}_\varepsilon,\tilde{h}_{\chi_\perp}\tilde{h}_{\chi_\parallel}](\chi_\perp+\varepsilon l,\chi_\parallel-\varepsilon l;\sqrt{2}k,0)\widetilde{\mathrm{STFT}}^{*}[\tilde{u}_\varepsilon,\tilde{h}_{\chi_\perp}\tilde{h}_{\chi_\parallel}](\chi_\perp-\varepsilon l,\chi_\parallel+\varepsilon l;\sqrt{2}k,0)\,P^{(2)}(\sqrt{2}l)dl
\end{aligned}
\tag{F.15}
$$

where $\widetilde{\mathrm{STFT}}$ stands for STFT of $\tilde{u}_\varepsilon$ in new coordinates.

Then we can calculate eq. (F.12) and eq. (F.14) numerically for coherent waves and incoherent waves as we did in section 4.2.3.

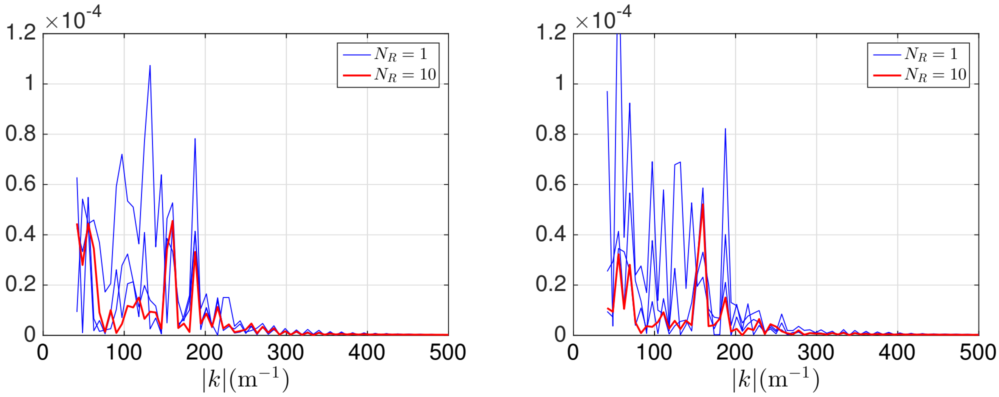

(a) (b)

Fig. F.3 Residual errors along the characteristic line for coherent forward wave: (a) $\left|\tilde{\mathrm{R}}^{\mathrm{sd}}_{T}\right|$, (b) $\left|\tilde{\mathrm{R}}^{\mathrm{sd}}_{TS}\right|$

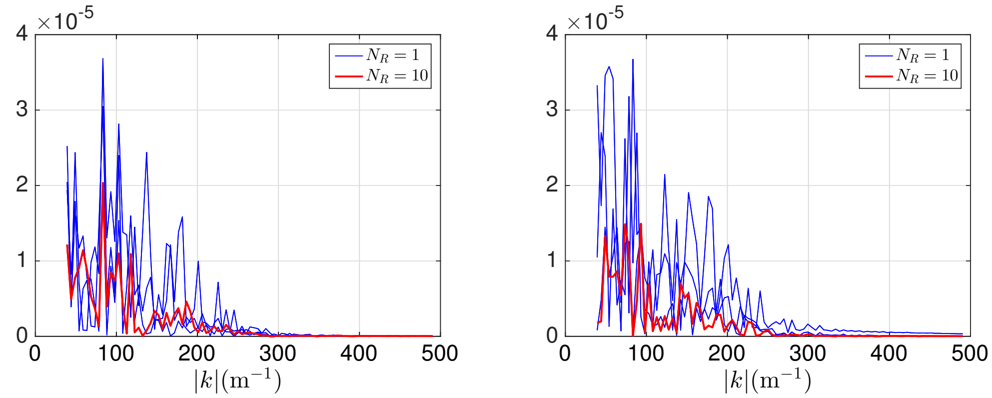

(a) (b)

Fig. F.4 Residual errors in $\omega = \pm c_0 k$ for incoherent wave: (a) $\left|\tilde{\mathrm{R}}_T^{\mathrm{sd}}\right|$, (b) $\left|\tilde{\mathrm{R}}_{TS}^{\mathrm{sd}}\right|$

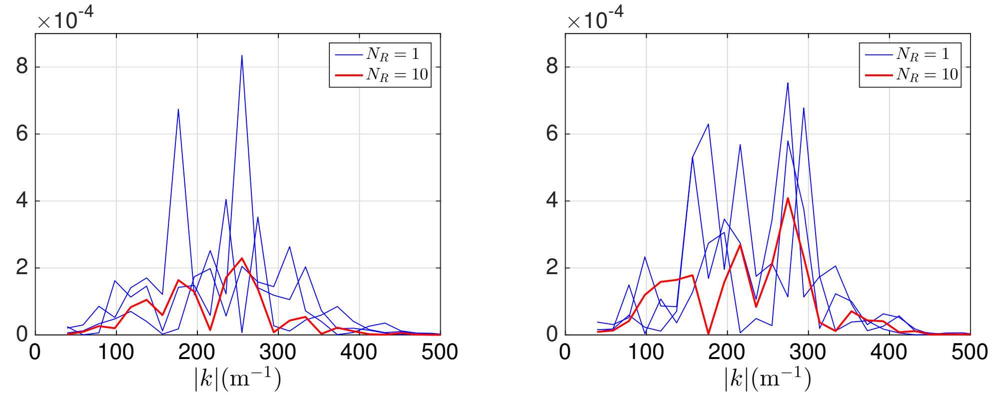

(a) (b)

Fig. F.5 Filtered residual errors in $\omega = \pm c_0 k$ for coherent forward waves: (a) $\left|\tilde{\mathrm{R}}_1^{\mathrm{sd}} * * \tilde{\mathrm{W}}[\tilde{h}_{\chi_\perp} \tilde{h}_{\chi_\parallel}]\right|$, (b) $\left|\tilde{\mathrm{R}}_2^{\mathrm{sd}} * * \tilde{\mathrm{W}}[\tilde{h}_{\chi_\perp} \tilde{h}_{\chi_\parallel}]\right|$

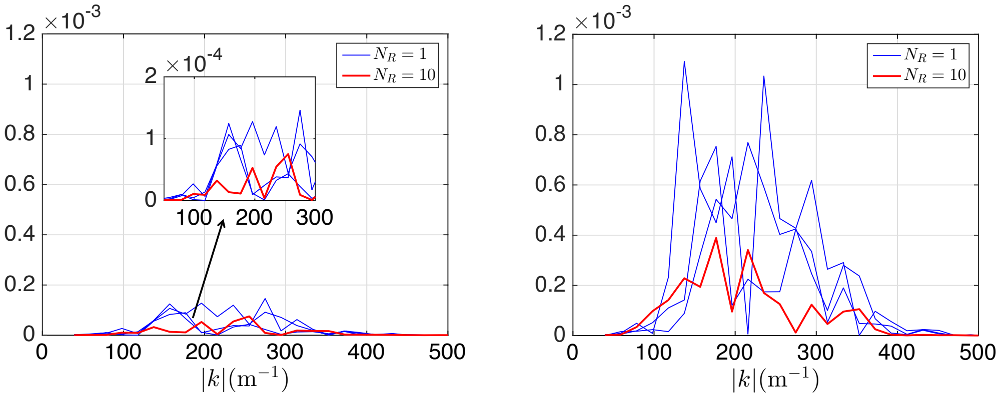

(a) (b)

Fig. F.6 Filtered residual errors in $\omega = \pm c_0 k$ for incoherent waves: (a) $\tilde{\mathrm{R}}_1^{\mathrm{sd}} * * \tilde{\mathrm{W}}[\tilde{h}_{\chi_\perp} \tilde{h}_{\chi_\parallel}]$, (b) $\tilde{\mathrm{R}}_2^{\mathrm{sd}} * * \tilde{\mathrm{W}}[\tilde{h}_{\chi_\perp} \tilde{h}_{\chi_\parallel}]$

Appendix G

Résumé substantiel

La simulation numérique de la propagation d'ondes en milieu hétérogène est un problème difficile car il nécessite de suivre les différents fronts d'ondes diffractés sur les hétérogénéités. C'est particulièrement vrai en régime mésoscopique à haute fréquence, car l'interaction des ondes avec le milieu est plus forte et les distances de propagation (relativement à la longueur d'onde) sont plus importantes. Ces travaux de thèse portent sur le développement d'outils d'estimation d'erreurs pour les solutions numériques d'équations d'ondes par éléments finis. Ces outils doivent permettre de contrôler la qualité des simulations et de piloter l'optimisation du coût numérique.

Dans une première partie, un estimateur d'erreur explicite *a posteriori* est proposé. Il permet d'évaluer une erreur en norme énergétique en espace et en norme L^∞ en temps entre la solution exacte de l'équation élastodynamique et une solution approchée reconstruite. L'idée principale du développement est basée sur une erreur en résidu et l'utilisation de reconstructions des champs. Pour tenir compte des régularités nécessaires à l'obtention d'une borne supérieure de l'erreur, plusieurs reconstructions en temps pour le déplacement et la vitesse sont proposées, ainsi que des reconstructions en espace-temps pour la contrainte. La performance de l'estimateur a été comparée par rapport à des erreurs numériques exactes pour des cas homogène et hétérogène, et pour des solutions éléments finis obtenues avec différents tailles de maillage et pas de temps. L'erreur estimée diminue bien avec le raffinement en temps et en espace, mais l'efficacité (rapport entre l'erreur estimée et l'erreur réelle) augmente également avec le raffinement. La convergence asymptotique de l'estimateur obtenu doit donc être améliorée. L'analyse des résultats montre que les composantes des erreurs liées aux résidus de l'équation d'équilibre dérivée en temps sont dominantes dans la contribution des erreurs totales estimées.

Dans une seconde partie, le travail se concentre sur le cas particulier de la propagation d'ondes à hautes fréquences dans des milieux hétérogènes en régime de couplage faible. Dans ce cas, les estimateurs classiques basés sur les champs de déplacement et de vitesse ne sont pas très efficaces, car ces derniers sont très fluctuants. L'énergie devient alors une quantité d'intérêt plus pertinente. Un nouvel estimateur d'erreur est proposé, basé sur le résidu des équations de transport en milieu homogène et de transfert radiatif en milieu hétérogène. Ces deux équations décrivent le transport des densités d'énergie en espace des phases (la transformée de Wigner du champs de déplacement), et peuvent être reliées à l'équation élastodynamique.

Dans les milieux 1D homogènes, l'évolution de l'estimateur d'erreur proposé est alors étudiée pour des solutions éléments finis obtenues avec différents maillage et différents pas de temps. La distribution des erreurs locales sur la relation de dispersion dans l'espace des phases est décrite. Compte tenu de l'existence de fluctuations numériques supplémentaires causées par les fuites spectrales (spectrale leakage), un filtrage des erreurs en espace des phases est proposé et une erreur résiduelle locale dans le domaine espace-temps (mais globales pour l'espace des phases pour chaque point espace-temps considéré) est définie. La diminution des erreurs locales dans l'espace des phases et dans le domaine espace-temps avec le raffinement permet de valider notre définition des erreurs et la méthode de calcul.

Pour les milieux 1D hétérogènes, différents examples sont proposés. Tout d'abord, le phénomène de localisation est mis en évidence, et les valeurs des paramètres physiques du milieu de propagation pour lesquels le régime de transfert radiatif est valable sont discuté. D'autre part, une comparaison entre l'énergie obtenue par l'équation de transfert radiatif et par l'équation de propagation des ondes permet de valider les outils de calcul des densités énergétiques développés. Enfin, deux erreurs résiduelles sont proposées dans le cas 1D: l'une basée sur les énergies de l'onde prograde et rétrograde, similaire à celles définies dans les milieux homogènes; l'autre basée sur l'énergie totale et l'énergie nette prograde. Les calculs numériques des erreurs pour un exemple de barre 1D avec un maillage fin montrent que les erreurs définies sont relativement faibles par rapport à l'énergie totale et diminuent si une moyenne d'ensemble sur plusieurs barres est considérée, de manière cohérente avec l'obtention de l'équation de transfert radiatif à partir de l'équation d'ondes. Cela permet de valider notre proposition de définition des erreurs pour les solutions d'ondes numériques en régime mésoscopique à haute fréquence.

Dans le cas hétérogène, les termes croisés et les fluctuations numérique perturbent le calcul de la transformée de Wigner, ce qui influence l'estimation des distributions d'erreurs en espace des phases. Afin de réduire cette influence et d'obtenir une estimation des erreurs plus fiable, un filtrage des erreurs résiduelles en termes de STFT a été proposé par la convolution de l'équation de transfert radiatif avec la transformée de Wigner d'une fonction de fenêtrage. La comparaison entre la STFT et la transformée de Wigner pour les champs d'ondes a montré que les termes croisés sont largement réduits. Les résultats numériques ont montré que ces erreurs résiduelles filtrées sont toujours relativement faibles par rapport à l'énergie totale et qu'elles diminuent à mesure que le nombre de réalisations aléatoires augmente. Ce filtrage permet en particulier de réduire les termes croisés accumulés en basse fréquence. En plus, la décroissance d'erreurs avec le raffinement a été observée pour les fronts d'ondes cohérentes mais c'est moins évidente pour ceux d'ondes incohérentes. Ce point reste donc à améliorer.

En ce qui concerne les futures travaux, pour l'estimateur explicite, il faut proposer de nouvelles reconstructions en espace et en temps qui possèdent un meilleur comportement asymptotique avec le raffinement de la discrétisation en espace et en temps. D'autre part, pour les erreurs énergétiques, des efforts doivent être faits pour comprendre les phénomènes exprimés à travers des résidus autour des fronts d'ondes incohérentes afin de répondre aux questions qui restent ouvertes. Il sera aussi intéressant d'appliquer les approches développées aux cas 2D ou 3D.

Titre : Méthodes d'analyse et de modélisation pertinentes pour la propagation des ondes à l'échelle méso dans des milieux hétérogènes

Mots clés : propagation des ondes élastiques, élément fini, estimation d'erreurs, ondes à hautes fréquences, équation de transfert radiatif, milieux hétérogènes

Résumé : Les travaux de la présente thèse portent sur l'estimation d'erreur *a posteriori* pour les solutions numériques par éléments finis de l'équation des ondes élastiques dans les milieux hétérogènes. Deux types d'estimation ont été développés. Le premier considère directement l'équation élastodynamique et conduit à un nouvel estimateur d'erreur *a posteriori* explicite en norme L^∞ en temps. Les principales caractéristiques de cet estimateur explicite sont l'utilisation de la méthode de résidus et le développement de reconstructions en temps et en espace selon les différentes régularités exigées par les différents termes contribuant à l'obtention d'une borne supérieure. L'analyse numérique de cet estimateur dans le cas des maillages uniformes montre qu'il assure bien une borne supérieure mais avec une propriété asymptotique qui reste à améliorer. Le deuxième type d'estimateur d'erreur est développé dans le contexte de la propagation des ondes à haute fréquence dans des milieux hétérogènes à l'échelle mésoscopique. Il s'agit d'une nouvelle erreur en résidus basée sur l'équation de transfert radiatif, qui est obtenue par un développement asymptotique multi-échelle de l'équation d'onde en utilisant la transformation de Wigner en espace-temps. Les résidus sont exprimés en termes de densités énergétiques calculés dans l'espace des phases pour les solutions d'onde numériques transitoires par éléments finis. L'analyse numérique de cette erreur appliquée aux milieux homogènes et hétérogènes en 1D a permis de valider notre approche. Les champs d'application visés sont la propagation des ondes sismiques dans les milieux géophysiques ou la propagation des ondes ultrasonores dans les milieux polycristallins.

Title : Relevant numerical methods for meso-scale wave propagation in heterogeneous media

Keywords : elastic wave propagation, finite element, error estimator, high frequency waves, radiative transfer equation, heterogeneous media

Abstract : This thesis work deals with *a posteriori* error estimates for finite element solutions of the elastic wave equation in heterogeneous media. Two different *a posteriori* estimation approaches are developed. The first one, in a classical way, considers directly the elastodynamic equation and results in a new explicit error estimator in a non-natural L^∞ norm in time. Its key features are the use of the residual method and the development of space and time reconstructions with respect to regularities required by different residual operators contributing to the proposed error bound. Numerical applications of the error bound with different mesh sizes show that it gives rise to a fully computable upper bound. However, its effectivity index and its asymptotic accuracy remain to be improved. The second error estimator is derived for high frequency wave propagation problem in heterogeneous media in the weak coupling regime. It is a new residual-type error based on the radiative transfer equation, which is derived by a multi-scale asymptotic expansion of the wave equation in terms of the spatio-temporal Wigner transforms of wave fields. The residual errors are in terms of angularly resolved energy quantities of numerical solutions of waves by finite element method. Numerical calculations of the defined errors in 1D homogeneous and heterogeneous media allow validating the proposed error estimation approach. The application field of this work is the numerical modelling of the seismic wave propagation in geophysical media or the ultrasonic wave propagation in polycrystalline materials.